THE UNIVERSITY OF CHICAGO

INTERACTIONS BETWEEN NITROGEN-BASED SPIN DEFECTS IN DIAMOND

A DISSERTATION SUBMITTED TO
THE FACULTY OF THE PRITZKER SCHOOL OF MOLECULAR ENGINEERING
IN CANDIDACY FOR THE DEGREE OF
DOCTOR OF PHILOSOPHY

BY
JONATHAN CHARTON MARCKS

CHICAGO, ILLINOIS
AUGUST 2023

To Shira, and the long life ahead of us

Where we're going, we don't need roads.

TABLE OF CONTENTS

LIST OF FIGURES

LIST OF TABLES

LIST OF PUBLICATIONS

This thesis represents the motivations, results, and conclusions from the following works:

1. Relaxation Mechanisms of a Single Dark Electron Spin in Diamond. **J. C. Marcks**, M. Onizhuk, Y.-X. Wang, B. Soloway, M. Fukami, N. Delegan, F. J. Heremans, A. A. Clerk, G. Galli, and D. D. Awschalom.

2. Predictive Methods for Low-Dimensional Electron Spin Bath Synthesis in Diamond. **J. C. Marcks***, M. Onizhuk*, N. Delegan, Y.-X. Wang, M. Fukami, M. Watts, A. A. Clerk, F. J. Heremans, G. Galli, and D. D. Awschalom.

3. A Roadmap for Quantum Interconnects. D. D. Awschalom, . . . , **J. C. Karsch (Marcks)**, et al.. United States (2021). https://doi.org/10.2172/1900586 [13]

4. Tunable and Transferable Diamond Membranes for Integrated Quantum Technologies. X. Guo, N. Delegan, **J. C. Karsch (Marcks)**, Z. Li, T. Liu, R. Shreiner, A. Butcher, D. D. Awschalom, F. J. Heremans, and A. A. High. *Nano Lett.* **12**, 10392 (2021). https://doi.org/10.1021/acs.nanolett.1c03703 [97]

Other publications:

5. Magnon-mediated qubit coupling determined via dissipation measurements. M. Fukami, **J. C. Marcks**, D. R. Candido, L. R. Weiss, B. Soloway, S. E. Sullivan, N. Delegan, F. J. Heremans, M. Flatté, and D. D. Awschalom.

ACKNOWLEDGMENTS

It goes without saying that I owe so much of the success of my PhD to my advisor, David Awschalom (and I owe the rest to everyone else who will be mentioned here). The research environment that David fosters in his group is truly unique; it encourages you to strike out on your own and forge your own path but at the same time collaborate heavily with those around you. I knew when I joined David's group that I would need to make a lot of decisions for myself. What I did not appreciate then is how much that independence would contribute to my growth as a scientist. The ability to propose an idea to David and have him tell you that you should absolutely pursue it is incredibly empowering, as is the opportunity to succeed on your own merit. And this is to say nothing of David's vision. I have literally spent years not understanding the point of some things our group was doing until David presented results in a cohesive way that made me realize how everything fit together. The track record of impactful research produced in David's group is a testament to his decisive understanding of the challenges and opportunities in the fields of spintronics and quantum information, and I hope to one day achieve such clarity.

Myriad thanks are also due to Joseph Heremans, Staff Scientist at Argonne National Laboratory, and effectively my second advisor (although this was never made official...). Joe took me under his wing when I first joined David's group and taught me how to be an NV scientist. Without his guidance in understanding ODMR results and learning about the diamond growth techniques at our disposal, my PhD would not have happened (this will be a common theme). I have been lucky to build such a strong relationship with Joe these past six years, and do not take for granted how critical it has been to my success.

I also must thank Alex High and Aash Clerk for agreeing to be on my thesis committee. The research coming out of Alex's group makes me go "wow" and I am honored to have been able to collaborate with him on some of it. I look forward to even more collaborations in the future. I took a class with Aash basically by accident, as it was the very beginning of the

COVID lockdown and I needed something to do. Little did I know that the material Aash was interested in teaching and the compelling way in which he taught it would totally change the course of what I was interested in researching and would redirect my efforts for the next three years (still ongoing). The focus in this thesis on understanding the microscopics of spin baths in diamond is in no small part influenced by my interactions with Aash.

Thanks are also due to those inside and outside the Awschalom Group that I worked closely with these past six years. Nazar Delegan at Argonne has been a constant source of camaraderie and knowledge (and diamond samples). To have such a close relationship with the person who grows your samples is truly special and has meant I've learned twice as much as I otherwise would have, and could tell you exactly how the samples studied in this thesis went from carbon and nitrogen atoms to single qubit measurements. I had no intention when I started grad school of knowing so much about diamond growth, but I see now that I would not be as well situated to do quantum science without working with Nazar. Masaya Fukami and Ben Soloway have both been stellar fellow grad students. Masaya always knows the right question to ask and isn't satisfied until you can prove what you're saying from first principles with at least one Hamiltonian. Working with him has no doubt made me a better and more precise physicist. It has been very valuable to first mentor Ben and now work with him as an equal. Every time I talk to Ben I clarify my ideas and gain a better appreciation for what I'm trying to do. Without my theory and computational collaborators, Nikita Onizhuk in the Galli Group and Yuxin Wang in the Clerk Group, I would know, to good approximation, nothing. I've enjoyed all our noise spectroscopy meetings these past couple years, especially the ones where my same theory questions are answered over and over, and *especially* the ones where we figured out the right place for factors of 2π.

The vibes in the group would not be the same without Grant Smith, Elena Glen, and Pratiti Deb, who have all been very much friends first and colleagues second. Grant has an uncanny ability to take-in and synthesize vast amounts of scientific literature and have more opinions about the direction of quantum science than I do in total. From our fledgling early-grad school projects that have failed to future collaborations that will hopefully succeed, I always look forward to time spent with Grant in and out of the lab. Elena surely deserves an award for biggest improvement in confidence throughout grad school. To see Elena graduate so technically proficient and confident in the lab is inspiring. I had the pleasure of living with Pratiti my first two years in Chicago and, more importantly, learning to navigate grad school with her. Pratiti, like Grant, always has opinions (in a good way, I swear, I value opinions!), and her opinions about science and UChicago have helped me clarify my views of the world. Leah Weiss, Yeghishe Tsaturyan, Sam Bayliss, and Gary Wolfowicz, fearless postdocs, have contributed so much to our lab and my growth as a scientist through their scientific vision, supportive mentoring, and opinions about American [attempts at] pastries. I always value their insights and look forward to their future successes. Chris Anderson, Paul Jerger, Berk Kovos, and Peter Mintun, all former fellow grad students, set a high standard for combining science and friendliness that I aspire to. Chris in particular deserves thanks for the many car rides down from the northside full of sage senior grad student advice. I count myself lucky to have worked with Leah and Chris on the beginnings of the Open Quantum Initiative, which they have spearheaded and turned into a full-fledged summer research fellowship starting from nothing but a book club in the summer of 2020. As Grant is fond of saying, "it's important to note that when you're in your n^{th} year of grad school, you've only *been here* for $n-1$ years," and as we've gotten on in our years there are more and more impressive and promising younger students around. I look forward to everything that Nolan, Joseph, Swathi, Chris E., Jacob, Sagar, Marquis, José, Michael, Chloe, and Cyrus (in alphabetical order) will accomplish, and I'm glad that I'll still be around ERC to see and take part in it. I also had the opportunity to work with two undergraduate students, Michael Haas and Maya Watts, who are now on their own PhD paths and will certainly do great.

In the vein of laying the groundwork for future accomplishments, I also must thank my former mentors at Cornell and Somers High School, Prof. Greg Fuchs, Jason Bartell, and Greg Horrace, for demonstrating early-on how to pursue science.

The Jewish community in Lakeview, Hyde Park, and Chicago writ large has been an amazing support system throughout my time in Chicago, whether through food, prayer, or ample opportunities to learn about things that are not physics. I had no idea what and who I would find when I moved to Chicago but I can't imagine it any other way.

It would be impossible to write acknowledgements without thanking my parents, Steve and Diane Karsch, and my brother Harris, for instilling in me a love of and curiosity about science and setting me on a path towards my PhD. Please accept this document in lieu of any missed birthday and holiday gifts over the past six years. My grandparents Charlotte and David (z"l) have been a steady source of support over the years, and I always aim to make them proud.

My in-laws have all played important roles in my time at UChicago, or more specifically, all the time I've been able to spend away from UChicago at holidays and other various non-physics activities (although biking is arguably a physics activity). Shira and I lived with Mindy and Larry for the better part of 2020, and for that alone they deserve heaps of thanks. Mindy in particular showed great aptitude for physics when she posed to me a complex question about gaseous emissions from bodies in automobiles with the windows down, the second time we met. Sammy, Leah, and Larry have shown lots of support but not the same inquisitiveness; hopefully there is still time for Mindy and I to teach it to my nephew.

The first night I met my now-wife, Shira, I tried to explain some physics to her. Little did she know that five years later she would have to sit at my defense and, once again, be bored by me talking about physics. Lucky for me, in the intervening time her support has been unwavering, and she never doubted that I would reach the end, even when fewer than no things were working in lab and I couldn't even estimate how much longer this would take.

Her contribution to my development of professional skills is also unmatched. Any piece of workplace advice I have ever given out is attributed 100% to Shira. Unlike many things in this thesis, my appreciation and love for her is unquantifiable.

תם ונשלם שבח לאל בורא עולם

ABSTRACT

Defect center-based spin qubits in solid-state materials show great promise as quantum sensors and nodes in quantum networks. The success of these applications relies on precise control and understanding of the qubit host material and noise environment, which ultimately dictate qubit coherence. The nitrogen vacancy (NV) center in diamond is a particular defect qubit with a robust spin-photon interface and long spin relaxation times, enabling a range of advances in quantum information science. However, open questions remain regarding the surrounding host material. In particular, while it is possible to routinely grow single crystal diamond with nitrogen doping, to synthesize NV centers, a reliable method for characterizing this doping under growth parameters relevant for many NV applications is lacking. Furthermore, unconverted nitrogen spins (P1 centers) constitute a major source of decoherence in the diamond lattice. While P1 center spin properties have been studied in bulk, there are few experiments that probe single P1 centers. Characterizing single P1 spins will advance understanding of P1-induced decoherence as well as aid in the implementation of P1 centers as auxiliary qubits in applications of the NV center.

In this thesis, I will describe our recent studies of interactions between the NV center and nearby P1 electron spins. After an introduction into quantum science and engineering in **Ch. 1**, I describe the two defect centers in **Ch. 2**. I then lay the groundwork for the studies in this thesis from two very different perspectives: In **Ch. 3** I review a theoretical treatment of noise and spin baths; in **Ch. 4** I discuss the details of plasma-enhanced chemical vapor deposition (PE-CVD) diamond growth and NV center synthesis that we implement in our studies. The results in **Ch. 5** and **Ch. 6** require an appreciation of these two disparate approaches to the systems we study. In **Ch. 5** I present quantitative computational studies of NV decoherence at the length and density scales relevant for synthesizing single NV centers, providing a reference for future NV synthesis, as well as revealing coherence behavior dependent on the spin bath dimensionality. These data are then applied to characterize nitrogen

density in-situ via a statistical model, bypassing the need for unreliable bulk characterization techniques. In **Ch. 6** I present measurements of spin bath dynamics at the single-spin level as a means to understand microscopic processes underlying central spin decoherence. I describe a polarization- and time-resolved measurement technique of a strongly coupled NV-P1 system that enables a probe of P1 polarization decay under arbitrary microwave and optical drives. These measurements reveal decay mechanisms on the single-spin level, allowing us to address open questions about the behavior of P1 spin baths in diamond.

CHAPTER 1

INTRODUCTION

The world of quantum information science (QIS) – let us loosely define this as the research field in which a project, at some point, necessitates writing down a non-classical Hamiltonian – has exploded in the past five to ten years, becoming remarkably well known in the public sphere for something that has traditionally required acquiring loads of esoteric knowledge to understand. This time has conveniently overlapped with my time in graduate school, making for an interesting time not only learning about engineering quantum systems, but also learning about the growth of a new engineering field. From a national and research funding perspective, programs are now explicitly focused on quantum science research, often with the goal of developing new technology that exploits quantum principles, not just gaining a better understanding of the basic underpinnings of the world. This was most evident in the passage of the National Quantum Initiative (NQI) bill, but QIS plays a notable part in other funding programs, and is a component of the more recently passed CHIPS Act. On an academic level, while the "Quantum Science and Engineering" PhD in this department did not even technically exist when I entered the University of Chicago, it is now commonplace for someone to express interest in studying quantum engineering, and job postings for quantum faculty pop-up alongside those in condensed matter and AMO physics.

This all, of course, raises the question of the definition of the field of quantum research. To go by my earlier definition, it has only existed at most since Schrödinger wrote his famous equation (or thereabouts) [236]. On the other hand, some would argue that magnets, dear to my heart, are inherently quantum mechanical; by this reasoning the first quantum engineer was whoever invented compasses, and the first quantum materials scientist lived in the iron age. By a similar reasoning, magnetic resonance imaging (MRI) is a quantum technology, as is classical computing technology, given the need to describe electrons in a lattice with band theory [137]. This is not useful.

We may instead take a less historical, more descriptive look at the field as one with a clear start in the unique properties of single quantum objects [76, 94, 236] and a less clear end in applications to sensing and information technologies [11, 13]. Here we may also see why we talk about quantum science and quantum engineering in the same sentence. A scientific approach might ask how one can better understand and an engineering approach might ask how we can better use, but both fill in gaps of the same story arc. Furthermore, we will find in this thesis that these lines are blurred, and motivations throughout will freely flow between the two. To follow this arc, we can understand the field by delving deeper into how we understand systems that exhibit discrete (read: quantum) energy levels, superposition and coherence, and entanglement; and how we can use such systems to realize advances in sensing, communication, and computing technology.

1.1 Quantum Science

We will first establish language to discuss quantum systems, and two-level systems (TLS) in particular. A given system S (this may be a single particle up to a macroscopic object) may exist in any state $|s\rangle$ contained within its Hilbert space. In quantum mechanics we may calculate physical properties of a system (position, momentum, energy, etc.) with operators that act on the system states [94, 237]. For a given operator $\hat{P}$ there are certain states $\left|s_p\right\rangle$ of the system such that $\hat{P}\left|s_p\right\rangle = p\left|s_p\right\rangle$, where p is a complex number. That is, operating on our state with the $\hat{P}$ operator returns the quantity we are looking for. These states $\left|s_p\right\rangle$ are called eigenstates, or eigenvectors of $\hat{P}$, with eigenvalues p. A result from linear algebra states that if we know the eigenstates of a matrix operator, we can describe the entire space spanned by the eigenbasis [144]. This will be useful for describing quantum systems.

1.1.1 The quantum spin

Let us flesh this out for the prototypical–and in this thesis, most important–two-level quantum system of a quantum spin. The relevant operators for our quantum spin are the Pauli matrices

$$\hat{\sigma}_x = \begin{pmatrix} 0 & 1 \\ 1 & 0 \end{pmatrix}, \ \hat{\sigma}_y = \begin{pmatrix} 0 & -i \\ i & 0 \end{pmatrix}, \ \hat{\sigma}_z = \begin{pmatrix} 1 & 0 \\ 0 & -1 \end{pmatrix}, \tag{1.1}$$

where z denotes the direction along which a symmetry has been broken, usually by applying a magnetic field (which interacts with the spin) along that direction, and x and y are orthogonal directions that form a (lamentably) right-handed coordinate system. These matrices describe the two-level system in three-dimensional space, and will enable us to measure the component of the spin along any axis. To understand how our spin can behave along the magnetic field axis, we first calculate the eigenstates of σ_z. An eigenstate v_i with eigenvalue λ_i is a state such that $\hat{\sigma}_z v_i = \lambda_i v_i$, as written earlier for system S. The two vectors that satisfy this are

$$v_\uparrow = \begin{pmatrix} 1 \\ 0 \end{pmatrix}, \ v_\downarrow = \begin{pmatrix} 0 \\ 1 \end{pmatrix}, \tag{1.2}$$

where the arrow labels will be explained in a moment. We can further calculate the eigenvalues

$$\hat{\sigma}_z v_\uparrow = \begin{pmatrix} 1 \\ 0 \end{pmatrix} = v_\uparrow, \ \lambda_\uparrow = 1 \tag{1.3}$$

and

$$\hat{\sigma}_z v_\downarrow = \begin{pmatrix} 0 \\ -1 \end{pmatrix} = -v_\downarrow, \ \lambda_\downarrow = -1. \tag{1.4}$$

Evidently if our system is in $v_\uparrow$ is takes a definite value $+1$, and if it is in $v_\downarrow$ is takes the value -1. This is why we label the states with arrows: we consider the spin to point either up or down in the magnetic field. In fact, we will label these states $|\uparrow\rangle, |\downarrow\rangle$. As the z-axis is the symmetry-breaking axis of our system, these two states define our TLS. Furthermore, they are orthonormal,

$$\begin{pmatrix} 1 \\ 0 \end{pmatrix} \cdot \begin{pmatrix} 0 \\ -1 \end{pmatrix} = 0 \tag{1.5}$$

1.1.2 Superposition and coherence

How is it actually useful that our system has two-levels, though? It is natural now to say that if our system can be in one of two eigenstates, it can also be in a linear combination, or superposition, of those eigenstates, with coefficients α, because any such state $v = \alpha_{\uparrow} v_{\uparrow} + \alpha_{\downarrow} v_{\downarrow}$ is also in the eigenspace. In quantum mechanics, there is actually no problem with our coefficients being complex numbers, so while we enforce normalization of the coefficient amplitudes such that $\sqrt{|\alpha_{\uparrow}|^2 + |\alpha_{\downarrow}|^2}{=}1$, we can maintain an arbitrary phase between the two, $\phi = \arg \frac{\alpha_{\downarrow}}{\alpha_{\uparrow}}$. This phase makes such states v quantum superpositions, and is essential to every application of quantum mechanics. It is many times convenient to work with another mathematical object called the density matrix, ρ [237], defined for a quantum state $|\psi\rangle$ as

$$\hat{\rho} \equiv |\psi\rangle \langle\psi| \,. \tag{1.6}$$

If our system is in a superposition $|S\rangle = \alpha_{\uparrow} |\uparrow\rangle + \alpha_{\downarrow} |\downarrow\rangle$, the density matrix is

$$\begin{aligned} \hat{\rho} = & \quad \left(\alpha_{\uparrow} |\uparrow\rangle + \alpha_{\downarrow} |\downarrow\rangle\right) \left(\alpha_{\uparrow}^{*} \langle\uparrow| + \alpha_{\downarrow}^{*} \langle\downarrow|\right) \\ = & \quad |\alpha_{\uparrow}|^2 |\uparrow\rangle\langle\uparrow| + |\alpha_{\downarrow}|^2 |\downarrow\rangle\langle\downarrow| + \alpha_{\uparrow}\alpha_{\downarrow}^{*} |\uparrow\rangle\langle\downarrow| + \alpha_{\downarrow}\alpha_{\uparrow}^{*} |\downarrow\rangle\langle\uparrow| \\ = & \quad \begin{pmatrix} |\alpha_{\uparrow}|^2 & \alpha_{\uparrow}\alpha_{\downarrow}^{*} \\ \alpha_{\downarrow}\alpha_{\uparrow}^{*} & |\alpha_{\downarrow}|^2 \end{pmatrix}, \end{aligned} \tag{1.7}$$

where the last line is enabled by keeping track of what eigenstates each matrix entry references. The density matrix is a beautiful way to explore properties of quantum systems.

Before calculating anything, I will first note that the normalization we imposed earlier naturally means that $\mathrm{Tr}(\hat{\rho}) = 1$. It is established to interpret the diagonal values in this matrix as the populations or probabilities of the system in each eigenstate. Thus, we would say there is a $|\alpha_\uparrow|^2$ probability that we are in the $|\uparrow\rangle$ state.

We can furthermore readily calculate the expectation value of our spin operator (or, really, any operator) with ρ as [237]

$$\begin{aligned} \langle \hat{\sigma}_z \rangle = & \quad \mathrm{Tr}(\hat{\rho}\hat{\sigma}_\mathrm{z}) \\ = & \quad \mathrm{Tr}\begin{pmatrix} |\alpha_\uparrow|^2 & -\alpha_\uparrow\alpha_\downarrow^* \\ \alpha_\downarrow\alpha_\uparrow^* & -|\alpha_\downarrow|^2 \end{pmatrix} \\ = & \quad |\alpha_\uparrow|^2 - |\alpha_\downarrow|^2. \end{aligned} \tag{1.8}$$

Evidently the expectation value is the difference in populations in each eigenstate, or the spin polarization. Note that the off-diagonal matrix components have no bearing on this value. Let us rewrite them in a more friendly manner, knowing that the probability $p_i = |\alpha_i|^2$.

$$\alpha_\uparrow\alpha_\downarrow^* = \sqrt{p_\uparrow p_\downarrow}e^{i(\phi_\uparrow - \phi_\downarrow)} \tag{1.9}$$

$$\alpha_\downarrow\alpha_\uparrow^* = \sqrt{p_\uparrow p_\downarrow}e^{i(\phi_\downarrow - \phi_\uparrow)}, \tag{1.10}$$

which we can use to define the "coherence" of our system, which encodes, in some sense, how well we know the phase relationship $\Delta\phi \equiv \phi_\uparrow - \phi_\downarrow$, as

$$W_{\uparrow\downarrow} \equiv \sqrt{p_\uparrow p_\downarrow}e^{i\Delta\phi} \tag{1.11}$$

$$W_{\downarrow\uparrow} = W_{\uparrow\downarrow}^*. \tag{1.12}$$

This leads to a more physically meaningful way to write the density matrix for our TLS

$$\hat{\rho} = \begin{pmatrix} p_{\uparrow} & W_{\uparrow\downarrow} \\ W_{\downarrow\uparrow} & p_{\downarrow} \end{pmatrix}. \tag{1.13}$$

We actually see that density matrices allow us to represent a classical superposition that is not possible to write with our vector format from above. We want to represent, for example, a high temperature thermal state, where the up and down populations are equal and there is no fixed phase relationship,

$$\hat{\rho}_{\text{therm}} = \begin{pmatrix} 1/2 & 0 \\ 0 & 1/2 \end{pmatrix}. \tag{1.14}$$

We can still calculate $\langle\hat{\sigma}_z\rangle$, finding a spin polarization of 0, as expected.

One can imagine that if there is a decay channel for the coherence, one could start in an equal quantum superposition and decay into a thermal state:

$$\frac{1}{2}\begin{pmatrix} 1 & 1 \\ 1 & 1 \end{pmatrix} \rightarrow \frac{1}{2}\begin{pmatrix} 1 & 0 \\ 0 & 1 \end{pmatrix}. \tag{1.15}$$

A formal treatment of this dissipation with a Lindblad master equation approach [150, 167] is beyond the scope of this thesis, and we will generally talk about loss of coherence as it is stated above.

1.1.3 Entanglement

Now, nobody can stop us[1] from adding another system (a second spin). We can now talk about the product-space formed by the two eigenspaces. Without loss of generality, let us

---

[1] I attribute the "nobody can stop us" mentality of physics to Prof. David Kutasov, who fearlessly inserted different forms of the indentity matrix into many derivations.

assume that we have two TLSs with bases

$$E_1 = \{\left|\uparrow\right\rangle_1, \left|\downarrow\right\rangle_1\},\ E_2 = \{\left|\uparrow\right\rangle_2, \left|\downarrow\right\rangle_2\} \tag{1.16}$$

such that the product space is

$$\begin{aligned} E_{1,2} = & \quad E_1 \otimes E_2 & (1.17)\\ = & \quad \{\left|\uparrow_1\right\rangle\left|\uparrow_2\right\rangle, \left|\uparrow_1\right\rangle\left|\downarrow_2\right\rangle, \left|\downarrow_1\right\rangle\left|\uparrow_2\right\rangle, \left|\downarrow_1\right\rangle\left|\downarrow_2\right\rangle\} & (1.18)\\ = & \quad \{\left|\uparrow\uparrow\right\rangle, \left|\uparrow\downarrow\right\rangle, \left|\downarrow\uparrow\right\rangle, \left|\downarrow\downarrow\right\rangle\}. & (1.19) \end{aligned}$$

Note that these are entirely different than when we had ↑ next to ↓ in some fashion above; we are now talking about two separate particles that can each be either up or down. Or. . . are we?

Each of the eigenstates of this product space, evident above, can be separated into a product state, the product of the state of particle 1 with the state of particle 2. But any linear combination of these states is also a valid state. Can the state $\left|S_1S_2\right\rangle = \frac{1}{\sqrt{2}}\left(\left|\uparrow\uparrow\right\rangle + \left|\uparrow\downarrow\right\rangle\right)$ be written as a product state? Yes.

$$\begin{aligned} \left|S_1S_2\right\rangle &= \frac{1}{\sqrt{2}}\left(\left|\uparrow\uparrow\right\rangle + \left|\uparrow\downarrow\right\rangle\right) & (1.20)\\ &= \frac{1}{\sqrt{2}}\left|\uparrow_1\right\rangle\left(\left|\uparrow_2\right\rangle + \left|\downarrow_2\right\rangle\right). & (1.21) \end{aligned}$$

It is separable. How about the state $\left|S_1S_2\right\rangle = \frac{1}{\sqrt{2}}\left(\left|\uparrow\uparrow\right\rangle + \left|\downarrow\downarrow\right\rangle\right)$? It is not possible; this state is non-separable, or, as is more fun to say, entangled. Heuristically, we will only ever find both spins up or both spins down. It is very easy to show mathematically that we will never find this entangled system in the state $\left|\uparrow\downarrow\right\rangle$ because when we project our system onto that state we get

$$\langle S_1 S_2 | \uparrow\downarrow \rangle = \frac{1}{\sqrt{2}} \left(\langle \uparrow\uparrow | + \langle \downarrow\downarrow | \right) | \uparrow\downarrow \rangle \tag{1.22}$$

$$= \frac{1}{\sqrt{2}} (1 \cdot 0 + 0 \cdot 1) \tag{1.23}$$

$$= 0. \tag{1.24}$$

1.1.4 Adding two electron spins

We now look at a prototypical "real-world" example of adding together two electrons. We will analyze this system using Clebsch-Gordon coefficients [231, 277]. Each electron is a total spin=1/2 system with possible spin states of $m_s = \pm 1/2 (\uparrow / \downarrow)$. Consulting a coefficient table, adding two spin-1/2 systems gives us

$$\frac{1}{2} \otimes \frac{1}{2} = 3 \cdot 1 \oplus 1 \cdot 0, \tag{1.25}$$

that is, three spin-1 states and one spin-0 state. Specifically, we have the following spin-1 states

$$\left| T_{\Uparrow} \right\rangle = | \uparrow\uparrow \rangle \tag{1.26}$$

$$\left| T_{\Downarrow} \right\rangle = | \downarrow\downarrow \rangle \tag{1.27}$$

$$| T_0 \rangle = \frac{1}{\sqrt{2}} \left(| \uparrow\downarrow \rangle + | \downarrow\uparrow \rangle \right) \tag{1.28}$$

and the following spin-0 state

$$| S_0 \rangle = \frac{1}{\sqrt{2}} \left(| \uparrow\downarrow \rangle - | \downarrow\uparrow \rangle \right), \tag{1.29}$$

where the first arrow in each ket refers to the first electron and the second to the second.

We see the spin-1 states form a triplet manifold with three states of different spin projections

$$
\begin{aligned}
\left\langle T_{\Uparrow}\right| (\hat{S}_{z1} + \hat{S}_{z2}) \left|T_{\Uparrow}\right\rangle = &\quad 1 && (1.30)\\
\left\langle T_{\Downarrow}\right| (\hat{S}_{z1} + \hat{S}_{z2}) \left|T_{\Downarrow}\right\rangle = &\quad -1 && (1.31)\\
\langle T_0| (\hat{S}_{z1} + \hat{S}_{z2}) |T_0\rangle = \langle T_0| (1/2 - 1/2) |T_0\rangle = &\quad 0 && (1.32)\\
& && (1.33)
\end{aligned}
$$

forming an effective spin-1 (three-level) system and motivating our labeling, while the single spin-0 state forms a singlet manifold with spin projection 0.

1.1.5 Spins in magnetic fields

It is worth noting for the future discussion of real qubit systems how these states behave in magnetic fields. First, consider a static magnetic field $\mathbf{B} = B_z\hat{\mathbf{z}}$. An electron spin state will shift in energy in response to this field by the Zeeman effect [292]

$$\Delta E = -|\gamma_e| S_z B_z, \tag{1.34}$$

where γ_e is the electron gyromagnetic ratio and S_z is the spin projection on the z-axis. Evidently, $\left|T_{\Uparrow}\right\rangle$ shifts down with increasing magnetic field, $\left|T_{\Downarrow}\right\rangle$ shifts up, and $|T_0\rangle$ and $|S_0\rangle$ do not shift. In particular, this now means that two states that were previously degenerate in energy are now split by a Zeeman energy. This will allow, for example, the definition of a TLS out of a triplet manifold, or as we will like to say, an effective spin-1/2 system.

1.2 Quantum Engineering

The above features of quantum mechanics have been known for over one hundred years, and have been true, well, for forever[2]. But in recent decades physicists have come up with experiments that take advantage of these properties to a technological end [64, 115, 129, 163, 219, 259]. I would like to broadly refer to these ends–quantum sensing, quantum computing, and quantum communication–as quantum engineering. I will provide a small taste here of how each application is made possible by the features covered in the previous section rather than provide an exhaustive overview of each field, which may be found in the literature.

1.2.1 Quantum sensing

The conceit of quantum sensing is that no TLS is perfectly isolated from its environment [65], and thus at some point its state populations and coherences–captured in its density matrix–must decay. If the decay sources are not known and are unwanted, we call this a bug: decoherence [167, 234]. If we know what is causing decay, and can moreover extract information about this decay source, it is a feature: sensing [45, 65]. This concept is of course not new to the field of quantum; classical sensing can operate in a broadly similar way. What is new here is the use of coherence–a quantum property–as a sensor.

Let us now consider how a TLS, composed of electron spins, may be used to sense a magnetic field. This approach applies in general to any system and sensing target with a linear coupling. We will initialize our system in a superposition of two states $|S\rangle = \frac{1}{\sqrt{2}}\left(|0\rangle + |1\rangle\right)$, where each state has a different spin projection, s_0 and s_1, respectively. We stated earlier than a magnetic field shifts the energy of a spin state. Applying the time-dependent Shrödinger equation to our system with the Hamiltonian $\hat{\mathcal{H}}$ given by the magnetic

---

[2] To good approximation; I'm not a cosmologist.

field shift,

$$\begin{align}
\hat{\mathcal{H}}\left|S\right\rangle &= -i\hbar\frac{d\left|S\right\rangle}{dt} \tag{1.35}\\
-|\gamma_e|\hat{S}_z B_z\left|S\right\rangle &= -i\hbar\frac{d\left|S\right\rangle}{dt} \notag\\
\left|S\right\rangle &= \frac{1}{\sqrt{2}}e^{i\hbar|\gamma_e|\hat{S}_z B_z}\left(\left|0\right\rangle+\left|1\right\rangle\right) \notag\\
&= \frac{1}{\sqrt{2}}\left(e^{i\hbar|\gamma_e|s_0 B_z t}\left|0\right\rangle+e^{i\hbar|\gamma_e|s_1 B_z t}\left|1\right\rangle\right) \notag\\
&= \frac{1}{\sqrt{2}}\left(\left|0\right\rangle+e^{i\hbar|\gamma_e|(s_1-s_0)B_z t}\left|1\right\rangle\right) \tag{1.36}\\
& \tag{1.37}
\end{align}$$

where in the last line we ignore the global phase that is pulled out of the parentheses. Evidently our system acquires a quantum phase, proportional to the difference in spin projection of the two states and directly proportional to the magnetic field strength,

$$\phi = \hbar|\gamma_e|(s_1-s_0)B_z. \tag{1.38}$$

We can calculate the time-dependent density matrix of our state

$$\begin{align}
\left|S\right\rangle &= \frac{1}{\sqrt{2}}\left(\left|0\right\rangle+e^{i\phi t}\left|1\right\rangle\right) \tag{1.39}\\
\hat{\rho}_S &= \left|S\right\rangle\left\langle S\right| \notag\\
&= \frac{1}{2}\begin{pmatrix} 1 & e^{-i\phi t}\\ e^{i\phi t} & 1\end{pmatrix} \tag{1.40}
\end{align}$$

and find the magnetic field *only* affects the state coherence, not the state populations. By measuring the quantum coherence, we can likewise measure the magnetic field value.

Quantum-enhanced sensing limits

A common measurement method will project the state coherence onto a population of a state $|S_{read}\rangle$, such that

$$|S_{read}\rangle = \frac{1}{2}\left[(e^{i\phi}+1)\,|0\rangle + (e^{i\phi}-1)\,|1\rangle\right] \tag{1.41}$$

$$p_{|0\rangle} = \frac{1}{2}(1+\cos\phi) \tag{1.42}$$

$$= \cos^2\frac{\phi}{2} \tag{1.43}$$

where the population in a real experiment will be measured N times to be some experimental value x_j, which is averaged in the usual way as $\sum_{j=1}^{N} x_j/N$ [90]. The associated error Δ is given by$\Delta x/\sqrt{N}$, where Δx is the error from a single measurement and is the same for each x_j [90]. We find a $1/\sqrt{N}$ dependence of error on the number of measurements.

Consider now how this interferometry progresses if we begin with multiple qubits in a highly entangled state. Without loss of generality, we will assume that all qubits are physically the same, i.e., all electrons. We begin in the GHZ state of N qubits [93] and follow the treatment in Ref. 90. Note that N here is the same as the number of independent measurements considered above.

$$|\psi_{in}\rangle = \frac{1}{\sqrt{2}}\left(|0\cdots 0\rangle + |1\cdots 1\rangle\right) \tag{1.44}$$

such that after some time evolution in an external field we acquire a phase $N\phi$

$$|\psi_{out}\rangle = \frac{1}{\sqrt{2}}\left(|0\cdots 0\rangle + e^{iN\phi}\,|1\cdots 1\rangle\right). \tag{1.45}$$

If we can perform a simultaneous measurement on all the qubits, the probability of being in $|0\cdots 0\rangle$ is now $\cos^2\frac{N\phi}{2}$ and the error is now $\propto 1/N$. This demonstrates that, in principle, a sensing experiment with N entangled qubits will be more precise than N independent measurements on a single qubit by a factor of $1/\sqrt{N}$ [90]. This is to say nothing of the experimental challenges in implementing this [282].

1.2.2 Quantum computing

Quantum computing [189] is generally considered to be quite important and also very difficult. That is, demonstrating quantum algorithms on quantum computers that truly exceed the capabilities of classical supercomputers is thought to require orders of magnitude more physical qubit systems than has currently been demonstrated. I seek here to only demonstrate an aspect of computing that is unlocked by working with quantum rather than classical bits. In classical computing we have bits that occupy either a (0) or a (1) state, where we have chosen to refer to the classical states with boring parentheses. We can examine the truth table for a common operation between two bits, a controlled-NOT gate, where the state of the second bit flips if the state of the first is (1):

$$\begin{array}{c|c} (00) & (00) \\ (01) & (01) \\ (10) & (11) \\ (11) & (10) \end{array}$$

We can likewise look at the same table for two qubits that can occupy $|0\rangle$ or $|1\rangle$

$$\begin{array}{c|c} |00\rangle & |00\rangle \\ |01\rangle & |01\rangle \\ |10\rangle & |11\rangle \\ |11\rangle & |10\rangle \end{array}$$

This appears boring, as it looks like we have achieved the same results. But now recall that quantum bits–qubits–can be in quantum superpositions of states, so our control qubit is not restricted to only $|0\rangle$ or $|1\rangle$. Consider if our control qubit starts in the arbitrary superposition $a|0\rangle + b|1\rangle$ and our second qubit begins in the $|0\rangle$ state, such that our two qubit system begins in $a|00\rangle + b|10\rangle$. Note that this is a separable state. Now, under our CNOT gate, the state becomes

$$a|00\rangle + b|10\rangle \rightarrow a|00\rangle + b|11\rangle, \tag{1.46}$$

in general a non-separable state. This of course does not on its own constitute a quantum computer, but it does illustrate how a fundamental two-(qu)bit operation acts radically differently when applied to a quantum system.

1.2.3 Quantum communication

As with the previous two applications, quantum communication is broadly the same as classical communication: transmit information, but make it quantum. We may consider quantum information to be information stored in a qubit, rather than a bit, and can imagine that this may be useful for connecting quantum systems such as quantum computers or quantum sensors. Consider two qubits that are entangled in a state $\frac{1}{\sqrt{2}}(|00\rangle + |11\rangle)$ but are spatially separated from each other by some technologically relevant distance, for example different rooms in a building or different buildings in a city. The mechanism by which this distributed entanglement occurs is beyond the scope of this thesis, but generally requires something called a "flying qubit," or a qubit that can coherently travel through space, usually a photon. We now measure the state of the first qubit. Of course, the two qubits are entangled, so we are not actually measuring the first qubit to be in either $|0\rangle$ or $|1\rangle$; we are measuring the composite system to be in either $|00\rangle$ or $|11\rangle$. If we measure the first qubit to be in $|0\rangle$, then we actually know the second qubit is also in $|0\rangle$, and likewise for $|1\rangle$. In this way, we can say that, upon a projective measurement of qubit one, information of its quantum state has also appeared on qubit two. There must be some accompanying classical information, for example about what state the qubits started in, transmitted as well to interpret the state of qubit two and properly transmit information. Nonetheless, we can see that entangled pairs of qubits can enable the communication of information about quantum states.

1.3 Motivation

I would like to situate the motivation of this thesis as quantum science for the sake of quantum engineering. What does this mean? I will generally be concerned with designing and measuring quantum systems, usually from a materials science perspective, but will focus solely on the characterization of these systems, rather than pursuing real applications. This can broadly be viewed through the lens of addressing challenges that arise to quantum engineering, presented in Fig. 1.1 specifically for generating multi-qubit entangled states that may be used for quantum sensing, although many of these apply equally well to computing and communication challenges.

Two are very explicitly materials-focused: material fabrication and surface processing. Many implementations of quantum science are hosted in material systems [62] (excluding ions/atoms and free-space photons), and materials have traditionally not been designed with quantum applications in mind. For example, a classical computing element may operate on the basis of the average behavior of roughly a mole of electrons in the device, while a quantum element may need to maintain the coherence of a single electron. These are operating at very different scales, and tolerances for material defects, both structural and doping, that may be acceptable for classical devices could be detrimental to quantum ones. Furthermore, functional quantum technologies will require scalable manufacturing at this same tight tolerance. This requires fabrication techniques to be developed with the requirements of quantum systems at the forefront. A related challenge lies in the surface of materials. Surfaces are generally weird; you are in your material system with your bulk properties, and then suddenly you are not. This can cause a problem. Perhaps the behavior of your system hosted in your crystal is different near surfaces where the host material stops. Perhaps the exposed surface is "noisy" and affects the coherence of a nearby qubit. Many quantum sensing applications require a sensing qubit to be near the host material surface in order to sense some target system external to the host, and many devices are necessarily fabricated with qubits near a surface to facilitate interaction with an external field, such as a photon. In either case, surface noise sources present a major challenge to quantum engineering, and process development is necessary to ensure low-noise material surfaces.

Another aspect of materials engineering is designing devices that can mediate interactions between disparate qubits, whether in real space or energy space, so-called quantum interconnects [11]. These types of devices are necessary, for example, for transmitting quantum information from a quantum computer to a quantum memory node for communication with another quantum computer. Another possibility is to mediate entanglement between multiple sensor qubits on a single chip, enabling a multi-qubit sensing module that does not require the sensing qubits to natively interact with one another. The development of quantum interconnects is beyond the scope of this thesis.

The two challenges presented on the right of Fig. 1.1 are more concerned with the interactions between the qubit and the surrounding environment, and the issues that arise when attempting to couple the qubit to a specific target system within that environment with coupling g. This target may be another qubit, a sensing target, or a mode in an interconnect device. In all cases, however, the qubit and the target are not the only systems in the universe; the rest of the environment is generally composed of other systems that couple to the qubit in a similar way to that of the target system. For example, coupling a spin to a photonic cavity also brings the spin into contact with free-space photonic modes, and attempting to couple an electron spin to a single nearby nuclear spin (in some host material) also must contend with coupling to other nuclear spins. This can be summed up by the statement "nature never lets you win," presented schematically in the top-right panel of Fig. 1.1, where we see that increasing a desired coupling, g, tends to increase undesired couplings that contribute to a T_2 decoherence, which diminishes the ability to resolve the desired coupling.

We can quantify this with a simple model of an environment composed of N identical spins all coupled with different strengths g_i to a central spin. Consider our qubit to be in a superposition; we can now treat the effect of these environment couplings as a phase added to the qubit's coherence, where the state of the qubit is

$$\begin{aligned} |S\rangle = & \quad \frac{1}{\sqrt{2}}\left(|0\rangle + e^{i\sum_{i=0}^{N} g_i t}\,|1\rangle\right) \\ = & \quad \frac{1}{\sqrt{2}}\left(|0\rangle + e^{ig_0 t}e^{i\sum_{i=1}^{N} g_i t}\,|1\rangle\right) && (1.47) \\ W(t) \equiv & \qquad e^{ig_0 t}e^{i\sum_{i=1}^{N} g_i t} && (1.48) \end{aligned}$$

where between the first and second line we pull out the coupling we wish to resolve and in the third line we define our coherence W. The effect of the unresolved couplings (here for $i \geq 1$) is to introduce some decoherence (See. Ch. 3), such that there is a challenge to measure the coupling to environment spin 0 before the amplitude of our coherence dies away. This may be addressed from a materials perspective–growing qubit systems that control for this coupling–or a control perspective–designing control schemes that isolate the desired coupling.

The conceit of the final challenge presented in Fig. 1.1 is that the environment can be leveraged as a potential resource for quantum information processing. Perhaps the environment presents a new means for generating entanglement between two quantum systems, or will enable new ways to protect qubit coherence. This requires both theoretical and experimental work to better understand.

Applications of NV centers face the myriad of challenges outlined above. Developments ranging from theoretical to material are needed to further advance NV-based quantum sensing and quantum communication. This thesis is broadly concerned with this task.

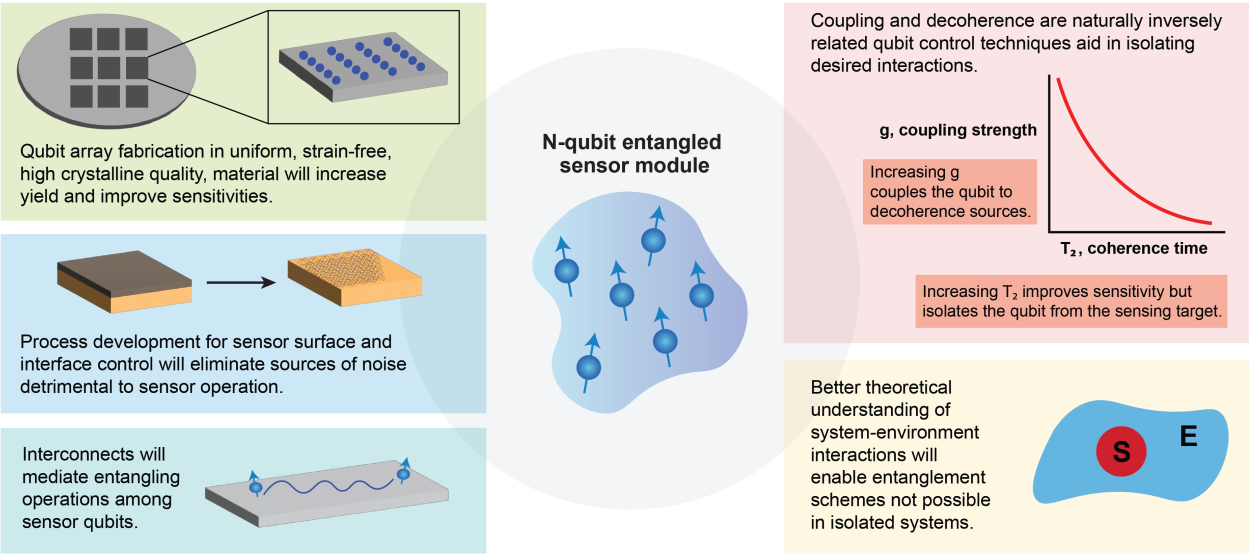

Figure 1.1: **Challenges in QIS.** A variety of challenges across a range of disciplines exist when considering long-term QIS goals such as multi-qubit entangled sensors. Figure reproduced from Ref. 13.

CHAPTER 2

NITROGEN QUBITS IN DIAMOND

2.1 Introduction

In this thesis I will be restricted to one material and two quantum systems hosted in said material. The material is diamond, a wide-bandgap semiconductor and carbon allotrope that has been studied as much for its industrial and technological applications as for its gemological ones [210, 290], going as far back as the 13th to 17th centuries [161, 216]. The quantum systems are the negatively charged nitrogen-vacancy (NV^-) center and the neutrally charged substitutional nitrogen ($\mathrm{N_s^0}$, P1) center, shown in Fig. 2.1 on the left and right, respectively. These are introduced into the diamond lattice either naturally or through various incorporation techniques, covered in Ch. 4.

The NV center consists of a nitrogen atom sitting on a carbon site next to a vacancy on a carbon site [58, 59] (it can be written more appropriately as $\mathrm{N_C V_C}$). The nitrogen brings an extra electron to the bound system, and another electron from the environment charges the defect, resulting in a six electron system [165]. The electron density is shown approximately in Fig. 2.1, left, with shaded green orbs, based on Ref. 30. NV centers may be oriented along any of the $\langle 111 \rangle$ crystal axes. Further details of the NV center not found in this chapter may be found in relevant reviews [69, 88]. The P1 center is simply a nitrogen atom sitting on a carbon site with its extra electron acting as a spin-1/2 system [73, 245]. The P1 center is far less studied than the NV center in QIS, and its properties are rarely investigated on its own merit in this context. The electron density in Fig. 2.1, right, is meant to schematically show that under the Jahn-Teller distortion [57], discussed in Sec. 2.3, the electron occupies an anti-bonding orbital along one of the N−C bonds and predominantly resides near the carbon atom [31, 155]; the shape is not strictly based on calculations.

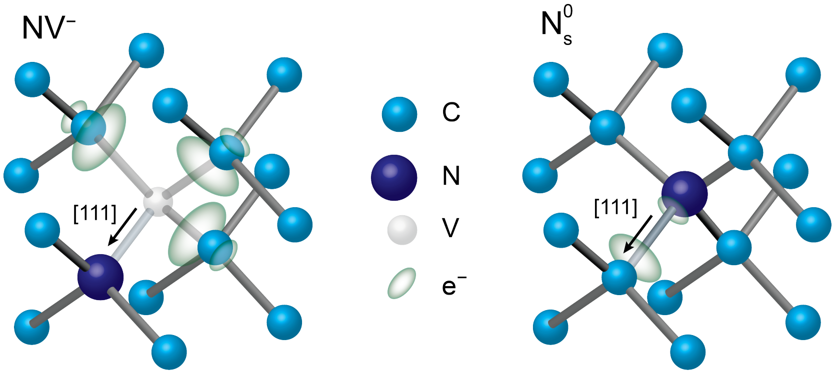

Figure 2.1: **Nitrogen defects in diamond.** Many nitrogen-based defects exist in diamond. Here we show the negatively charged nitrogen vacancy center (NV^-) (left) and neutrally charged substitutional nitrogen center ($N_s{}^0$, also called P1 center) (right). Green orbs showing electron density follow calculations [30] for the NV and are only schematic for the P1. The N$-$C bond that the electron lies along is elongated by $\approx 30\,\%$ due to a Jahn-Teller distortion [9, 57]. Figure adapted from Heremans, et al. [106].

2.2 NV center

2.2.1 NV center level structure

Aspects of the NV center necessary to understand the work in this thesis are presented in Fig. 2.2(a) [68]. The NV electron system has an optical ground to excited state transition addressable with visible light [68]; both the ground and excited states are composed of spin triplets [82, 154, 155, 185, 271]. Owing to the wide bandgap of diamond, these states are situated well within the bandgap and do not interact with the valence and conduction bands [69, 73, 154, 155]. The radiative ground to excited state transition is spin-conversing [165]. A singlet manifold exists at an intermediate energy; the optical states both couple to this middle system with a smaller, non-radiative coupling compared to the radiative optical coupling [100, 165, 168]. The relative coupling rates of these three manifolds combine to manifest two properties of the NV center that have enabled a wide range of advances in quantum technology. The ±1 spin projections in the excited state manifold couple more strongly to the intermediate singlet state than the 0 projection, which in turn couples to the optical ground state [22, 165, 190]. This so-called shelving process, from the singlet state back to the ground state, is also about an order of magnitude slower than the radiative decay from the excited state [165]. This means that under optical illumination with light energetic enough to excite the optical transition, a NV center that begins in the ±1 state will emit fewer photons back into the environment as it goes through the optical cycle than one that begins in the 0 state. This provides a method to optically measure the spin state of NV centers down to the single spin level. Furthermore, the preferential coupling back into the 0 ground state means that even a NV that begins in ±1 will, after a few optical cycles, fall back into the 0 state, providing a pathway to initialize the ground state spin state [100, 154]. This optical initialization and readout through the inter-system crossing operates up to and above room temperature [37, 96, 263], truly remarkable for a quantum system. In fact, light resonant with the optical transition is not even required; off-resonant excitation, commonly green light at or around $532\,\mathrm{nm}/2.3\,\mathrm{eV}$, efficiently drives the optical cycle [69, 96, 264]. From these properties it is clear why the NV center has been such a boon for quantum science and engineering over the past two decades since the first demonstration of single NV coherent spin control [121].

2.2.2 NV center fine structure

Fig. 2.2(b) shows the fine structure that arises in the NV spin levels in the presence of a variety of magnetic stimuli, which we can understand by studying the general NV center spin Hamiltonian [43, 68]

$$\hat{\mathcal{H}}_{NV} = \hat{\mathbf{S}} \cdot \boldsymbol{\gamma} \cdot \mathbf{B} + \hat{\mathbf{S}} \cdot \mathbf{D} \cdot \hat{\mathbf{S}} + \hat{\mathbf{S}} \cdot \mathbf{A}_N \cdot \hat{\mathbf{I}}_N + \sum_i \hat{\mathbf{S}} \cdot \mathbf{A}_{C_i} \cdot \hat{\mathbf{I}}_{C_i} + \sum_j \hat{\mathbf{S}} \cdot \mathbf{D}_{P_j} \cdot \hat{\mathbf{R}}_j \tag{2.1}$$

where $\hat{\mathbf{S}}$ is the NV spin operator, $\hat{\mathbf{I}}_N$ is the nitrogen nuclear spin operator, $\hat{\mathbf{I}}_C$ is the carbon nuclear spin operator, $\hat{\mathbf{R}}$ is the spin operator for a fourth spin species, $\boldsymbol{\gamma}$ is the gyromagnetic tensor, $\mathbf{B}$ is the external magnetic field vector, $\mathbf{D}$ is the zero-field splitting (or the crystal field splitting), $\mathbf{A}_N$ is the hyperfine tensor with the N nuclear spin, $\mathbf{A}_C$ is the hyperfine tensor with each C nuclear spin, and $\mathbf{D}_R$ is the dipolar tensor with a generic fourth spin species. Note that we ignore terms that only involve the nuclear spin energy (nuclear Zeeman, nuclear quadrupole). We can simplify Eq. (2.1) with a combination of facts about the NV and assumptions about the NV environment we will be studying. We will list them and then present a simplified Hamiltonian. The NV gyromagnetic ratio is isotropic [154, 155]; the NV ground state is spin-1 [154]; we measure ^{15}NV centers, such that the N nuclear spin is spin-$\frac{1}{2}$ and there is no quadrupolar moment [211]; we measure NV centers in ^{12}C isotopically purified diamond (see Ch. 4) such that there are no ^{13}C nuclear spins [15, 192]; in general the NV Larmor frequency is far detuned from other spin species P such that we only keep secular terms (see Ch. 6 for treatment and consequences of another case). Our resulting Hamiltonian is [43]

$$\begin{aligned}
\hat{\mathcal{H}}_{NV} = \; & (D_{gs} + \epsilon_{\parallel}\Pi_z)\left(\hat{S}_z^2 - \tfrac{2}{3}\right) + \gamma(B_x\hat{S}_x + B_y\hat{S}_y + B_z\hat{S}_z) + \epsilon_{\perp}\Pi_x\left(\hat{S}_y^2 - \hat{S}_x^2\right) + \\
& \epsilon_{\perp}\Pi_y\{\hat{S}_x, \hat{S}_y\} + \epsilon'\Pi_x\{\hat{S}_x, \hat{S}_z\} + \epsilon'\Pi_y\{\hat{S}_y, \hat{S}_z\} \qquad (2.2) \\
& + A_{N,zz}\hat{S}_z\hat{I}_N^z + \textstyle\sum_j D_{R_j,zz}\hat{S}_z\hat{R}_j^{(z)} \qquad (2.3)
\end{aligned}$$

where $D_{gs}{\approx}3\,\text{GHz}$ is the axial zero-field splitting [154], $\mathbf{\Pi}$ terms consist of axial and transverse strain and electric fields, $\epsilon^{(\prime)}_{(\parallel,\perp)}$ are the relevant susceptibilities to those fields, and $\{\cdot,\cdot\}$ is the anti-commutator. We may reformulate this in a matrix form that makes explicit how each term either shifts the energy level of a NV spin state (diagonal elements) or couples two states (off-diagonal terms), where the elements are ordered $m_s = +1, 0, -1$: [43]

$$\hat{\mathcal{H}} = \begin{pmatrix} \begin{matrix} \frac{D_{gs}}{3} + \frac{\epsilon_\parallel}{3}\Pi_z + \gamma B_z \\ + \frac{A_{N,zz}}{2} + \sum_j D_{R_j,zz} R_j^z \end{matrix} & \frac{\epsilon'}{\sqrt{2}}\Pi_- + \frac{\gamma}{\sqrt{2}}B_- & -\epsilon_\perp \Pi_+ \\ \frac{\epsilon'}{\sqrt{2}}\Pi_+ + \frac{\gamma}{\sqrt{2}}B_+ & -\frac{2D_{gs}}{3} - \frac{2\epsilon_\parallel}{3}\Pi_z & -\frac{\epsilon'}{\sqrt{2}}\Pi_- + \frac{\gamma}{\sqrt{2}}B_- \\ -\epsilon_\perp \Pi_- & -\frac{\epsilon'}{\sqrt{2}}\Pi_+ + \frac{\gamma}{\sqrt{2}}B_+ & \begin{matrix} \frac{D_{gs}}{3} + \frac{\epsilon_\parallel}{3}\Pi_z - \gamma B_z \\ - \frac{A_{N,zz}}{2} - \sum_j D_{R_j,zz} R_j^z \end{matrix} \end{pmatrix} \tag{2.4}$$

where $B_\pm = B_x \pm iB_y$ and $\Pi_\pm = \Pi_x + i\Pi_y$.

We may now make some statements about the spin-triplet manifold in the presence of fields. First, it is clear from the diagonal terms that the zero-field splitting, axial strain/electric fields, and axial magnetic fields introduce a splitting between the three spin sub-levels. In the left-most segment in Fig. 2.2(b) we show the case of $B_z = 0$ and $D_{gs} \gg \epsilon\Pi$, such that $|-1\rangle$ and $|+1\rangle$ are degenerate and there is a spin-allowed transition between $|0\rangle$ and a superposition of $|-1\rangle$ and $|+1\rangle$. In the second segment we show how an axial magnetic field lifts this degeneracy, leading to two allowed $\Delta m_s = 1$ transitions. These transitions are driven specifically by the off-diagonal $B_\pm$ terms in Eq. (2.4) when ac magnetic fields are resonant with the transition energy. The hyperfine coupling (third segment) and dipolar coupling to other spins (fourth segment, assuming a single spin-$\frac{1}{2}$ P spin) further shift the $|-1\rangle$ and $|+1\rangle$ energy levels depending on the spin states, leading a total of eight possible magnetic NV electron spin transitions. Throughout the experiments in this thesis we will see magnetic resonance spectra elucidating these various couplings. We additionally see that strain and electric fields provide couplings between states that enable driving spin transitions non-magnetically [159, 278], although these effects are beyond the scope of this thesis.

A salient feature arises out of Eq. (2.4) if we consider that any of the $\mathbf{B}$ and $\mathbf{\Pi}$ fields may in general consist of fluctuations whose noise spectrum overlaps with a spin transition frequency. We further explore this concept in Ch. 3, but we note here that these fluctuations clearly couple to multiple NV electron spin transitions, dependent on both the direction and physical origin of the fields [43].

2.3 P1 center

Nitrogen is an electron donor in group-IV semiconductors [245]. It carries one extra electron relative to group-IV atoms, and its small size means it can sit in a diamond lattice without greatly perturbing the crystal [245]. In diamond, the substitutional nitrogen $\mathrm{N_s}$ can exist in three charge states, +, 0, and −, although the − charge state has been shown to be short-lived [267], and the + charge state does not possess an electron spin [143]. A $\mathrm{N_s}^0$ spin doublet state lives within the diamond bandgap ≈2 eV below the conduction band [79, 105, 221]. At room temperature ($k_B T_{RT} = 26\,\mathrm{meV}$) this is much too far away to dope the diamond in the sense of turning it conductive, although the $\mathrm{N_s}^0$ has been studied as a local donor to the NV center, generating the $\mathrm{NV^-}$ charge state, in type 1b ([N]≈100 ppm) diamond [166].

2.3.1 Structure and Jahn-Teller effect

The structure of the P1 center[1] is shown on the right in Fig. 2.1 [245]. The N atom sits on a carbon site with a single extra electron. Unlike in the case of the NV center, where the N−V bond lowers the symmetry to C_{3v} and the electron spin has a preferred orientation along this [111] axis set by the crystal field, the P1 center structure does not a priori break the crystal symmetry. The electron can occupy one of four degenerate anti-bonding orbitals between the N and one of the four neighboring C atoms. The Jahn-Teller effect (JTE) requires the crystal to distort to break this symmetry, and at any given time the electron only occupies one of the four [56, 245]. The crystal distorts along the specific N−C bond [245], with the bond lengthening around 30% according to recent calculations [9, 202], although it was estimated

---

[1] "P1" is the name given to the $\mathrm{N_s}^0$ center as identified through ESR measurements. When it is necessary to distinguish charge states we may use the $\mathrm{N_s}$ nomenclature, but otherwise default to "P1 center."

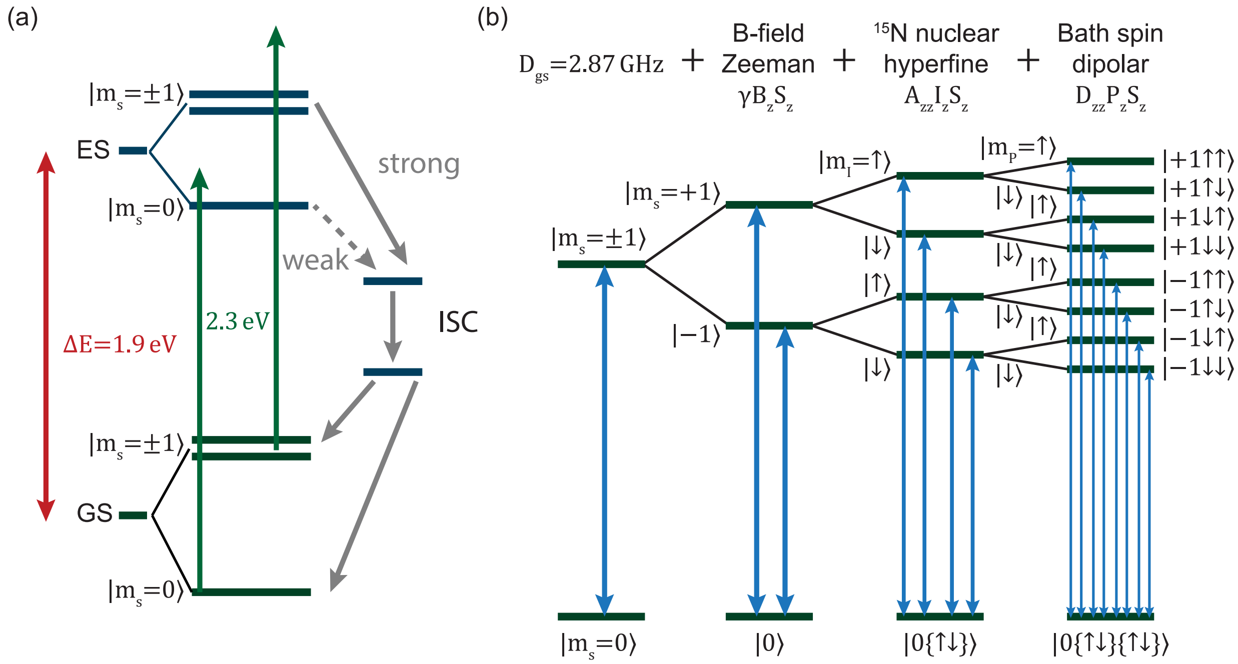

Figure 2.2: **NV center level structure.** (a) The optical structure of the NV center, with a ground state (GS) and first excited state (ES) separated by 1.9 eV, both spin-triplet states. Spin-conserving optical transitions between the magnetic sub-levels of each manifold may be off-resonantly excited, for example by 2.3 eV light. The excited state spin states couple at different rates (strong, weak) to a non-radiative transition into a singlet inter-system crossing (ISC), which in turn decays into the ground state spin states. Through optical pumping, this mechanism allows for optical readout and initialization. (b) The fine-structure of the spin-triplet ground state manifold. The largest energy scale is typically the zero-field splitting D_{gs} between the $|m_s = 0\rangle$ and $|m_s = \pm 1\rangle$ sub-levels of the electron spin. Zeeman, nuclear spin hyperfine, and other dipolar interactions may further split the NV levels, shown here for a spin-$\frac{1}{2}$ nuclear spin and a spin-$\frac{1}{2}$ bath spin with ZZ couplings. All states with $m_s = 0$ remain degenerate. $\Delta m_s = \pm 1$ electron spin transitions may by driven with microwaves resonant with the transition.

in the past to be between 5% and 36% [4, 54, 245]. This results in the same C_{3v} symmetry as the NV center.

Barring external stimuli that distort the lattice, there is nothing to prevent the P1 bond from reorienting (relaxing) onto a different neighboring carbon atom. This has been observed in ESR measurements, and at relatively warm temperatures $\gtrsim 250\,\mathrm{K}$ the reorientation has been ascribed to thermal excitation of the electron providing enough energy to overcome the energy barrier E_{JT} imposed by the JTE [4, 77, 153, 239]. The reorientation rate ν_r is then described by an Arrhenius equation

$$\nu_r = \nu_0 e^{-\beta E_{JT}} \tag{2.5}$$

where ν_0 is the vibrational frequency of the N atom. These parameters have been measured experimentally as $\nu_0 \approx 1 \times 10^{13}\,\mathrm{s}^{-1}$ and $E_{JT} \approx 0.7\,\mathrm{eV}$ [4, 77, 153, 239] and see good agreement with theory [35]. At lower temperatures the reorientation diverges from this classical behavior but may still occur via tunnelling across the JT barrier [4]. At room temperature, the reorientation rate is $17\,\mathrm{s}^{-1}$, or every 60 ms. Recent theoretical work [280] has proposed observing the JT reorientation in a single P1 center via a single NV center using single-shot readout techniques such as those recently demonstrated in Ref. 66.

2.3.2 Nuclear hyperfine coupling

If we assume some external magnetic field aligned along the [111] axis of a NV in a diamond, the P1 center can be either aligned to this field, with its wavefunction sitting along the same [111] axis, or misaligned to this field, with its wavefunction along one of the other $\langle 111 \rangle$ axes [54, 56, 245]. However, the electron spin behaves mostly like a free electron with isotropic gyromagnetic ratio [155] that will align to the magnetic field. Thus, depending on the orbital orientation, the relative orientation of the electron spin and the nitrogen

Table 2.1: Hyperfine tensor values for the P1 center.

Isotope	Hyperfine coupling (MHz)
^{14}N	$A_{\parallel} = 114.032(3)$ $A_{\perp} = 81.318(2)$
^{15}N	$A_{\parallel} = -159.730(7)$ $A_{\perp} = -113.838(6)$

nuclear spin changes, modifying the hyperfine couplings. We may write the P1 electron spin Hamiltonian as

$$\hat{\mathcal{H}} = \hat{\mathbf{P}} \cdot \boldsymbol{\gamma} \cdot \mathbf{B} + \hat{\mathbf{P}} \cdot \mathbf{A} \cdot \hat{I_N} \tag{2.6}$$

where $\hat{\mathbf{P}}$ is the spin-$\frac{1}{2}$ operator of the P1 center and $\mathbf{A}$ is again the hyperfine tensor with the nitrogen nuclear spin. As in Eq. (2.1) we ignore nuclear-only terms. We can rewrite this as

$$\hat{\mathcal{H}} = \gamma \hat{P}_z B_z + A_{\parallel} \hat{P}_z \hat{I}_N^{(z)} + A_{\perp} \left(\hat{P}_x \hat{I}_N^{(x)} + \hat{P}_y \hat{I}_N^{(y)} \right) \tag{2.7}$$

with parallel ($A_{\parallel}$) and perpendicular ($A_{\perp}$) hyperfine components. As with the NV center, the P1 nitrogen can be either ^{14}N (spin-1) or ^{15}N (spin-$\frac{1}{2}$). ^{14}N is much more commonly treated in the literature, although we work exclusively with ^{15}N. The hyperfine parameters for both species have been measured in Refs. 54, 56 and are presented in Table 2.1. These numbers appear shockingly high to someone who is used to the few MHz scale of hyperfine couplings in NV centers. From this we can calculate the ESR transitions with Eq. (2.7) assuming that the Zeeman energy is the dominant energy scale. This is necessary to assume that $|(\uparrow, \downarrow)\rangle$ are good eigenstates of $\hat{P}_z$, and requires external magnetic fields of at least 100 G; the experiments performed in this thesis operate around 300 G to 400 G. We present hyperfine shifts for both aligned and misaligned axes relative to the Zeeman energy with $\mathbf{B} = B_z \hat{\mathbf{z}}$ in Table 2.2.

As we expect the JT axis states and nuclear spin states to be thermally populated, we

Table 2.2: Hyperfine-induced splitting of P1 electron spin.

Isotope	Axis	I_z	Hyperfine $\Delta E - \gamma B_z$ (MHz)
^{14}N	aligned	-1	117.6
	mis.	-1	90.9
	aligned	0	7.8
	mis.	0	10.9
	aligned	$+1$	-109.8
	mis.	$+1$	-79.5
^{15}N	aligned	$-1/2$	-77.07
	mis.	$-1/2$	-55.91
	aligned	$+1/2$	82.66
	mis.	$+1/2$	63.89

expect the P1 ESR transitions to be distributed as 1 : 3 : 1 : 3 : 3 : 1 for ^{14}N and 1 : 3 : 3 : 1 for ^{15}N, moving from lowest to highest energy. This applies for the distribution of energies in a P1 ensemble and for the population of a single P1 center. In Fig. 2.3 we plot the calculated spectrum for the allowed $\Delta m_s = 1$ transitions from Eq. (2.7) for both isotopes, with the same assumptions as above. Note that the spectra are plotted in an arbitrary way and do not refer to any specific mode of measurement. See, e.g., Refs. 75, 245 for comparison.

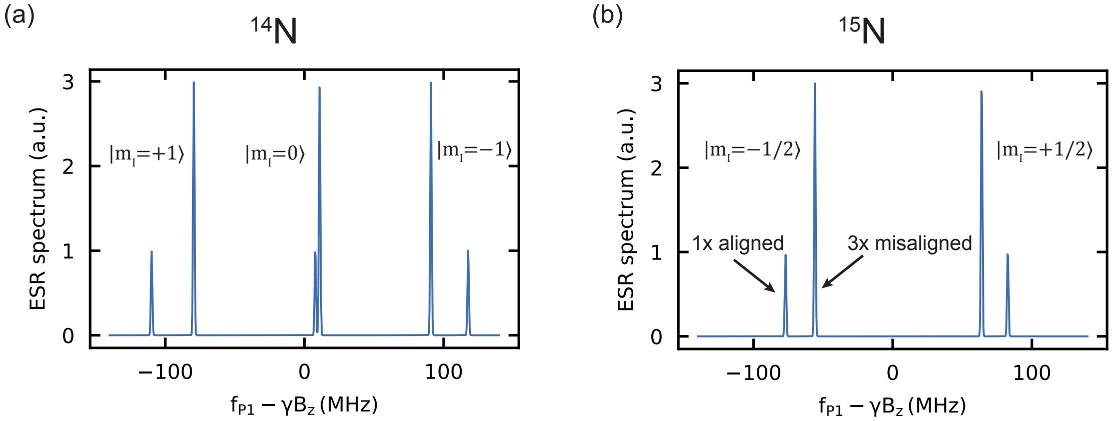

Figure 2.3: **Calculated P1 ESR spectrum.** P1 electron spin transitions calculated with hyperfine parameters in Table 2.2 for ^{14}N (a) and ^{15}N (b). Nuclear spins states are indicated. The aligned/misaligned axis labelling in (b) applies to all pairs of resonances.

CHAPTER 3

CENTRAL SPIN DECOHERENCE

3.1 Motivation

The perfect qubit does not exist [167, 189, 234]. Something external to the qubit state will always limit the qubit lifetime (T_1) and the qubit coherence time ($T_2^{(*)}$), the characteristic decay times of the diagonal and off-diagonal elements of the qubit's density matrix as defined in Eq. (1.7) [123, 167, 233, 234, 254, 303, 304]. Across quantum applications, these place limits on the efficacy of a qubit. More specifically, T_1 places an ultimate limit on how long a quantum state is available as a resource. This motivates, for example, using nuclear spins opposed to electron spins in solid state systems as quantum memories, as they generally have longer T_1 times owing to smaller gyromagnetic ratios [149]. The coherence time limits the availability of the coherent state for interactions with both other qubits and potential sensing targets. Applying gates to a qubit is only meaningful so long as the qubit coherence is maintained (see Sec. 1.1.2). On the flip side, the strength of a field to be sensed is roughly limited by the coherence time or lifetime of the qubit under the given sensing modality; otherwise the target cannot be resolved.

The actual sources of coherence decay, however, can be quite complex. Environmental noise sources can, in general, be thought of as a "bath" coupled to the two-level system qubit that can absorb (add) excitations from (to) the qubit, shown schematically in Fig. 3.1 [52, 167]. In general we have knowledge about our qubit, with one quantum degree of freedom, but we do not know the microscopics of our bath, which has many degrees of freedom. If we assume that the reservoir has no memory (an assumption that we will interrogate later), then the excitation/decay process erases our knowledge of the qubit state. In this chapter we will explore different descriptions of noise sources, ranging from semi-classical to quantum treatments, mainly following the lecture notes of Prof. Aash Clerk's Quantum Dissipation and Quantum Measurement class [51], the review article "Introduction to quantum noise, measurement, and amplification" by Clerk, et al. [52], and the chapter "Electron spin as a spectrometer of nuclear-spin noise and other fluctuations" by Rogerio de Sousa, in the book "Electron spin resonance and related phenomena in low-dimensional structures" [63]. One may find additional treatments in Refs. 123, 167, 233, 234, 254. We will focus specifically on the case of decoherence due to a spin bath surrounding a central spin, which is a good description of the systems studied in this thesis, see Chs. 5 and 6.

The system-bath description takes our initially isolated qubit, a closed quantum system with totally unitary evolution, and turns it into an open quantum system, where the bath induces non-unitary evolution of the qubit [51, 167]. But if we expanded our system to include all the degrees of freedom of the bath, this whole system would be closed. In this case we can write the entire system+bath Hamiltonian

$$\hat{\mathcal{H}}_{tot} = \hat{\mathcal{H}}_{sys} + \hat{\mathcal{H}}_{bath} + \hat{\mathcal{H}}_{int} \tag{3.1}$$

where $\hat{\mathcal{H}}_{int}$ denotes interactions. We can then write the system dynamics

$$\frac{d\left|\psi_{tot}(t)\right\rangle}{dt} = -i\hat{\mathcal{H}}_{tot}\left|\psi_{tot}(t)\right\rangle \tag{3.2}$$

and then extract our qubit density matrix from the total system as

$$\hat{\rho}_{sys} = \mathrm{Tr}_{\mathrm{bath}}\left[\left|\psi_{\mathrm{tot}}(\mathrm{t})\right\rangle\left\langle\psi_{\mathrm{tot}}(\mathrm{t})\right|\right] \tag{3.3}$$

where the trace is performed over the bath degrees of freedom. But the bath is very complex, and we do not know $\hat{\mathcal{H}}_{bath}$ or even its degrees of freedom, so this approach is generally intractable.

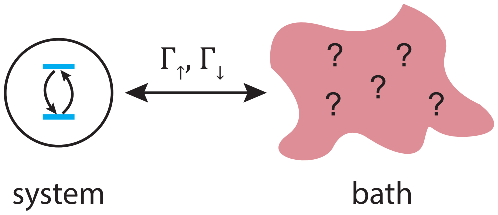

Figure 3.1: **Two level system and noisy bath**. In general, we have a two level system as our qubit with a known Hamiltonian and a known, or measurable, state. The TLS is coupled to a noisy bath of unknown character with unknown modes that we cannot measure. The bath is coupled to the system and can drive excitations at rate $\Gamma_\uparrow$ and decay at rate $\Gamma_\downarrow$.

3.2 Basic noise spectrum derivation

We now formalize the concept of a noise spectrum as a description of the bath, following Ref. 52. In a simplest case, noise acting on a quantum mechanical system is assumed to be classical; we will look at both classical and quantum noise, and the approximations necessary to treat noise in different regimes.

3.2.1 Classical noise

We first assume that there is some time-varying field $V(t)$ arising from a bath that couples to a qubit operator $\hat{\mathbf{S}}$ as

$$\hat{\mathcal{H}}_{sc} = V(t)\hat{\mathbf{S}}. \tag{3.4}$$

Note here that $V(t)$ is not an operator, it is a classical fluctuating field. There may be a static or well-characterized (e.g., a microwave signal drive) component to this field; here we are only concerned with the behavior of the "noisy" part. As an example, a spin bath composed of many electron spins where at any given instance each spin is in a random state, and thus imparts a random magnetic field to the central spin, is noisy. In this case, and without loss of generality, the mean value of the field is $\langle V(t)\rangle = 0$, and we assume that the state of the noise source, and thus the value of V, changes over some characteristic timescale τ_c. The goal now is to derive the noise spectrum, in order to understand how noise will drive a qubit. The auto-correlation function tells us how correlated or independent the field is at different times t and t', defined as

$$G_{VV}(t-t') = \overline{V(t)V(t')}, \tag{3.5}$$

where we assume that the noise process is stationary, and thus write it as a function of only the time difference $t-t'$. In the long time limit, $t-t' \gg \tau_c$, there is no correlation between the two values, and the function goes to 0. For shorter times there is in general some non-trivial functional dependence. A common assumption is that the noise is stochastic and is captured by the function $v^2 e^{-t/\tau_c}$, for some amplitude v^2.

We now calculate the spectral density of $V(t)$ as

$$S_{VV}[\omega] = \lim_{T\to\infty} \frac{1}{T} \int_0^T dt \int_0^T dt' e^{i\omega(t-t')} \overline{V(t)V(t')} \tag{3.6}$$

where T is the time range over which we watch the bath. Rewriting with $\tau = t - t'$ and assuming $T \gg \tau_c$, we can rewrite the first integral with infinite bounds and find

$$\begin{aligned} S_{VV}[\omega] = &\ \tfrac{1}{T} \textstyle\int_0^T \int_{-\infty}^{\infty} d\tau e^{i\omega\tau} \overline{V(\tau)V(0)} \\ = &\ \textstyle\int_{-\infty}^{\infty} d\tau e^{i\omega\tau} \overline{V(\tau)V(0)} && (3.7) \\ G_{VV} = &\ \textstyle\int_{-\infty}^{\infty} \frac{d\omega}{2\pi} e^{-i\omega\tau} S_{VV}[\omega] && (3.8) \end{aligned}$$

where we notice that the second part of the integrand is exactly the auto-correlation function $G_{VV}(\tau) = \overline{V(\tau)V(0)}$. Thus the noise spectrum is exactly determined to be the Fourier transform of the auto-correlation function. Likewise, if one is able to measure the noise spectrum, one can back-out $G_{VV}(\tau)$.

$V(t)$ is a real value that commutes with itself, thus $G_{VV}(t-t') = \overline{V(t)V(t')} = \overline{V(t')V(t)} = G_{VV}(t'-t)$ is symmetric in time and the noise spectrum is symmetric in frequency, i.e.,

$S_{VV}[\omega] = S_{VV}[-\omega]$.

3.2.2 Quantum noise

We start by considering an operator $\hat{v}(t)$ that couples to the qubit operator $\hat{\mathbf{S}}$ with coupling strength A as

$$\hat{\mathcal{H}}_{sc} = A\hat{v}(t) \cdot \hat{\mathbf{S}} + h.c. \tag{3.9}$$

and define the quantum noise spectrum as

$$S_{vv} = \int_{-\infty}^{\infty} d\tau e^{i\omega\tau} \left\langle \hat{v}(\tau)\hat{v}(0) \right\rangle . \tag{3.10}$$

Fermi's golden rule allows us to write the transition rates of the qubit transition at energy ω as

$$\Gamma_{\uparrow} \ = A^2 S_{vv}[-\omega] \tag{3.11}$$

$$\Gamma_{\downarrow} \ = A^2 S_{vv}[+\omega] \tag{3.12}$$

$$\tag{3.13}$$

for excitation (↑) and relaxation (↓), i.e., absorbing energy from the reservoir or losing energy to it. If the reservoir is in thermal equilibrium, detailed balance requires

$$\frac{\Gamma_{\uparrow}}{\Gamma_{\downarrow}} = e^{-\beta\omega}, \tag{3.14}$$

where $\beta \equiv 1/T$. We thus find the following relationship between positive and negative frequency values for the quantum noise spectrum

$$S_{vv}[+\omega] = e^{\beta\omega} S_{vv}[-\omega]. \tag{3.15}$$

We see that, unlike in the classical case, the spectrum for quantum noise is not symmetric in frequency. In the high-temperature limit $\beta\omega \ll 1$ and we recover a frequency-symmetric spectrum.

Consider, for example, a spin in a magnetic field B with some coupling A to a thermal bath, for example phonons. The low energy state is parallel to the field and the high energy state is antiparallel. The energy required to flip the spin is set by the magnetic field, $\omega = \gamma B$. At high temperature, $\beta\gamma B \ll 1$, the rate to flip the spin up to down is the same as down to up, and the equilibrium state is a spin that spends half its time up and half its time down. In the low-temperature regime, we saw that $\frac{\Gamma_\uparrow}{\Gamma_\downarrow} = e^{-\beta\gamma B}$ such that the flip rate to the higher-energy antiparallel state is always less than the flip rate to the lower-energy parallel state. Evidently, at low temperatures the thermal bath will tend to put the spin in the low energy state, polarizing the spin into the parallel state.

3.3 Decoherence from a spin bath

Now that we have an abstract[1] picture of how to describe a bath, as a continuous noise spectrum that drives a qubit, we can zoom in and tackle a specific, and very relevant, noisy system: a central electron spin surrounded by a spin bath. This applies, of course, to the NV center electron spin surrounded by ^{13}C nuclear spins or $\mathrm{N_s}^0$ electron spins in diamond [20]. In principle we could initialize, control, and readout each individual spin in the bath, and indeed in Ch. 6 we will do this for a single bath spin, but in general this is very difficult. However, we can of course perform these operations on the central NV spin, our qubit (see Ch. 2), and will treat all other spins as the bath.

We begin with a microscopic treatment of decoherence, analyzing how dipolar interactions between the central spin and the bath spins induce decoherence. We will then zoom out and take an approach that takes a semi-classical noise spectrum as the starting point to recover

---

[1] To an experimentalist

decoherence.

3.3.1 Microscopic picture

The microscopic details of our system are shown in Fig. 3.2(a). The system and bath are in a magnetic field $\mathbf{B} = B_z\hat{\mathbf{z}}$ and all spins interact via dipolar interactions $\propto 1/\left|r_{ij}\right|^3$, where r_{ij} is the distance between spin i and spin j. The system is described by [234, 244]

$$\begin{aligned} \hat{\mathcal{H}}_{tot} = & \quad \hat{\mathcal{H}}_e + \hat{\mathcal{H}}_{bath} + \hat{\mathcal{H}}_{e,bath} \\ \hat{\mathcal{H}}_e = & \quad \gamma_e B_z \hat{S}_z \\ \hat{\mathcal{H}}_{bath} = & \quad \textstyle\sum_j \gamma_{bath} B_z \hat{I}_z^{(j)} + \sum_{j'<j} \sum_{\alpha,\beta=x,y,z} \hat{D}_{\alpha\beta}[\mathbf{r}_j, \mathbf{r}_{j'}] \hat{I}_\alpha^{(j)} \hat{I}_\beta^{(j')} \\ \hat{\mathcal{H}}_{e,bath} = & \quad \hat{S}_z \textstyle\sum_j A(\mathbf{r}_j) \hat{I}_z^j, \end{aligned} \tag{3.16}$$

where $\gamma_{e(bath)}$ is the electron (bath spin) gyromagnetic ratio, $\hat{S}_z$ ($\hat{I}_z$) is the electron (bath) spin Pauli-Z operator, $I_{\alpha,\beta}$ are bath spin Pauli operators, $\hat{D}$ is the dipolar interaction operator, and A describes the hyperfine (dipolar) interaction with bath nuclear (electron) spins. For this derivation we will exclude intra-bath interactions, the second term in $\hat{\mathcal{H}}_{bath}$. At high magnetic fields (Larmor frequency $\gg$ interaction strengths) this is a good approximation for a nuclear spin bath; it is less good for an electron spin bath. This can be treated with numerical methods, see Ch. 5.

The electron spin qubit begins in an arbitrary superposition

$$\begin{aligned} |\psi_s\rangle = & \quad \cos\theta\,|0\rangle + e^{i\phi}\sin\theta\,|1\rangle \\ \hat{\rho}_s = & \quad \begin{pmatrix} \cos^2\theta & \cos\theta\sin\theta e^{-i\phi} \\ \cos\theta\sin\theta e^{i\phi} & \sin^2\theta \end{pmatrix}. \end{aligned} \tag{3.17}$$

Without loss of generality we will put the spin in $|\psi_s\rangle = \frac{1}{\sqrt{2}}\left(|0\rangle + e^{i\phi}\,|1\rangle\right)$ and, assuming a

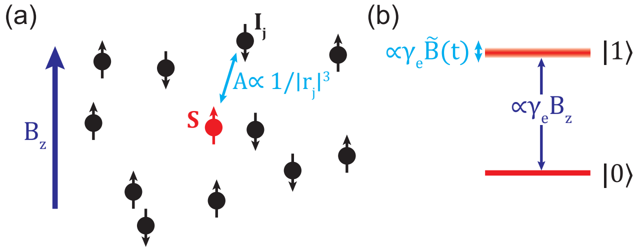

Figure 3.2: **Qubit in a noisy environment.** (a) A central spin (red) with spin operator $\hat{\mathbf{S}}$ is surrounded by an environment of bath spins with operators $\hat{\mathbf{I}}_j$, interacting with dipolar interactions $A \propto 1/|r_j|^3$. There is a global magnetic field $B_z\hat{\mathbf{z}}$ that sets the quantization axis of all spins. All bath spins are in an eigenstate (up or down) in a given instance. (b) The qubit two-level system with states $|0\rangle$ and $|1\rangle$ has a transition frequency $\gamma_e S_z(B_z + \tilde{B}(t))$, where $\tilde{B}(t)$ is a random field produced by the bath spins and leads to a time dependent shift of the energy levels.

pure-dephasing form of the qubit evolution that is spin population-conserving [167], describe the coherence with the phase ϕ. The spin bath has many energy modes $|e_n\rangle$

$$\begin{aligned} \hat{\mathcal{H}}_{bath} |e_n\rangle &= E_n |e_n\rangle \\ \hat{\rho}_{e_n} &= \tfrac{1}{Z} \textstyle\sum_n e^{-\beta E_n} |e_n\rangle \langle e_n| \\ &= \tfrac{1}{Z} e^{-\beta \hat{\mathcal{H}}_{bath}}, \end{aligned} \tag{3.18}$$

where Z is the partition function. The total system-bath state is then described by

$$\begin{aligned} \hat{\rho}_{tot} &= \hat{\rho}_s \otimes \hat{\rho}_{e_n} \\ i\hbar \frac{d\rho_{tot}}{dt} &= \left[\hat{\mathcal{H}}_{tot}, \hat{\rho}_{tot}\right]. \end{aligned} \tag{3.19}$$

We are only concerned with the state of the electron spin, specifically the coherence $\langle 1| \rho_s(t) |0\rangle$, so we can trace out the bath degrees of freedom such that

$$\hat{\rho}_s = \mathrm{Tr}_n \hat{\rho}_{tot}(t). \tag{3.20}$$

We once again arrive at the question of how to treat the bath. The interaction term $\mathcal{H}_{e,bath}$

is essentially a Zeeman shift on the central spin by the magnetic moment of each bath spin. For a given state of the bath at some time t, the bath spins exert a net magnetic field $\tilde{B}(t) = \frac{1}{\gamma_e}\sum_j A(\mathbf{r}_j)\hat{I}^j_{z,int}(t)$ such that we can write

$$\hat{\mathcal{H}}_{e,bath} = \gamma_e \tilde{B}(t) S_z. \tag{3.21}$$

Note that we are not saying anything about the statistics of this bath field or about its quantum or classical nature, only that spins produce magnetic fields.

We now move into the interaction picture with respect to the bath unitary operator $\hat{U}_{int}(t) = e^{i\hat{\mathcal{H}}_{bath}t}$ [237]. The density matrix and Hamiltonian in this picture are

$$\begin{aligned} \hat{\rho}_{tot,int}(t) = &\quad \hat{U}_{int}(t)\hat{\rho}_{tot}\hat{U}^{\dagger}_{int}(t) && (3.22) \\ \hat{\mathcal{H}}_{tot,int}(t) = &\quad \hat{\mathcal{H}}_s + \hat{\mathcal{H}}_{s,bath;int}(t) && \\ = &\quad \gamma_e S_z(B_z + \tilde{B}(t)), && (3.23) \end{aligned}$$

as shown in Fig. 3.2(b), where the qubit transition frequency is dependent on both the static field B_z and the fluctuating field $\tilde{B}(t)$. Time evolution in the interaction picture is achieved with $\hat{V}(t) = \hat{T}\exp\left[-i\int_0^t dt'\hat{\mathcal{H}}_{tot,int}(t')\right]$, where T is the time-ordering operator. Thus the density matrix evolves as

$$\begin{aligned} \hat{\rho}_{tot}(t) = &\quad \hat{V}(t)\hat{\rho}_{tot}(0)\hat{V}^{\dagger}(t) && (3.24) \\ \rho_{s,01}(t) = &\quad \textstyle\sum_n \langle 1, e_n|\,\hat{\rho}_{tot}(t)\,|0, e_n\rangle\,, && (3.25) \end{aligned}$$

and we note that $\mathcal{H}_{tot,int}$ conserves total central spin polarization. Then

$$\begin{aligned}
\rho_{s,01}(t) = & \textstyle\sum_n \langle 1, e_n | \hat{T} e^{-i\int_0^t dt' \hat{\mathcal{H}}_{tot,int}(t')} \hat{\rho}_e(0) \otimes \hat{\rho}_n(0) \tilde{T} e^{i\int_0^t dt' \mathcal{H}_{tot,int}(t')} | 0, e_n \rangle \quad (3.26) \\
= & \langle 1 | e^{i\gamma_e S_z B_z} \hat{\rho}_s(0) e^{-i\gamma_e S_z B_z} | 0 \rangle \cdot \\
& \textstyle\sum_n \langle e_n | \hat{T} e^{\frac{i}{2}\gamma_e \int_0^t dt' \tilde{B}(t')} \hat{\rho}_n(0) \hat{\tilde{T}} e^{-\frac{i}{2}\gamma_e \int_0^t dt' \tilde{B}(t')} | e_n \rangle \quad (3.27) \\
= & \rho_{s,01}(0) e^{i\gamma_e B_z t} W_\phi(t) \quad (3.28)
\end{aligned}$$

where $\hat{\tilde{T}}$ is the anti-time ordering operator, $W_\phi(t)$ is the decoherence function, defined as everything after and including the sum in Eq. (3.27), and the factor of 1/2 arises from the eigenvalues of $|0, 1\rangle$.

The first time-dependent term in Eq. (3.28) is simply phase accumulation in a static magnetic field, and does not decohere the qubit. Why, then, does the magnetic field from the bath spins decohere the qubit? For one, we do not know the initial state of the bath. We can generally say the bath is in a thermal state, but this is a macrostate; it says nothing about the microstate, the specific configuration of bath spins. As each bath spin is in general coupled to the central spin with a different $A(\mathbf{r}_j)$, each microstate in general produces a different magnetic field at the location of the central spin. Second, the bath is actually dynamic, such that even for a given initial bath state, after some time there can be spin flips and mutual flip-flops in the bath (although we treated these as perturbations to be ignored earlier). I will again emphasize that the decoherence–the "open" nature of our qubit–is in some ways a consequence of the limits of our knowledge, although the "measurement problem" in quantum mechanics [234] is beyond the scope of this thesis. It should be evident from Eq. (3.27) that the qubit coherence does not disappear, but rather the qubit interacts with and becomes entangled with the bath spins [233]. But we do not have enough knowledge about the bath here to theoretically describe or experimentally recover the coherence that leaks into the bath spins, and it is thus lost.

3.3.2 Microscopic picture with classical noise

To make this problem tractable, we will describe the spin bath magnetic field, which depends on an initial microstate and the bath spin dynamics, as a classical random variable $b(t)$ with the Hamiltonian

$$\hat{\mathcal{H}}_e = \gamma_e S_z B_z + S_z b(t). \tag{3.29}$$

This reduces the decoherence function to

$$W_\phi(t) = \overline{e^{i\phi(t)}} \tag{3.30}$$

$$\phi(t) \equiv \int_0^t dt' b(t'). \tag{3.31}$$

Now, ignoring the global phase from the static field, the coherence is

$$\rho_{e,01}(t) = \rho_{e,01}(0) e^{i\phi(t)}, \tag{3.32}$$

where we know $\phi(t)$ from $b(t)$ for a single experiment.

We find the average coherence over many measurements

$$\overline{\rho_{e,01}} = \rho_{e,01}(0)\overline{e^{i\phi(t)}}. \tag{3.33}$$

We can Taylor expand the phase as $e^{i\phi(t)} = 1 + i\phi - \frac{1}{2}\phi^2 + \cdots$. The first term is a trivial factor. Without loss of generality we can assume $\overline{\phi} = 0$. The third term and higher even moments generally survive. If the noisy magnetic field, and thus the phase, is Gaussian, that is, the randomness is described by a Gaussian distribution $p(x) = \frac{1}{\sqrt{2\pi}\sigma} e^{-x^2/2\sigma^2}$, then all information is contained in the second moment $\overline{x^2} = \sigma^2$. Higher even moments can be decomposed using Wick's theorem, such as $\overline{x^4} = 3\overline{x^2} \cdot \overline{x^2}$. We thus only keep the second moment term, and arrive at

$$\overline{e^{i\phi}} = e^{-\frac{1}{2}\overline{\phi^2}}. \tag{3.34}$$

This tells us that the decoherence arises from the mean-square of the magnetic interactions between the central spin and the bath spins,

$$\begin{aligned}
\phi(t) &= \sum_j \int_0^t dt' A_j I_z^{(j)} && (3.35)\\
\phi^2(t) &= \left(\sum_j A_j I_z^{(j)} t\right)^2 && (3.36)\\
\overline{\phi^2(t)} &= \overline{\sum_j A_j^2 I_z^{(j),2} t^2} + \overline{\sum_{i\neq j} A_i A_j I_z^{(i)} I_z^{(j)} t^2} && (3.37)\\
&= \left(\sum_j A_j^2 \overline{I_z^{(j),2}}\right) t^2, && (3.38)
\end{aligned}$$

where the cross term in Eq. (3.37) averages to 0 because the spin states I_z of each bath spin are uncorrelated from each other. We can then rewrite the coherence as

$$W_\phi(t) = e^{-\frac{1}{2}\Delta^2 t^2}, \tag{3.39}$$

where $\Delta^2 \equiv \sum_j A_j^2 \overline{I_z^{(j),2}}$ and $\overline{I_z^{(j),2}}$ is a constant dependent on the spin multiplicity of the bath spins.

This assumes the noise is Gaussian distributed. For a general probabilistic distribution function $p(\phi)$, the decoherence can be calculated as

$$\overline{e^{i\phi}} = \int_{-\infty}^{\infty} e^{i\phi} p(\phi) d\phi. \tag{3.40}$$

3.4 Coherence measurements

It is natural to ask what the above looks like in an experiment. In general we are concerned with the type of experiment shown in Fig. 3.3(a). First, the qubit is initialized into an eigenstate. Then, a $\pi/2$ operation prepares the qubit in an equal superposition state

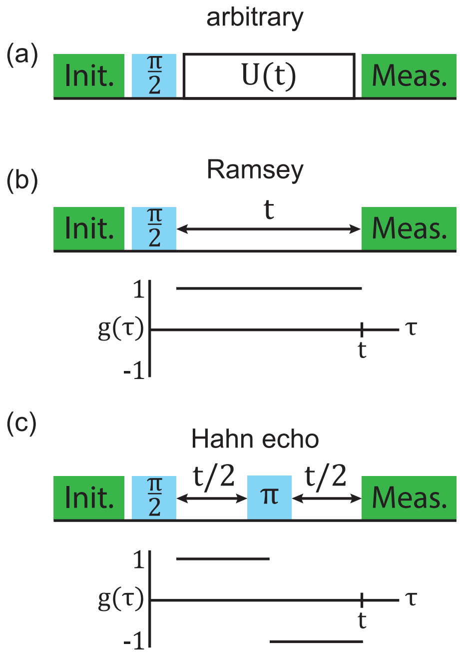

Figure 3.3: **Coherence measurements.** (a) General qubit coherence measurement. After preparation in a superposition state, the qubit evolves under free evolution or unitary operations $U(t)$. (b) In a Ramsey measurement, there is only free evolution. (c) In a Hahn echo measurement, a π-pulse applies an X or Y gate on the qubit halfway through free evolution. Weighting functions $g(t)$ are shown for the Ramsey and Hahn echo measurements below the sequences.

$\hat{\rho} = \frac{1}{\sqrt{2}} \begin{pmatrix} 1 & 1 \\ 1 & 1 \end{pmatrix}$. The qubit evolves, possibly under some set of unitary operations $\hat{U}(t)$ that modifies the qubit-bath coupling through dynamical decoupling [272, 273]. The qubit coherence is then measured, often by projecting the coherence onto a state population.

We now describe decoherence here in terms of a noise spectrum. Assuming some time evolution of the qubit during the coherence experiment described by the weighting function $g(t)$, the phase acquired in a single shot is

$$\phi(t) = \int_0^t dt' b(t') g(t'). \tag{3.41}$$

Recalling Eq. (3.8)

$$\overline{\phi^2(t)} = \int_0^t dt_1 \int_0^t dt_2 \overline{b(t_1)g(t_1)b(t_2)g(t_2)} \tag{3.42}$$

$$= \int_0^t dt_1 \int_0^t dt_2 g(t_1)g(t_2)\overline{b(t_1)b(t_2)} \tag{3.43}$$

$$G_{bb}(t_1 - t_2) = \int_{-\infty}^{\infty} \frac{d\omega}{2\pi} e^{-i\omega(t_1-t_2)} S[\omega] \tag{3.44}$$

$$\overline{\phi^2(t)} = \int_{-\infty}^{\infty} \frac{d\omega}{2\pi} S[\omega] \cdot \int_0^t dt_1 g(t_1) e^{-i\omega t_1} \int_0^t dt_2 g(t_2) e^{i\omega t_2}. \tag{3.45}$$

Analogous to the noise spectrum $S[\omega]$ for $b(t)$, we can also define the spectral weight, or filter function, arising from the $g(t)$ dynamics, as

$$g[\omega] = \int_0^t dt' g(t') e^{-i\omega t'} \tag{3.46}$$

$$\mathcal{F}[\omega, t] \equiv \int_0^t dt_1 g(t_1) e^{-i\omega t_1} \int_0^t dt_2 g(t_2) e^{i\omega t_2} \tag{3.47}$$

$$= |g[\omega]|^2$$

such that decoherence is exactly described by

$$W_\phi(t) = \exp\left[-\frac{1}{2}\int_{-\infty}^{\infty} \frac{d\omega}{2\pi} S[\omega]\mathcal{F}[\omega, t]\right], \tag{3.48}$$

where the time dependence indicates that the filter in general changes with qubit evolution time. This is a very powerful statement. If one knows the nature of environmental noise and the qubit evolution (usually controlled by the experimentalist), one can calculate a qubit's decoherence. More common in an experimental setting, one can measure the decoherence and can, using the knowledge of $\mathcal{F}[\omega]$, back out the noise spectrum, see, e.g., Refs. 41, 182, 217, 230, 285.

3.5 Common filter functions and noise spectra

We can now look at expected qubit behavior under common coherence measurements [20, 98, 212] and noise spectrum functions [63].

3.5.1 Ramsey and Hahn echo coherence measurements

In a Ramsey measurement [20, 212], Fig. 3.3(b), there is no qubit control during the evolution period and the weighting function is $g(t') = 1$, shown in Fig. 3.3(b) below the sequence. For measurement time t

$$g[\omega] = -\tfrac{i}{\omega}(1 - e^{-i\omega t}) \tag{3.49}$$

$$\begin{aligned} \mathcal{F}[\omega, t] &= \tfrac{1}{\omega^2}(2 - 2\cos\omega t) \\ &= \frac{\sin^2 \omega t/2}{(\omega/2)^2}. \end{aligned} \tag{3.50}$$

The width and peak height in Eq. (3.50) are determined by t. Importantly, this filter is finite in the dc limit

$$\lim_{\omega\to 0} \mathcal{F}_{Ramsey}[\omega, t] = t^2,$$

revealing that a Ramsey measurement is sensitive to static disorder.

In a Hahn echo measurement [20, 98], Fig. 3.3(c) the qubit is flipped halfway through the measurement, $g(t') = 1, t' < t/2$; $g(t') = -1, t' > t/2$, shown below the sequence. Then

$$g[\omega] = -\tfrac{i}{\omega}e^{-i\omega t}(e^{i\omega t/2} - 1)^2 \tag{3.51}$$

$$\begin{aligned} \mathcal{F}[\omega, t] &= \tfrac{1}{\omega^2}\left[(e^{i\omega t/2} - 1)(e^{-i\omega t/2} - 1)\right]^2 \\ &= \frac{1}{2}\frac{\sin^4 \omega t/4}{(\omega/4)^2}. \end{aligned} \tag{3.52}$$

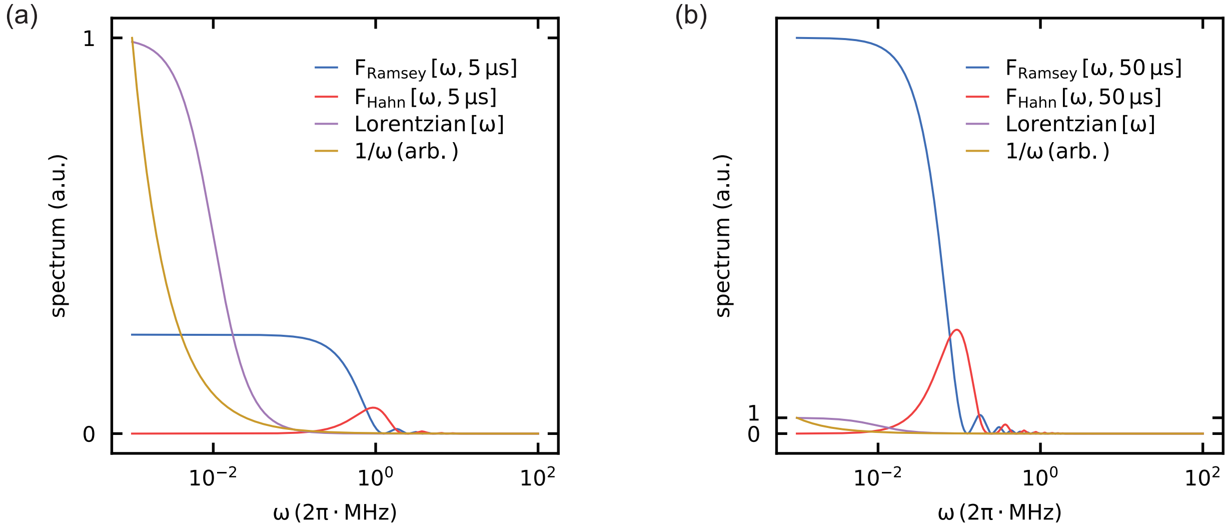

Figure 3.4: **Noise spectra and filter functions.** Two common noise spectral functions, Lorentzian (purple) and $1/f$ (yellow) are plotted alongside Ramsey (Eq. (3.50), blue) and Hahn echo (Eq. (3.52), red) filter functions for measurement times of 5 µs (a) and 50 µs (b). The y-axis is a linear scale, and the relative magnitude of spectra and filters is constant between (a) and (b).

Notably, the Hahn echo filter is zero in the dc limit

$$\lim_{\omega \to 0} \mathcal{F}_{Hahn}[\omega, t] = 0, \tag{3.53}$$

thus a Hahn echo measurement is ideally insensitive to static disorder.

In Fig. 3.4 we plot Ramsey and Hahn echo filter functions for measurement times of $t =$ 5 µs (a) and 50 µs (b). The Ramsey filter is dominated by a low-frequency component while the Hahn echo filter is peaked around $\omega = 4/t$. As the measurement window increases, both functions shift to lower frequencies and increase in peak amplitude, where there is increased overlap with the noise spectra shown (Lorentzian and $1/f$ noise are plotted, discussed below).

3.5.2 Coherence in a Lorentzian bath

A simple model of noise assumes that the bath decorrelates exponentially over a single timescale τ_c [51]

$$G_{bb}(t) = \Delta^2 e^{-|t|/\tau_c} \tag{3.54}$$

$$S[\omega] = 2\Delta^2 \tau_c \frac{1}{1+(\omega\tau_c)^2} \tag{3.55}$$

where the second line is simply the Fourier transform, a symmetric Lorentzian function centered at zero frequency with a roll-off frequency of $1/\tau_c$, and Δ^2 is the mean square coupling to the bath as defined above. This noise spectrum, plotted in Fig. 3.4, is roughly constant at low-ω and decays as $1/\omega^2$ at high-ω.

Before calculating coherence, we can already get a sense of how different measurements interact with the qubit environment from the overlap of the filter functions and the noise spectra in Fig. 3.4. It is evident that $\mathcal{F}_{Ramsey}[\omega, t]$ has a larger overlap with both Lorentzian and $1/f$ noise compared to $\mathcal{F}_{Hahn}[\omega, t]$, which according to Eq. (3.48) directly determines the coherence.

When measuring a qubit with a Ramsey measurement in the presence of a single Lorentzian noise source, the expected coherence is

$$\begin{aligned} \overline{\phi^2} &= \int_{-\infty}^{\infty} \frac{d\omega}{2\pi} \frac{1}{2} \left(2\Delta^2 \tau_c \frac{1}{1+(\omega\tau_c)^2}\right) \left(\frac{\sin^2 \omega t/2}{(\omega/2)^2}\right) && (3.56) \\ &= \Delta^2 \tau_c^2 \left[t/\tau_c + (e^{-t/\tau_c} - 1)\right] \\ W_\phi(t) &= e^{-\Delta^2 \tau_c^2 \left[t/\tau_c + (e^{-t/\tau_c} - 1)\right]}. && (3.57) \end{aligned}$$

We plot this for bath parameters $\tau_c = 100\,\mu\text{s}$ and $\Delta = 0.1\,\mu\text{s}^{-1}$, estimated from Ref. 23, in Fig. 3.5(a). This is in general a complicated function of central spin-bath coupling and bath correlation time. In the short time limit, where $t \ll \tau_c$,

$$\begin{aligned} \overline{\phi^2} \approx & \quad \Delta^2\tau_c^2\left[t/\tau_c + (1 - t/\tau_c + (t/\tau_c)^2 - 1)\right] \\ W_\phi(t) \approx & \qquad\qquad e^{-\Delta^2 t^2/2}, \end{aligned} \tag{3.58}$$

exactly the result in Eq. (3.39). In that case, we did not include any time evolution in our bath during a single qubit measurement, equivalent to taking the limit $\tau_c \to \infty$ in this picture. The decoherence here is entirely determined by Δ with no impact of τ_c. If the coherence decays within this time range, we can define a characteristic coherence decay time

$$T_2^* = \sqrt{2}/\Delta \tag{3.59}$$

such that $W_\phi = e^{-(t/T_2^*)^2}$. If this is not the case, that is, coherence persists beyond $t \gg T_2^*$, we may consider the other limit, $t \gg \tau_c$, where

$$W_\phi(t) \approx e^{-\Delta^2\tau_c t}. \tag{3.60}$$

Notably, the exponent of the time-dependence, the so-called "stretch factor," in this case is 1 opposed to 2, indicating a path to infer from a coherence measurement which limit one is in based on the stretch factor [60, 72]. In Fig. 3.5(b) we show the cross-over in stretch factor, where we can extract the stretch factor by plotting $\overline{\phi^2} = -\log(coherence)$ on a log-log plot and extracting the slope.

In the case of a Hahn echo measurement with a single Lorentzian noise source

$$\overline{\phi^2} = \int_{-\infty}^{\infty} \tfrac{d\omega}{2\pi}\left(2\Delta^2\tau_c\tfrac{1}{1+(\omega\tau_c)^2}\right)\left(\tfrac{1}{2}\tfrac{\sin^4\omega t/4}{(\omega/4)^2}\right) \tag{3.61}$$

$$= \Delta^2\tau_c^2\left(t/\tau_c - 3 + 4e^{-t/2\tau_c} - e^{-t/\tau_c}\right) \tag{3.62}$$

$$W_\phi(t) = e^{-\Delta^2\tau_c^2\left(t/\tau_c - 3 + 4e^{-t/2\tau_c} - e^{-t/\tau_c}\right)}. \tag{3.63}$$

We plot this for the same bath parameters as above in Fig. 3.5(a). We can again look in the short-time limit relative to bath dynamics

$$\begin{aligned} \overline{\phi^2} \approx&\ \Delta^2\tau_c^2\left[t/\tau_c - 3 + 4(1 - t/2\tau_c + t^2/8\tau_c^2 - t^3/48\tau_c^3) - (1 - t/\tau_c + t^2/2\tau_c^2 - t^3/6\tau_c^3)\right] \\ W_\phi(t) \approx&\ e^{-\Delta^2 t^3/12\tau_c}, \end{aligned} \tag{3.64}$$

where the stretch factor is 3 and we can again define a short-time limit coherence time

$$T_2 = (12\tau_c/\Delta^2)^{1/3}. \tag{3.65}$$

In the long-time limit relative to bath dynamics we recover the leading order term

$$W_\phi(t) \approx e^{-\Delta^2\tau_c t} \tag{3.66}$$

with a stretch factor of 1. We once again see a cross-over in the stretch factor as we change time regimes, plotted in Fig. 3.5(b).

In general, when considering decoherence from a single Lorentzian noise source, the full profile recovered from Eq. (3.48) must be used. However, in experiment, one is often concerned only with the timescale of decoherence and not the full functional form. In this case, experimental data is often fit to the functional form $e^{-(t/T_2)^n}$, where n is the stretch factor. This is often sufficient to enable qubit characterization and sensing, although recent work has observed the cross-over of the stretch factor [60, 72].

3.5.3 Coherence in the presence of multiple Lorentzian noise sources

Treating the bath as a single mesoscopic object with a Lorentzian noise spectrum and one Δ and τ_c is a stringent assumption. More generally, we may consider qubit decoherence in the presence of multiple quasi-independent noise sources. By quasi-independent we mean that

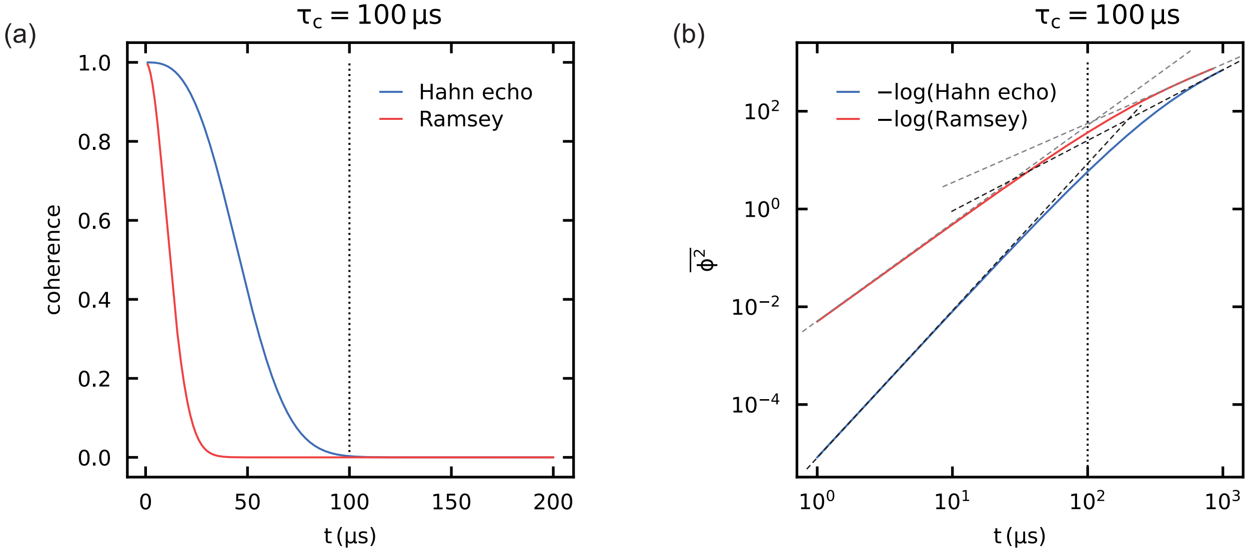

Figure 3.5: **Coherence function example.** Coherence in a Lorentzian bath with $\tau_c = 100\,\mu s$, $\Delta = 0.1\,\mu s^{-1}$ [23]. Under these parameters the lineshape, plotted in (a), is dominated by the short-time behavior. In (b) we plot directly the acquired dephasing factor on a log-log plot such that the slope is equal to the stretch factor. We show with dashed lines on each curve how the slope changes between the short- and long-time limits, with a cross-over around τ_c.

each sub-bath is governed independently by its own correlation function $G_i(\tau)$, but that in general spins in different sub-baths can interact via ZZ couplings, and thus the correlation of one sub-bath may be influenced by the presence of another sub-bath. This situation may arise, for example, from a spin bath with multiple spin species of different densities ρ_i, as with different Jahn Teller-hyperfine states of a P1 center bath, see Ch. 2. We expect $\Delta_i \propto \rho_i$ [23] as the interaction strength has a $1/r^3$ dependence (for non-dipolar interactions this scaling may not hold). If bath evolution is dominated by resonant flip-flop interactions between bath spins, then we can similarly naïvely expect $\tau_c \propto \rho^{-1}$ [23], although this picture is complicated by many-body effects in electron spin baths [302].

Each sub-bath can be considered to independently contribute to central spin decoherence, such that

$$W_\phi(t) = \prod W_\phi(t, \Delta_i, \tau_c^{(i)}) \tag{3.67}$$

In the common Ramsey case, where $t \ll \tau_c^{(i)}$, $\forall i$, we recover

$$\begin{aligned} W_\phi(t) = & \; e^{-\sum_i \Delta_i^2 t^2/2} \\ = & \; e^{-\Delta_{tot}^2 t^2/2} \end{aligned} \tag{3.68}$$

where Δ_{tot} is calculated over the entire bath. In this case we find that there is no need to treat sub-baths separately.

The Hahn echo coherence is in general

$$W_\phi(t) = e^{-\sum_i \Delta_i^2 \tau_c^{(i),2}\left(t/\tau_c^{(i)} - 3 + 4e^{-t/2\tau_c^{(i)}} - e^{-t/\tau_c^{(i)}}\right)} \tag{3.69}$$

becoming

$$\begin{aligned} W_\phi(t \ll \tau_c) \approx & \; e^{-\left(\sum_i \Delta^2/\tau_c^{(i)}\right)t^3/12} \\ = & \; e^{-(t/T_2)^3},\, T_2 = \left(\sum_i \Delta_i^2/12\tau_c^{(i)}\right)^{-1/3} \end{aligned} \tag{3.70}$$

$$\begin{aligned} W_\phi(t \gg \tau_c) \approx & \; e^{-\left(\sum_i \Delta_i^2 \tau_c^{(i)}\right)t} \\ = & \; e^{-t/T_2},\, T_2 = \left(\sum_i \Delta_i^2 \tau_c^{(i)}\right)^{-1}. \end{aligned} \tag{3.71}$$

While it is still possible to define a coherence time T_2, this time is non-trivially related to the bath dynamics.

An interesting situation arises when performing a double electron-electron resonance (DEER) measurement on a multi-component bath (or, in the case of a nuclear spin bath, electron-nuclear double resonance [ENDOR]). A DEER measurement applies a π-pulse to bath spins synchronously with the π-pulse on the central spin, thus negating the central spin weighting function relative to the bath spin states (see App. B for more details of DEER measurements). Thus the appropriate filter function is $\mathcal{F}_{ramsey}[\omega, t]$ and this can be viewed as performing a Ramsey measurement on the component of the bath that is flipped, along with a Hahn echo measurement on all noise sources that are not flipped. If a bath is composed of multiple spin species that are not resonant with each other, a single microwave tone will in general only flip one species, leading to this situation. The DEER measurement is used extensively in Ch. 6.

Consider a two-component bath with two detuned species with parameters $\Delta_1, \tau_c^{(1)}$ and $\Delta_2, \tau_c^{(2)}$. A DEER (Ramsey) measurement is performed on the first sub-bath and a standard Hahn echo on the second. The resulting coherence for $t \ll \tau_c^{(i)}$, $\forall i$ is

$$\begin{aligned} W_\phi(t) = & \left[e^{-\Delta_1^2 t^2/2}\right] \cdot \left[e^{-\Delta_2^2/\tau_c^{(2)} t^3/12}\right] \\ = & \quad e^{-\left(\Delta_1^2 t^2/2 + \Delta_2^2/\tau_c^{(2)} t^3/12\right)}. \end{aligned} \tag{3.72}$$

There is now a bi-exponential decay with multiple stretch factors. If there is sufficient separation of timescales – $T_2^{(2)} \gg T_2^{*(1)}$ – decoherence is dominated by bath 1 and this measurement can be used to independently characterize Δ_1.

3.5.4 Telegraph noise

Sec. 3.5.2 assumed the entire bath can be described by $G_{bb} = \Delta^2 e^{-|t|/\tau_c}$. In reality, the bath may be composed of many fluctuators that evolve on different time-scales [270]. Consider first a “bath” composed of a single two-level system that flips between states stochastically at some rate Γ such that the correlation function is $\propto e^{-\Gamma|t|}$. This is the same as the Lorentzian case, and it trivially produces a Lorentzian bath spectrum in Eq. (3.55)

$$S[\omega] = 2\Delta^2 \frac{\Gamma}{\Gamma^2 + \omega^2}, \tag{3.73}$$

where we retain the concept of Δ as denoting the strength of the noise spectrum.

An ensemble of two-level systems may see different flip rates due to inhomogeneity in a real device or inhomogeneity in the density, for example. We can consider a continuous distribution of rates $\Gamma_{min} \leq \Gamma \leq \Gamma_{max}$ where the probability of each rate is $P(\Gamma) \propto 1/\Gamma$. This situation may arise from a thermally activated or tunneling process [200, 270]. The resulting noise spectrum

$$\begin{aligned} S_{tot}[\omega] = & \quad 2\Delta^2 \int_{\Gamma_{min}}^{\Gamma_{max}} \frac{d\Gamma}{\Gamma} \frac{\Gamma}{\Gamma^2+\omega^2} \\ = & \quad (2\Delta^2)\frac{\tan^{-1}(\Gamma_{max}/\omega)-\tan^{-1}(\Gamma_{min}/\omega)}{\omega}. \end{aligned} \tag{3.74}$$

At large $\omega \gg \Gamma_{max}$ we get $S_{tot}[\omega] \approx (2\Delta^2)\frac{\Gamma_{max}-\Gamma_{min}}{\omega^2}$, the same functional form as a Lorentzian spectrum at large ω. In an intermediate frequency regime $\Gamma_{min} < \omega < \Gamma_{max}$ we recover $S_{tot}[\omega] \propto 1/\omega$, the ubiquitous "$1/f$" noise, plotted in Fig. 3.4 for arbitrary amplitude alongside measurement filter functions. In general we can expect some spectrum $\propto 1/\omega^{\alpha}$, $\alpha \in [0,2]$.

As this spectrum diverges at low frequency we will only consider the resulting coherence under a Hahn echo measurement, where the filter function goes to 0 at dc, and assume some low-frequency cut-off. The coherence is then

$$\begin{aligned} \int_{-\infty}^{\infty} \frac{d\omega}{2\pi} S[\omega]\mathcal{F}[\omega,t] \propto & \quad 2\cdot\frac{1}{2}\int_{0^+}^{\infty} \frac{d\omega}{\omega^{\alpha}}\frac{1}{2}\frac{\sin^4 \omega t/4}{(\omega/4)^2} \\ \propto & \quad t^{\alpha+1} \end{aligned} \tag{3.75}$$

with some constant of proportionality. Importantly, here we discover that, if α is constant over our spectral range, the stretch factor is $\alpha + 1$.

3.6 Conclusion

Fluctuating fields are a fact of the physical world, and inevitably impact quantum states in every application of quantum mechanics. It is thus imperative to understand how noise sources behave and interact with a qubit. In this chapter we started from a microscopic picture and found that we can describe noisy processes in both the time domain, with correlation functions, and in the frequency domain, with noise spectra. We then saw how classical noise directly causes decoherence of a qubit. Ramsey and Hahn echo measurements were analyzed from the perspective of frequency-domain filter functions that expose the qubit to some part of the bath noise spectrum. In the case of Lorentzian noise spectra, we saw how the stretch factor inside the exponential decay can vary at different time-scales, with implications for interpreting coherence measurements.

From one perspective, noise presents a problem by introducing decoherence into a system. This limits, for example, sensitivity to a sensing target, or the number of coherent operations that can be performed. However, noise may also be a resource, for example through reservoir engineering of entangled states [130, 140, 152, 276, 286]. We saw in this chapter that the underlying physics of the noise is imprinted on the functional form of the coherence. This enables a potentially very powerful sensing approach where the entire coherence, not just the coherence time, is utilized. This idea has been explored recently in NV-P1 ensembles for quantum simulation [60]. Recent work has explored nanoscale noise sensing as a means to detect phase transitions [47, 71, 158]. Broadly, the nature of correlations and types of excitations in a material will be imprinted on the noise spectrum, indicating that there should be information in the sensor coherence about this underlying physics.

CHAPTER 4

DIAMOND GROWTH AND NITROGEN VACANCY CENTER SYNTHESIS

Portions of this chapter are published in Ref. 97: X. Guo, N. Delegan, J. C. Karsch (Marcks), Z. Li, T. Liu, R. Shreiner, A. Butcher, D. D. Awschalom, F. J. Heremans, and A. A. High, Tunable and Transferable Diamond Membranes for Integrated Quantum Technologies, Nano Lett., **21**, 10392 (2021).

4.1 Motivation

Physics does not exist in a vacuum. In condensed matter physics it often exists in, well, matter [137]. An electron spin with no host lattice or atmosphere would have nothing to scatter off of, with no spin bath or environmental noise with which to interact (see Ch. 3). The spin lifetime and coherence time would be nearly infinite, and we would have an incredibly boring qubit. An electron in a solid lattice, by contrast, can exhibit a rich tapestry of non-trivial phenomena, from a spin-photon interface (as in the defects in this thesis) to superconductivity [69]. In fact it is often not even appropriate to talk about a single electron in a material, but rather delocalized Bloch waves or Cooper pairs [137]. The material, which we can consider vaguely as some assemblage of atoms that exhibits emergent phenomena, clearly impacts the physics we can observe.

One can predict physical properties of a material, but there is no guarantee that these will be measured. For example, the electrical conductivity of a perfect, defect-free, zero-temperature lattice is 0 [27], but good luck growing a perfect material. Likewise, one can measure a physical property of a sample, say, again, the electrical conductivity, but can only connect it to the underlying physics so far as one knows about the material being measured. How crystalline is the sample? What is the density of dopant atoms? What are the species of dopant atoms? How does the measurement probe affect the sample? These questions tie a critical knot between theory and experiment with the thread of one's knowledge of a sample. By no means does a sample need to be perfect, "simply" understood.

In the study of spin qubits in solid-state hosts it is abundantly clear that qubit properties are dependent on the properties of the host and how a sample was processed. In our case of single NV centers in diamond, the coherence–a critical property that we have explored in Ch. 3–is a function of diamond host carbon isotope [15], nitrogen dopants [23], other defects and dopants [104, 132, 157, 283], and in some cases, surface treatment [131, 230]. We will see in the studies in Chs. 5 and 6 that connection between the underlying physics and the measured quantities relies critically on how good our initial understanding of our sample is. To this end, for a variety of experiments extending beyond the confines of UChicago, we[1] synthesize diamond samples at Argonne National Laboratory via plasma enhanced chemical vapor deposition (PE-CVD), enabling exquisite isotopic and dopant control as well as control over the final NV centers that are studied [97, 192]. In this chapter we will review the processes by which the samples studied in the rest of the thesis are synthesized. In the latter portion of the chapter, Sec. 4.5, we discuss the fabrication of high-aspect ratio diamond membranes for quantum technologies, work contained in Ref. 97, with a focus on coherent NV center spin states hosted therein (the work contributed by this author).

4.2 Crystal growth

Before describing the specifics of our diamond growth, I will review the concept of step-flow growth, the situation applicable to our diamond CVD growth. I pull heavily from "The Growth of Crystals and the Equilibrium Structures of Their Surfaces" by W. K. Burton, N. Cabrebra, and F. C. Frank [39] in describing both the process and the thermodynamics. See

---

[1] When I say "we" in this regard I am mainly referring to Nazar Delegan and F. Joseph Heremans, Argonne staff scientists, who developed recipes, maintain the tools, process the samples, and actually do more-or-less everything sample-related described in this chapter.

Ref. 6 for an overview of the development of diamond CVD.

It is important to note that at a perfectly flat crystal surface with no disorder there would be no step-flow growth. Consider a crystal whose surface is in contact with a vapor composed of the crystal's constituent atoms (e.g., diamond with some carbon-containing vapor). In equilibrium, some concentration of adatoms will be adsorbed from the vapor onto the surface with some rate of exchange between the two. A uniform surface presents a uniform potential energy environment to the adsorbed atoms, and there is no thermodynamic reason why an adsorbed atom will stick (grow) onto the crystal rather than eventually return to the vapor. In this case there is no crystal growth, only crystal stasis. Luckily, real crystal surfaces are imperfect, even if only by single atomic steps, and these imperfections will enable crystal growth [39].

We can formalize this process, following Ref. 39. The crystal surface will have some density n_{s0} of adsorbants

$$n_{s0} = n_0 e^{-\beta W_s}, \tag{4.1}$$

where n_0 is roughly the areal density of possible adsorbant positions on the surface and W_s is the energy of evaporation. Each adsorbant on the surface will in general diffuse around to other energetically equivalent sites by some distance

$$x_s^2 = D_s \tau_s \tag{4.2}$$

for diffusion coefficient D_s and mean lifetime on the surface before evaporation τ_s. Diffusion is given by

$$D_s = a^2 \nu' e^{-\beta U_s} \tag{4.3}$$

for distance a between sites, frequency factor ν', and activation energy U_s. The lifetime is given by

$$\tau_s = \nu e^{-\beta W_s} \tag{4.4}$$

with frequency factor ν. The frequency factors are given by the atomic frequency of the crystal and are approximately equal. We then calculate the diffusion length as

$$x_s = ae^{\beta(W_s - U_s)/2}. \tag{4.5}$$

Consider the case of $U_s > W_s$. Then $x_s < a$ and the average adsorbant evaporates back into the vapor before moving a single site. For growth to happen, we need the adsorbant to find a lower energy state and stick to the surface, so this will not do. We require $x_s > a$ and thus $W_s > U_s$ to effect crystal growth. This is generally the case.

Further details of the thermodynamics of steps on the surface may be found in Ref. 39. It is sufficient here to assume that there is some negative energy $-U_{step}$ associated with an adsorbant attaching to the exposed face at a kink in an atomically thin step, where we assume some thermodynamic density of kinks rather than a perfect straight step face. Then, if the diffusion length x_s is larger than the average distance between kink sites x_0, we can expect adsorbants to, on average, find kink sites and grow the crystal face rather than evaporate. The step then essentially moves along the crystal face creating more crystal, hence “step-flow growth.” We show this process schematically in Fig. 4.1. In the figure we show first (A) adsorbants on the crystal surface near a growth step with thermodynamic kinks. If there is not enough thermal energy for the adsorbants to diffuse on the surface they will stick on the surface in place or evaporate. With sufficient thermal energy they will diffuse and find a kink (B), assuming $x_s > a$ as above. If there is too high a density of adsorbants on the surface they may instead stick to each other (C), forming islands on the surface and leading to rougher growth [261].

Step-flow growth is critical for the preparation of high-quality NV-containing diamond samples for a variety of reasons. Growth defects, such as islands, can induce strain, reducing NV ensemble coherence [20] and leading to variation in optical frequency, although moderate transverse strain may contribute to reduced spectral diffusion [170]. Incorporating point

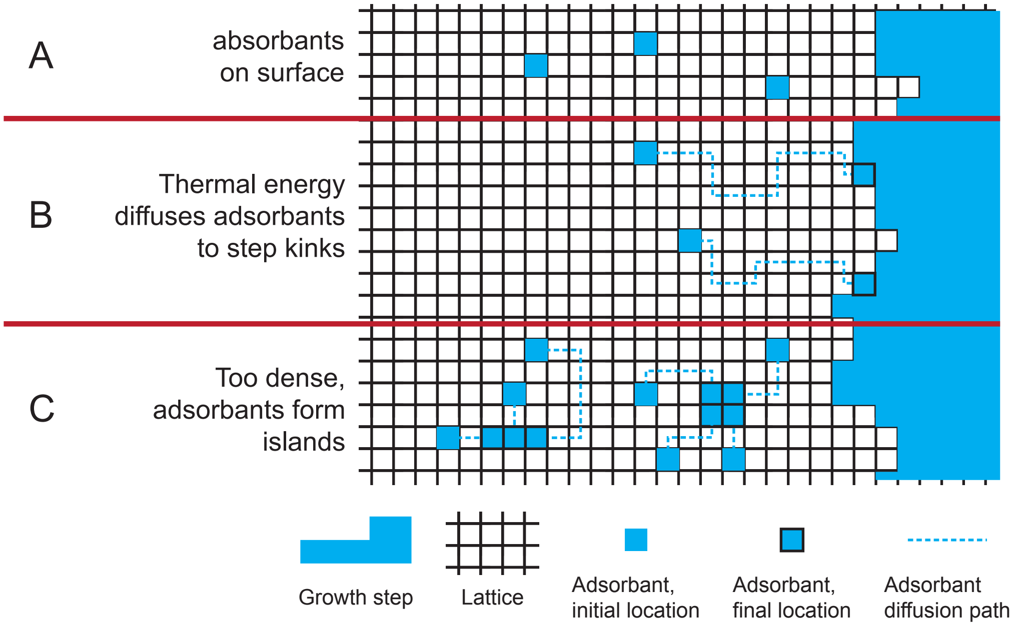

Figure 4.1: **Adsorbant behavior on surfaces.** Depending on the adsorbant density and available thermal energy, adsorbants on a crystal surface during CVD may evaporate or stick on the surface away from the step (A), diffuse and fall into a step kink, generating step-flow growth (B), or form 2D islands away from the step (C).

defects during growth can also reduce optical and spin coherence. Surface roughness, which may arise from island formation or from growth on a rough substrate, can increase decoherence for near-surface NV centers by introducing more sites for noisy surface spins and charge traps [50, 230], reducing sensitivity to external sensing targets. Uniform step-flow growth also enables depth-confined in-situ doping of diamond with a so-called delta(δ)-doping technique [192], discussed in more detail in Sec. 4.4.

4.3 PE-CVD diamond growth

We now describe our current standard process for PE-CVD diamond step-flow growth. Note that this process is subject to development.

4.3.1 Substrate preparation

We begin with “electronic-grade” or “quantum-grade” single-crystal diamond substrates from Element 6 with {100} faces and <110> edges. These are quoted to have <5 ppb naturally occurring nitrogen dopants, which is necessary for producing optically resolvable single NV centers in our growth region. For reference, this corresponds to around 500 nitrogen atoms within a 532 nm laser optical spot. It is not advisable to synthesize NV centers in material grown on “optical grade” (now called “PL” substrates) with [N]<1 ppm. While these substrates host features such as preferential alignment of in-grown NV centers [205], the native concentration is too high to resolve single NVs above.

The as-received substrates come polished to a surface roughness of $R_a < 5\,\mathrm{nm}$, much larger than a single atomic step in {100} diamond, 0.089 nm [261]. To prepare smooth surfaces for growth we first send substrates to Syntek, LLC for chemical-mechanical polishing, leading to a surface roughness $R_q \approx 0.3\,\mathrm{nm}$ (Fig. 4.2(a)). However, this polishing introduces strain into the substrate, which may propagate during growth and affect NV properties. To mitigate this issue we subject the polished substrates to an inductively coupled plasma-reactive ion etch (ICP-RIE). ICP-RIE etching is performed in an Oxford Lab100. The recipe has two distinct etch steps performed in order:

1. 10 min of Ar/Cl_2 etch: Ar 25 sccm, Cl_2 40 sccm, 10 mTorr, 400 W ICP power, 200 W bias, resulting in a 40(6) $\mathrm{nm\,min^{-1}}$ etch rate.
2. 1 min of O_2 etch: O_2 50 sccm, 10 mTorr, 700 W ICP power, 100 W bias, resulting in a 130(20) $\mathrm{nm\,min^{-1}}$ etch rate.

The etching steps are performed in sequence to provide a ≈533 nm etch depth per step. Due to an overabundance of caution, all the samples discussed in this paper were submitted to five cycles of etching for a total removal of ≈2.5 µm. Post-etching surfaces are characterized via AFM to ensure $R_q \leq 0.4\,\mathrm{nm}$, confirming that the polished roughness is maintained

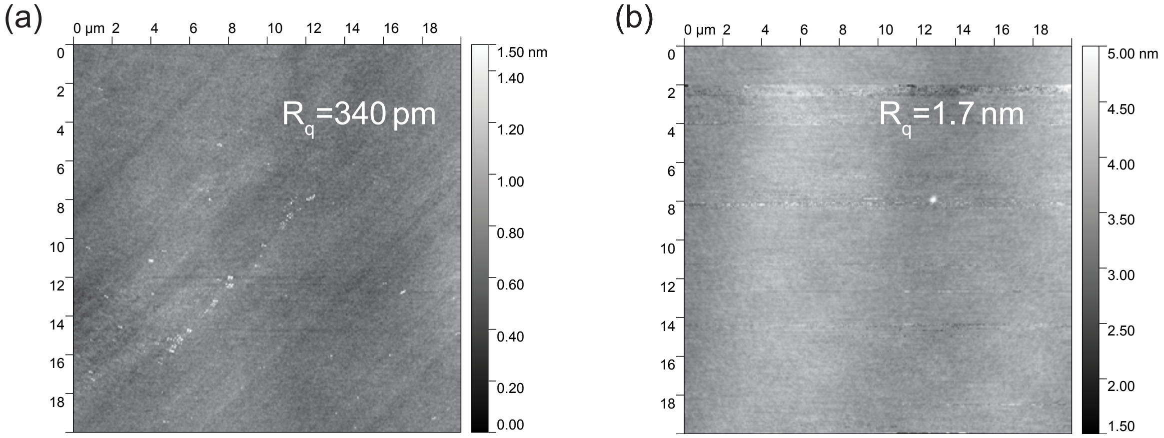

Figure 4.2: **AFM characterization of surface roughness, etch step.** We confirm that the surface roughness changes minimally from the polished value (a) to after ICP-RIE (b).

(Fig. 4.2(b), tip artifacts in this dataset lead to overestimation of the R_q value shown).

Element 6 substrate surfaces are not perfectly oriented along the $\{100\}$ axis, but rather have a quoted miscut of $\pm 3^\circ$. A miscut actually provides natural terraces for growth, and can suppress formation of growth defects such as hillocks [174, 261]. Correspondingly, the miscut angle affects the step-flow growth rate. In practice, the growth rate for each batch of substrates is re-calibrated as in Fig. 4.5.

To further prepare the substrates we subject them to a multi-step anneal under vacuum to mobilize and annihilate vacancy clusters [230]. Pre- and post-anneal, substrates undergo a tri-acid clean in $1:1:1$ NHO_3 (nitric) 68 % : H_2SO_4(sulfuric) 98 % : $HClO_4$ (perchloric) 70 % acids (trace metal grade or better) at 200 °C for 2 h or until the perchloric boils off. These samples are then DI sonicated and N_2 dried right before any subsequent steps. This removes non-diamond carbon from the surface. The anneal recipe is shown in Table 4.1. The surface roughness remains low post-anneal, pre-growth (Fig. 4.3(a,b)). At this point substrates are ready to be loaded into the custom-configured Seki Diamond SDS6350 system.

Table 4.1: Anneal recipe for pre-growth substrate preparation.

Step #	Type	°C/min (ramp) or °C (dwell)	Time (min)
1	Ramp	1.6	
2	Dwell	200	720
3	Ramp	1.6	
4	Dwell	400	480
5	Ramp	1.6	
6	Dwell	850	480
7	Ramp	1.6	
8	Dwell	1200	120
9	Ramp	-5	

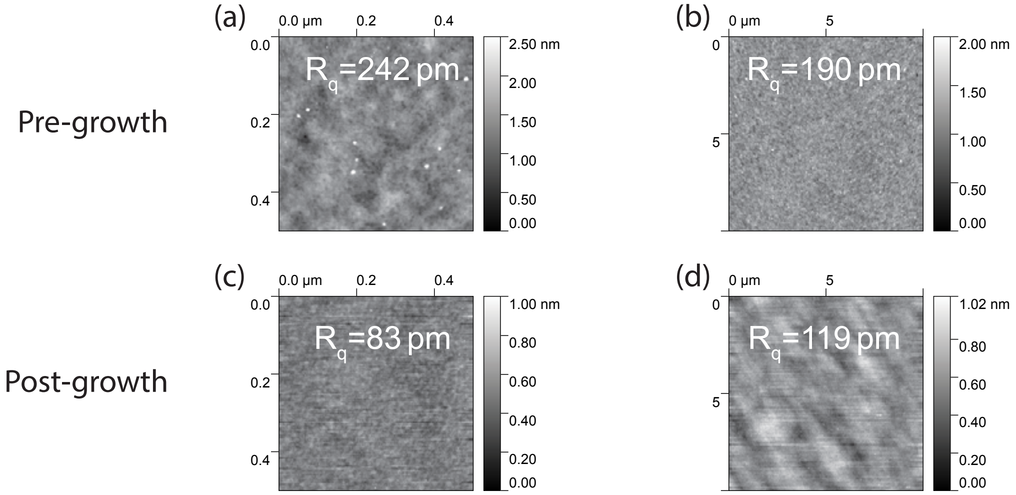

Figure 4.3: **AFM characterization of surface roughness, growth step.** We confirm that the surface roughness remains low after a post-etch (pre-growth) anneal, following the steps in Table 4.1, in (a,b), and after step-flow growth (c,d), at two different length scales. Note, the pre-growth and post-growth data are shown from different samples.

4.3.2 PE-CVD

PE-CVD is performed in a hydrogen plasma with methane CH_4 as a carbon precursor. Before reviewing the details of our growth, we first look at the chemistry of this process. We note that the lack of in-situ measurements during growth makes it difficult to fully characterize all the processes at play during CVD growth [261].

Growth chemistry

The mechanism of CVD diamond growth is less straightforward than the process laid out in Sec. 4.2 owing to the fact that the high concentration of hydrogen in the growth chamber actually terminates the carbon bonds at the diamond surface, preventing chemisorption of carbon groups [261]. The presence of active sites is governed by the competition of hydrogen adsorption to an active carbon site $\mathrm{C_d}\cdot$, where d denotes that the carbon is part of the diamond and the "." indicates the site is available, and a hydrogen radical reacting with the hydrogen termination and removing it from the surface (hydrogen abstraction). These are captured by

$$\mathrm{C_d}\cdot + \mathrm{H} \rightarrow \mathrm{C_d} - \mathrm{H} \tag{4.6}$$

$$\mathrm{C_d} - \mathrm{H} + \mathrm{H} \rightarrow \mathrm{C_d}\cdot + \mathrm{H_2} \tag{4.7}$$

The hydrogen plasma is necessary to produce precursor species from the methane gas. All four carbon bonds of methane are satisfied, and thus a methane molecule will not adsorb onto a $\mathrm{C_d}\cdot$ site. However, hydrogen radicals break apart methane molecules via

$$\mathrm{H} + \mathrm{CH_4} \rightarrow \mathrm{CH_3} + \mathrm{H_2} \tag{4.8}$$

where the $\mathrm{CH_3}$ radical may then partake in growth. Further reactions may produce other $\mathrm{CH_x}$ and $\mathrm{C_2H_y}$ compounds that also participate. As hydrogen is the dominant species, these reactions have a small impact on the hydrogen plasma density.

Now that active carbon sites and precursors are available, the carbon radicals can chemisorb on the surface via

$$\mathrm{C_d}\cdot + \mathrm{CH_3} \rightarrow \mathrm{C_d} - \mathrm{CH_3} \tag{4.9}$$

where hydrogen radicals may then abstract the hydrogen away and diamond growth may proceed [269]. The diamond faces exposed at step edges have a higher density of carbon sites such that it is favorable for an adsorbed carbon to sit at a step edge, satisfying the conditions in Sec. 4.2.

Current growth parameters

At present, growth parameters are as described below. However, these parameters are subject to change, and require re-calibration after, for example, servicing the tool. Note that parameters here, used for sample growth in Ch. 5 and 6, are different than those used in Ref. 97 (the sample studied in Sec. 4.5), as the tool was serviced in the intervening time. A schematic of the growth chamber is shown in Fig. 4.4(a). The prepared substrate sits in the chamber in a sample holder, where the edge is at the same height as the sample to aid in plasma uniformity. A mw source sparks the hydrogen plasma. A gas inlet flows in $\mathrm{H_2}$, $^{12}\mathrm{CH_4}$, and $^{15}\mathrm{N_2}$ precursor gases at variable rates controlled via mass flow controllers (MFCs). Gas flows out through the exhaust. Precursor gases are broken apart in the plasma, leaving hydrogen radicals, methyl groups ($\mathrm{CH_2}$ and $\mathrm{CH_3}$), and nitrogen to partake in CVD growth.

The growth chamber is pumped down to 8×10^{-8} Torr to minimize background contamination. Thereafter, high purity $\mathrm{H_2}$ (99.999 99 %) is introduced into the chamber, with the process microwave power of $11.5\,\mathrm{W\,mm^{-2}}$ and pressure of 25 Torr maintained throughout.

The substrate temperature was maintained in the range of 800(27) °C as tracked by an IR pyrometer. Before introduction of the diamond growth precursor, the sample is submitted to a H_2 & O_2 etch (4 % of O_2) for 5 min and a subsequent 20 min etch using H_2 only, to etch away any residual surface contaminants and defects, and expose the growth surface atomic step edges [191, 258]. Thereafter, $^{12}CH_4$ (99.9999 % chemical purity, 99.99 at % isotopic purity) is introduced as the carbon precursor. Isotopic growth enables the study of electron spins in the absence of the natural ^{13}C nuclear spin bath and greatly decreases the inhomogeneous linewidth of NV center spins [97]. The methane-to-hydrogen ratio is maintained constant at 0.1 % (H_2:$^{12}CH_4$ = 400 sccm : 0.4 sccm) as to ensure step-flow growth [97, 191], confirmed by the low surface roughness post-growth (Fig. 4.3(c,d)). Growth rates for the obtained films were determined to be 40(10) $\mathrm{nm\,h^{-1}}$ via ex-situ secondary ion mass spectroscopy (SIMS) analysis averaged over multiple calibration substrates. Example SIMS data is shown in Fig. 4.5 for two calibration substrates grown at different CH_4 flow rates, ND64 and ND66, plotting the carbon isotope concentrations in the overgrowth (shaded blue) and the underlying substrate (shaded red). In each case the ^{12}C isotopic purity is around 99.995%; the ^{13}C (nuclear spin containing) concentration is reduced from natural abundance (1.09%) by a factor of 200. The clear boundary in isotopic concentration enables us to distinguish the overgrowth from the substrate and thus determine the overgrowth thicknesses and growth rates, assuming constant growth rate throughout.

Our standard CVD overgrowth utilizes isotopically purified methane precursors. However, natural methane, as well as ^{13}C isotopically purified methane (i.e., higher than natural abundance) may also be used to achieve natural or higher carbon nuclear spin densities. This may be advantageous for studies of nuclear spin baths, such as Ref. 122 (although this work studied naturally occurring substrate NV centers).

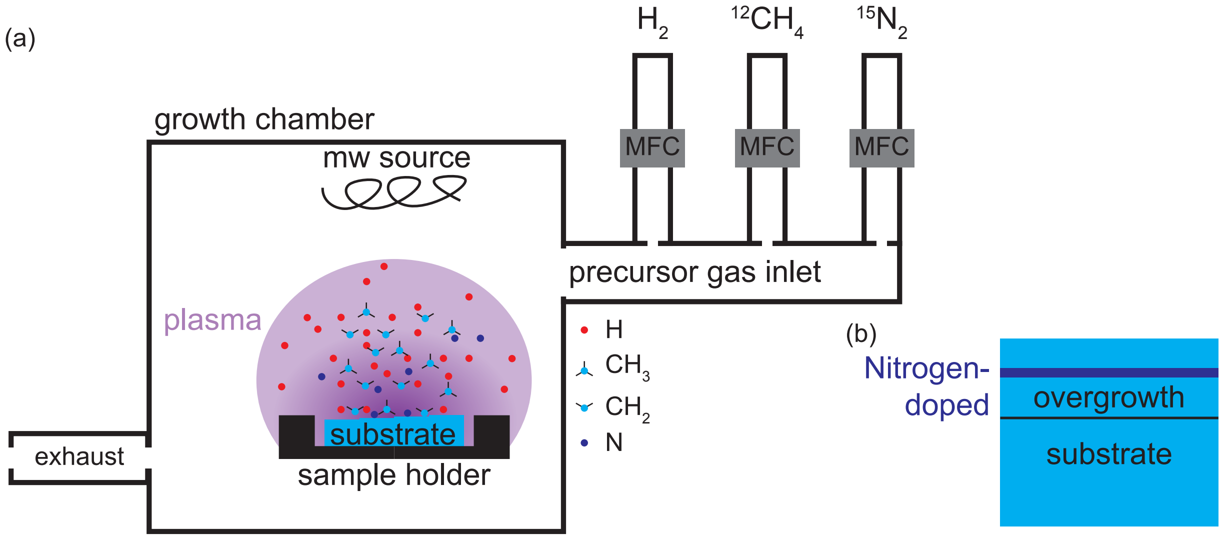

Figure 4.4: **CVD growth.** (a) CVD growth chamber with gas inlets controlled by mass flow controllers (MFCs), a sparked plasma with dissociated precursors, and a prepared substrate sitting in a sample holder. (b) Schematic of resulting δ-doped growth with clean overgrowth material and thin nitrogen-doped layer.

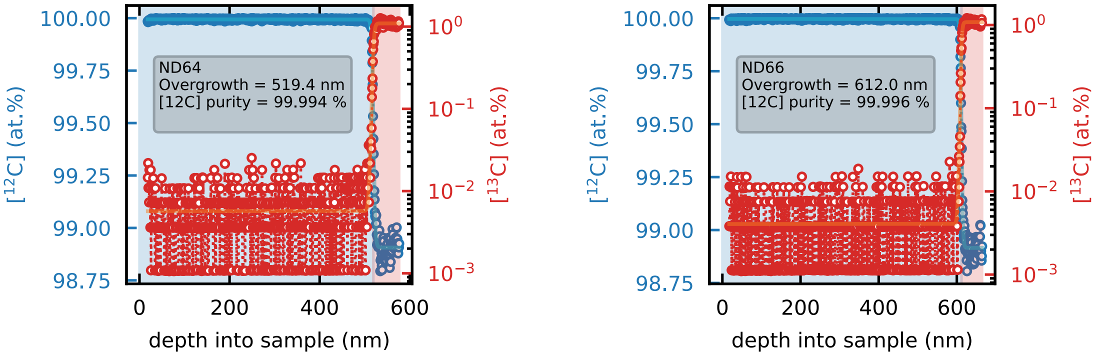

Figure 4.5: **Isotopic overgrowth.** SIMS results of carbon isotope concentrations and overgrowth thicknesses for two calibration samples with different CH_4 flow rates.

4.4 NV synthesis

Nitrogen is incredibly pervasive in our world. Our atmosphere is almost 80% nitrogen. Naturally occurring diamonds typically contain between 1 ppm and 1 ppk nitrogen dispersed throughout the crystal [9]. This nitrogen can exist in multiple different defect centers: single substitutional nitrogen (the $\mathrm{N_s}^0$, P1 center, sometimes also called C-centers), nitrogen pairs (A-centers), $\mathrm{N_4V}$ (B-centers) and so on [9]. As we have noted, even the cleanest synthetic diamond still contains $\leq$ 5 ppb nitrogen. In all cases, a NV center created at a N site in one of these crystals will not have any sort of controlled location, and in many cases the background nitrogen concentration will limit the NV center spin coherence [23].

Many studies of NV centers, especially early on, were performed on naturally occurring centers in either natural or synthetic material [58, 120, 121, 133, 155]. However, to achieve scalable quantum technologies, it is necessary to control the synthesis of NV centers in order to interface with devices and sensing targets [11, 97], as well as control spin coherence [20], ideas explored in the rest of this thesis [13]. A very widespread approach is ion implantation [25, 55, 70, 87, 112, 118, 173, 186, 193, 211, 222, 229, 246, 262]. In order to form a NV center, one needs at least one nitrogen atom, one crystal vacancy, and an electron donor (commonly considered to be another nitrogen atom) [166]. Ion implantation of nitrogen achieves all of these; as nitrogen travels to its stopping place in the diamond it leaves a large trail of crystal damage (vacancy complexes). Upon appropriate annealing conditions, interstitial nitrogen relaxes into crystal sites, and vacancies mobilize and combine with substitutional nitrogen $\mathrm{N_s}$ to form a NV center [88] as

$$\mathrm{N_s}^0 + \mathrm{V}^0 + \mathrm{e}^- \rightarrow \mathrm{NV}^-. \tag{4.10}$$

Not every $\mathrm{N_s}$ is converted to a NV, and other complexes such as multi-vacancy, multi-nitrogen, and hydrogen-containing complexes may form [9].

4.4.1 δ-doping nitrogen incorporation

Here, we summarize the δ-doping approach to NV synthesis [172, 191, 192] and discuss recent challenges that have arisen in our studies as well as paths forward to address some of them. Along the way we highlight how this approach differs from ion implantation.

The concept of nitrogen δ-doping is fairly straightforward. We know from nature that nitrogen likes to incorporate into diamond, as discussed earlier; in order to control nitrogen incorporation we just need to control the presence of nitrogen during diamond formation. This is readily achieved during PE-CVD growth, in Fig. 4.4(a), with an additional N_2 gas feed line. Other than the introduced nitrogen, background N impurities in the chamber and crystal remain low. N atoms in the plasma can chemisorb onto an available carbon site on the substrate and grow in alongside the crystal [192]. Here we see the first advantage of δ-doping over ion implantation: the nitrogen is incorporated during growth, precluding the need to damage the crystal, as during implantation. Other than the created N_s centers we expect no impact on crystal quality.

At our growth rates and nitrogen concentrations we do not expect this process to significantly affect the crystal growth. However, under higher microwave powers (faster growth) nitrogen actually increases the crystal growth rate [257]. Additionally, methyl groups in the next growth layer are less likely to sit above a nitrogen site than another carbon site, such that for fast CVD growth rates vacancies will incorporate above nitrogen sites, producing in-grown NV centers with preferential orientations [74, 85, 114, 175, 179, 198, 199, 205, 255]. We do not expect this effect in our slow growth regime on (100) diamond, either.

A major advantage of δ-doping is the ability to control the depth and spread of N incorporation independently. In ion implantation, barring post-implantation overgrowth techniques [81, 148, 250], these parameters are both determined by the implantation energy. When δ-doping, the spread is set by how long N_2 is flowed into the chamber, with a tail set by the nitrogen residency time [191]. By maintaining low growth rates on the order of

10 nm/h we are able to achieve doped layers down to a few nm, as shown in Fig. 4.6, where we present SIMS of the two stable nitrogen isotopes in a test sample with five δ-doped layers. We note a few features. First, the concentrations in the substrate (grey region) are at or close to the SIMS detection limit (dashed lines). Second, the ^{14}N concentration peaks alongside the intentionally doped ^{15}N (see below discussion on isotopic tagging). This may result from $^{15}N_2$ gas impurity (99.9% isotopic purity) or be an artifact of the SIMS measurement. The marked maximum ^{15}N concentration corresponds to 100 ppm doping, one-to-two orders of magnitude larger than what we believe we are doping. In practice, the quantified values for nominally similar doping runs always vary, and we believe that SIMS density is not a reliable metric at the densities and thicknesses at which we operate. In Ch. 5 we explore an alternative method for characterizing nitrogen incorporation density based on NV coherence measurements. We leave the tick markings in Fig. 4.6 as is but note that we do not find them quantitatively meaningful.

Doping may occur over larger thicknesses than those shown in Fig. 4.6 [75], although in practice when synthesizing single NV centers it is beneficial to grow thin layers. At the $\leq$few ppm doping levels achievable in our growth, thin δ-doped layers actually produce quasi-two dimensional distributions of nitrogen [60, 110], leading to non-trivial effects on spin bath-central spin interactions. This idea is explored in Ch. 5.

The depth of incorporation is determined arbitrarily by the amount of diamond overgrowth post-doping. In this way a sample can be tailored to its application. Many sensing schemes, especially for NMR, require NV centers 5 nm to 10 nm from the diamond surface, whereas others, such as current and magnon sensing, are less stringent and operate with NV centers 50 nm to 100 nm deep [45]. The biggest difference between these regimes, from a growth perspective, is the amount of overgrowth. A schematic of a δ-doped sample with overgrowth is shown in Fig. 4.4(b). Near-surface NV centers, however, suffer from spin and charge noise introduced by the surface, a topic of ongoing re-

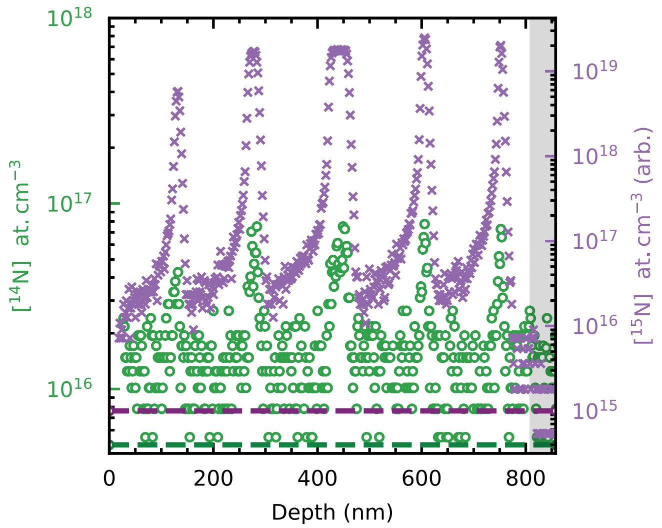

Figure 4.6: **SIMS of nitrogen incorporation.** ^{14}N and ^{15}N concentrations in a calibration sample with five δ-doping layers of varying densities and thicknesses, down to 5.7 nm (leftmost purple [x] peak). Grey region on the right is the substrate, determined through carbon SIMS (see Fig. 4.5), and dashed purple and green lines at the bottom are the SIMS detection limits for ^{15}N and ^{14}N, respectively.

search [28, 29, 50, 67, 119, 131, 136, 181, 182, 206, 218, 223, 227, 230, 284, 295]. Alongside surface reconstruction, surface dangling bonds, and surface termination, NV centers demonstrate reduced coherence times as well as charge instability. When synthesizing NV centers for non-near-surface applications, we overgrow >50 nm of diamond above the δ-doped region to prevent these effects [181, 184]. This depth was shown in Ref. 181 to mitigate the influence of surface noise on spin properties. However, the bulk T_2 coherence times were found to be $\approx 400\,\mu$s, far below times that are theoretically achievable, see Ch. 5. In future studies that seek to improve coherence times through engineering the bulk defect environment, larger overgrowth layers are advisable.

It is necessary when studying grown NV centers to confirm that one is not measuring a NV center in the substrate. In our samples this is achieved through isotopic engineering. As noted above, we generally grow ^{12}C purified diamond. NV centers in ^{13}C nuclear spins baths exhibit $T_2^* \lesssim 5\,\mu$s and usually exhibit oscillations in Hahn echo measurements at the nuclear spin Larmor frequency in mis-aligned magnetic fields [249]. Thus coherence measurements are one method for screening for grown NV centers, as T_2^* times in our samples should generally be longer [15, 20], see Ch. 5. Additionally, we almost exclusively incorporate ^{15}N (nuclear spin-$\frac{1}{2}$, 0.4% natural abundance) opposed to the more common ^{14}N (nuclear spin-1, 99.6% natural abundance) with 99.99% isotopically pure precursor gas [192]. Thus the vast majority of δ-doped nitrogen is isotopically distinct from substrate nitrogen. Specifically, the different nuclear spin multiplicity manifests in a different NV hyperfine spectrum [173, 192] that is readily identifiable. As an example, see Fig. 4.9(d). With this isotopic engineering we ensure identifiable NV centers in low nuclear spin-density environments.

4.4.2 Post-growth processing

Electron irradiation and annealing

In contrast to ion implantation, which introduces both N_s and vacancies to the diamond lattice, δ-doping only incorporates N_s. We thus induce vacancies post-growth, again, independent of nitrogen incorporation parameters. Vacancy creation for δ-doped NV centers has been demonstrated with bulk relativistic electron irradiation [97, 181, 192], transmission electron microscope (TEM) irradiation [75, 78, 110, 172], and ^{12}C ion implantation [193]. Each offers a variety of advantages and disadvantages. Vacancy creation and NV formation may also be achieved via high-intensity laser pulses, although this has not yet been demonstrated with δ-doped diamond.

Bulk irradiation is straightforward, uniform, and forgiving with regards to irradiation energy. The uniformity ensures that NV centers are created over an entire sample, which is beneficial for experiments that must first identify a “hero” NV, or for preparing many chiplets from one substrate [97]. However, this uniformity is also a downside if the aim is to localize the in-plane position of NV centers, an ongoing challenge. A further downside is that relativistic electrons penetrate mm into diamond, such that they generate vacancies throughout the entire sample, leading to formation of bulk NVs with substrate nitrogen. We say this method is forgiving because a range of electron energies in the MeV range will fully penetrate a standard diamond substrate and create about 2 vacancies/cm [42, 111, 265].

TEM irradiation offers the ability to further localize NV formation by confining the vacancy creation with a TEM beam [172] and potentially reach very high (10s of %) N to NV conversion efficiency [75, 110]. However, if the diamond sample is not thin enough for electrons to pass through (as may be possible with diamond membranes [97]) then there is no reference point for navigation other than the corners of the sample, and irradiation is essentially "flying blind," which will limit the scalability of this technique. Furthermore, above an initial 145 keV required to remove a C atom at the diamond surface, vacancies are formed approximately 1 µm deeper for every additional 1 keV of energy [172]. Thus the TEM technique may still form substrate NVs. Furthermore, at TEM energies the electrons do not pass all the way through the sample and it is unclear what happens to them.

Low energy (2 keV to 7 keV) ^{12}C implantation enables modest localization to a volume $(179\,\mathrm{nm})^3$ while mitigating crystal damage near NV centers by spatially separating vacancy creation–between the surface and the ^{12}C stopping range–and $\mathrm{N_s}$ sites [193]. It was also shown to integrate with aperture implantation techniques that have been demonstrated with nitrogen ion implantation [25, 112, 118, 193, 229, 246, 262]. However, this approach requires extra processing steps compared to in-house electron irradiation.

Our standard process utilizes 2 MeV relativistic bulk electron irradiation at the Argonne National Laboratory Low-Energy Accelerator Facility (LEAF)[2]. Electrons pass through the entire substrate (generally 100 µm to 500 µm thick) and create around 2 vacancies/cm [42, 111] (compare experimental 1.53 vacancies/cm [111] to calculated 2.15 vacancies/cm [42]). For an electron dose $\mathrm{X\,cm^{-2}}$ and diamond density $176\,\mathrm{nm^{-3}}$ we calculate a resulting vacancy density, assumed to be constant throughout the sample, of $X \cdot 1.1 \times 10^{-14}$ ppb.

Irradiation is followed by annealing under vacuum at 850 °C for 2 h. Monovacancies are

---

[2] For years I though LEAF was a person at ANL named Leif, but I was wrong.

mobile for temperatures above 600 °C [53, 142] but N_s and NV centers are stable to around 1400 °C [9, 207]. This ensures that vacancies can diffuse around the crystal and combine with N_s as in Eq. (4.10) without N_s leaving their initial positions. In this way we ensure, as in ion implantation, that NV centers are pinned to the region of nitrogen doping. We do not follow the full multi-step anneal in Ref. 230 because we do not believe that electron irradiation damages the crystal to the same degree as ion implantation. When we followed a $2 \times 10^{14}\,\mathrm{cm}^{-2}$ electron dose with this full ≈50 h process we generated light ensembles of NVs (not optically resolvable), likely from too high a conversion ratio as well as conversion of substrate N. However, this merits further exploration, and it should be possible to operate with a lower dose and longer anneal time if necessary.

Our usual goal is to generate single, optically resolvable NV centers. For excitation with laser light of wavelength λ through an optic with numerical aperture NA of a sample with a δ-doped layer of volume density ρ and thickness $t < \lambda$, the number of nitrogen atoms in a diffraction limited optical spot is

$$N_{N,spot} = \pi \left(\frac{\lambda}{2NA} \right)^2 \rho\, t. \tag{4.11}$$

Assuming 532 nm laser light, a $0.9\,NA$ objective, and a 4 nm thick δ-doped layer, we find $N_{N,spot}(\rho) = 193\,\rho\,[\mathrm{ppm}]$, where density is in units of ppm. If we assume that every vacancy diffuses and combines with a N_s[3], then we would conservatively limit ourselves to only one vacancy passing through an optical spot area during an anneal. For vacancy diffusion constant D and anneal time τ we can roughly estimate the desired vacancy density as

$$\rho_{V,max} \approx \left[\pi \left(\frac{\lambda}{2NA} \right)^2 \sqrt{D\tau} \right]^{-1}. \tag{4.12}$$

---

[3] This is not necessarily a good assumption. Vacancies may combine to form multi-vacancy complexes; vacancies may annihilate at the diamond surface; vacancies may never find a N_s.

D has been estimated to be $1.8\,\mathrm{nm}^2/\mathrm{s}$ to $6.5\,\mathrm{nm}^2/\mathrm{s}$ [3, 193] at 850 °C, leading to a conservative estimate for the maximum vacancy density with a 2 h anneal of 0.1 ppb to 0.2 ppb. This corresponds to a 2 MeV dose of $1 \times 10^{13}\,\mathrm{cm}^{-2}$ to $2 \times 10^{13}\,\mathrm{cm}^{-2}$. Of course, this estimate ignores a lot of factors. In the sample studied in Ch. 5, which underwent $2 \times 10^{14}\,\mathrm{cm}^{-2}$ irradiation and a 2 h anneal, we estimate that less than one-in-twenty vacancies produces a δ-doped NV center. This efficiency is likely limited by vacancy diffusion, and leaves an excess density of vacancies on the order of the background [N] of ≈1 ppb. Monovacancies in diamond may also be spin-ful [116, 265] and contribute to NV decoherence. It is likely that there is room for improvement with respect to irradiation dose and anneal time to maintain optically resolvable NV creation while reducing vacancy density, but that study is beyond the scope of this thesis.

Mitigating hydrogen contaminants

It is not surprising that, given the hydrogen content of the plasma during CVD growth, hydrogen also incorporates into the diamond [240]. Hydrogen, specifically H^+, is mobile in diamond [48, 228], with an estimated diffusion constant of $6 \times 10^5\,\mathrm{nm}^2/\mathrm{s}$ at 775 °C [247], although this number varies in the literature [48, 228]. Thus hydrogen can form defect complexes with vacancies and NV centers [9, 203] during annealing, precluding NV formation either by "eating-up" vacancies and converting them to $\mathrm{VH_x}$ centers [203] or by combining with NV centers to form $\mathrm{NVH_x}$ centers, which are optically dark spin defects that are stable up to around 1800 °C [135], and thus are not annealed out during NV formation. A specific worry on our end is that post-growth and irradiation the crystal contains N, V, and H. During annealing the H-containing complexes form and we do not produce NV centers [46, 247].

As we were re-tuning our NV synthesis process we initially did not optically observe NV centers. To mitigate the potential hydrogen contamination we introduced a post-growth outgassing step. The plasma is turned off and the chamber is pumped down to 1×10^{-6} torr. The sample is then heated to 500 °C to 600 °C and allowed to bake for a few hours. Critically, this step is added post-nitrogen incorporation but before vacancy creation. While VH_x complexes can form, NH_x complexes do not appear in the literature [9] beyond theoretical investigations [92], thus it should be possible to rid the crystal of hydrogen before introducing vacancies in order to mitigate the effects of hydrogen. Indeed, after introducing this step to our process we observed NV formation and proceeded with experiments.

In Fig. 4.7 we show results that suggest the out-gassing step indeed removes hydrogen from the diamond crystal. Fig. 4.7 shows the partial pressure of five gasses, including H_2, measured in a chamber as a diamond sample is heated post-growth to 850 °C. The pressure significantly increases when the sample temperature is raised to $\approx$500 °C, which we believe is related to hydrogen mobilizing in the diamond and out-gassing into the chamber. The partial pressure remains elevated for around 3 h. These temperatures are exceeded during growth, but then the hydrogen-containing plasma is on and thus any equilibrium would leave hydrogen in the diamond. These observations motivate a more complete study of hydrogen out-gassing as it relates to NV formation, but our initial observations are promising and motivate the inclusion of a post-growth step in our standard process where the sample is heated above 500 °C for at least 3 h.

Surface termination

After electron irradiation and sample annealing to form NV centers, each sample is subject to a final tri-acid clean following the same recipe as in Sec. 4.3.1. This terminates the surface with oxygen to improve charge and spin properties of near-surface NV centers [101, 230].

4.5 Diamond membranes

A major roadblock to the development of diamond-based quantum technologies is the integration of the phenomenal properties of diamond qubits with devices and sensing targets.

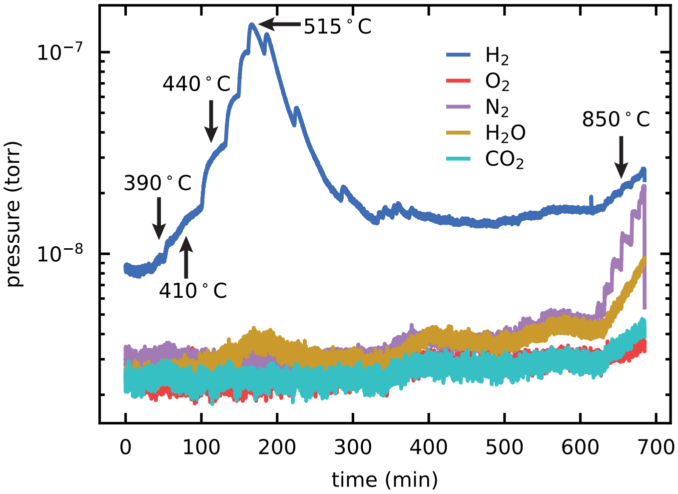

Figure 4.7: **Hydrogen out-gassing.** Pressure of chamber gasses measured while heating up a diamond sample post-growth to 850 °C. Above 500 °C the H_2 pressure increases for around 3 h, indicating the diamond out-gasses H_2. There is minimal change observed in other measured gasses. (Data courtesy of Dr. Jessica Catharine Jones, Argonne National Laboratory.)

As discussed in this chapter, highly crystalline diamond growth requires a highly crystalline starting substrate, already precluding methods of integration that would involve diamond growth on a device substrate. Nanodiamonds, a popular avenue for quantum sensing, do not reliably host coherent color centers with low-strain. Although recent work is addressing these issues with surface coatings (unpublished), it is unlikely that nanodiamonds will be used in diamond-based quantum networking applications. A potential avenue is to work with diamond thin films. However, high quality, single crystal heteroepitaxial growth of diamond thin films remains challenging despite recent progress [89, 235]. In response, a variety of processing and integration schemes have been developed to derive low dimensional structures out of bulk diamond [2, 38, 83, 108, 225, 274]. While promising, a scalable, high yield approach that enables full heterostructure-like integration of diamond while maintaining bulk-like properties – specifically, crystallinity, surface roughness, and color center coherence – is still lacking.

In this section we first summarize the efficient synthesis and manipulation of ultra-thin diamond membranes suitable for quantum applications. The process is based on a “smart-cut” technique [2, 34, 86, 162, 208] in conjunction with (PE-CVD) overgrowth. The full results of this study may be found in Ref. 97. We then report that these structures, even at thickness $\leq$150 nm, are suitable hosts for NV centers created via implantation. Specifically we show that NV centers demonstrate bulk-like spin coherence properties at room-temperature.

4.5.1 Diamond Membrane Synthesis

The step-by-step fabrication procedure of the diamond membrane quantum platform is demonstrated in Fig. 4.8(a)-(e). The process starts with a low energy (150 keV) He^{+} implantation ($5 \times 10^{16}\,\mathrm{cm}^{-2}$) into diamond substrates, as shown in Fig. 4.8(a). This step forms a depth-localized graphitized underlayer $\approx$410 nm deep [300] via damage-induced phase transition of the carbon bonds from sp^3 to sp^2. The substrates are then subjected to a multi-step anneal. The high temperature allows for the mobilization and subsequent annihilation of implantation-induced crystal damage in the top layer [183, 230]. However, this process is imperfect, resulting in the top layer remaining unsuitable as a host for highly coherent color centers.

To achieve pristine crystal quality in the membranes, we follow the “smart-cut” with homoepitaxial PE-CVD of an isotopically engineered diamond thin film overlayer as shown in Fig. 4.8(b). During growth, the hydrogen to methane flow rate ratio is kept at 0.05 % to ensure a morphology preserving step-flow growth regime [174, 192]. The growth rates herein were $6.2(4)\,\mathrm{nm\,h^{-1}}$ to $9.3(8)\,\mathrm{nm\,h^{-1}}$ for 700 °C to 500 °C heating plate temperature, respectively. We maintained low rates compared to other works [2, 34] to ensure a more accurate depth-localization of dopant layers, i.e., δ-doping precision [192]. δ-doping may be performed during growth, as in the right of Fig. 4.8(b), to synthesize color centers, or overgrown samples may be ion-implanted, as in the left of Fig. 4.8(b). In both cases a post-growth anneal generates color centers, see Sec. 4.4.

To realize a fully integrable diamond platform, we have engineered a high yield, controllable process to lithographically pattern arbitrarily shaped membranes into the overgrown films and subsequently transfer them onto other substrates/devices. The left of Fig. 4.8(f) shows inductively coupled plasma (ICP)-defined square-shaped membrane arrays (200 µm side length) used in this work, which are of sufficient size for photonics integration [26, 40, 274]. Each step of the membrane definition and transfer utilizes established cleanroom techniques. The size and shape of the membranes are fully defined and can be tailored to specific applications, with the maximum size only limited by the substrate dimensions.

Membrane manipulation starts with an EC etching of the graphitic underlayer as shown in Fig. 4.8(c). Critically, in contrast to previous studies, [34, 147] a small portion of the underlayer is left unetched, creating a tether that prevents premature membrane detachment before the dry transfer. The transfer process, depicted in Fig. 4.8(d), draws inspiration from those utilized in van der Waals heterostructure fabrication [301], using a polydimethylsiloxane (PDMS) - polycarbonate (PC) stack mounted on a micropositioner to uniformly dry-adhere and subsequently break-off the target membrane from the tether. The membrane is then flipped with another PDMS stamp and placed on a hydrogen silsesquioxane (HSQ) - coated carrier wafer. Next, the structure is annealed at 600 °C to allow the HSQ to transition into an easy to process SiO_x film [241]. The success of this process is underpinned by the adhesion differences between PC, PDMS, and HSQ layers. In this work, we bond diamond membranes to fused silica and thermal oxide wafers with pre-defined trenches, generating locally suspended regions. Suspension allows us to control the chemical termination of both surfaces and reduce HSQ-related fluorescence for photoluminescence (PL) characterizations of the embedded point defects.

Finally, by flipping the membrane, we are able to fully etch-away the He^+-damaged, graphitized diamond layer with chlorine-based ICP, as shown in Fig. 4.8(e). This ICP etching eliminates the undesired fluorescence and built-in strain caused by crystallographic imperfections and lattice mismatch [162], while tuning the final membrane thickness. The right part of Fig. 4.8(f) shows a 20 h grown diamond membrane on a fused silica wafer with 100 nm final thickness.

4.5.2 Embedded NV Centers

We now investigate the spin coherence of NV centers in the membranes using a home-built room temperature PL microscope (see App. C). While the Zeeman splitting frequencies of group IV diamond color centers are one to two orders of magnitude larger than those of the NV center [226, 243, 252], NV coherence measurements reveal magnetic noise levels which are also relevant to group IV coherent control [20, 181, 230, 283]. All NV center measurements presented herein were performed with a 15 G static magnetic field applied at 10° angle to the [111] crystal axis. We measured NV centers along all four possible crystal orientations, determined by different transition frequencies.

Fig. 4.9(a)-(b) show representative free induction decay and spin echo decay curves on a single long-lived NV spin, with the fitted T_2^* and T_2 coherence times. The oscillations in the first 100 µs of Fig. 4.9(b) arise from aliasing of electron spin echo envelope modulation. Together, these measurements demonstrate that membrane fabrication does not preclude the formation of highly coherent spin qubits. 4.9(c) presents a scatter plot of the T_2^* and T_2 times, showing a spread of 4.3(3) µs to 149(7) µs and 8(2) µs to 400(100) µs, with most times (median 50 %) falling above 10 µs and 30 µs, respectively.

Comparing the background nitrogen concentration and the observed areal NV density versus the $[N]$ implantation dose of $2 \times 10^8\,\mathrm{cm}^{-2}$, we expect that many of our observed NV centers formed from in-grown nitrogen and vacancies introduced during ion implantation and not exclusively from the implanted nitrogen. Thus, the observed NV centers are likely distributed throughout the thickness of the membrane, with some residing within

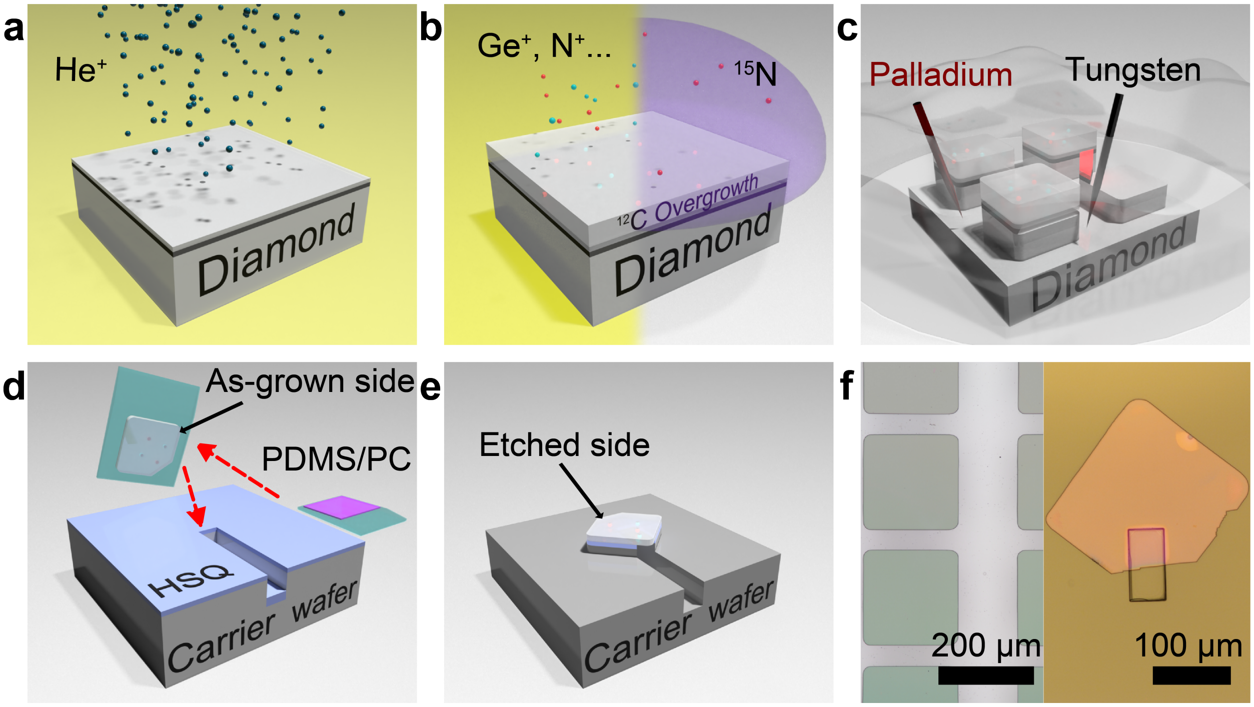

Figure 4.8: **Schematics of the diamond membrane fabrication process.** (a) He^+ implantation with subsequent annealing to form the membrane (light gray on the top) and the graphitized layer (dark grey underneath). (b) Color center incorporation via either ion implantation post isotopically (^{12}C) purified overgrowth (left) or in-situ doping (right). Red dots: N^+. Blue dots: Ge^+. Other implanted species (Si^+, Sn^+) are not shown. (c) Diamond membrane undercut via EC etching in DI water, with palladium anode (dark red) and tungsten cathode (dark grey) aiming at the target membrane. A transfer tether is colored red for better visualization. (d) Membrane dry transfer. The membrane is picked up by the PDMS/PC stamp (green/purple), flipped onto another PDMS stamp (green), and bonded to the carrier wafer by HSQ resist (blue). (e) Membrane back etch. The pedestal-like structure underneath the membrane is formed by ICP etching on the HSQ layer and the carrier wafer. (f) Microscope images of patterned overgrown membranes (left) and a transferred and back etched membrane on a fused silica wafer (right). The green squares on the left are patterned membranes with underneath graphitized layer, and the rectangle on the right indicates the trench etched prior to the transfer. (Reproduced from Ref. 97)

$\leq$15 nm of both surfaces, where previous work demonstrated marked decoherence from surface noise [181]. However, statistically, the surface proximity distribution of the NV alone cannot fully account for the large number of NV centers with $T_2 \leq$100 µs. The multi-species implantation process is known to introduce crystal damage throughout the ion path, which can create spin-full vacancy complexes that are not mobilized, nor annihilated during the annealing process [283]. It is likely that the resulting inhomogeneity of the bulk spin bath is the main factor limiting NV coherence times. Nonetheless, the spin echo coherence time (T_2 up to 400 µs) is competitive with near bulk-like properties, and the free induction decay (T_2^* up to 150 µs) outperforms commercially available bulk material due to the ^{12}C purification. Therefore, the coherence times presented herein are fully compatible with applications in quantum sensing and hybrid quantum systems [20, 44, 84].

This membrane fabrication technique is also highly amenable to in-situ δ-doping of ^{15}N during overgrowth [192]. As a proof of concept we introduced 2 nm-thick area of ^{15}N doping $\approx$36 nm from the as-grown side of a 110 nm thick diamond membrane ($\approx$250 nm overgrowth at 700 °C). Fig. 4.9(d) shows a PL map of NV centers in such a sample. The ^{15}NV$^-$ centers are labeled in teal circles, while background ^{14}NV$^-$ are in white rectangles, with representative hyperfine-resolved ODMR spectra presented to the right of the figure. We observed a $7 : 11$ ratio of [^{15}NV] : [^{14}NV] (SIMS characterized [^{15}NV] of 31(6) ppb). This is in a good alignment with what was observed for the implantation-synthesised NV centers, showing a consistent background ^{14}NV density throughout the membrane from the overgrowth process. A rigorous quantitative comparison of optimized implanted and in-grown defects as they relate to the membrane surfaces proximity is left for subsequent studies.

4.6 Summary

In this chapter we have explored the materials science that enables the physics explored in NV experiments, namely, how we achieve clean diamond growth and NV synthesis. We

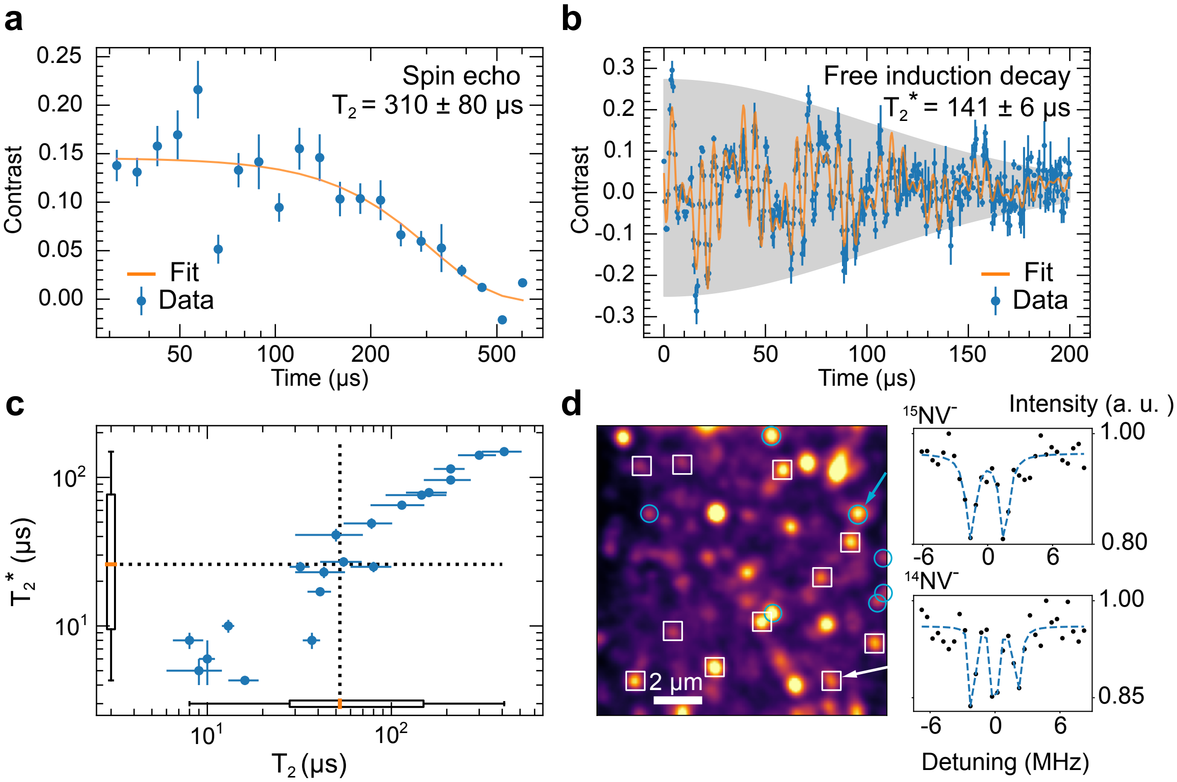

Figure 4.9: **Spin characterization of embedded NV centers at room temperature.** (a-b) Representative spin echo and free induction decay curves on a single long-lived NV spin, accompanied by the T_2^* and T_2 coherence times. The oscillations in the first 100 µs of (b) arise from aliasing of electron spin echo envelope modulation. (c) A scatter plot of T_2^* and T_2 times for the 20 measured NV centers. Inset box plots denote median values of 26 µs and 52.5 µs (dashed lines) and lower-quartile values of 9.5 µs and 28 µs. Error bars are fit errors. (d) NV PL map of a δ-doped membrane with ^{15}NV$^-$ centers (teal circles) and ^{14}NV$^-$ centers (white squares) labeled. At right, pulsed-ODMR spectra of the indicated NV centers. (Reproduced from Ref. 97)

started with the basics of CVD crystal growth and looked at the complexities of growing diamond before reviewing everything that goes into our standard growth process, including δ-doped nitrogen incorporation, bulk electron irradiation, and the mitigation of hydrogen contaminants. While this process is always in development, we have presented here the current process as well as made recommendations for future improvements where appropriate. We closed with a demonstration of the power of advanced diamond fabrication to produce high-aspect ratio diamond membranes for integration in quantum sensing and communication applications. In particular, we demonstrated that even these thin membranes host coherent color centers suitable for quantum technologies.

CHAPTER 5

COMPUTATIONALLY INFORMED SYNTHESIS OF NV CENTERS IN LOW-DIMENSIONAL SPIN BATHS

The contents of this chapter are presented in J. C. Marcks*, M. Onizhuk*, N. Delegan, Y.-X. Wang, M. Fukami, M. Watts, A. A. Clerk, F. J. Heremans, G. Galli, D. D. Awschalom, Predictive methods for low-dimensional electron spin bath synthesis in diamond, *manuscript in preparation.*

5.1 Summary

The nitrogen vacancy (NV) center in diamond, a well-studied, optically active spin defect, is the prototypical system in many state-of-the-art quantum sensing and communication applications. In addition to the enticing properties intrinsic to the NV center, its diamond host's nuclear and electronic spin baths can be leveraged as a resource for quantum information, rather than allowed to act solely as a decoherence source. However, current synthesis approaches result in stochastic defect spin positions, reducing the technology's potential for deterministic control and yield of NV-spin bath systems, as well as scalability and integration with other technologies. Here, we demonstrate the use of theoretical calculations of central spin decoherence as an integral part of an NV-spin bath synthesis workflow, providing a path forward for the quantitative design of NV center-based quantum sensing systems. We use computationally generated coherence data to characterize the properties of single NV qubits across relevant growth parameters to find general trends in coherence time distributions dependent on spin bath dimensionality and density. We then build a maximum likelihood estimator with our theoretical model, enabling the characterization of a test sample through NV T_2^* measurements. Finally, we explore the impact of dimensionality on the yield of strongly coupled electron spin systems. The methods presented herein are general

and applicable to other qubit platform that can be appropriately simulated.

5.2 Introduction

Defect color centers in diamond [32, 69] have been demonstrated as quantum magnetometers [14, 45, 145, 160, 164, 169, 220, 251, 298] and nodes in quantum communication networks [107, 127, 187, 188, 209]. Quantum applications of the nitrogen vacancy (NV) center, with a spin-photon interface and coherent operation up to and above room temperature [69, 106, 151, 263], will benefit from interfacing the central NV spin qubit with accessible dark spins in the diamond lattice for quantum memories [33, 66, 204] and many-body metrological states [282, 299]. These applications promise to enable national-scale quantum networks and quantum sensing beyond the standard quantum limit. Explorations of such multi-spin systems have relied on NV centers that are either naturally occurring [33, 66, 99, 107, 139, 209], precluding scalability, or that are formed via nitrogen implantation [55, 70, 87, 146, 173, 186, 211, 222], introducing crystal damage-induced qubit decoherence sources [283].

Diamond-based quantum applications benefit greatly from the ongoing optimization of bottom-up color center synthesis via plasma-enhanced chemical vapor deposition (PECVD) [16, 75, 191, 194]. δ-doping studies [172, 192] have demonstrated vacancy diffusion-limited spatially localized NV centers, while avoiding the crystal damage and processing inherent to aperture mask or focused implantation [25, 112, 118, 193, 229, 246, 262]. PECVD of diamond quantum systems has enabled engineering of NV center spin environments via isotopic purification [15, 180, 192], dimensionality control [60, 110, 192], and co-doping techniques [104, 132, 157]. However, the development of these techniques has outpaced computational efforts to model spin bath-induced decoherence [23, 201], and theoretical approaches have not yet been applied to investigate diamond qubit synthesis. Cluster Correlation Expansion (CCE) methods provide an accurate tool to model decoherence in varied and tailored electron and nuclear spin bath environments [195]. Such approaches have recently been applied to study material systems relevant for quantum applications [24, 128, 196, 201], indicating that CCE may indeed be a powerful tool to enable more efficient synthesis procedures, which are crucial for the design of quantum materials [62].

In this work, we apply CCE methods, as implemented in the open source framework PyCCE [196], to predict and characterize bottom up solid state spin qubit synthesis. We first introduce the computation and materials growth techniques. We then explore a common defect created during NV center synthesis: the neutrally charged substitutional nitrogen ${\mathrm{N}_\mathrm{s}}^0$ with electron spin $S = 1/2$ (P1 center). We investigate the P1 center spin bath-induced decoherence [23, 238] of NV centers in diamond across the parameter space of our growth regime (P1 density and layer thickness), developing a maximum likelihood estimation (MLE) model based on Ramsey T_2^* coherence times. We apply this model to characterize nitrogen incorporation in a test sample through coherence measurements. We then study low-dimensional electron spin baths as hosts to strongly coupled electron spin systems, demonstrating how our computational techniques can help improve the yield of future quantum devices and aid in experimental design.

In Fig. 5.1 we show the strategy adopted in this work to improve upon the current NV synthesis process. The blue boxes show the commonly adopted process for generating single NV centers. After identifying a desired sample density and geometry, iterations of growth and secondary ion mass spectroscopy (SIMS) are necessary to confirm the nitrogen doping density. In practice, we have observed large variations in SIMS results that reduce the efficacy of this approach, as discussed in Sec. 5.3.2. Here we show that it is beneficial to incorporate theoretical spin bath predictions as well as an *in-situ* density characterization tool into our workflow (green boxes). The understanding of low-dimensional spin bath decoherence obtained through theory and computation improves initial experiment design, and the local density feedback enabled by the MLE model circumvents the need for SIMS characterizations

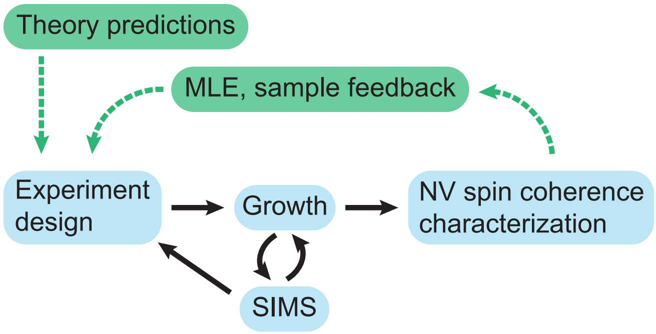

Figure 5.1: **Growth process workflow.** The current process steps (blue) for synthesizing a diamond NV sample. Iterations of growth and SIMS analysis are required to confirm nitrogen doping densities. The theoretical predictions and density maximum likelihood estimation model in this work (green) enable a non-destructive feedback process to circumvent SIMS and allow for an efficient experimental design.

of doping density.

5.3 Results

5.3.1 Validation of theoretical calculations

Within the CCE approach [287, 288] the coherence function $\mathcal{L}(t) = \frac{\langle 0|\hat{\rho}(t)|1\rangle}{\langle 0|\hat{\rho}(0)|1\rangle}$, defined as the normalized off-diagonal element of the density matrix of the qubit $\hat{\rho}(0)$, is approximated as a product of irreducible contributions of bath spin clusters, where the maximum size of the cluster n corresponds to the order n of the CCE approximation (Fig. 5.2(a)). We find that the Ramsey signal of the electron spin in the electron spin bath is converged at first order, enabling the analytical extraction of T_2^* from the interactions between the NV and the weakly coupled P1 centers. The Hahn echo signal is instead simulated at the CCE4 level of theory (see Sec. 5.4.1).

We validate our theoretical calculations against a reference dataset of NV ensemble coherence times in bulk ^{14}N P1 spin baths. We extract T_2 from the coherence curve by fitting the signal to a stretched exponential function, $\exp\left[-\left(\frac{t}{T_2}\right)^n\right]$, as shown in Fig. 5.2(b). Results for T_2^* and T_2 are overlaid in Fig. 5.2(c) with experimental data, taken from Ref. 23. We

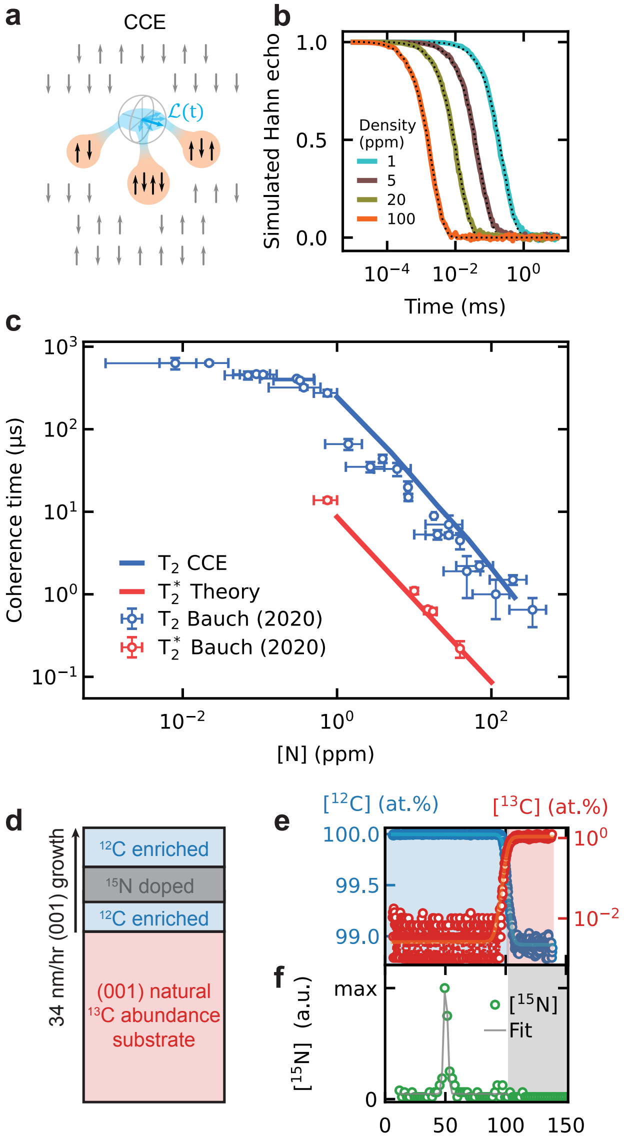

Figure 5.2: **Computational and diamond growth methods.** (a) Schematic representation of the cluster correlation expansion (CCE) approach. (b) Example of the Hahn-echo coherence calculated using the PyCCE code [196] for various ^{14}N P1 spin baths. The values of T_2 times are extracted from a stretched exponential fit of the form $\exp[-(\frac{t}{T_2})^n]$ (dashed line). (c) T_2 and T_2^* coherence times overlaid with corresponding experimental data [23], validating our computational methods. (d) Schematic of isotopically pure (^{12}C) PE-CVD (100) diamond overgrowth with isotopically tagged ^{15}N nitrogen δ-doping. This sample geometry with varying nitrogen incorporation density and thickness is considered throughout this paper. (e,f) Carbon (top) and nitrogen (bottom) isotope concentrations measured via SIMS on characterization sample, demonstrating isotopic purification of host material and isotopically tagged nitrogen incorporation. Carbon SIMS is used to calibrate growth rate, shown in (d). The nitrogen concentration is quantified with NV coherence measurements in Sec. 5.3.5.

find excellent agreement with the experimental data, showing that the CCE method yields a quantitative description of the decoherence due to P1 spin baths. The stretched exponent parameter of the computed Hahn-echo decay is between $n = 1.2$-1.3, in excellent agreement with the data of Ref. 23.

5.3.2 Diamond growth and defect synthesis

The sample studied in this paper, shown schematically in Fig. 5.2(d) was grown with a 3 min 10 sccm $^{15}N_2$ flow at a time corresponding to a depth of ≈50 nm. Nitrogen δ-doping is achieved by introducing $^{15}N_2$ gas (99.99 % chemical purity, 99.9 at% isotopic purity) during diamond growth. According to the SIMS characterization of a calibration sample, shown in Fig. 5.2(e-f), this creates a 3.8(2) nm thick (compared to $1.3^{+2.2}_{-0}$nm predicted from growth calibrations) ^{15}N-doped layer at a depth of 50.2(1) nm, with a SIMS-quantified [^{15}N] density of 0.39(2) ppm. These values are obtained from a calibration sample, processed and grown identically to the sample studied in this paper.

While SIMS is ideal for detecting low concentrations of dopants in semiconducting materials, sample geometries unique to our application remain difficult to characterize accurately due to experimental trade-offs. Specifically, the trade-off between depth resolution and overall sensitivity is dictated by the analysis/sputtering energy. Under our characterization conditions, the ideal detection limits for $^{15}N_2$ and $^{14}N_2$ densities are $1 \times 10^{15}\,\mathrm{cm}^{-3}$ (≈0.006 ppm) and $5 \times 10^{15}\,\mathrm{cm}^{-3}$ (≈0.028 ppm), respectively. However, the obtained densities can vary significantly as a function of sample inhomogeneities, the presence of growth defects, and experimental conditions. While studying samples that were nominally grown under the same conditions, SIMS quantification of [^{15}N] has been observed to regularly vary by at least an order of magnitude, requiring rigorous statistics over growth of multiple samples, a time- and resource-consuming process. A truly local spin-defect materials characterization method is necessary, motivating the *in-situ* maximum likelihood estimation of the density characterization presented in Sec. 5.3.5, a new capability enabled by our computational results. A different approach with NV ensemble coherence measurements has also recently been developed [60, 110].

5.3.3 *Single spin coherence in quasi-2D electron bath*

We now turn to investigating single spin coherence properties across the density and thickness parameter space available for the PECVD growth recipe adopted in this work and described in Sec. 5.4.2.

We compute Ramsey coherence time T_2^* (Fig. 5.3(a), left) for 10^4 spin bath configurations with spin bath thickness of 0.5 nm to 12 nm (0.5 nm steps) and density of 0.5 ppm to 12 ppm (0.5 ppm steps) from the coupling between the central NV spin and weakly coupled P1 spins (see Sec. 5.4.1). We simulate Hahn-echo measurements (Fig. 5.3(a), right) with spin bath thicknesses of 1 nm to 10 nm (1 nm steps) and densities of 1 ppm to 12 ppm (1 ppm steps) (See Sec. A.1.2 for justification of CCE order).

We characterize the distributions of the coherence times with the mean $\mu = 10^{\langle \log T_2 \rangle}$ and the variance $\sigma^2 = \langle \log^2 T_2 \rangle - \langle \log T_2 \rangle^2$ of the logarithm of the coherence times at each density and thickness (Fig. 5.3). Using the logarithm of the coherence we can directly compare the coherence distributions at different timescales.

Figs. 5.3(b,c) and (d,e) depict μ and σ over the chosen range of parameters for T_2^* and T_2, respectively. In each case, the computed average coherence time decreases with increasing spin density and/or increasing thickness, as expected. In the three-dimensional limit, the average coherence time is independent of bath thickness. Observed decrease in μ as a function of thickness (Fig. 5.3(b) and (d)) suggests the presence a low-dimensional spin bath regime in the chosen range of parameters.

We analytically derive the distribution of the interaction strength between the central spin and bath spins in low-dimensional baths in Sec. 5.3.6. In the case of T_2, we predict

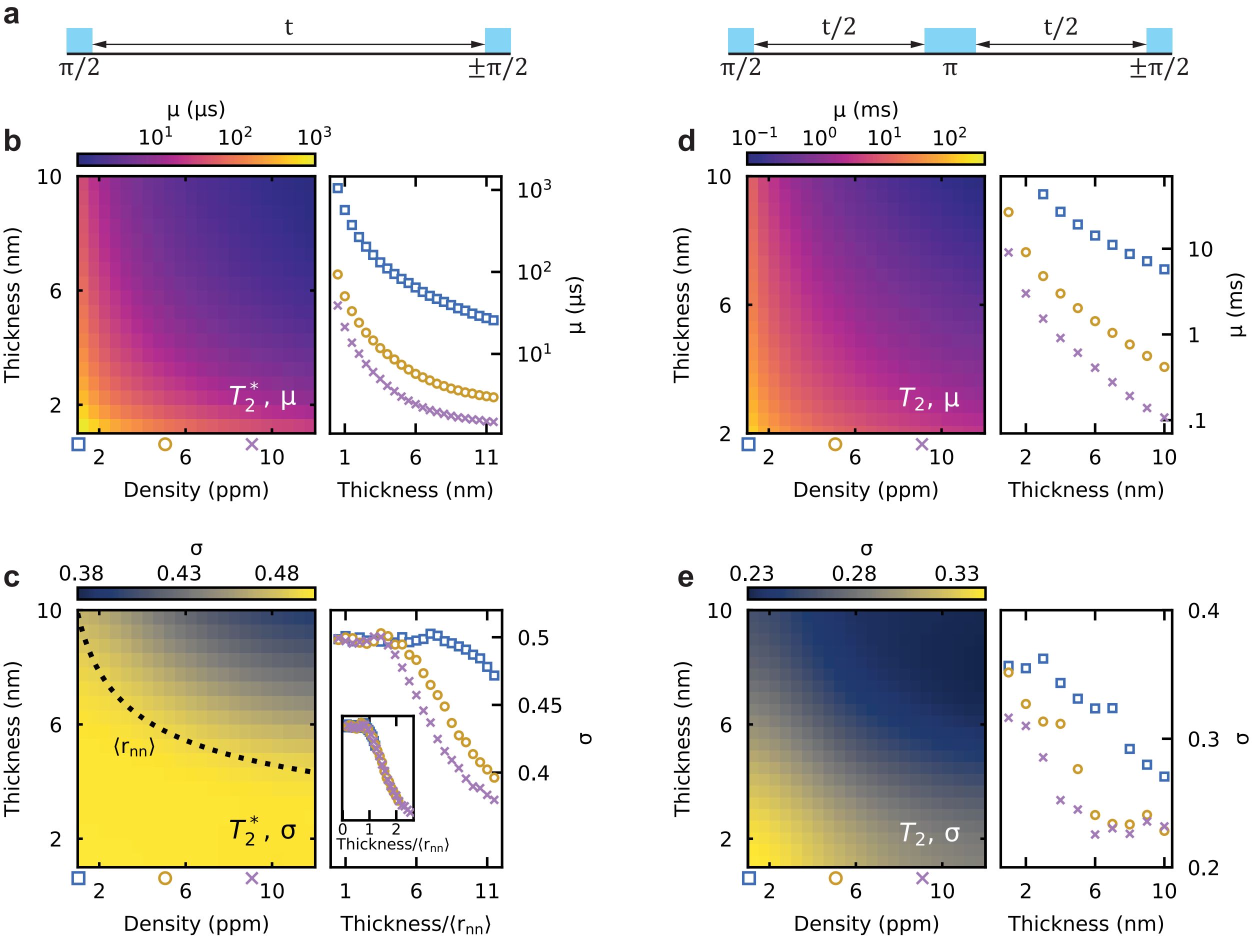

Figure 5.3: **Single spin coherence in low-dimensional spin baths.** (a) Ramsey (left) and Hahn echo (right) microwave measurement pulse sequences. (b,c) Mean of $\log T_2^*$ distributions $\mu = 10^{\langle \log T_2^* \rangle}$ (b) and variance $\sigma^2 = \langle \log^2 T_2^* \rangle - \langle \log T_2^* \rangle^2$ (c) as a function of P1 density and layer thickness. Values are linearly interpolated between datapoints. The black dashed line in (c) indicates the thickness equal to the average nearest-neighbor bath spin distance $\langle r_{nn} \rangle = 0.554\rho^{-1/3}$ for each density ρ (see text, Sec. 5.3.6), demonstrating a boundary between dimensionalities. At right in (b,c) are line-cuts of μ and σ at densities of 1, 5, and 9 ppm. Inset in (c) is σ at multiple densities with thickness normalized by $\langle r_{nn} \rangle$, demonstrating universal behavior versus dimensionality. (d,e) Same data as (b,c) presented for T_2 coherence times.

times >1 ms, beyond what is generally observed in experiment. This suggests that experimental T_2 times in thin, low density spin baths are limited by noise sources not captured in our model, as suggested previously [23]. However, our calculations predict that, in principle, low dimensional lightly doped samples can realize T_1 limited coherence times at room temperature.

Bath dimensionality further impacts the relative distribution of coherence times, described by standard deviation σ. Focusing on inhomogeneous dephasing time T_2^* (Fig. 5.3(c), right), σ exhibits unexpected behavior in the region where the thickness equals the average nearest neighbor distance in three dimensions, $\langle r_{nn} \rangle$, plotted as a function of density in the left plot. σ plateaus when the thickness is smaller than $\langle r_{nn} \rangle$ and decreases when thicknesses are larger. Inset in Fig. 5.3(c), right, the x-axis is normalized to $\langle r_{nn} \rangle$, demonstrating universal behavior of coherence times relative to the bath dimensionality. This indicates that two-dimensional spin baths naturally have a wider spread of NV coherence times. While thin and less dense samples may optimize coherence times, they typically also lead to greater fluctuations in single-qubit coherence properties.

We see similar trends in Hahn-echo T_2 times (Fig. 5.3(e), right). We find in general that $\sigma_{T_2^*} > \sigma_{T_2}$. In Sec. A.1.2, we find convergence for T_2^* and T_2 at twelve and 100 bath spins, respectively, suggesting heuristically that Ramsey measurements are sensitive to the variation of a fewer number of spins. In general, one expects a smaller standard deviation in physical quantities that are sensitive to larger numbers of randomly placed spins due to the central limit theorem. We thus expect a larger impact of the stochasticity in P1 position on the T_2^* distributions. These results inform solid-state qubit synthesis characterization, where both T_2^* and T_2 are standard measurements performed on multiple NV centers.

Our theoretical results constitute a full computational characterization of spin-bath induced coherence times across a range of bath geometries and densities. Our computational strategy is not limited to NV centers in diamond and can be applied to other spin defect systems, as well as other spin bath measurements, as long as the appropriate pulse sequence can be simulated using the PyCCE code. Additionally, our approach will inform future diamond growth and NV synthesis. Rather than extrapolating from bulk data [23] or measurements on single δ-doped NV centers, growth may now be informed by the theoretical predictions of coherence times distributions.

5.3.4 Sample characterization

We now characterize the coherence of an exemplar sample grown under the conditions outlined in Sec. 5.4.2. Fig. 5.4(a) presents frequency-dependent double electron-electron resonance measurements of a single NV center in a P1 center bath. This measurement essentially performs electron spin resonance (ESR) spectroscopy on target spins by recoupling their dipolar interactions to the NV probe spin, which are otherwise decoupled by the Hahn-echo sequence. At the experimental magnetic field of 311 G, and given ^{15}N P1 hyperfine couplings, we expect, based on the possible P1 Jahn-Teller axis directions and ^{15}N nuclear spin states, transitions near 935 MHz and 954 MHz for the three misaligned and one aligned axes, respectively, and the nitrogen nuclear spin state +1/2 probed here (only half the bath is probed in this data). We observe resonances at mircowave light frequencies f_{P1} of 934.8 MHz ($f_{P1,3/8}$) and 953.1 MHz ($f_{P1,1/8}$). The subscripts indicate the fraction of the bath probed at that frequency. This confirms the presence of ^{15}N P1 centers in our sample.

We measure T_2^* times for a set of eight single NV centers in the same test sample. Fig. 5.4(b) shows characteristic Ramsey interferometry data for the one of these NV centers. Data is fit to an exponential decay with oscillations capturing coupling to single nearby P1 centers, as in the Ramsey analysis in Sec. 5.3. While the ^{15}NV center exhibits a ≈3 MHz splitting from its nitrogen nuclear spin, CCE calculations do not account for the central spin's nuclear spin. We are careful to drive with 909 kHz Rabi rate pulses to avoid mixing nuclear hyperfine effects into our measurement. This NV exhibits T_2^*=25(2) µs. This process

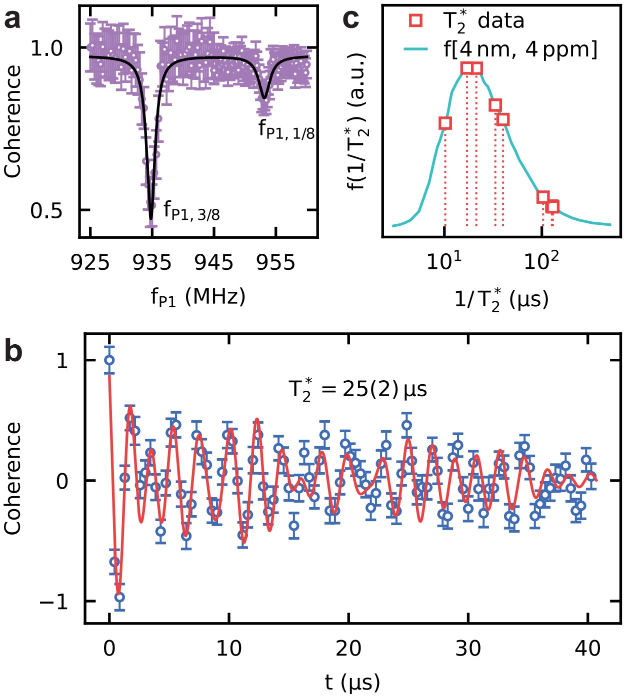

Figure 5.4: **NV center measurements.** (a) DEER spectroscopy with NV center confirming the presence of a P1 center electron spin bath. Marked values of f_{P1} correspond to P1 ESR transitions corresponding to the static magnetic field and internal P1 hyperfine parameters. (b) Ramsey interferometry measurement to extract T_2^* coherence time. (c) Compiled decoherence rates for eight measured NV centers overlaid with the best calculated distribution fit. The height of each data point indicates the PDF value for that time, and is not extracted from the measurement.

is followed for the remaining NV centers.

Decoherence rates for the set of measured NV centers are plotted in Fig. 5.4(c) along with the calculated probability distribution function (PDF) that best fits the measured distribution as determined via MLE, discussed in the next section. The aim in the following section will be to determine which calculated distribution best fits this dataset.

5.3.5 Maximum likelihood estimation

We develop a MLE model using the data presented in Fig. 5.3. Taking interpolated distributions $f(1/T_2^*)$, recovered from the numerical data, the likelihood of a given bath configuration is calculated as the joint probability of the $\{T_2^*\}$ dataset for each pair of bath thickness t

and density ρ as [7]

$$L(t, \rho) = \prod_i f(t, \rho, T_{2,i}^*). \tag{5.1}$$

The MLE procedure determines what coherence distribution best predicts the measured distribution in Fig. 5.4(c). In Fig. 5.5(a) we plot $L(t, \rho)$ over the computational phase space for the coherence times in Fig. 5.4(c). We find a band of potential bath geometries that satisfy the observed coherence time distribution, rather than uniquely predicting a single set of values. Based on the CVD growth discussed in Sec. 5.4.2, we estimate the bath thickness at t_{SIMS} =4 nm and plot the linecut of L in Fig. 5.5(b). This provides a measure of the bath density of 3.6(7) ppm, where the error is found by fitting $L(t_{SIMS}, \rho)$ to a normal distribution.

We now benchmark the error in the MLE procedure versus the number of coherence time samples in Fig. 5.5(c). For each number of samples, N, and set of bath parameters, 200 random T_2^* datasets of N coherence times are chosen from the numerical datasets used in Sec. 5.3. Then, the likelihood is calculated for a fixed thickness t_0, and the relative error for one dataset is calculated as $\epsilon_{\rho_0}^2 = (\rho_{mle} - \rho_0)^2/\rho_0^2$, where ρ_{mle} is the density such that $L(t_0, \rho_{mle}) = \max\left[L(t_0, \rho)\right]$. This is averaged over a range of tested densities, plotted in Fig. 5.5(c). We calculate the error for eight samples to be 25%, corresponding to an uncertainty of 0.9 ppm for the density estimate from Fig. 5.5(a). This is similar to the error from fitting L, and is stable when the thickness is varied. We fit the average error as $A \cdot N^{-p}$, shown over the calculated error in Fig. 5.5(c), finding a $N^{-1.6}$ trend.

5.3.6 Strong coupling yield

Entangled qubit-based sensors promise to greatly enhance quantum sensing capabilities as compared to the current state-of-the-art [299]. The applicability of these schemes is enabled by high-yield synthesis of strongly coupled quantum systems, e.g. NV center spins and

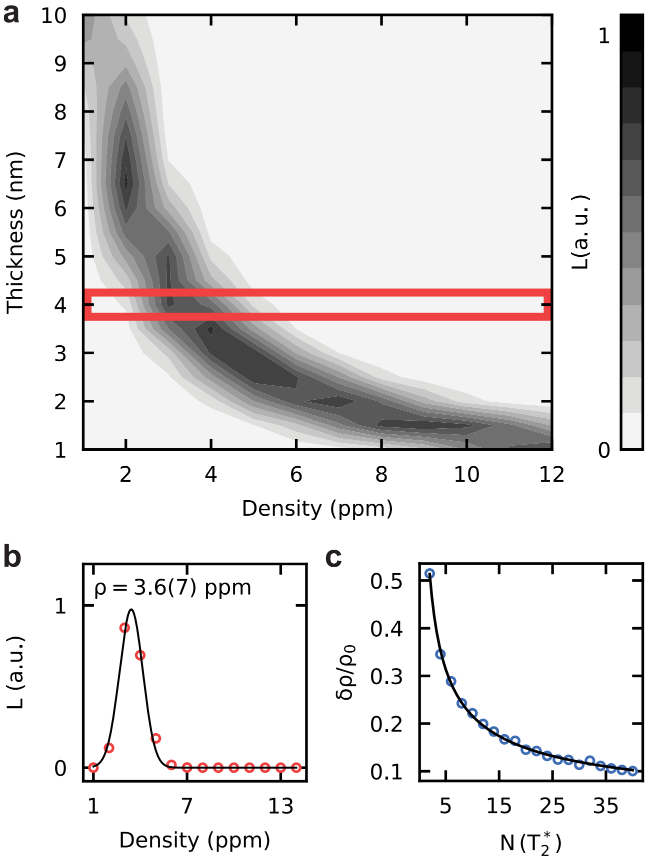

Figure 5.5: **Maximum likelihood estimation.** (a) Likelihood of dataset in Fig. 5.4(c) calculated for each set of bath parameters, from theoretical results. (b) Likelihood restricted to a thickness of $t_{SIMS} = 4\,\text{nm}$ (from Fig. 5.2(e)), from which we extract a density of 3.6(7) ppm. (c) Calculated error of density estimation across full density range with fixed thickness, calculated for 200 random datasets at each density.

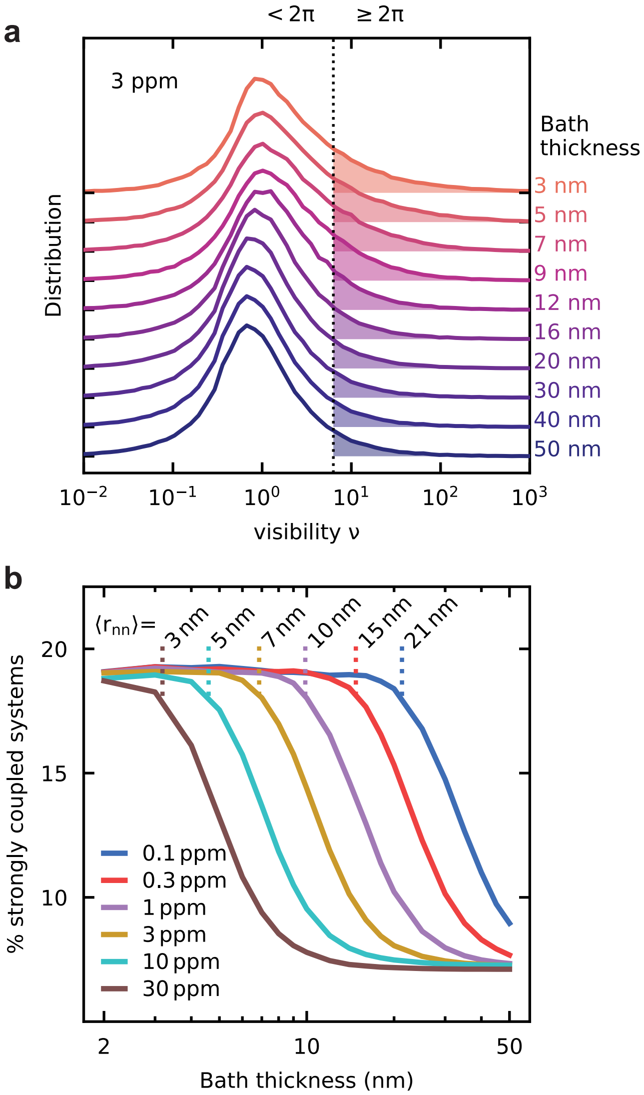

Figure 5.6: **Dimensionality dependence of strong coupling.** (a) Computed distribution (using PyCCE) of ratio of nearest-neighbor P1 coupling to background decoherence rate for 10^5 3 ppm density P1 bath configurations with varying thickness. Curves are offset for clarity. Shaded regions right of the dashed line indicate coupling ratio $\geq 2\pi$. (b) Percentage of NV-P1 bath systems with at least one strongly coupled bath spin for varying bath density and thickness. Average spin-spin distance is marked atop curves for each density.

multiple single bath spins. We consider the impact of growth dimensionality on the yield of such systems analytically, quantifying our results with numerical predictions. In our calculations we consider central NV spins and P1 bath spins, but our approach is easily generalized to other spin systems.

Each bath spin couples to the NV with a dipolar coupling strength A_z^i. The NV coherence in the absence of dynamical protocols and coupled to a bath of many weakly coupled spins can be described as a product of individual coupling contributions (see Sec. 5.4.1).

We aim to describe how likely the coupling to the nearest spin, A_0, is to be greater than the dephasing from the rest of the bath, A_{bath}. The distributions of nearest neighbor distance r_{nn} in two and three dimensions are

$$g_{2D} = \exp(-\pi r_{nn}^2 \varsigma)\varsigma\, 2\pi r_{nn}, \tag{5.2}$$

$$g_{3D} = \exp(-4\pi r_{nn}^3 \rho/3)\rho\, 4\pi r_{nn}^2, \tag{5.3}$$

where ρ is the 3D density and $\varsigma = \rho t$ is the 2D density for bath thickness t nominally less than the average nearest neighbor distance. Notably, the distributions depend on the bath dimensionality. The bath decoherence can be estimated as follows

$$\Gamma_{2D}^{\text{bath}} \propto \sqrt{\sum_{2D} |1/r^3|^2} = \sqrt{\textstyle\int_0^\infty dr 2\pi r \varsigma r^{-6}}, \tag{5.4}$$

$$\Gamma_{3D}^{\text{bath}} \propto \sqrt{\sum_{3D} |1/r^3|^2} = \sqrt{\textstyle\int_0^\infty dr 4\pi r^2 \rho r^{-6}}. \tag{5.5}$$

We now define the visibility ν of the nearest neighbour spin as a ratio between its coupling to the central spin A_0 and the decoherence rate induced by all other spins A_{bath}

$$\nu = \frac{|A_0|}{\sqrt{2} A_{\text{bath}}}, \tag{5.6}$$

and evaluate average ν over many bath configurations. Assuming the point dipole approximation to compute the coupling between central and bath spins, we find the average visibility at the given dimensionality as $\langle \nu_{kD} \rangle = \langle |A_0|/\sqrt{2}A_{\text{bath}} \rangle \simeq \langle r_{nn}^{-3}/\sqrt{2}\Gamma_{kD} \rangle$, where the distributions Γ_{kD} ($k = \{2, 3\}$) are given by Eqs. (5.2) and (5.3). We note here that averaging Γ_{kD} assumes the dephasing rate due to the rest of the spin bath follows a highly peaked distribution. We then ask if this average is larger for lower dimensional spin baths by evaluating

$$\frac{\nu_{2D}}{\nu_{3D}} = \frac{\langle r_{nn}^{-3}/\Gamma_{2D} \rangle}{\langle r_{nn}^{-3}/\Gamma_{3D} \rangle} = \sqrt{2}. \tag{5.7}$$

We find that the visibility of the nearest neighbour spin is $\sqrt{2}$ larger in the 2D case, pointing at the fact that yield of strongly coupled bath spins is significantly higher in the low dimensional systems.

We confirm these analytical predictions with numerical simulations. Using the PyCCE code we generate 10^5 50 nm-thick P1 electron spin baths in a (001)-oriented diamond lattice whose densities range over two orders of magnitude, and divide each bath into slices of varying thickness. For each density and thickness we compute visibility ν (Eq. (5.6)). Representative histograms for 3 ppm spin baths are shown in Fig. 5.6(a). As the bath thickness decreases, the visibility distribution shifts to higher values, in line with the prediction from Eq. (5.7). We follow the criterion laid out in Sec. 5.4.1 and Eq. (5.11) below to identify strongly coupled bath spins. We set a threshold for the visibility at $\nu \geq 2\pi$. At this value coherence goes through a full oscillation period when the signal contrast reaches $1/e$.

We plot the resulting probability of obtaining strongly coupled spins in Fig. 5.6(b) for each density. At all densities, the likelihood of finding a NV-spin bath configuration with the desired coupling ratio is almost three times as high in the thin bath limit. Furthermore, there is a crossover transition for each density from three-dimensional to two-dimensional behavior, which intersects with the average nearest neighbor spacing $\langle r_{nn} \rangle = 0.554\rho^{-1/3}$, obtained from Eq. (5.3). Heuristically, as the thickness reduces below $\langle r_{nn} \rangle$, there are no spins proximal to the central spin in the out-of-plane direction, only in the plane of the central spin. In Sec. A.2 we present a point of comparison between the analytical and numerical approaches, finding agreement between calculated coupling distributions and the result in Eq. (5.7).

5.4 Methods

Our work builds on two previously established techniques, CCE calculations and PECVD synthesis of NV centers in diamond as described below and in Fig. 5.2. We focus on the ^{15}N isotope of nitrogen for the majority of the calculations as this allows us to experimentally distinguish intentionally doped defects from background occurring defects.

5.4.1 Theory

The dynamics of the systems are simulated using the following Hamiltonian:

$$\begin{aligned}\hat{H} = &-\gamma_e B_z \hat{S}_z + D\hat{S}_z^2 + \textstyle\sum_i a(m_i)\hat{P}_{z,i} - \gamma_e B_z \hat{P}_{z,i} \\ &+ \textstyle\sum_i \mathbf{S}\mathbf{A}^{(i)}\mathbf{P}_i + \sum_{i\neq j} \mathbf{P}_i \mathbf{J}^{(ij)} \mathbf{P}_j,\end{aligned} \tag{5.8}$$

where γ_e is the electron spin gyromagnetic ratio, B_z is the magnetic field aligned with the z-axis, $\mathbf{S} = (\hat{S}_x, \hat{S}_y, \hat{S}_z)$ are NV spin operators, D is the NV zero field splitting, $\mathbf{P} = (\hat{P}_x, \hat{P}_y, \hat{P}_z)$ are spin operators of the P1 center, and $a(m_i)$ is the hyperfine coupling between the P1 ^{15}N nuclear spin and the P1 electron spin, dependent on the random orientation of the Jahn-Teller axis along one of four crystal directions and the nuclear spin state for each P1 (m_i), where i runs over all the simulated P1 centers [56]. $\mathbf{A}^{(i)}$ are dipolar couplings between the NV center and P1 centers, and $\mathbf{J}^{(ij)}$ is the coupling between two P1 electron spins. The applied 50 G is sufficiently past the high field limit and these calculations translate over to measurements at higher fields as well (see Sec. A.1.1).

In Sec. A.1.2 and A.1.3 we show convergence tests for Ramsey and Hahn echo simulations versus both CCE order and total number of simulated bath spins. We use CCE methods with bath state sampling [197] to achieve convergence for the electron spin bath. For each pure electron bath state the state of ^{15}N spin and the P1 orientation is chosen at random. More details about the method are available in [196].

The CCE approach [287, 288] approximates the coherence function $\mathcal{L}(t) = \frac{\langle \sigma_-(t) \rangle}{\langle \sigma_-(0) \rangle} = \frac{\langle 0|\hat{\rho}(t)|1\rangle}{\langle 0|\hat{\rho}(0)|1\rangle}$, the normalized off-diagonal element of the density matrix $\rho_{m,n}$ of the qubit, where m and n are either the ground or excited spin states $|0\rangle$ and $|1\rangle$, respectively. $\mathcal{L}(t)$ is approximated as a product of cluster contributions:

$$\mathcal{L}(t) = \prod_i \tilde{L}^{\{i\}} \prod_{i,j} \tilde{L}^{\{ij\}} ..., \tag{5.9}$$

where $\tilde{L}^{\{i\}}$ is the contribution of a single bath spin, $\tilde{L}^{\{ij\}}$ is the contribution of spin pairs, and so on for higher order clusters (Fig. 5.2(a)). The maximum size of the cluster n included in the expansion denotes the order of CCEn approximation.

The Ramsey signal is converged at the first order of CCE. As such, we can represent the high-field Ramsey coherence function in the rotating frame for a bath in a fully mixed state as [297]:

$$\begin{aligned} \mathcal{L}(t) \approx \prod_j^N \cos\frac{A_z^j t}{2} \approx & \exp\left[\tfrac{A_{\text{bath}}^2}{2} t^2\right] \textstyle\prod_i^n \cos\frac{A_z^i t}{2} \\ = & \exp\left[-(\tfrac{t}{T_2^*})^2\right] \textstyle\prod_i^n \cos\frac{A_z^i t}{2} \end{aligned} \tag{5.10}$$

where $A_{\text{bath}}^2 = \frac{\sum_j (A_z^j)^2}{4}$, $T_2^* = \frac{\sqrt{2}}{A_{\text{bath}}}$ index i goes over only n the strongly coupled P1 centers, and index j goes over all other P1s. We define strongly coupled bath spins as those distinguishable from the background decoherence, setting threshold for its visibility

(Eq. (5.6)) as:

$$\nu_i = \frac{\left|A_z^{(i)}\right|}{2} \geq 2\pi \cdot \frac{A_{\mathrm{bath}}}{\sqrt{2}}, \tag{5.11}$$

so that at least one full period of oscillation of the coherence function is visible when the signal contrast reaches $1/e$. For each random bath configuration we order the P1 spins by strength of the coupling, and one-by-one select out the strongly coupled spins until the condition (5.11) is violated. T_2^* is then recovered from the coupling to the remaining bath spins.

Ref. 201 shows that CCE at second order can be used to qualitatively recover the behaviour of T_2 coherence times in the P1 bath. We further extend this approach, and converge CCE Hahn echo calculations at 4th order with bath-state sampling (see Sec. A.1.2 and Fig. A.1(c)).

5.4.2 Materials growth

All defects studied in this work are doped *in-situ* during diamond PECVD with subsequent electron irradiation and annealing for NV^- activation. See Ch. 4 Sec. 4.3.2 for the growth recipe used in this work.

Post-growth and nitrogen incorporation, bulk electron irradiation with a $2 \times 10^{14}\,\mathrm{cm}^{-2}$ dose at 2 MeV and a 2 h anneal at 850 °C under an Ar atmosphere converts a fraction of doped nitrogen into NV centers with $[^{15}\mathrm{NV}] \approx 0.01\,\mathrm{ppb}$ to $0.1\,\mathrm{ppb}$, with the remaining nitrogen sites remaining as $\mathrm{N_s}$ (P1 centers). NV activation is intentionally performed in a vacancy diffusion-limited regime [193] in order to reliably obtain optically resolvable single NV centers. As the nitrogen doping is buried 50 nm below the diamond surface, we do not expect band-bending effects on the defect charge states [36, 184].

5.5 Outlook

Point-defects in diamond and other wide-bandgap semiconductors are promising platforms for qubit-based sensors. Deterministic synthesis of such systems will benefit from feed-forward techniques that optimize host crystal parameters for specific outcomes and applications. Additionally, such systems pave the way for entangled qubit-based sensors which hold great promise to enhance current quantum sensing capabilities. In this paper, we have demonstrated holistic quantum simulations of NV center coherence (with techniques applicable to other spin defects) as a tool for quantum system coherence characterization driven synthesis, minimizing the need for large-scale and destructive materials characterization. Practically, we showed how our approach allows, with basic prior sample knowledge, for the use of rudimentary T_2^* measurements to approximate *in-situ* doping densities. Specifically, we have demonstrated a MLE model based on a CCE-generated distribution library as an aid to process calibration and sample characterization. This method is non-destructive and operates at the density scales relevant for quantum technologies.

Additionally, the coherence distribution results presented in this paper explore the expected sample properties in low-dimensional spin baths. By going beyond approximate analytical treatments and sampling over a wide distribution of random bath configurations with a range of central spin-bath couplings, the CCE calculations quantitatively capture the connection between bath geometries and coherence time distributions, providing an invaluable analytical tool for experimental design.

While in this work we focus on a single dominant spin bath species in low-dimensional geometries, our MLE method is not limited to this regime. CCE methods can readily be extended to additional spin bath species in diamond, as well as mixed nuclear and electronic spin baths. By calculating coherence times in these other situations, dopant densities in samples with multiple dominant noise sources can be characterized. Furthermore, the strategy presented here can be applied to other solid state hosts where qubit coherence is limited by spin bath noise.

CHAPTER 6

RELAXATION MECHANISMS OF A SINGLE DARK ELECTRON SPIN IN DIAMOND

The contents of this chapter represent a draft of: J. C. Marcks, M. Onizhuk, Y.-X. Wang, B. Soloway, M. Fukami, N. Delegan, F. J. Heremans, A. A. Clerk, G. Galli, D. D. Awschalom, Relaxation mechanisms of a single dark electron spin in diamond, *manuscript in preparation.*

6.1 Summary

Spin baths in solid state hosts both limit coherent central spin operation as well as present a potential resource for quantum sensing and quantum communication applications with multi-qubit entangled states. Evolution of a many-body spin bath in general decoheres the central spin via dipolar interactions, but these same couplings also enable coherent interaction with suitable qubit control. The optically active nitrogen vacancy (NV) and the optically dark neutrally charged substitutional nitrogen ($\mathrm{N_s}^0$, P1) centers in diamond are a widely studied central spin-spin bath system. However, little work has focused explicitly on the P1 center, and is usually concerned with mesoscopic bath properties and not single spins. A better understanding of single P1 electron spins will inform NV center decoherence as well as help evaluate the feasibility of the P1 center as a qubit. In this work, we realize resonant polarization and off-resonant readout of a single P1 electron spin mediated by the NV center electron spin, enabling polarization- and time-resolved measurements of the P1 spin decay. We first measure decay in the dark, finding room temperature, phonon-limited $T_1 \approx 2.5\,\mathrm{ms}$ despite an environment of ostensibly resonant spins. We then measure long relaxation times under optical illumination with green light limited by P1 ionization. These results provide a microscopic view of spin bath dynamics in diamond, and our approach may be applied to probe spin systems external to a diamond sensor, such as electron spins in spin-labelled

molecules.

6.2 Introduction

Quantum information technologies are limited by loss of coherence due to the environment [20, 65]. Solid-state host systems often dictate both challenges and solutions to engineering coherent qubits [10, 62]. Diamond, a wide bandgap semiconductor, is an amenable host to many emitters with robust spin-photon interfaces [12, 32, 69] that have enabled advances in quantum sensing [45, 65] and communication [107, 187, 188], as well as interpretations of quantum mechanics [103, 268]. Weak spin relaxation in diamond-hosted spin defects such as the nitrogen vacancy (NV) center [213] enable above room-temperature coherent control and readout [151, 263], facilitating NV-based sensing from condensed matter [45] to biological [294] systems. However, qubit performance for these applications remains limited by decohering interactions [20].

Broadly, efforts to engineer coherent NV centers fall into two separate yet complementary categories: (i) minimize bath interactions via extrinsic fields [5, 18, 29, 49, 61, 124, 256, 272, 273], and (ii) optimize bath spin density and dimensionality via intrinsic sample control [15, 80, 104, 132, 157, 180, 192, 283]. In both cases, optimizing the qubit interaction with the spin bath is key. Optically dark, electronic spin-1/2 $\mathrm{N_s}^0$ defects in the diamond lattice, P1 centers [245], are one of these abundant spin bath species in naturally occurring [126] and synthesized diamond NV environments [20], and the P1 spin bath is generally treated as a decoherence source to be mitigated [23]. However, P1 centers have recently been highlighted and investigated on their own merit for quantum information applications [66, 91, 289, 296], which motivates investigating properties of single P1 centers. While many studies of NV center decoherence have characterized mesoscopic properties of the P1 spin bath [17, 23, 60, 102], such as a correlation time, this does not necessarily capture relaxation mechanisms relevant at the single-spin level.

In this work, we extend previous techniques to polarize and probe proximal electronic spins with NV centers [55, 139, 222] to study spin relaxation mechanisms of a single P1 center resolved above the background spin bath via strong coupling to an optically active NV center, shown schematically in Fig. 6.1(a). We begin with double electron-electron resonance (DEER) measurements alongside cluster correlation expansion (CCE) calculations to approximate the P1 spin configuration near the NV center, enabling simulations of spin bath dynamics. Then, a time-resolved method to polarize and measure single dark bath spins is demonstrated that allows for arbitrary and independent control of both NV and bath spins. We apply this method to probe P1 decay.

Through comparison of spin decay to simulations of spin bath dynamics we find that spin flips in our system are not dominated by intra-bath flip-flops at room temperature, finding a single spin T_1 commensurate with phonon-limited T_1 observed in ensemble ESR measurements [19, 77, 214, 260, 291]. We propose that these spin flips may be a source of NV decoherence stronger than many-body bath interactions at room temperature. We further study P1 decay under illumination, which has been demonstrated to photoionize P1 centers [21, 105], finding spin lifetimes limited by ionization of the P1 electron. Finally, we discuss how the methods used here for the P1 center spin may be readily applied to other electron spin systems proximal to NV centers in order to elucidate relaxation mechanisms.

6.3 Results

6.3.1 System characterization

We study a strongly coupled NV-P1 system in a two-dimensional ^{15}N δ-doped [192] layer hosted in ^{12}C isotopically purified PE-CVD grown diamond, shown schematically in Fig. 6.1. See Ch. 4 and Ch. 5 for a detailed description of sample synthesis. An external magnetic field of 413 G is aligned within 0.5° of the [111] crystal axis (NV axis), such that optical

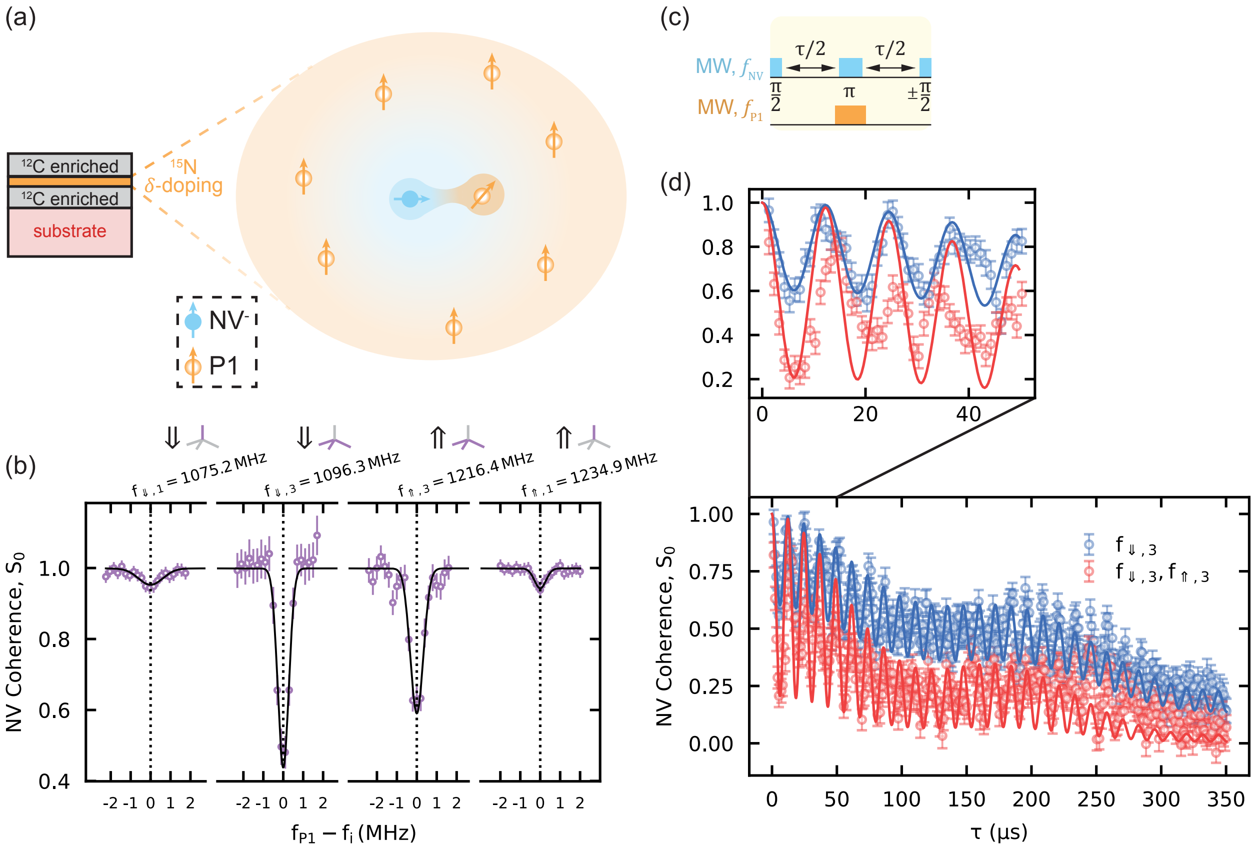

Figure 6.1: **Spin bath characterization.** (a) Sample geometry. The NV center and surrounding P1 centers are hosted in a 4 nm-thick, [N] = 3.6 ppm ^{15}N δ-doped layer within isotopically purified PECVD diamond. The schematic at right demonstrates the NV strongly coupled to a P1 bath spin as well as weakly coupled to other P1 bath spins. (b) P1 spin resonance spectrum with four resonances corresponding to different nuclear spin and Jahn-Teller states, indicated above the data. (c) Double electron-electron resonance measurement sequence to recouple interactions between NV and P1 spins. (d) DEER decay with resonant driving at one ($f_{\Downarrow,3}$) and two ($f_{\Uparrow,3}$ and $f_{\Downarrow,3}$) tones. Simulated signal of best-fit configuration as determined via CCE is overlaid. The region of 0 μs to 50 μs is zoomed in.

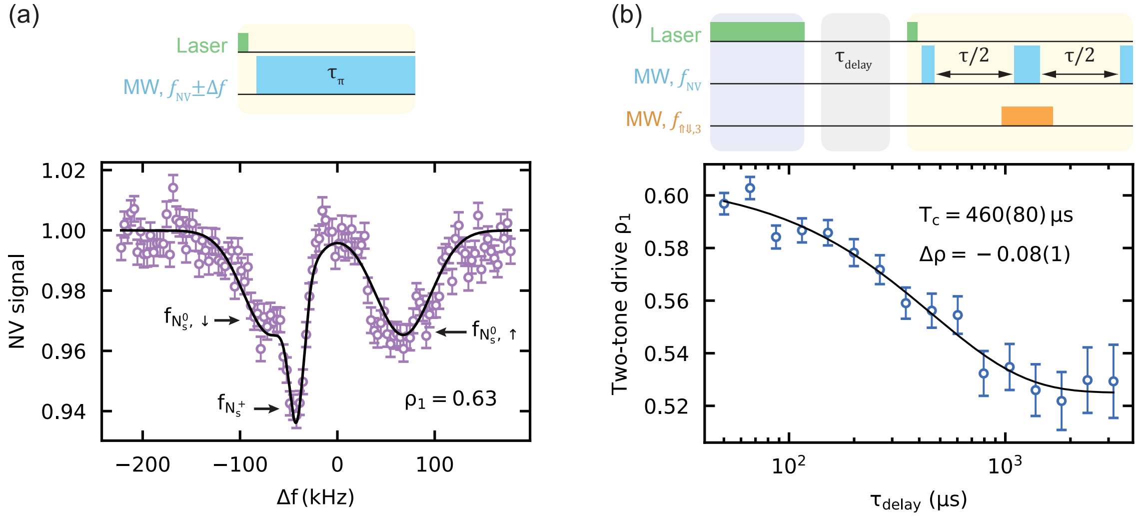

Figure 6.2: **N_s charge population.** (a) NV ESR spectrum revealing strongly coupled P1 spin as well as a central frequency that appears when the N_s is in the + charge state and spinless. (b) Charge population decay measured via DEER contrast at $\tau = 5\,\mu s$.

illumination polarizes the NV nuclear spin [117] to 69%. This enables the < 1 MHz Rabi rates in this work with minimal impact on signal (App. B.1). Under this condition there are four unique P1 electron spin transitions, measured in Fig. 6.1(b) via the double electron-electron resonance (DEER) pulse sequence in Fig. 6.1(c) with a frequency-dependent π-pulse on MW2. See App. B.2 for more details of the DEER measurement. The four transitions correspond to the two ^{15}N nuclear spin states and the four Jahn-Teller (JT) states (see Ch. 2), three of which are nearly degenerate due to the magnetic field alignment. Above the spectrum we identify the corresponding nuclear and JT states, and henceforth refer to these four frequencies as $f_{\Downarrow,1}$, $f_{\Downarrow,3}$, $f_{\Uparrow,3}$, and $f_{\Uparrow,1}$, moving from left to right in the spectrum.

We approximate the configuration of P1 centers surrounding the single NV center with a combined experimental and computational DEER study. In Fig. 6.1(d) we first measure the in-phase NV coherence under a DEER measurement, $S_0(t)$, driving π-pulses at both one ($f_{\Downarrow,3}$) and two ($f_{\Downarrow,3}$ and $f_{\Uparrow,3}$) resonance tones, observing slow characteristic coherence decay as well as two visible sets of oscillations that we identify as arising from nearby strongly coupled spins. Comparing the measured signal to the theoretical expression for DEER in the presence of strong coupling derived in App. B.2.3, the observed signal contrast is smaller than expected for driving 3/8 (6/8) of the bath population in the one (two) tone signal. We fit the decay curve assuming two strongly coupled spins with non-unit populations ρ_j and dipolar couplings A_j, as may arise from multiple charge states, and a background coherence function with time $T_{2,DEER}$ and stretch factor n,

$$S_0(t) = e^{-(t/T_{2,DEER})^n} \prod_j \left[(1 - 3/8 \cdot \rho_j) + \rho_j \cdot \cos \frac{A_j}{2} t \right]. \tag{6.1}$$

We fix $\rho_1 = 0.528$, calculated from the amplitude of the first coherence dip in S_0, which is only sensitive to the strongest coupled spin. We then find $\rho_2 = 0.35$, and coupling strengths of $A_1 = 2\pi \cdot 154\,\mathrm{kHz}$ and $A_2 = 2\pi \cdot 9\,\mathrm{kHz}$ for the first and second resolvable spins, respectively. We then generate 10^5 potential spin bath configurations with the parameters in Fig. 6.1. We fix the populations of all bath spins except the strongest coupled spin to 0.35 and fix the population of the strongest spin to 0.528. We simulate the resulting NV DEER coherence with cluster correlation expansion (CCE) methods and evaluate each configuration based on how well it matches the experimental signal. Based on CCE convergence tests in App. A.1.2, we expect DEER to be most sensitive to the ≈ 5 strongest coupled spins with a smaller dependence on the background spin bath density, due to the incomplete driving of the spin bath and resulting Ramsey-like and Hahn echo-like behavior. The DEER trace from the best-matched configuration, calculated with 50 bath spins, is overlaid on the data in Fig. 6.1(d). We also identify 47 other configurations that match well to our data[1]. These bath configurations are used for spin diffusion and T_2 simulations in Sec. 6.3.3.

We further investigate the observed P1 population reduction in Fig. 6.2. We first probe the NV electronic fine structure via high-resolution (pulse bandwidth 14 kHz) optically detected magnetic resonance (ODMR) in Fig. 6.2(a) with laser pulses identical in power and

---

[1] This number reflects the number of available computing cores (48) and is not on its own meaningful.

time to those used in the DEER measurement. We identify the outer two resonances as arising from the P1 electron spin-induced splitting, resolvable above the spin linewidth. We further ascribe the central resonance to a Stark shift [178] that occurs when the nearest $\mathrm{N_s}$ center is in the $\mathrm{N_s}^+$ charge state, thus removing the electron spin but introducing a point charge. Assuming the dipolar and Stark shifts correspond to the $\mathrm{N_s}^0$ and $\mathrm{N_s}^+$ states, respectively, we extract a population of $\rho_1 = 0.63$ based on the NV contrast reduction at each resonance, 19% larger than the value extracted from the coherence dip in Fig 6.1(d).

To better understand the charge population we perform a time-resolved charge decay measurement, first demonstrated in Ref. 156, in Fig. 6.2(b) using the pulse sequence shown on top. After a sufficiently long laser pulse (see Sec. 6.3.5) to scramble the $\mathrm{N_s}$ charge states the system is allowed to evolve in the dark for a variable time. We then probe S_0 at the first coherence dip, where the NV is only sensitive to the strongest coupled P1 spin. We observe a signal corresponding to an initial population $\rho_1(0) = 0.61$ that decays to the ρ_1 observed in Fig. 6.1(d) with exponential decay time $T_c = 460(80)\,\mu\mathrm{s}$. We thus believe that the time-dependent S_0 signal represents the steady-state charge population of the $\mathrm{N_s}$ bath that arises from optical illumination and nearby charge traps [95]. We note that this bath-induced Stark shift may contribute additional decoherence in $\mathrm{N_s}$ baths, although this is beyond the scope of this work.

6.3.2 P1 Polarization and Readout

Polarization and readout of the strongly coupled P1 center is achieved via a combination of resonant and off-resonant dipolar interactions on both the NV and P1 electron spins, controlled via the microwave pulse sequence shown in Fig. 6.3(a), with schematics of the relevant interactions shown above the sequence. The NV begins spin-polarized, after optical illumination, in the $|m_s = 0\rangle$ spin state; the P1 spin begins in a thermal state. Throughout the measurement the P1 is driven with two microwave tones at $f_{\Downarrow,3}$ and $f_{\Uparrow,3}$ to improve

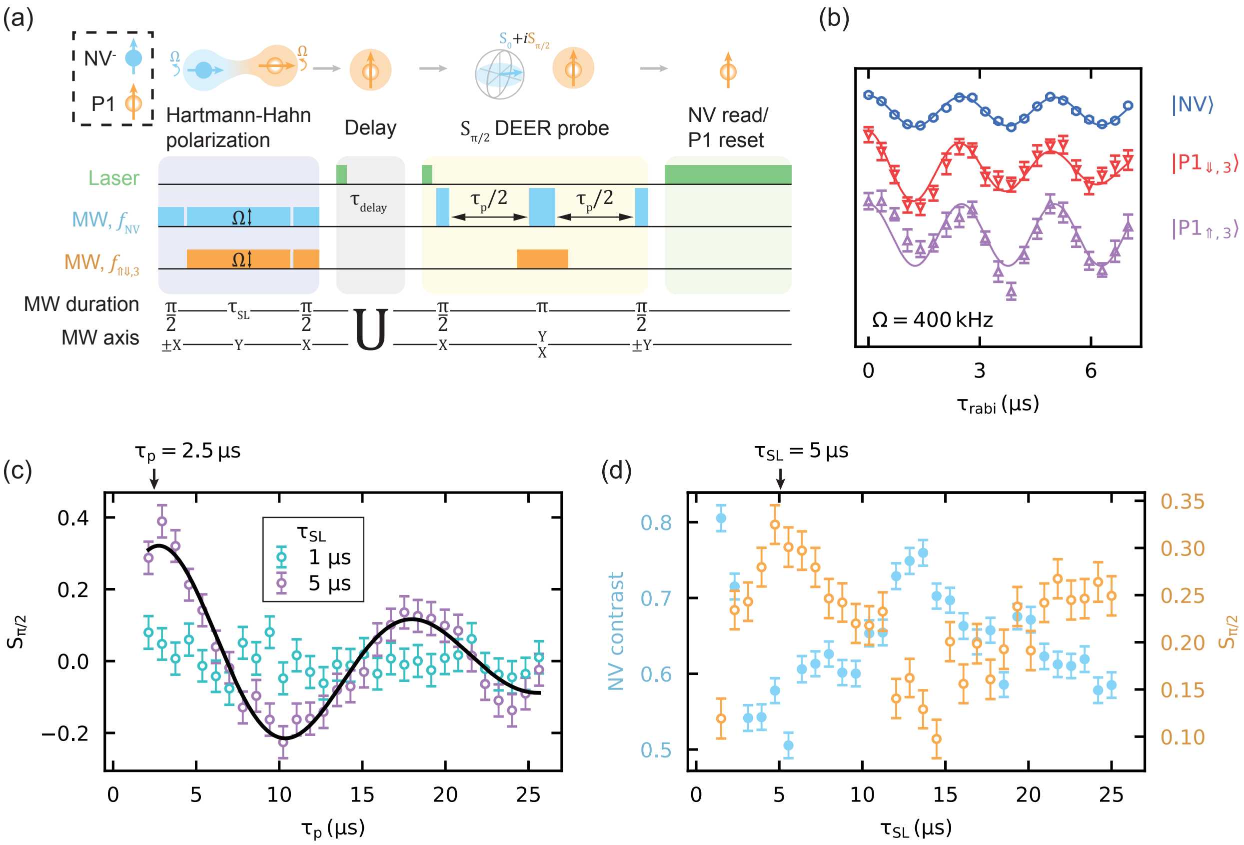

Figure 6.3: **P1 polarization and measurement.** (a) NV-P1 polarization-probe measurement sequence. Hartmann-Hahn spin locking turns on polarization transfer between the initialized NV and the P1. Initial NV pulse axis ($\pm X$) determines the sign of the P1 polarization, enabling differential measurement of the P1 spin. The P1 spin polarization (signified by the shaded circle) evolves during an arbitrary delay time. An out-of-phase DEER measurement, $S_{\pi/2}$, on the NV probes the P1 polarization. The NV is driven at 2Ω in this segment to avoid resonance with the P1 during the π-pulse. After NV readout, a long laser pulse resets the P1 spin state, explored more completely in Sec. 6.3.5. When overlapping microwave pulses are present, the duration refers to both pulses, with duration referenced to the drive period. When only one microwave axis is present, it refers to both pulses. “U” stands in for an arbitrary unitary pulse sequence. (b) Resonant tuning of Rabi drive rate Ω for all three drive tones. P1 drives are measured via the DEER sequence in Fig. 6.1(c) with a variable time P1 pulse. (c) $S_{\pi/2}$ versus probe time τ_p for two different fixed spin locking times, with maximum signal at $\tau_p = 2.5\,\mu\text{s}$. (d) NV polarization, measured optically, after a variable spin locking time τ_{SL} (blue, filled circles) and P1 polarization, measured through $S_{\pi/2}$ (orange, open circles), after the same time. Correspondence between the two indicates that $S_{\pi/2}$ properly measures the polarization transferred to the P1 spin. Maximum polarization is at $\tau_{SL} = 5\,\mu\text{s}$.

signal collection.

Both spins are then driven in a spin locking scheme, first panel, at the Hartmann-Hahn resonance condition $\Omega_{NV} = \Omega_{P1}$, where Ω is the Rabi drive rate. Note that although the spin-1 NV and spin-$\frac{1}{2}$ P1 couple with different strengths to ac magnetic fields, we are concerned here with the drive rate, not the drive field. Fig. 6.3(b) presents tuning of Ω for the three drive tones for the NV, $\text{P1}_{\Downarrow,3}$, and $\text{P1}_{\Uparrow,3}$ populations. Rabi measurements of the P1 are performed with the DEER sequence in Fig. 6.1(b), where we vary the time of the P1 π-pulse, remaining resonant with the P1 ESR frequency. The strong NV-P1 coupling shifts the P1 resonance frequency by more than the P1 electron spin linewidth when not in the $|m_s = 0\rangle$ state, which is always the case for DEER coherence measurements. Throughout these measurements, we are careful to tune f_{P1} and Ω_{P1} with DEER measurements that are only sensitive to the single strongly coupled P1 and not the other bath spins by probing the NV coherence at $\tau \lesssim 10\,\mu\text{s}$.

In general, Hartmann-Hahn resonance turns on resonant flip-flop interactions of the type $\hat{S}_+\hat{P}_- + h.c.$, where $\hat{S}$ is the NV electron spin operator and $\hat{P}$ is the P1 electron spin operator, between the NV and all driven P1 spins. In the strongly coupled case, flip-flops with the strongest coupled P1 will dominate at short times and polarization is coherently transferred to the P1 spin, shown schematically above the sequence, with the shaded region representing polarization. The direction of the P1 polarization depends on the phase of the initial pulse on the NV ($\pm\pi/2$). After spin locking for a variable time τ_{SL}, the P1 spin state is stored in an eigenstate, and the NV is repolarized with a short laser pulse that does not significantly perturb the P1 spin state (see Sec. 6.3.5 for details). During the delay period, second panel, the P1 spin is allowed to freely evolve. Additional stimuli may be added here, such as microwave and laser pulses, to modify the P1 or NV evolution.

An out-of-phase DEER measurement of the NV coherence, $S_{\pi/2}$, after interacting with the P1 spin directly probes the P1 spin state (third panel). In this segment the NV drive amplitude is doubled to avoid any resonant interactions with the P1 during the π-pulse. Details of this readout interaction can be found in Sec. B.2. After the P1 readout, both the NV and the P1 are reset with a sufficiently long laser pulse around 100 µs, as measured in Sec. 6.3.5 (fourth panel).

In Fig. 6.3(c), $S_{\pi/2}$ is measured versus DEER probe time τ_p at two different spin lock times, $\tau_{SL} = 1, 5\,\mu\text{s}$. In the case of a NV center strongly coupled to a single bath spin with coupling A and background decoherence $\Pi(\tau)$, we find

$$S_0(\tau) + iS_{\pi/2}(\tau) = \Pi(\tau) \cdot \left(\cos\frac{A}{2}\tau + i \cdot p \cdot \sin\frac{A}{2}\tau\right), \tag{6.2}$$

see Sec. B.2.4 for derivation details. At $\tau_{SL} = 5\,\mu\text{s}$, corresponding to $\approx 1/(4A)$, we observe oscillations that match the strong coupling observed in Fig. 6.1(e), as expected. We extract $\tau_p = 2.5\,\mu\text{s}$ as the probe point that maximizes readout signal.

Fig. 6.3(d) demonstrates the direct probe of polarization coherently exchanged between the NV and P1 spins. The blue, filled in circles, show the NV population measured after Hartmann-Hahn polarization transfer (the leftmost panel in Fig. 6.3(a)) at $\Omega \approx 400\,\text{kHz}$, revealing resolvable coupling to the strongest coupled P1 spin. The orange, open circles, show the P1 polarization read through $S_{\pi/2}(\tau_p = 2.5\,\mu\text{s})$ for the same τ_{SL}, with $\tau_{delay} = 0\,\mu\text{s}$. These two curves are mirror images of each other; we observe that as polarization leaves the NV, it transfers to the P1. Probing at $\tau_p = 2.5\,\mu\text{s}$ ensures that $S_{\pi/2}$ is only sensitive to polarization on the strongly coupled P1; weaker coupled spins would contribute slower signals. We identify $\tau_{SL} = 5\,\mu\text{s}$ as the optimal spin locking time to maximize polarization transfer with a single polarization step.

In comparison to NV correlation measurements that have probed bath evolution, for example in diamond surface spins [72, 253], or used nuclear spin memories [224] to enhance spectral resolution, this P1 initialization and readout is not limited by the NV T_1 lifetime, as no signal is stored in the NV spin state. As long as the laser power is low enough such that the NV repolarization pulse does not disturb the P1 electron spin, τ_{delay} is only limited by signal collection at long measurement times. Essentially, the NV center is combined with appropriate microwave tones to enact the same deterministic polarization and spin-state probe that is routinely performed optically on the NV electron spin. We note that similar experiments have combined Hartmann-Hahn polarization transfer with a DEER probe on NV center-dark spin systems in diamond [139, 222], but these did not include the time-resolved delay component present here.

6.3.3 P1 electron spin depolarization

We now explore single P1 polarization loss with the measurement described in Sec. 6.3.2. We begin by considering intra-bath resonant flip-flop processes between the single P1 and surrounding bath spins as a potential loss mechanism. These processes have been proposed as the mechanism of spin-bath induced decoherence in NV centers [23] and are the basis for CCE computational methods.

To obtain an accurate comparison to experiment, we perform a semi-classical Fermi's Golden Rule simulation [302] of spin diffusion, where the rate of polarization transfer Γ_{ij} between any two bath spins is modified from the isolated dipolar coupling A_{ij} to $\Gamma_{ij} = A_{ij}^2 \frac{2\gamma}{\gamma^2+(\delta_i-\delta_j)^2}$, where γ is the intrinsic spin linewidth, approximated as $1/T_{2,NV}$, and δ_i is the detuning on a given bath spin. We simulate spin diffusion in our system with the spin configurations determined in Sec. 6.3.1. We evolve the system under couplings Γ_{ij} between spins and average over many trajectories with different initial thermal states, calculating δ_i directly from the spin bath state. We perform this simulation for initial NV states $|0\rangle$ and $|-1\rangle$, where the non-zero dipolar field produced by the second state induces an additional fixed detuning on the polarized spin of A_1, strong enough to suppress the Γ_{1j} to other bath spins and gap out spin diffusion. We present the results in Fig. 6.4(b), with the simulation trajectories shown in purple and blue for $|\text{NV}(t)\rangle = |0\rangle, |-1\rangle$, respectively, with the two-

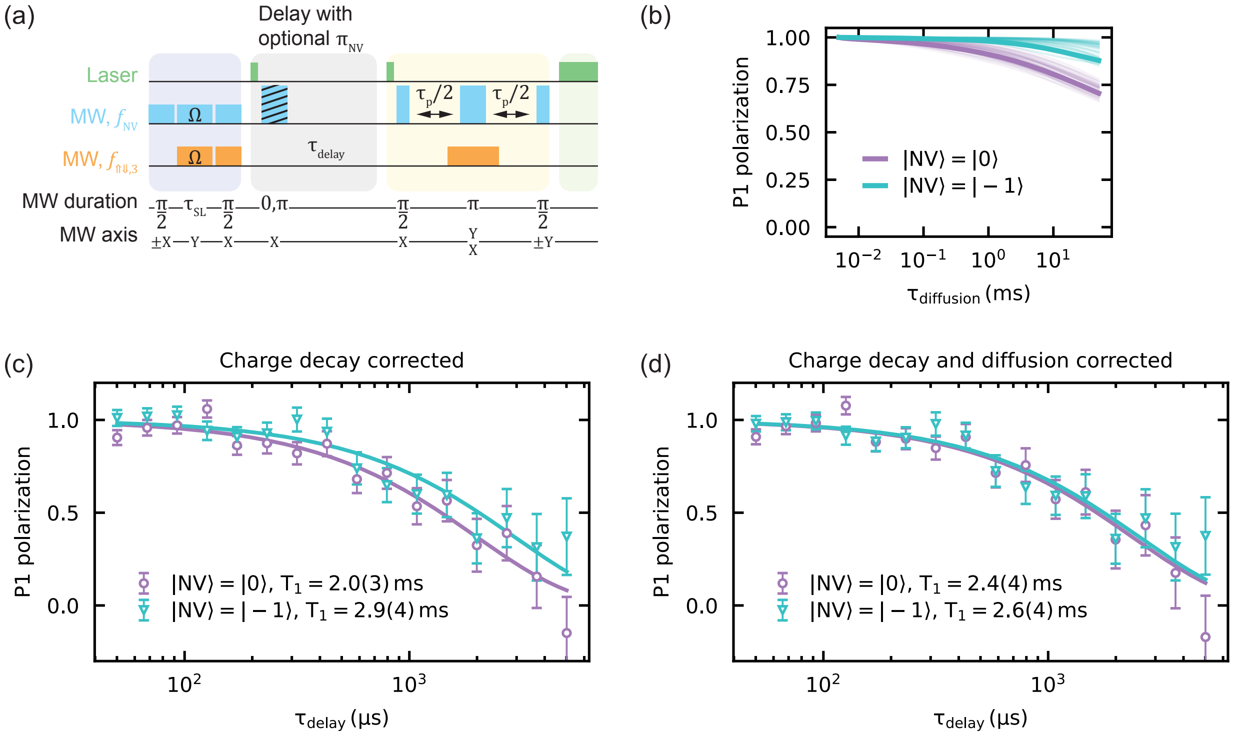

Figure 6.4: **P1 spin polarization decay.** (a) Pulse sequence for time-resolved polarization decay measurement on strongly coupled P1 electron spin. A π-pulse on the NV center is added to modify the static detuning of the P1 Larmor frequency. (b) Fermi's Golden Rule semi-classical simulations of spin diffusion out of the polarized central P1 spin for best-matched configurations data in Fig. 6.1(d) with the NV center in the $|m_s = 0\rangle$ and $|m_s = -1\rangle$ states. Best-fit is shown in bold trace. (c) Polarization decay of the P1 spin measured with the sequence in (a) for both NV spin states, corrected for charge decay observed in Fig. 6.2(b). (d) Polarization decay of the P1 spin measured with the sequence in (a) for both NV spin states, corrected for charge decay as well as background diffusion calculated for best-fit configuration in (b). We find $T_{1,P1} = 2.5(3)$ ms.

spin estimate shown as a dashed line. The simulations predicts polarization decay due to spin diffusion over tens of ms, and furthermore reveal that the A_1 gap strongly modifies the diffusion at timescales less than the NV T_1 time, see App. B.4.

In Fig. 6.4(c) we perform a T_1 measurement of the single P1 center with the sequence in Fig. 6.4(a), where τ_{delay} measures the free evolution time after the NV reinitialization laser pulse and optional π-pulse. After correcting for the background charge state decay, we find decay times of 2.0(3) ms and 2.9(4) ms for $|NV(t=0)\rangle = |0\rangle, |-1\rangle$, respectively, significantly shorter than the times predicted from flip-flop processes in Fig. 6.4(b), suggesting another source of polarization decay. Prior work has measured the ^{14}N P1 ensemble spin relaxation time via EPR measurements of bulk samples, finding room temperature relaxation times $\approx 2\,\mathrm{ms}$ [19, 77, 214, 291], in good agreement with our single P1 result. Prior works posit that the main depolarization mechanism arises from phonon-induced tunneling between P1 Jahn-Teller states accompanied by spin-orbit coupling.

We correct for the calculated slow diffusion by fitting the best-fit simulation in Fig. 6.4(b) to decay of the form $a \cdot e^{-(t/t_d)^n}$ to normalize our decay data, shown in 6.4(d). We recover a spin relaxation time $T_{1,P1} = 2.5(3)\,\mathrm{ms}$.

6.3.4 Bath spin T_1 limit to central spin T_2

Single spin-flips of nearby spins have recently been explored analytically [171] and experimentally (in the context of superconducting qubits) [125] as a source of central spin decoherence. In Fig. 6.5(a) we explore the finite spin lifetime of the P1 bath spins as a main source of decoherence in our system. We calculate the central spin coherence time with the analytical results in Ref. 125 for a range of $T_{1,P1}$ times for each bath configuration determined in Sec. 6.3.1 (the same shown in Fig. 6.4(b)).

We also calculate via CCE the intra-bath dynamics-limited coherence times for each configuration. $T_{1,P1} = 2.5\,\mathrm{ms}$ is marked off on the plot, predicting a range for T_2 of 545 µs to 740 µs, an order of magnitude smaller than the CCE prediction, and of 581 µs for the best-fit configuration. We measure a NV T_2 of 362(9) µs (Fig. 6.5(b)), which falls within a factor of 2 of the predicted range. Accounting for finite spin lifetimes of bath spins produces a more accurate prediction of central spin decoherence compared to current methods [196]. This suggests that the finite room temperature $T_{1,P1}$ bath spins may be a dominant source of NV center decoherence, a prospect not previously explored for NV center systems. The relevant physics, however, has been previously described in the literature [109, 138] and explored in oxide [176, 177] and silicon systems [266].

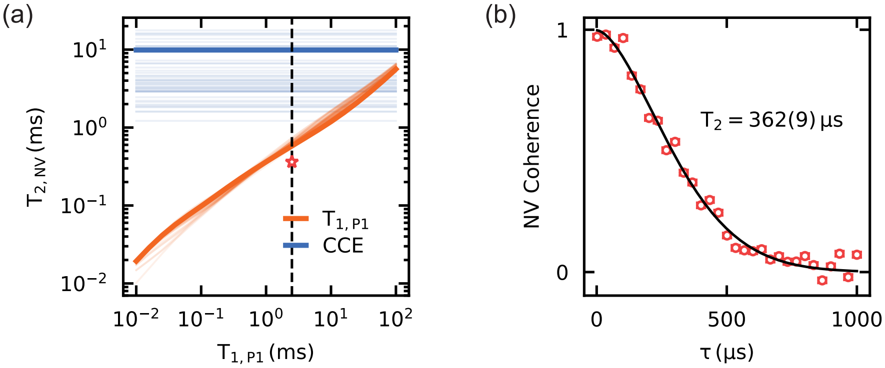

Figure 6.5: **P1 T_1 limit to NV T_2.** (a) Calculation of NV center $T_{2,NV}$ times limited by P1 single spin-flips (orange), characterized by the $T_{1,P1}$ time, and CCE bath interaction-limited T_2 (blue) calculated for each spin bath configuration determined in Sec. 6.3.1. (b) Single NV Hahn echo coherence. The T_2 time marked by the red star in (a) at $T_{1,P1}$ determined in Sec. 6.3.3.

We now combine theoretical results from Ch. 5 with the theoretical estimate for bath spin lifetime-limited coherence [266, 279] of

$$T_2(T_{1,P1}) \approx (2\pi T_2^* \cdot T_{1,P1})^{1/2} \tag{6.3}$$

to explore spin bath geometry and density regimes where the P1 lifetime is relevant for NV center coherence. In Fig. 6.6(a) we plot T_2 versus [N], as measured in Ref. 23, both with and without the low-density plateau, alongside the calculated T_2 from Eq. (6.3) based on the measured T_2^* values in Ref. 23. We find that the bath spin lifetime is only limiting for three-dimensional densities below around 16 ppb. In Fig. 6.6(b) we calculate T_2 from Eq. (6.3), inputting calculated T_2^* values from Ch. 5 and $T_{1,P1}$ measured in Sec. 6.3.3. We normalize this value by the coherence times calculated in Ch. 5 via CCE, denoted $T_{2,CCE}$. We find that the bath spin lifetime limits coherence up to a much higher density, >10 ppm, in low- and quasi-low-dimensional spin baths. Note that the T_2^* calculations in Ch. 5 exclude strongly coupled spins (see Sec. 5.4.1) and thus the calculated $T_2(T_{1,P1})$ is likely overestimated.

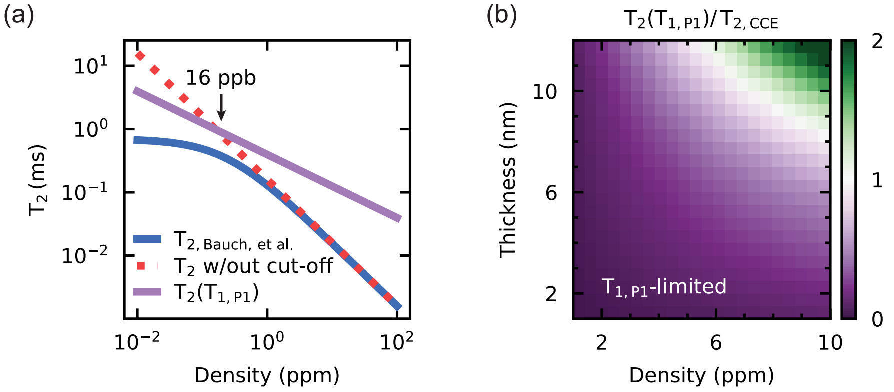

Figure 6.6: **P1 T_1 limit to NV T_2, modelling.** (a) Comparison between measured [23] T_2 coherence times in bulk N spin baths and expected limit from $T_{1,P1}$ in the same systems. (b) Comparison between $T_{1,P1}$-limited and CCE (intra-bath interactions)-limited T_2 times based on modelling in Ch. 5.

6.3.5 Depolarization under laser illumination

We now apply the technique from Sec. 6.3.2 to measure P1 decay in the presence of green illumination, ubiquitous in NV center measurements. The pertinent components of the measurement are shown in the sequence in Fig. 6.3(a) with a variable-power illumination during the delay window. As in Fig. 6.4 we measure the spin polarization, although we highlight here that this signal is also sensitive to the charge state. In Fig. 6.7(b) we show time-traces of P1 decay at powers ranging from 0.1 mW to 6.6 mW, covering the range of typical off-resonant laser powers employed in NV ODMR-based experiments. Fig. 6.7(c) shows the extracted mono-exponential decay rates Γ_{P1} at each laser power. These data exhibit saturation behavior; we fit Γ_{P1} to a saturation curve $\Gamma_{P1}(P) = 2\Gamma_{sat}\frac{P}{P+P_{sat}}$ for rate Γ_{sat} at saturation power P_{sat}. We find saturation at $P_{sat} = 2\,\text{mW}$, likely arising from saturation of surrounding charge traps.

Ionization is expected to play a dominant role in the observed decay, as the 2.3 eV laser energy is larger than the depth of the P1 electron level in the diamond bandgap ($\approx 2\,\text{eV}$). Assuming ionization is the only relevant process, i.e., the spin polarization persists until the electron is ionized and subsequently captured by a nearby charge trap or decayed through

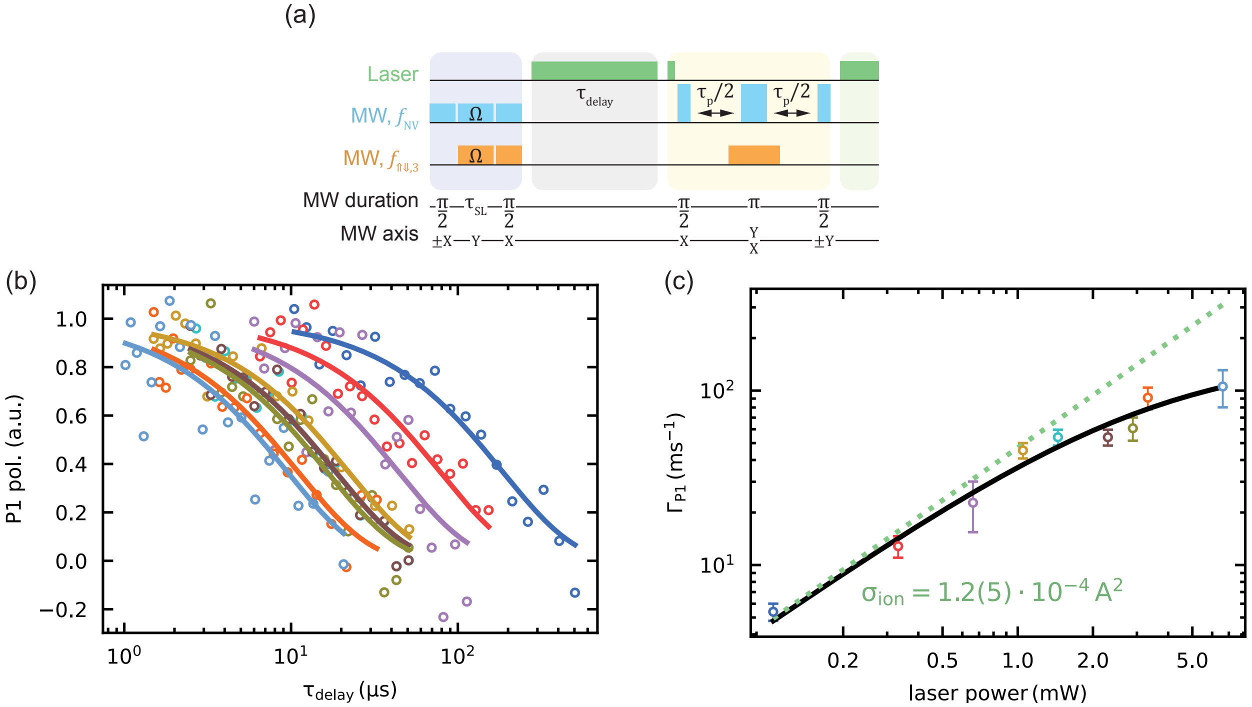

Figure 6.7: **P1 decay under illumination.** (a) Pulse sequence for time-resolved decay under green illumination. After P1 spin initialization, the laser is turned on for variable time τ_{delay}, after which the $S_{\pi/2}$ probe is performed. The reset laser pulse at the end is fixed at a power-dependent time long enough to fully decay the P1. (b) P1 polarization decay under range of laser powers (color-coded in (c)), with mono-exponential fits overlaid. (c) Γ_{P1} decay rates extracted from (b) versus laser power, with saturation fit in black and low-power linear fit in dashed green.

conduction band scattering processes, we extract an ionization cross section from the low-power data in Fig. 6.7(b) of $\sigma_{ion} = 1.2(5) \times 10^{-4}\,\mathrm{A}^2$, similar to prior work in ensemble measurements [67, 113] (see App. B.6 for calculation details). These measurements demonstrate that the P1 spin polarization persists under illumination beyond the times usually employed to reinitialize the NV center spin state. This separation of timescales enables the polarization measurements presented in this work.

6.4 Discussion

Central spin decoherence arises from evolution of the surrounding spin bath, which is in turn composed of both single spin and multi-spin interactions. Here we have presented, to our knowledge, the first study of single P1 spin relaxation mechanisms room temperature, highly relevant for NV center quantum sensing applications. Specifically, we have leveraged a method to initialize and probe the P1 electron spin to enable arbitrary microwave and optical excitation on both the NV and P1 spin systems. This allowed us to shift the local dipolar field at the strongly coupled P1 spin, in Sec. 6.3.3, and to study spin depolarization under optical illumination in Sec. 6.3.5, measurements that are not possible under similar time-resolved correlation studies of bath dynamics.

Under certain spin bath conditions, such as those relevant for single NV center and thin ensemble synthesis, we have shown that at room temperature, intra-bath flip-flops are not the dominant mechanism for bath spin dynamics. This motivates a modification to both theoretical and experimental studies of central spin decoherence. From a modeling perspective, we have shown that it is necessary to include a Γ_1 spin-flip rate for each bath spin independent of spin bath density and geometry. Specifically, we demonstrated that the inclusion of Γ_1 accounts for the mismatch between prior T_2 coherence time calculations and measurements in low-density spin baths [110, 201]. This also suggests that, in low-density spin baths, central spin coherence times should improve at lower temperatures as Γ_1 is reduced [214, 291].

We note that the polarization and probe technique in Sec. 6.3.2 does not depend on the nature of the target electron spin as long as the NV-target coupling can be resolved above background decoherence. This may thus be applied to study electron spins external to the diamond lattice with near-surface NV centers. Considering the strong coupling condition presented in Ch. 5 $A \geq 2\pi/T_2$, a single spectrally isolated electron spin may be polarized and probed with a NV center near the (100) diamond face given sufficient geometry.

In Fig. 6.8 we study the dependence of the maximum NV-target spin distance, and specifically the height h of the target above the diamond surface, for a NV center at a given depth d and a maximum dynamically decoupled coherence time $T_{2,DD}$. As a function of $T_{2,DD}$ and $\theta_{B,r}$, the angle between the magnetic field $\mathbf{B}$ and the NV-target vector $\mathbf{r}$,

$$h(T_{2,DD}, \theta_{\mathbf{B},\mathbf{r}}) = \left(\frac{\mu_0}{4\pi} \frac{\gamma_e^2 \hbar T_{2,DD}}{2\pi} \frac{\left|1-3\cos^2\theta_{\mathbf{B},\mathbf{r}}\right|}{2} \right)^{1/3} \cdot \left|\sin(\theta_{111} + \theta_{\mathbf{B},\mathbf{r}})\right| - d, \tag{6.4}$$

where μ_0 is the magnetic constant, γ_e is the electron gyromagnetic ratio, and θ_{111} is the angle that the NV axis and the magnetic field (assumed to be parallel) make with the plane of the diamond surface, shown schematically in the bottom part of Fig. 6.8. In the top of Fig. 6.8, we plot the positions of the furthest strongly coupled electron spin for a given maximum coherence time, where the colormap labels $T_{2,DD}$, such that spins at positions closer to the diamond surface are also strongly coupled. We set $d = 12\,\text{nm}$ for the calculation, following measurements in Ref. 230 of a 12 nm NV with maximum $T_{2,DD} = 600\,\mu\text{s}$ with 51 π-pulses after an oxygen anneal surface treatment. For these NV properties, strong coupling should be possible for external electron spins ≈20 nm away. This calculation assumes that the target electron spin is spectrally isolated from the dominant spin noise source, enabling DEER measurements that do not interact with the dominant source.

Polarization- and time-resolved probes of external target spins will enable measurements of the spin dynamics of surface spins [72, 215] and in spin-labelled molecules [232, 293]. Diamond surface functionalization [1, 281] would enable these studies in confined systems with an a priori structure, in contrast to stochastic spin baths. Furthermore, external electron spins may act as reporter spins that probe a nearby spin system that is not strongly coupled to the NV center [253, 296]. In this case the target electron may further polarize and measure a surrounding nuclear spin environment, as in Ref. 122.

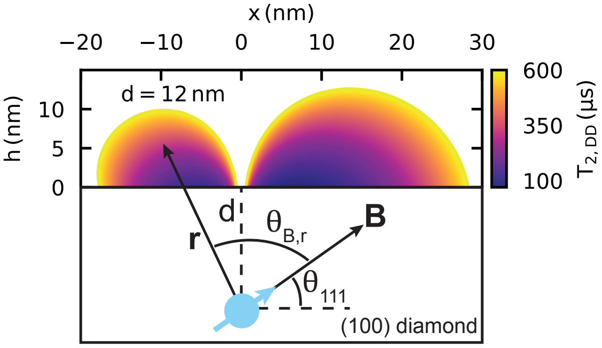

Figure 6.8: **Strong coupling to external electron spin.** For a given maximum coherence time $T_{2,DD}$, color-coded, the top plot shows the contour of furthest positions where strong coupling between a 12 nm NV center and external electron spin is achievable. The bottom schematic shows the geometry for Eq. (6.4).

APPENDIX A

SUPPLEMENTAL NUMERICAL RESULTS

A.1 Cluster correlation expansion

A.1.1 High-field limit

Calculations are performed for a 50 G field, while NV measurements are at 311 G. A main concern for CCE calculations is if the electron spins are in the high-field limit relative to other energy scales. In our case, the dipolar coupling between electron spins is the next highest energy scale after the Larmor frequency (the nuclear hyperfine, at ≈3 MHz, is not considered in CCE and is not relevant for NV decoherence in our measurements). The lowest P1 Larmor frequency at 50 G is 64 MHz. At the densities considered in this work, the smallest average spin-spin distance is 4.3 nm (12 ppm), corresponding to a dipolar coupling of ≈645 kHz, two orders of magnitude smaller than the Larmor frequency. Even accounting for variation in spin-spin position, the Larmor frequency is the dominant energy scale and 50 G is already in the high-field limit for our system. We thus expect no difference in CCE calculations at the two field values.

A.1.2 CCE order convergence

We evaluate convergence in a 10 ppm, 5 nm P1 spin bath, although the convergence holds over our simulated range.

We run Hahn echo simulations on a single NV and extract decay times for CCE-2 to CCE-5, presenting the average coherence time in Fig. A.1(a). Calculations converge at order 4. All Hahn echo simulations in the main text are performed at order 4. Fig. A.1(b) shows that Ramsey simulations are consistent across all orders, indicating the NV decoherence is dominated by dipolar coupling with single bath spins. These data are the ensemble averaged times for many NV centers, with the spread of results shown as background shading.

A.1.3 Convergence with number of spins

In this section we look at the number of spins necessary to converge our calculations, as well as draw interesting conclusions about NV-bath measurements. In Fig. A.1(c), T_2 convergence for a single NV is plotted versus the number of bath spins. We find convergence at N_{T_2} =100 spins, setting a lower bound for all simulations in the main text. In Fig. A.1(d), T_2^* converges at $N_{T_2^*}$ =10 spins, setting a lower bound for Ramsey results in the main text.

This convergence is more than a computational exercise. This also reveals the number of bath spins necessary to fully capture the central spin coherence, with physical meaning. First, we can intuitively see why $N_{T_2} = N_{T_2^*}^2$. From the T_2^* convergence, we conclude that the NV signal is dominated by dipolar coupling to 10 bath spins. Heuristically, T_2 will be sensitive to fluctuations in these coupling strengths, a direct result of fluctuations in the energy, or the linewidth, of each bath spin. The T_2^* convergence already tells us the linewidth depends on the coupling to 10 nearby spins, so we can claim that the 10 spins nearby the NV are further influenced by the 10 spins closest to each of them, and arrive at a total of 100 spins necessary to describe Hahn echo decoherence.

A.2 Analytical and computational coupling ratio comparison

In Ch. 5 Sec. 5.3.6 we calculate in Eq. (5.7) that the coupling ratio for the nearest bath spin should be $\sqrt{2}$ larger in a two-dimensional bath compared to a three-dimensional bath. We then use numerical simulations to analyze the incidence of strongly coupled systems. In Fig. A.2 we present the calculated ratios and show approximate agreement with the analytical result. Fig. A.2(a) presents the same calculated distributions as in Fig. 5(a) for a 3 ppm bath. In Fig. A.2(b) we scale the coupling ratios in the 2D bath (at 3 ppm) by $1/\sqrt{2}$, in accordance with the prediction in Eq. (6). The distributions do not overlap exactly, but

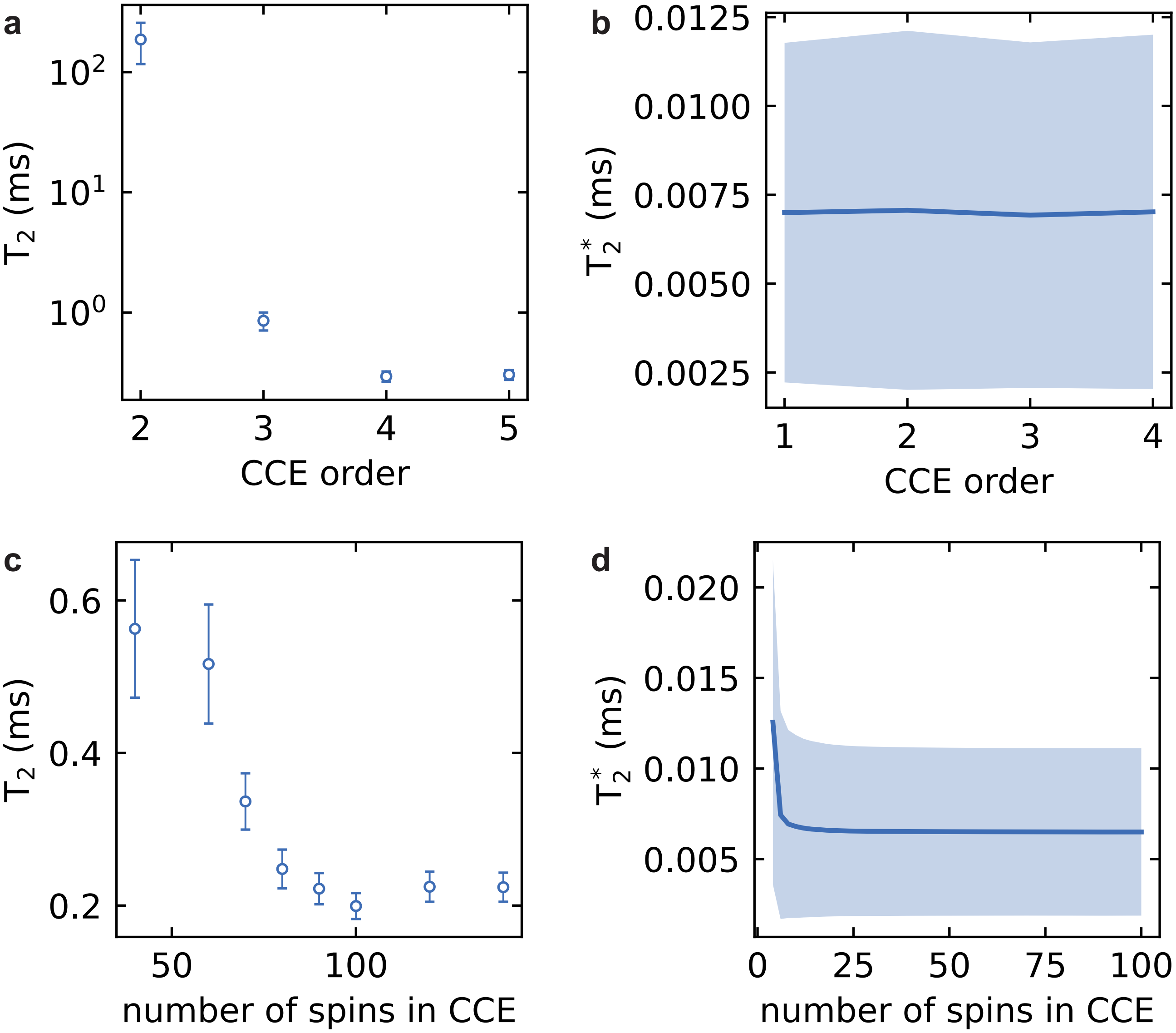

Figure A.1: **CCE convergence.** Convergence of T_2 coherence time CCE calculations versus CCE order (a) and number of simulated bath spins (b).

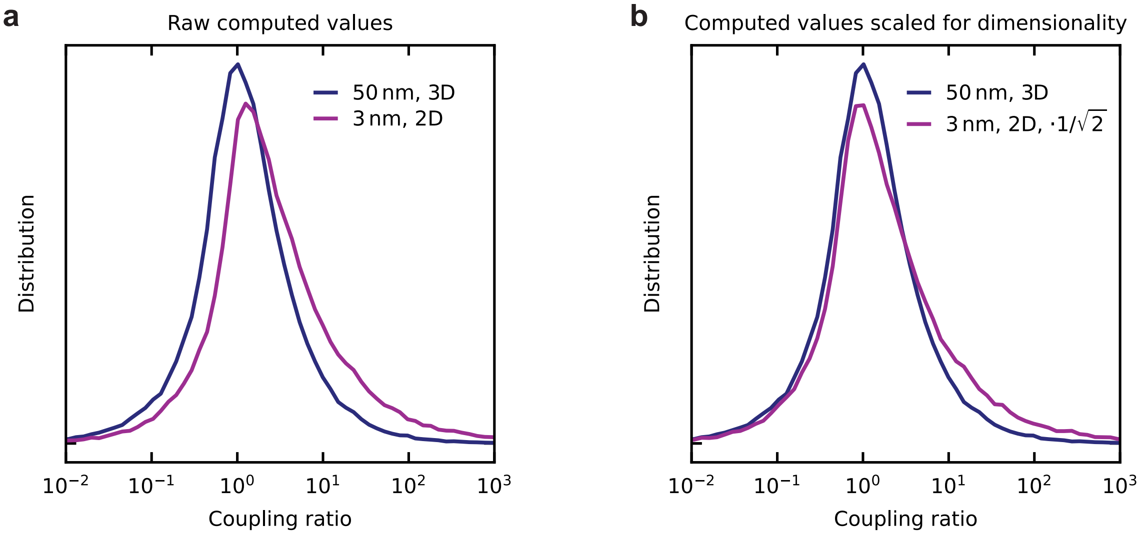

Figure A.2: **Coupling distribution versus dimensionality.** (a) Calculated coupling distributions at 3 ppm for 3 nm and 50 nm baths. (b) Same data as in (a), but the coupling ratios for the 2D bath (3 nm are scaled by $1/\sqrt{2}$).

we do find agreement in the peak ratio positions (the most likely values), providing a point of comparison between the analytical and numerical approaches.

APPENDIX B

SUPPLEMENTAL P1 RELAXATION RESULTS

B.1 NV nuclear spin polarization

Fig. B.1 shows the pulsed ODMR spectrum of the NV center taken with a gaussian-shaped π-pulse, with two peaks corresponding to the ±1/2 nuclear spin states of the ^{15}N. The nuclear spin polarization is calculated as $I_{15} = |d_1 - d_2|/(d_1 + d_2)$ where d_i is the contrast depth of each peak. The polarization of $I_{15} = 69\%$ corresponds to less than 0.5° misalignment between the magnetic field and the NV axis.

B.2 DEER ESR detection

Conventional electron spin resonance (ESR) measures the resonant absorption of a spin transition of a paramagnetic sample. In the precense of an external dc magnetic field, resonant microwaves excite spin precession in a microwave cavity, which is detectable due to the un-balanced population between the two spin levels, or the thermal polarization [134]. In the absence of polarization no energy is absorbed and there is no ESR signal.

The NV center is a nanoscale ESR detector through double electron-electron resonance

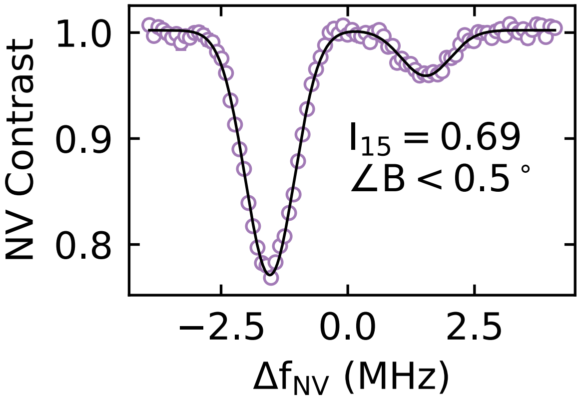

Figure B.1: **NV hyperfine spectrum.** Pulsed ODMR measurement of NV showing nuclear spin splitting and polarization of $I_{15} = 69\%$.

(DEER). Rather than absorption, the NV electron spin detects nearby spins through their effect on the NV coherence. The NV acquires a phase $\phi = \gamma B \tau$ from the magnetic field B of the environment during a measurement of length τ, where γ is the electron gyromagnetic ratio. When we average many NV measurements, we average this quantity to recover the observed NV decoherence

$$\left\langle e^{i\phi} \right\rangle = e^{-\langle \phi^2 \rangle /2}, \tag{B.1}$$

where the signal ultimately depends on $\left\langle \phi^2 \right\rangle$. This is in contrast to a conventional ESR measurement, which depends on $\langle B \rangle \propto \langle \phi \rangle$. These different averages amount to the mean and standard deviation of the field produced by target spins. In section B.2.1 we derive these quantities thermodynamically.

DEER-ESR with a Hahn echo NV measurement is shown in Fig. B.2. A given (in general random) configuration of electron spins decoheres the central NV spin through electron-electron dipolar interactions. Interactions with a resonant species are isolated by simultaneously inverting the NV spin and the target spins, the so-called double resonance.

We can consider our central NV spins $\hat{\mathbf{S}}$ and environment spins $\hat{\mathbf{I}}_i$, which we can break into target spins $\hat{\mathbf{I}}_{t,i}$ and other spins $\hat{\mathbf{I}}_{o,i}$. In the first free evolution window in Fig. B.2, the NV evolves according to interactions

$$\hat{\mathcal{H}}_{SI,1} = \sum_i \hat{\mathbf{S}} \cdot \hat{\mathbf{I}}_{t,i} + \sum_j \hat{\mathbf{S}} \cdot \hat{\mathbf{I}}_{o,j}. \tag{B.2}$$

After inverting the central and target spins, the NV evolves in the free second evolution window under

$$\hat{\mathcal{H}}_{SI,2} = \sum_i (-\hat{\mathbf{S}}) \cdot (-\hat{\mathbf{I}}_{t,i}) + \sum_j (-\hat{\mathbf{S}}) \cdot \hat{\mathbf{I}}_{o,j}. \tag{B.3}$$

We see that interactions with the target spins proceed as if there were no inversion, and interactions with the other spins are reversed and effectively cancelled for equal evolution

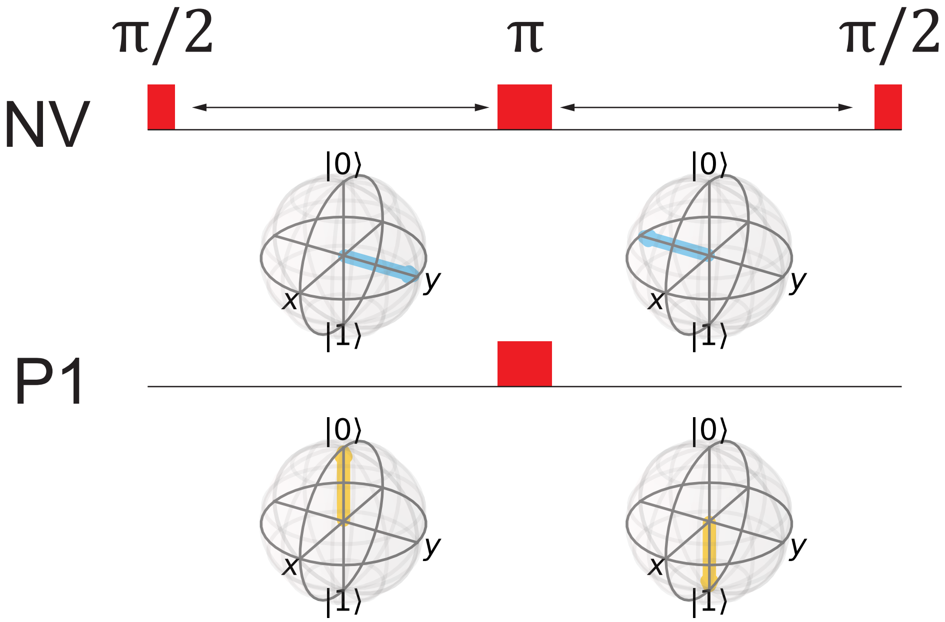

Figure B.2: **DEER measurement sequence.** The NV is initialized to a superposition on the Bloch sphere equator, while the other spin, in our case a P1 center electron spin, is in an eigenstate. When the NV center is flipped with a π pulse, the P1 spin is also flipped, negating any reversal of the NV-P1 interaction.

times (they are "echoed out"). This analysis shows no dependence on average polarization, only on a quasi-static (slower than a single measurement window) random configuration of up and down spins, which can change from measurement to measurement.

B.2.1 Thermal and statistical polarization

Electron spin level separations tend to be in the MHz-GHz range, and spin levels are populated according to a Maxwell-Boltzmann distribution. In the high temperature limit of $\beta\gamma B_z \ll 1$, where $\beta \equiv 1/T$ and γB_z is the electron Zeeman energy. This results in a rather small thermal polarization in the system, given by

$$P_{therm} = \frac{1}{3}\beta\gamma B_z(S+1) \tag{B.4}$$

for a spin-S system. At typical operating conditions, $P_{therm} \approx 10^{-4}$. Measuring the average magnetization of the target system, $\langle S_z \rangle$ amounts to measuring this thermal polarization. However, as noted in section B.2, an NV DEER measurement is sensitive to $\left\langle S^2 \right\rangle$, the fluctuations in the magnetization. This is termed the statistical polarization, given by

$$P_{stat} = \sqrt{\frac{S+1}{3S}\frac{1}{N}} \tag{B.5}$$

for a system of N spins. These fluctuations are larger in smaller systems. In section B.2.2 we determine how many bath spins participate in our DEER measurements and calculate P_{stat} for the system.

We now derive Eqs. B.4 and B.5, following Slichter [244]. $\hbar = k_B = 1$ in the following. We begin with the partition function

$$Z = \sum_n e^{-\beta E_n}, \tag{B.6}$$

where E_n is the energy of each level in the system. E_n is given by the Zeeman Hamiltonian for a single spin

$$\hat{\mathcal{H}}_z = -\gamma B_z \hat{S}_z. \tag{B.7}$$

We are generally in the high temperature limit where $\beta \hat{\mathcal{H}}_z \ll 1$. In this limit we can reduce the partition function to

$$\begin{aligned} Z &\approx \textstyle\sum_{S_z=-S}^{S}(1+\gamma B_z S_z) \\ &= 2S+1, \end{aligned} \tag{B.8}$$

as the terms linear in S_z cancel. With the density matrix

$$\hat{\rho} = \frac{1}{Z} e^{-\beta \hat{\mathcal{H}}_z}, \tag{B.9}$$

physical quantities can be computed. The magnetization for an N-spin system is given by

$$\langle M_z \rangle = N \mathrm{Tr}[\hat{S}_z \hat{\rho}] = \frac{N}{Z} \mathrm{Tr}\left[S_z e^{-\beta \hat{\mathcal{H}}_z} \right]. \tag{B.10}$$

In the high temperature limit we expand the exponential and use $\mathrm{Tr}[\hat{S}_z] = 0$ to arrive at

$$\begin{aligned} \langle S_z \rangle &= \tfrac{1}{Z} \mathrm{Tr}[\hat{S}_z (1 - \beta \hat{\mathcal{H}}_z + \cdots)] \\ &\approx \tfrac{1}{Z} \mathrm{Tr}[\gamma^2 \beta B_z \hat{S}_z^2]. \end{aligned} \tag{B.11}$$

Plugging in $Z = 2S+1$ and $\mathrm{Tr}[\hat{S}_z^2] = \frac{1}{3} S(S+1)(2S+1)$, we arrive at the thermal polarization

$$P_{therm} \equiv \frac{\langle M_z \rangle}{\gamma N S} = \frac{1}{3} \gamma \beta B_z (S+1), \tag{B.12}$$

where $\gamma N S$ is the total fully polarized magnetization. We can likewise calculate the standard deviation for an N-spin system.

$$\sigma_{M_z}^2 = \sum_N \sigma_{S_z}^2 = N \sigma_{S_z}^2, \tag{B.13}$$

where

$$\sigma_{S_z} = \sqrt{\langle S_z^2 \rangle - \langle S_z \rangle^2}. \tag{B.14}$$

As $\langle S_z \rangle^2 \propto \beta^2$, we can take it to zero and calculate

$$\begin{aligned} \langle S_z^2 \rangle &= \mathrm{Tr}[\hat{S}_z^2 \hat{\rho}] \\ &= \tfrac{1}{Z} \mathrm{Tr}\left[\hat{S}_z^2 e^{-\beta \hat{\mathcal{H}}_z} \right] \\ &\approx \tfrac{1}{Z} \mathrm{Tr}[\hat{S}_z^2], \end{aligned} \tag{B.15}$$

where the last line is the highest order term. Using the same expressions from above, we define the statistical polarization as the fluctuations

$$P_{stat} \equiv \frac{\sigma_{M_z}}{\gamma N S} = \sqrt{\frac{S+1}{3S}\frac{1}{N}}. \tag{B.16}$$

For our spin-1/2 system of interest,

$$\begin{aligned} P_{therm} &= \tfrac{1}{2}\beta\gamma B \\ P_{stat} &= 1/\sqrt{N}. \end{aligned} \tag{B.17}$$

B.2.2 Polarization and spin estimate

In PyCCE convergence calculations in App. A, we find that the number of spins probed in a Ramsey-style measurement is around 10. From this we calculate statistical fluctuations of $P_{stat} = 1/\sqrt{10}$ in a DEER measurement.

B.2.3 Polarized DEER signal

We experimentally probe a system where the NV is strongly coupled to a single P1 above the background P1-induced decoherence. The NV coherence in this system with no net polarization is given by $L = \Pi(\tau)\cos\frac{a}{2}\tau$, for NV-P1 coupling a and measurement time τ. $\Pi(\tau)$ is a function capturing the background decoherence. When the P1 is polarized with some polarization p, the NV coherence is $L = \Pi(\tau)\left[\cos\frac{a}{2}\tau + i \cdot p \sin\frac{a}{2}\tau\right]$. This result is critical to our polarization measurement. A polarization of the coupled spin imparts an extra, imaginary coherence to the NV spin, directly proportional to the polarization. Experimentally, we predict maximum readout fidelity for measurement time τ such that

$$\frac{a}{2}\tau = \frac{\pi}{2}(2k+1). \tag{B.18}$$

Accounting for background decoherence, we will measure at the first peak, $\tau_p = \frac{1}{2a}$. Assuming some fitted decoherence function $\Pi(t)$, we can normalize the measured L_y to obtain a quantitative polarization of

$$p_{exp} = \frac{L_y(\tau_p)}{\Pi(\tau_p) \cdot L_x(0)}. \tag{B.19}$$

Below, we derive the DEER signal.

B.2.4 Analytical derivation of DEER signal

In the pure dephasing regime the Hamiltonian of a NV center interacting with a single bath spin can be written as:

$$\hat{\mathcal{H}} = \hat{\mathcal{H}}_0 \otimes |0\rangle \langle 0| + \hat{\mathcal{H}}_1 \otimes |1\rangle \langle 1| \tag{B.20}$$

Where $\hat{\mathcal{H}_i}$ is a bath spin Hamiltonian, conditioned on the NV state i:

$$\hat{\mathcal{H}}_0 = \omega \hat{S}_z, \quad \text{and} \quad \hat{\mathcal{H}}_1 = (w + a)\hat{I}_z + b\hat{I}_x \tag{B.21}$$

Where $\hat{I}_\alpha$ are bath spin operators, ω is the bath spin larmor frequency, a and b are coupling parameters.

The coherence of the NV can be then expressed in terms of the evolution of the bath spin:

$$L(t) = \mathrm{Tr}[\hat{\rho} \hat{V}_1^\dagger \hat{V}_0] \tag{B.22}$$

Where $\hat{\rho}$ is a density matrix of the bath spin, and propagators $\hat{V}_0$, $\hat{V}_1$ are defined in terms of the Hamiltonians from Eq. (B.21). In the DEER-type of measurement, the π pulse is applied simultaneously to the bath spin and the central spin, thus the propagators can be written as:

$$\hat{V}_0 = e^{-i\hat{\mathcal{H}}_1 \tau/2} \hat{R}_x(\pi) e^{-i\hat{\mathcal{H}}_0 \tau/2}, \tag{B.23}$$

and

$$\hat{V}_1 = e^{-i\hat{\mathcal{H}}_0\tau/2}\hat{R}_x(\pi)e^{-i\hat{\mathcal{H}}_1\tau/2} \tag{B.24}$$

Where $\hat{R}_x(\pi) = -2i\hat{I}_x$ is a rotation operator acting on the bath spin and τ is the measurement time.

Using this definition, for the completely unpolarized bath spin ($\hat{\rho}_0 = \frac{1}{2}\mathbb{I}$) we recover the following expression for the coherence of the central spin:

$$L_0(\tau) = \frac{k_x^2}{2}\left(1 - \cos\frac{\theta_1}{2} + \cos\frac{\theta_0}{2}\right) + (1 - \frac{k_x^2}{2})\cos\frac{\theta_0}{2}\cos\frac{\theta_1}{2} + k_z \sin\frac{\theta_0}{2}\sin\frac{\theta_1}{2}, \tag{B.25}$$

where $\theta_0 = \omega\tau$, $\theta_1 = \tau\sqrt{(\omega+a)^2+b^2}$ are bath spin precession angles, and $k_x = \frac{b}{\sqrt{(\omega+a)^2+b^2}}$, $k_z = \frac{\omega+a}{\sqrt{(\omega+a)^2+b^2}}$ define tilt of the precession axis. Notice that the coherence is real, thus the $\langle\hat{S}_y\rangle$ signal of the central spin is strictly zero.

We define the density matrix for the polarized bath spin as:

$$\hat{\rho}_p = \frac{1}{2}\mathbb{I} - p\cdot\hat{I}_z. \tag{B.26}$$

Then the NV coherence becomes complex

$$L(\tau) = L_0(\tau) + i\cdot p\cdot(\frac{k_x^2}{2}\sin\frac{\theta_0}{2} + (1 - \frac{k_x^2}{2})\sin\frac{\theta_0}{2}\cos\frac{\theta_1}{2} - k_z\cos\frac{\theta_0}{2}\sin\frac{\theta_1}{2}) \tag{B.27}$$

The equation is significantly simplified in the large magnetic field limit ($\omega \gg a, b$). In this case, $k_x \approx 0$, $k_z \approx 1$ and we recover:

$$L(\tau) = \cos(\frac{\theta_0 - \theta_1}{2}) + i\cdot p\cdot\sin(\frac{\theta_0-\theta_1}{2}) \approx \cos\frac{a}{2}\tau + i\cdot p\cdot\sin\frac{a}{2}\tau. \tag{B.28}$$

B.3 NV-P1 dipolar coupling

Here we provide a detailed derivation for the Hamiltonian of the system consisting of NV and neighboring P1 centers. The total system Hamiltonian can be generally written as the sum of intrinsic NV and P1 Hamiltonians, as well as their interaction, as

$$\hat{\mathcal{H}}_{\text{sys}} = \hat{\mathcal{H}}_{\text{NV}} + \hat{\mathcal{H}}_{\text{P1}} + \hat{\mathcal{H}}_{\text{int}}. \tag{B.29}$$

We first consider the NV-P1 interaction Hamiltonian $\hat{H}_{\text{int}}$, which is given by the dipolar coupling. Thus, we can express $\hat{H}_{\text{int}}$ in terms of the NV (P1) vector spin operators $\hat{\mathbf{S}}$ ($\hat{\mathbf{P}}$), and the distance vector $\mathbf{r} \equiv r\mathbf{e}_r$ that connects NV to the P1 spin, i.e., we have

$$\hat{\mathcal{H}}_{\text{int}} = \frac{\mu_0 \gamma_{\text{e}}^2}{4\pi r^3} \left[\hat{\mathbf{S}} \cdot \hat{\mathbf{P}} - 3 \left(\hat{\mathbf{S}} \cdot \mathbf{e}_r \right) \left(\hat{\mathbf{P}} \cdot \mathbf{e}_r \right) \right]. \tag{B.30}$$

For convenience, we choose the quantization axis such that the local NV (P1) eigenbasis are $\hat{S}_z$ ($\hat{P}_z$) eigenstates. Thus, the local NV and P1 Hamiltonians are given by

$$\hat{\mathcal{H}}_{\text{NV}} = \Delta \hat{S}_z^2 + \omega_{\text{NV}}^{(0)} \hat{S}_z, \quad \hat{\mathcal{H}}_{\text{P1}} = \omega_{\text{P1}} \hat{P}_z. \tag{B.31}$$

Note that under this convention, the quantization axes for different spins in general correspond to different geometrical axes. More specifically, we can introduce a different unit vector $\mathbf{e}_z^{(\text{NV})}$ ($\mathbf{e}_z^{(\text{P1})}$) for each spin Pauli z operator, as

$$\hat{S}_z = \hat{\mathbf{S}} \cdot \mathbf{e}_z^{(\text{NV})}, \quad \hat{P}_z = \hat{\mathbf{P}} \cdot \mathbf{e}_z^{(\text{P1})}. \tag{B.32}$$

We are interested in the regime where NV and P1 spin transition frequencies are highly off-resonant, which formally requires that

$$|\omega_{\mathrm{NV}} - \omega_{\mathrm{P1}}| \gg J(r) \equiv \frac{\mu_0 \gamma_{\mathrm{e}}^2}{4\pi r^3}. \tag{B.33}$$

Note that with typical values of magnetic field, the LHS is greater than 100 MHz, whereas the dipolar coupling strength $J(r)$ for randomly distributed P1 spins with density of order 1 ppm concentration is predominantly smaller than 100 kHz. In this regime, we can further simplify the NV-P1 interaction term $\hat{\mathcal{H}}_{\mathrm{int}}$, as any interaction-induced spin flips will be highly off-resonant and hence strongly suppressed. We can now apply the standard rotating wave approximation, so that in the rotating frame defined with respect to the local NV and P1 Hamiltonians, the NV-P1 interaction can be approximated as

$$\hat{\mathcal{H}}_{\mathrm{int}}^{(\mathrm{RWA})} = \frac{\mu_0 \gamma_{\mathrm{e}}^2}{4\pi r^3} \hat{S}_z \hat{P}_z \left[\mathbf{e}_z^{(\mathrm{NV})} \cdot \mathbf{e}_z^{(\mathrm{P1})} - 3 \left(\mathbf{e}_z^{(\mathrm{NV})} \cdot \mathbf{e}_r \right) \left(\mathbf{e}_z^{(\mathrm{P1})} \cdot \mathbf{e}_r \right) \right]. \tag{B.34}$$

In the specific case where the NV and P1 spin quantization axes are parallel to each other, we can further simplify Eq. (B.34) via the angle set by the quantization axis and the real space NV-P1 vector $\vec{r}$, so that we obtain

$$\hat{H}_{\mathrm{int}}^{(\mathrm{RWA})} = \frac{\mu_0 \gamma_{\mathrm{e}}^2}{4\pi r^3} \hat{S}_z \hat{P}_z \left(1 - 3\cos^2 \phi \right), \quad \cos\phi = \mathbf{e}_z^{(\mathrm{NV})} \cdot \mathbf{e}_r. \tag{B.35}$$

For convenience, we denote this parallel component of dipolar coupling as A_{zz} in the main text and in what follows, so that Eq. (B.34) can be rewritten as

$$\hat{H}_{\mathrm{int}}^{(\mathrm{RWA})} = A_{zz} \hat{S}_z \hat{P}_z. \tag{B.36}$$

B.3.1 NV-P1 Hamiltonian with spin locking drives

For the purpose of our discussion, we can view the NV as a spin-1/2 with transition frequency ω_{NV}. Following discussion on Eq. (B.36), the total system Hamiltonian under the rotating frame approximation can be written as

$$\hat{\mathcal{H}}_0^{(\text{RWA})} = \omega_{\text{NV}}\hat{S}_z + \omega_{\text{P1}}\hat{P}_z + A_{zz}\hat{S}_z\hat{P}_z. \tag{B.37}$$

Here, A_{zz} is the parallel component of the dipolar coupling as given by Eq. (B.34). We now consider the case where both NV and P1 spins are driven, with Hamiltonian $\hat{\mathcal{H}}_{\text{dr}} = 2\Omega_{\text{NV}}\hat{S}_x \cos\omega_{\text{dr,NV}}t + 2\Omega_{\text{P1}}\hat{P}_x \cos\omega_{\text{dr,P1}}t$. Since the NV and P1 transition frequencies are much greater than dipolar coupling strength $\omega_{\text{NV}}, \omega_{\text{P1}} \gg A_{zz}$, we can further go to the rotating frame with respect to the drive frequencies, so that the system Hamiltonian becomes

$$\hat{\mathcal{H}}_{\text{SL}} = \delta_{\text{NV}}\hat{S}_z + \delta_{\text{P1}}\hat{P}_z + \Omega_{\text{NV}}\hat{S}_x + \Omega_{\text{P1}}\hat{P}_x + A_{zz}\hat{S}_z\hat{P}_z. \tag{B.38}$$

It is interesting to consider the case where both drives are resonant, i.e. $\delta_{\text{NV}} = \delta_{\text{P1}} = 0$, and satisfy the Hartmann Hahn condition $\Omega_{\text{NV}} = \Omega_{\text{P1}} \equiv \Omega_0$. In this regime, for convenience we can rotate the NV and P1 quantization axes such that $\hat{S}'_z = \hat{S}_x$ and $\hat{P}'_z = \hat{P}_x$. The spin-locking Hamiltonian can thus be rewritten as

$$\hat{\mathcal{H}}_{\text{HH}} = \Omega_0(\hat{S}'_z + \hat{P}'_z) + A_{zz}\hat{S}'_x\hat{P}'_x. \tag{B.39}$$

In the limit where the spin-locking drive amplitude is much greater than dipolar coupling strength, we can also apply the rotating frame approximation and neglect the counter-rotating term, i.e.

$$\Omega_0 \gg |A_{zz}| : \quad \hat{\mathcal{H}}_{\text{HH}} \simeq \Omega_0(\hat{S}'_z + \hat{P}'_z) + \frac{A_{zz}}{4}(\hat{S}'_+\hat{P}'_- + \hat{S}'_-\hat{P}'_+). \tag{B.40}$$

In this case, the NV spin Rabi ocsillation rate is determined by A_{zz}.

B.3.2 observed spectrum in a strongly coupled system

Let us now consider the spectra we will measure of a strongly coupled NV and P1 system. The NV spectrum is measured via ODMR; at each frequency we measure how efficiently a π pulse flips the NV spin. During the NV measurement the nearby P1 is in either $|\uparrow\rangle$ or $|\downarrow\rangle$. In addition to the external field, the NV sees an additional dipolar coupling to the P1 spin. It is important to note here than the P1 T_1 time should be much longer than the measurement time, so we can consider the P1 state to be constant.

If $|P1\rangle = |\uparrow\rangle$, its spin projection is $\mathrm{Tr}(\hat{S}_z\hat{\rho}_\uparrow) = 1/2$, and if $|P1\rangle = |\downarrow\rangle$, its spin projection is $\mathrm{Tr}(\hat{S}_z\hat{\rho}_\downarrow) = -1/2$. The P1 has equal probability to be in each state, so half the time the NV sees a positive dipolar field, and half the time it sees a negative dipolar field. Averaging over many measurements, we expect to see a splitting equal to the dipolar coupling in ODMR.

The P1 spectrum is measured in a DEER measurement. We similarly measure how efficiently a π pulse flips the P1 spin (for a strongly coupled system one can set the NV evolution time to read out only the strongly coupled P1). However, here the NV is in a superposition state while we measure the P1 spectrum, a necessity of the DEER readout technique. What is the NV spin projection?

$$S_z = \mathrm{Tr}\left[\frac{1}{2}\begin{pmatrix} 1 & 1 \\ 1 & 1 \end{pmatrix}\begin{pmatrix} 1 & 0 \\ 0 & -1 \end{pmatrix}\right] = 0.$$

We see that during the DEER measurement, the P1 sees a constant field from the NV and we do not expect to observe a dipolar splitting in the P1 spectrum.

As an example, compare the NV pulsed ODMR measurement in Fig. B.3(a) with the DEER-detected P1 spectrum in Fig. B.3(b).

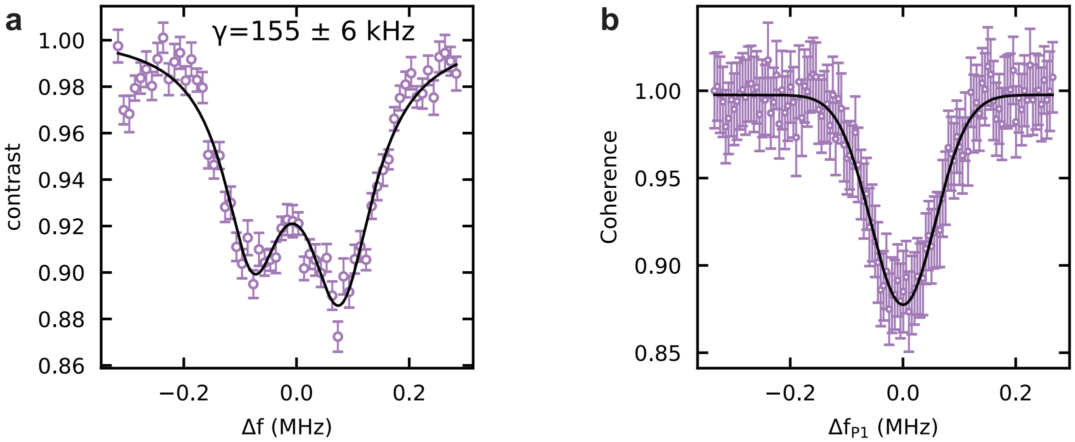

Figure B.3: **Single spin spectra.** NV and single P1 spectra captured with pulsed ODMR (a) and NV-DEER detection (b), respectively, at 311 G.

B.4 NV T_1 measurement

Here we measure the T_1 decay of the NV center and extract both $\Delta m_s = 1$ and $\Delta m_s = 2$ decay rates, probing both magnetic and electric field noise [43, 182]. Fig. B.4(a) and (b) show a NV T_1 measurement probing decay from $|0\rangle$ to $|-1\rangle$ and from $|+1\rangle$ to $|-1\rangle$, respectively. Importantly, the decay of $P_{+1} - P_{-1}$, where P_i indicates the population in $|i\rangle$, is exactly the decay of the NV dipolar field that the P1 center feels in Sec. 6.3.3. However, even within the time $\tau_{diffusion} \lesssim T_{1;+1,-1} = 1.4(1)\,\mathrm{ms}$ there is significant divergence between the spin diffusion trajectories.

We calculate $\Omega = 151(9)\,\mathrm{s}^{-1}$ and $\gamma = 270(20)\,\mathrm{s}^{-1}$, where Ω characterizes the $\Delta m_s = 1$ decay rate between $|0\rangle$ and $|\pm1\rangle$ and γ characterizes the $\Delta m_s = 2$ decay rate between $|+1\rangle$ and $|-1\rangle$ [43, 182]. γ consists entirely of electric field noise, while Ω consists mainly of magnetic field noise, although recently it has been shown that electric field noise also contributes to Ω [43]. This indicates that there is significant bulk electric field noise in our sample, in line with observations in Ref. 182. This is not necessarily surprising, as we observe time-dependent charge processes in Fig. 6.2, and thus expect bulk electric field noise. We note that this places a limit on T_2 of 2.8 ms, within the range of CCE simulations presented in Fig. 6.5(a) but well above the $T_{1,P1}$ limit at room temperature.

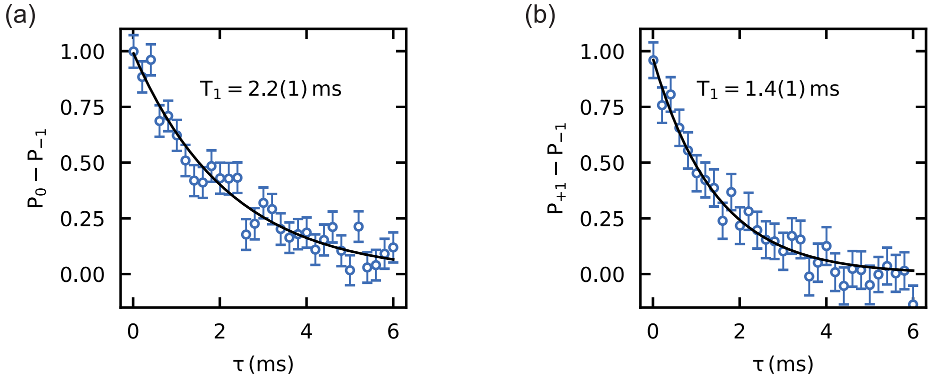

Figure B.4: **NV differential polarization decay**. T_1 measurements on both $\Delta m_s = 1$ (a) and $\Delta m_s = 2$ (b) transitions. Labels P_i indicate the population of the $|NV\rangle = |i\rangle$ spin state. Extracted T_1 times are from a monoexponential fit.

B.5 P1 density variation with laser illumination

Ref. 275 has demonstrated tuning of the P1 spin density with green laser illumination due to a charge transfer process with other defects in the diamond lattice. We follow the same measurement protocol here, comparing P1 densities through the NV coherence dip in a DEER spectrum of one of the P1 transitions. In Fig. B.5 we plot the normalized DEER spectrum for two laser initialization pulses: (i) 330 µW for 1.5 µs and (ii) 3.3 mW for 30 µs. The time in (i) is chosen to be long enough to repolarize the NV but short enough to not significantly decay the P1 polarization, as measured in the main text. The time in (ii) is chosen to be long enough to depolarize the P1 spin. We find no significant difference in the NV contrast and thus the steady-state P1 population, suggesting that across our range of laser powers there is no difference in the P1 population.

B.6 Ionization cross-section calculation

The ionization rate in terms of laser power P, cross-section σ_{ion}, and gaussian laser beam radius r, is

$$\Gamma_{ion} = \frac{P\sigma}{3.73 \times 10^{-19}\,\mathrm{J} \cdot \pi r^2}, \tag{B.41}$$

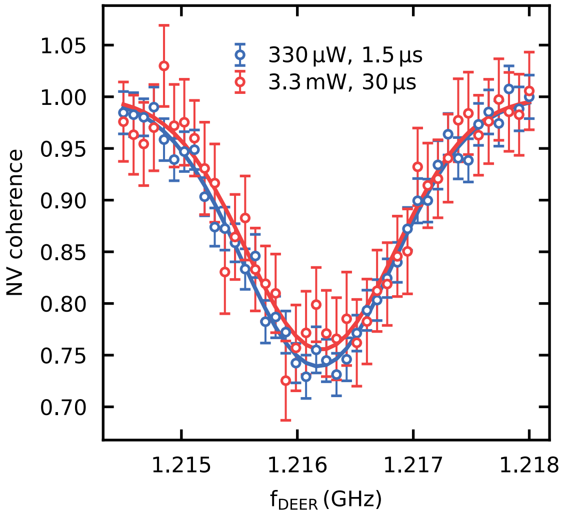

Figure B.5: **P1 spectrum versus laser.** P1 spectrum measured via NV DEER at two laser powers (330 µW, 3.3 mW) and initialization times (1.5 µs, 30 µs). We observe no difference in the P1 population.

where 3.73×10^{-19} J is the energy of a single 532 nm photon. The diffraction-limited gaussian beam radius for our 0.9 NA objective is 150 nm. Extracting the slope of Γ_{P1}/P from Fig. 6.7(c) in the low-power limit we arrive at

$$\sigma_{ion} = 1.2(5) \times 10^{-4}\,\mathrm{A}^2 \tag{B.42}$$

APPENDIX C

EXPERIMENTAL SETUP

Measurements of single NV centers in Chs. 4, 5, and 6 are performed with a home-built confocal microscope with single-color excitation for optical initialization and readout, and microwave electronics for driving ground-state spin transitions (see Ch. 2), shown in Fig. C.1. I herein describe each component in the optical and electronic systems and their purposes in Tables C.1, C.2, C.3, C.4, and C.5.

Table C.1: Laser beam setup components.

Label	Component	Purpose
a	532 nm CW laser (Oxxius, **LCX-532S-150-CSB-PPA**)	optical excitation
b	variable optical density filter	attenuate laser power
c	AOM focusing optics	focus laser beam incident on AOM crystal/re-collimate
d	AOM (Gooch&Housego, custom)	acousto-optic modulator, gate laser pulse on/off with extinction >40 dB
e	mirror pair	redirect laser path (not all mirrors are shown/labelled)
f	beam expansion pair	expand beam to ensure the beam overfills the objective back-aperture

Table C.2: Collection components.

Label	Component	Purpose
g	594 nm dichroic beam-splitter	direct (green) laser to sample and (red) signal to collection optics
h	620 nm long-pass filter	clean up signal
i	532 nm notch filter	filter out residual laser light
j	fiber-coupled APD (Perkin Elmer, **SPCM-AQRH-13**) and focusing lens	count single photons emitted by defect

Table C.3: Imaging components.

Label	Component	Purpose
k	flip-mounted pellicle beam-splitter, 8:92 (R:T)	selectively couple white-light and camera paths into sample path
l	white-light source and collimation optic	illuminate sample for imaging
m	camera (Hitachi, **KP-D20B**)	image the sample
n	pellicle beam-splitter, 45:55	combine white-light and camera paths

Table C.4: Excitation components. Certain lens materials, such as N-BK7 (the 4f lenses in my setup) fluoresce in the red when excited with green light, just like the NV center. It is thus impossible to entirely remove the background signal from the lenses. This effect can be mitigated by placing irises to remove some of this background or by choosing different lens materials.

Label	Component	Purpose
o	fast steering mirror (Newport, **FSM-300**)	adjust angle of laser beam into objective to scan focused spot on the sample
p	4f lens pair	map angle of beam at the FSM onto an incident angle at the objective back-aperture
q	periscope	redirect optical path into objective, like in a submarine; may also be integrated with 3-axis stage, although this one is fixed
r	objective (Olympus, **MPLFLN100x**, NA0.9)	focus light to sub-micron spot for single defect excitation/collection; large numerical aperture improve signal collection
s	sample	hosts spin defects

Table C.5: Electronic components.

Label	Component	Purpose
t	computer/data acquisition device (DAQ, NI, **USB-6341**)	run experiments, initialize electronics, analyze data, measure photon counts (DAQ)
u	Arbitrary waveform generator (Swabian, **Pulse Streamer 8/2**)	generate analog and digital electrical signals for IQ modulation of mw signal (v), gating of mw signal (w), and gating of signal counts (z)
v	microwave signal generator (SRS **SG396** or **SG384**, or **HMC1197** eval board	deliver mw signals of variable frequency and amplitude to sample to manipulate spin state; in Chs. 5 and 6 the first listed model drives the NV spin and the second two drive the P1 spin
w	rf switch (Minicircuits, **ZASWA-2-50DR+**)	fast gating of mw signal to reduce signal leakage beyond IQ modulation
x	power combiner (Minicircuits, **ZFRSC-123-S+**)	couple in additional signal generators (dashed line)
y	high power amplifier (Minicircuits, **ZHL-16W-43+**)	amplify mw signal to improve spin drive rate and overcome myriad losses in the signal path
z	rf switch/logic tree (Minicircuits, **ZYSWA-2-50DR**)	gate signal counts; multiple levels of switches may be used to tag counts as bright signal, dark signal, reference, etc.

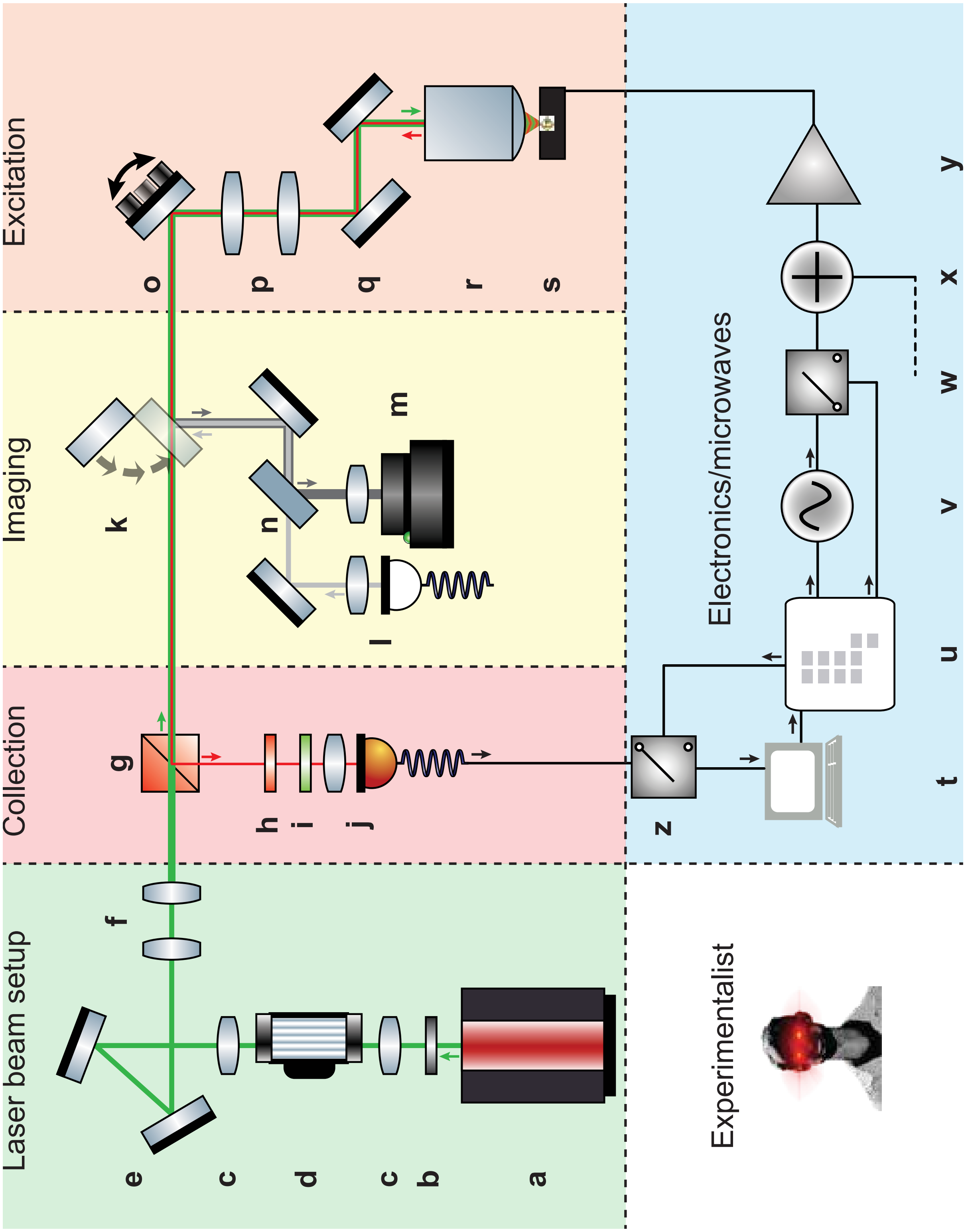

Figure C.1: **Experimental setup.** Home-built confocal microscope with laser beam setup (Table C.1), signal collection (Table C.2), sample imaging (Table C.3), and sample excitation (Table C.4), and accompanying microwave and timing electronics (Table C.5). Experimentalist courtesy of Grant Smith.

APPENDIX D

PLANAR METAL DEVICE FABRICATION

It is sometimes necessary to venture into the clean room with a perfectly nice diamond crystal and fabricate metal devices on top of it. These typically act as alignment marker for optical measurements, microwave striplines, microwave terminations, or electric field pads. In this Appendix, I lay out the fabrication process I followed to deposit 100 nm to 200 nm thick Ti/Pt/Au metal devices atop diamond. I then discuss the alternate method of spin driving used for experiments in Ch. 5 and 6 that does not require patterning microwave drive devices.

D.1 On-chip fabrication

The basic process steps are as follows: photoresist spinning, optical patterning/mask creation, metal deposition, metal lift-off.

D.1.1 Photoresist spinning

The initial photoresist (PR) spinning is not on top of the diamond chip but rather to adhere the diamond, generally 2 mm x 2 mm square, to a large carrier wafer. The benefits are twofold: the diamond is very small, hard to handle, and may be too small for vacuum mounts in instruments; and this allows us to add sacrificial chips on the diamond edges to prevent photoresist beading, shown schematically in Fig. D.1. We use a 4 inch Si carrier wafer and AZ nLOF 2020 negative photoresist.

PR recipe

- Clean all chips in acetone and IPA followed by a DI water rinse and 5 min, 180 °C bake to dry

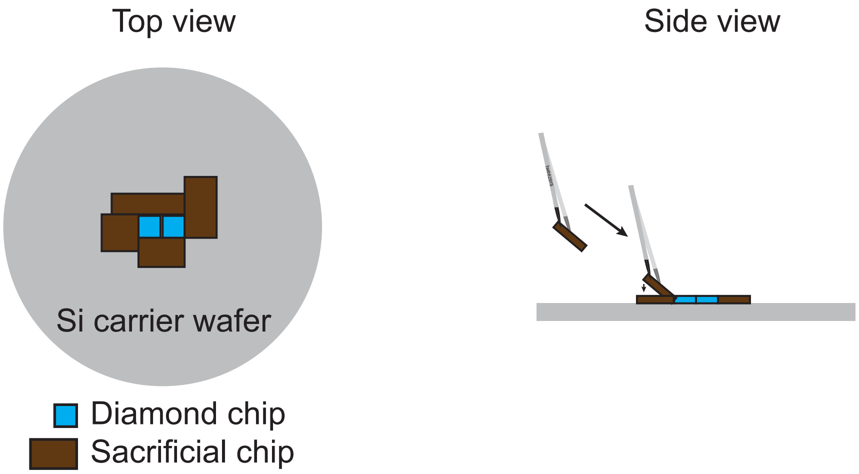

Figure D.1: **Sacrificial chip.** Sacrificial chip placement around two diamond samples on a carrier wafer from top view (left) and side view (right). At right we show how to approach and place the sacrificial chips to minimize PR sample contamination.

- Spin AZ nLOF 2020 on the Si carrier wafer with
  - Step 1: 500 rpm, 250 rpm/s ramp, 10 s (4.5 µm layer)
- Remove carrier wafer from spinner, place diamond chip(s) as close to wafer center as possible, being careful to drop it straight down to avoid PR climbing atop the diamond
- Place sacrificial chips one-by-one around the edges of the diamond chip(s), as shown in Fig. D.1. These sacrificial chips are in general not perfect rectangles so this may require some finagling. It is important to get the sacrificial chips as close as possible to the diamond edge before dropping onto the carrier wafer to minimize the chip-diamond distance as well as prevent PR from climbing up the diamond sides. I recommend approaching the diamond edge with the sacrificial chip at an angle from your dominant side and then lowering it down into the PR.
- Bake for 12 min at 115 °C to harden the PR adhesion layer, then cool for a few minutes.
- Spin second layer of AZnLOF 2020 on the diamond and sacrificial chips with
  - Step 1: 500 rpm, 100 rpm/s ramp, 10 s. Confirm by eye at beginning of this step

    that the diamond is centered. If not, abort, reposition carrier wafer, and restart. Once diamond is centered, start adding PR starting on diamond and moving outward.
  - Step 2: 4500 rpm, 2000 rpm/s ramp, 45 s (1 µm to 2 µm thick)
  - Step 3: 0 rpm, 1000 rpm/s ramp, 0 s
- Pre-bake PR for 1 min at 115 °C
- Check PR coverage and edge beading in optical microscope with GREEN filter

D.1.2 Optical patterning

Presently at UChicago we use a Heidelberg MLA150 Direct Write Lithographer. This is a wonderful tool that directly optically exposes the PR to your pattern by rastering a light source over the wafer. It can generate features down to 1 µm.

Exposure process

- Expose sample to pattern
- Post-bake PR for 1 min at 115 °C
- Develop in 300 MIF developer for 1 min
- DI water quench to stop developing
- Check in microscope that mask was formed. If underdeveloped, put back in developer.

You will initially want to perform a dose test of your sample, which is readily achieved in the Heidelberg software. This will tell you the proper dose to expose your PR and get the features you desire. A standard method is to use a series of vertical lines with pitch equal to your feature size, expose your sample to the dose test, post-bake and develop, and check in a microscope for which dose best produced your features. While this number likely changes over time, I found that for AZ nLOF 2020 on transparent, 500 µm-thick diamond on a Si carrier wafer with the AZ nLOF 2020 adhesion layer a dose of 240 $\mathrm{mJ/cm^2}$ works well. But you should probably recalibrate this.

D.1.3 Metal deposition

Deposition is performed in the Angstrom Nexdep Thermal E-Beam Evaporator. We tend to deposit Ti(10)/Pt(20)/Au(**x**) metal stacks, where x is the desired gold thickness. The Ti acts as an adhesion layer to substrate for the rest of the stack. However, Ti readily oxidizes to TiO_2, which will lead to delamination from the substrate. We thus add a Pt layer to act as an oxygen diffusion barrier[1]. The main conductive pathway is through the Au, which is typically at least 100 nm. The metal thickness may depend on the end device goal. For example, a microwave termination should be as low resistance as possible in order to optimally reflect the microwave signal and maximize the drive current through the short. However, a through-device should be matched to 50 Ω to minimize reflections in the microwave path[2].

Deposition recipe

- Perform O_2 descum in the downstream asher, recipe 1 (25 s, room temperature. If the MW fails just reset and run again)
- Mount carrier wafer in deposition chamber

---

[1] This is the inherited group fab knowledge. As we all know, fab is 50% science and 50% black magic, and it is possible there is a different explanation for why the Pt layer is valuable, or a different metal stack that achieves the same goal.

[2] In older theses from our group you will find shorted devices that were matched to 50 Ω, which serves to dump maximum power into the sample. This was a mistake and should not be replicated, especially for low-temperature measurements.

- Pump chamber down to $< 2 \times 10^{-6}$ torr
- Ti deposition, I find is stable at 1 A/s
- Pt deposition. Pressure will have risen, proceed. This deposition is more finicky, I find it is stable up to around 0.2 A/s, although this may have changed.
- Au deposition, stable at > 1 A/s
- Remove carrier wafer from chamber
- Metal lift-off in NMP, agitating and sonicating until chips come off carrier wafer
- Transfer samples to smaller NMP beaker to finish lift-off with reduced worry of redepositing all the other metal floating around.
- IPA clean of all chips.

D.2 Draped wirebond

Given that devices fabricated on diamond are much smaller than the microwave wavelength λ (see App. E) and thus act simply as a load resistance and not a microwave component, one may ask if it is even necessary to go through the work of creating these little wires. The answer, in fact, is that one can circumvent this with the draped wirebond method. The idea is as follows, demonstrated in Fig. D.2. Mount the sample on a printed circuit board between a signal pin and ground plane. In a wirebond tool, bond a wire between the signal and ground planes draped over the sample, aiming for the wire to be as close as possible to the sample. As long as the sample is within $\lambda/8$ of the ground plane connection (see App. E) the wire will deliver a sufficient drive field to the sample for mw control of spin qubits.

This method is sufficient for many experiments, but has some major drawbacks compared to on-chip devices that should be considered. To start with, between a clean diamond surface and a draped wirebond there is no fixed reference system and it is thus very difficult to navigate a sample. So even with a draped wirebond, it is advisable to fabricate a navigation system, such as alignment markers. Additionally, the wirebond is typically a 25 µm-diameter Al wire, compared to a 2 µm to 4 µm by 100 nm fabricated wire. As the wire is draped over the surface, is partially occludes the excitation and collection, necessitating one to work with NV centers around 50 µm away from the wire, assuming the wire is very close to or sitting at the surface. One can image NVs within a diffraction limited spot of a fabricated wire, in contrast. These difference lead to a large difference in the achievable drive fields.

Assuming the resistance of both wires is far from 50 Ω, in both cases the wires carry a load current I_L set by the signal power, such that the circulating magnetic field magnitude some distance r from the wire is

$$B_\phi(r) = \frac{\mu_0 I_L}{2\pi r}, \tag{D.1}$$

assuming $r << \ell$, the wire length. Even though both wires carry the same current, geometric constraints mean the drive field will be at least 50 times smaller with the thicker draped wirebond. This corresponds to a 2500 times larger power, 34 dB, to achieve the same drive rate. In this sense, a fabricated device is much more efficient. However, devices restrict the sample region that can be addressed with microwaves to the regions around devices, whereas draped wirebonds can access the entire length of a sample along the wire axis, and can be rebonded with little overhead. Thus from an experimental process perspective, draped wirebonds can be more practical.

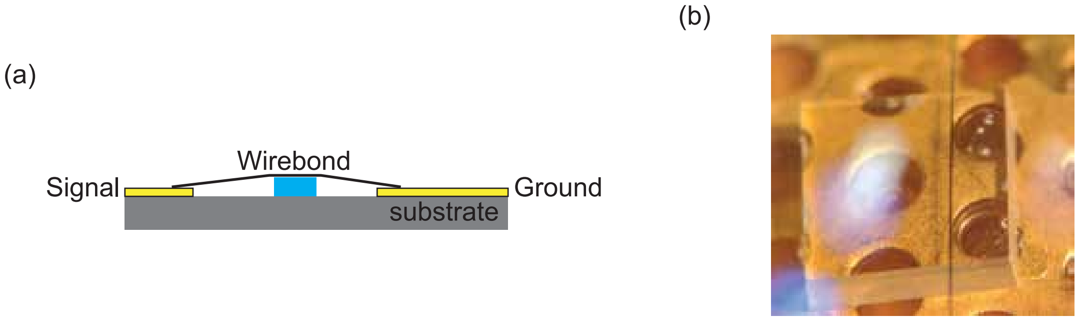

Figure D.2: **Draped wirebond.** (a) Schematic of how the wirebond is draped over a sample, bonded from signal pin to ground plane. (b) An example of a draped wirebond over a diamond chip sitting on a circuit board. Note that the wire and diamond surface are both in focus, indicating the wire is very close to the sample.

APPENDIX E

MICROWAVE NOTES

At modest magnetic fields ($\lesssim 1000\,\mathrm{G}$) Larmor frequencies of typical solid state spin qubits are in the GHz regime, which is great. It is simple to purchase a microwave signal generator that operates in this regime and plug coaxial cables into it. It is generally necessary to design some interface between microwaves travelling in a coaxial cable and a sample of interest, and it is thus helpful to understand the physics underlying microwaves. We begin by deriving formulae for propagating electrical signals, following David Pozar's textbook Microwave Engineering[1] and then consider a few situations relevant to devices used for NV measurements, and the general concept of impedance matching.

E.1 Transmission line wave equation

Consider a transmission line, such as a coaxial cable with ground and signal planes/pins separated by a dielectric medium, on the order of or longer than a signal wavelength λ. There is a time- and space-dependent current $i(z,t)$ traveling along the signal pin and a voltage $v(z,t)$ between signal and ground. The transmission line in general possesses some series resistance R and series inductance L along the line, and shunt capacitance C and shunt conductance G (dielectric loss) between signal and ground. Over some differential length Δz of line we can then relate the voltage, current, and circuit parameters as

$$v(z,t) - R\Delta z i(z,t) - L\Delta z\frac{\partial i(z,t)}{\partial t} - v(z+\Delta z,t) = 0 \tag{E.1}$$

$$i(z,t) - G\Delta z v(z+\Delta z,t) - C\Delta z\frac{\partial v(z+\Delta z,t)}{\partial t} - i(z+\Delta z,t) = 0 \tag{E.2}$$

---

[1] The best textbook, first introduced to me by Prof. Greg Fuchs, whose response to a question about microwaves was "just read Pozar." The book Electromagnetic Waves by David Staelin (it's Davids all the way down, folks) also deserves a mention, alongside a shoutout to Dr. Lisa Wickham who taught me AEP 3560 at Cornell.

which in the limit of $\Delta z \to 0$ become

$$\begin{aligned} \frac{\partial v(z,t)}{\partial z} &= -Ri(z,t) - L\frac{\partial i(z,t)}{\partial t} && \text{(E.3)} \\ \frac{\partial i(z,t)}{\partial z} &= -Gv(z,t) - C\frac{\partial v(z,t)}{\partial t} && \text{(E.4)} \end{aligned}$$

in the time-domain, so-called telegrapher equations. We now assume that voltage and current can be written as phasors

$$\begin{aligned} v(z,t) &= V(z)e^{j\omega t} && \text{(E.5)} \\ I(z,t) &= I(z)e^{j\omega t} && \text{(E.6)} \end{aligned}$$

where $V(z)$ and $I(z)$ are in general complex numbers with different phases, and we follow Pozar with $j = \sqrt{-1}$ but not the electrical engineering convention to add a negative sign in the exponent. Plugging these into Eqs. (E.3) and (E.4) and taking another spatial derivative we find

$$\begin{aligned} \frac{d^2V(z)}{dz^2} - \gamma^2 V(z) &= 0 && \text{(E.7)} \\ \frac{d^2I(z)}{dz^2} - \gamma^2 I(z) &= 0 && \text{(E.8)} \\ \gamma &= \sqrt{(R + j\omega L)(G + j\omega C)}. && \text{(E.9)} \end{aligned}$$

These are simply wave equations for voltage and current, more natural quantities in our quasi-circuit model than electric and magnetic fields, although they function the same way and can be directly relate to one another. Our standard traveling wave solutions give us forward and backward propagating waves along the line of

$$\begin{aligned} V(z) &= V_+e^{-\gamma z} + V_-e^{\gamma z} && \text{(E.10)} \\ I(z) &= I_+e^{-\gamma z} + I_-e^{\gamma z}. && \text{(E.11)} \end{aligned}$$

The telegraph equations allow us to rewrite the current as

$$I(z) = \sqrt{\frac{G + j\omega C}{R + j\omega L}} \left(V_+ e^{-\gamma z} - V_- e^{\gamma z} \right) \tag{E.12}$$

where critically a minus sign shows up relating the backward propagating wave amplitudes, such that we can define a characteristic impedance

$$Z_0 = \sqrt{\frac{R + j\omega L}{G + j\omega C}} = \frac{V_+}{I_+} = -\frac{V_-}{I_-}. \tag{E.13}$$

In a lossless line, which we tend to consider, $G = 0$, $R = 0$, and we reduce to $Z_0 = \sqrt{L/C}$ with $\gamma = j\omega\sqrt{LC}$.

E.2 Load impedance

The wavelengths of microwaves are fairly long. At 1 GHz the freespace wavelength is 12 ft. This is much larger than typical diamond chips and it is unlikely that any device fabricated on the diamond will act as a microwave device versus a load resistance with a quasistatic current ($\frac{\partial E}{\partial t} = 0$, *cf.* Maxwell's Equations) and thus no radiation. I.e., it will be a wire, not an antenna. We will first treat these devices as lumped element load impedances at the end of microwave transmission lines and then look at the case of a draped wirebond that may look worryingly long.

E.2.1 Reflection coefficient

We saw above that voltage and current waves travel along the transmission line with a characteristic impedance Z_0. In general we have forward and backward propagating waves. Recall that impedance is pretty general, and the relationship $V/I = Z$ should always hold locally. Where the transmission line terminates in a load impedance Z_L at $z = 0$ the relationship

$$Z_L = \frac{V(0)}{I(0)} \quad = \tfrac{V_+ + V_-}{I_+ + I_-}$$
$$= \tfrac{V_+ + V_-}{V_+ - V_-} Z_0 \tag{E.14}$$

holds. We are specifically interested here in what affect Z_L has on the amplitude of the backward travelling wave, so we solve for V_-

$$V_- = \frac{Z_L - Z_0}{Z_L + Z_0} V_+. \tag{E.15}$$

We see that the load impedance indeed modifies the relative wave amplitudes, and can even impart a phase if Z_L is complex. We then define the reflection coefficient

$$\Gamma = \frac{Z_L - Z_0}{Z_L + Z_0}. \tag{E.16}$$

Γ imposes a fixed relation between the two wave directions, leading to standing waves on the transmission line. By enforcing continuity of voltage we can also define a transmission coefficient

$$T = 1 - \Gamma = \frac{2Z_L}{Z_L + Z_0}. \tag{E.17}$$

We note here for completeness that this formulation of electrodynamics is more general and can be applied to any kind of electromagnetic wave propagating in a medium with permittivity ϵ and permeability μ such that the characteristic impedance of the medium relating the amplitudes of electric and magnetic fields is $\eta = \sqrt{\mu/\epsilon}$. Reflection and transmission coefficients can be similarly defined, where $\eta_0 = \sqrt{\mu_0/\epsilon_0} \approx 377\,\Omega$. This, however, is not at the moment relevant. The treatment here assumes a transverse electric and magnetic (TEM) mode where the electric and magnetic field vectors are both orthogonal to the direction of propagation, the simplest case of electromagnetic wave propagation.

E.2.2 Real impedance

With our relatively short wires it should be sufficient to consider them to only have a resistance such that $Z_L = R_L$. Furthermore, coaxial cables almost always have $Z_0 = 50\,\Omega$, such that we can write

$$\Gamma = \frac{R_L - 50\,\Omega}{R_L + 50\,\Omega}. \tag{E.18}$$

We now consider three common cases

$$R_L = \begin{cases} \approx 0, \ll Z_0 \\ Z_0 \\ \approx \infty, \gg Z_0 \end{cases} \tag{E.19}$$

where the first may occur with a draped wirebond or a very thick fabricated device (or a short circuit–be careful) and the third may occur with an open circuit. The middle case is a special case termed impedance matching. For $R_L \ll Z_0$, Eq. (E.18) tells us that the reflection coefficient is $\Gamma = -1$. So what are the implications of this? The amplitude of the reflected voltage wave is $V_- = -V_+$, such that at $z = 0$ the standing voltage wave amplitude is actually 0. This is intuitive; when we short the signal to ground, Maxwell's equations require the voltage to be continuous, and ground is defined as 0 voltage. However, since $I_- = -V_-/Z_0$, the reflected current amplitude is $I_- = I_+$ such that the total current is actually at a maximum value of $2V_+/Z_0$. Stepping back for a minute, this is actually great. We conventionally drive spin qubits with magnetic fields sourced from currents. Maximum current passing through the load wire means maximum driving efficiency; we don't even want a voltage. An effective short between signal and ground is thus a great way to drive spins if one does not mind all of the microwave power being reflected into the signal path (check your amplifier specs or use a circulator!), motivating the draped wirebond in App. D.

Curiously, in the case of infinite load resistance, $\Gamma_R = 1$, such that the all of the power is also reflected at the load. However, now $V_- = V_+$, $I_- = -I_+$, and there is maximum voltage across and no current passing through the load. This is a bad way to magnetically drive spins, although it has accidentally lead to some neat physics with electrical drives [8].

Finite length load

It is possible that some devices may occupy an intermediate length-scale where we cannot assume that their length $\ell \ll \lambda$ but also they are not quite waveguides. Consider a long wire-bond that effectively shorts signal to ground. Then, as above, $I(0) = 2V_+/Z_0 = 2I_+$. Propagating backwards along the wire the standing wave amplitude is $I(z) = 2I_+ \cos(2\pi z/\lambda)$. This motivates remaining in a quasistatic regime where $z < \lambda/8$ [248], or else one risks hitting nodes along the wire at $z = (2n+1)\lambda/4$ where $I(z) = 0$ and there is no net drive current. For reference, $\lambda/8 = 12.5\,\text{mm}$ at $3\,\text{GHz}$.

E.2.3 Impedance matching

When the load impedance is equal to the characteristic impedance, $Z_L = Z_0$, we find $\Gamma = 0$ and $T = 1$. Nothing is reflected. If the load is a termination, then it follows that all power is transmitted into the load. In general, this is an incredibly important condition to consider when connecting multiple microwave components. Most components you can buy are $50\,\Omega$, and thus when you plug a cable into a device, signal will pass between them with no reflection.

However, if one is designing a waveguide, for example, to deliver microwaves to a sample, one must design the impedance of the waveguide as well as consider the impedance that terminates the waveguide in order to deliver said microwaves. Essentially, the waveguide termination, as we saw above, sets a fixed relationship between voltage and current along the entire device. We can generalize the reflection coefficient to some distance ℓ from the end of the device as

$$\Gamma(\ell) = \frac{V_+ e^{-j\beta\ell}}{V_- e^{j\beta\ell}} = \Gamma e^{-2j\beta\ell}, \tag{E.20}$$

where $\beta = \omega\sqrt{LC}$ for the lossless line considered here, and Γ is at the end of the device as defined in Eq/ (E.16). It is then natural to ask what the resulting impedance is at the beginning of this device by evaluating the resulting standing waves:

$$V(-\ell) \;= V_+ \left(e^{j\beta\ell} + \Gamma e^{-j\beta\ell}\right) \tag{E.21}$$

$$I(-\ell) \;= V_+ \left(e^{j\beta\ell} - \Gamma e^{-j\beta\ell}\right) \tag{E.22}$$

such that the input impedance is

$$Z_{in} = \frac{V(-\ell)}{I(-\ell)} = Z_0 \frac{Z_L + jZ_0 \tan\beta\ell}{Z_0 + jZ_L \tan\beta\ell}. \tag{E.23}$$

Let us assume for simplicity that the waveguide is designed to have a characteristic impedance of $50\,\Omega$ (not a given) because the designer referenced the textbook Coplanar Waveguide Circuits, Components, and Systems by Rainee N. Simons [242]. If the waveguide terminates in another $50\,\Omega$ component, such as another coaxial cable and a $50\,\Omega$ termination cap, then $Z_{in} = Z_0 = 50\,\Omega$ and we do not have to worry. However, if the end of the waveguide is shorted, $Z_{in} = jZ_0 \tan\beta\ell$, and if it is open, $Z_{in} = -jZ_0 \cot\beta\ell$. The input impedance is then a function of how many wavelengths long the waveguide is. For experiments where the magnetic field, and thus the NV resonance frequency, may be changing, this is bad news. But in general, this just adds another design constraint.

APPENDIX F

DO WE BREATHE MORE NITROGEN THAN WE PUT IN OUR DIAMONDS?

I was asked by a friend as to what contains more nitrogen: a human breath, or the diamonds we study. For the sake of science communication, I present my results here.

Ref. 141 finds that a single human breath is about 490 mL. Standard atmospheric air is 78% N_2, such that a breath contains 380 mL nitrogen. Using $PV = Nk_BT$, we find around 2×10^{22} atoms of nitrogen in a single breath.

We study diamonds that are generally $1\,\mathrm{mm}^3$ to $2\,\mathrm{mm}^3$ (1 µL to 2 µL, or 0.0175 carat to 0.035 carat). We grow diamond with a very low background nitrogen content of < 5 ppb (see Ch. 4), giving us around 2×10^{12} atoms of nitrogen in a given sample. This is 10 billion times less than a breath. This is an extreme limit, though.

Consider a 1 carat diamond with a natural abundance of 100 ppm nitrogen [9]. This diamond contains 1×10^{18} atoms of nitrogen, only 20,000 times less than a breath.

REFERENCES

[1] J. M. Abendroth, K. Herb, E. Janitz, T. Zhu, L. A. Völker, and C. L. Degen. Single-Nitrogen-Vacancy NMR of Amine-Functionalized Diamond Surfaces. *Nano Lett.*, 22 (18):7294–7303, 2022. doi:10.1021/acs.nanolett.2c00533.

[2] I. Aharonovich, J. C. Lee, A. P. Magyar, B. B. Buckley, C. G. Yale, D. D. Awschalom, and E. L. Hu. Homoepitaxial Growth of Single Crystal Diamond Membranes for Quantum Information Processing. *Adv. Mater.*, 24(10):OP54–OP59, 2012. doi:10.1002/adma.201103932.

[3] S. T. Alsid, J. F. Barry, L. M. Pham, J. M. Schloss, M. F. O'Keeffe, P. Cappellaro, and D. A. Braje. Photoluminescence Decomposition Analysis: A Technique to Characterize N-V Creation in Diamond. *Phys. Rev. Appl.*, 12(4):044003, 2019. doi:10.1103/PhysRevApplied.12.044003.

[4] C. A. J. Ammerlaan and E. A. Burgemeister. Reorientation of Nitrogen in Type-I*b* Diamond by Thermal Excitation and Tunneling. *Phys. Rev. Lett.*, 47(13):954–957, 1981. doi:10.1103/PhysRevLett.47.954.

[5] C. P. Anderson, E. O. Glen, C. Zeledon, A. Bourassa, Y. Jin, Y. Zhu, C. Vorwerk, A. L. Crook, H. Abe, J. Ul-Hassan, T. Ohshima, N. T. Son, G. Galli, and D. D. Awschalom. Five-second coherence of a single spin with single-shot readout in silicon carbide. *Sci. Adv.*, 8(5):5912, 2022. doi:10.1126/sciadv.abm5912.

[6] J. C. Angus. Diamond synthesis by chemical vapor deposition: The early years. *Diam. Relat. Mater.*, 49:77–86, 2014. doi:10.1016/j.diamond.2014.08.004.

[7] M. Annis, W. Cheston, and H. Primakoff. On Statistical Estimation in Physics. *Rev. Mod. Phys.*, 25(4):818–830, 1953. doi:10.1103/RevModPhys.25.818.

[8] S. Asaad, V. Mourik, B. Joecker, M. A. I. Johnson, A. D. Baczewski, H. R. Firgau, M. T. Mądzik, V. Schmitt, J. J. Pla, F. E. Hudson, K. M. Itoh, J. C. McCallum, A. S. Dzurak, A. Laucht, and A. Morello. Coherent electrical control of a single high-spin nucleus in silicon. *Nature*, 579(7798):205–209, 2020. doi:10.1038/s41586-020-2057-7.

[9] M. N. R. Ashfold, J. P. Goss, B. L. Green, P. W. May, M. E. Newton, and C. V. Peaker. Nitrogen in Diamond. *Chem. Rev.*, 120(12):5745, 2020. doi:10.1021/acs.chemrev.9b00518.

[10] M. Atatüre, D. Englund, N. Vamivakas, S. Y. Lee, and J. Wrachtrup. Material platforms for spin-based photonic quantum technologies. *Nat. Rev. Mater.*, 3(5):38–51, 2018. doi:10.1038/s41578-018-0008-9.

[11] D. Awschalom, K. K. Berggren, H. Bernien, S. Bhave, L. D. Carr, P. Davids, S. E. Economou, D. Englund, A. Faraon, M. Fejer, S. Guha, M. V. Gustafsson, E. Hu, L. Jiang, J. Kim, B. Korzh, P. Kumar, P. G. Kwiat, M. Lončar, M. D. Lukin,

D. A. B. Miller, C. Monroe, S. W. Nam, P. Narang, J. S. Orcutt, M. G. Raymer, A. H. Safavi-Naeini, M. Spiropulu, K. Srinivasan, S. Sun, J. Vučković, E. Waks, R. Walsworth, A. M. Weiner, and Z. Zhang. Development of Quantum Interconnects (QuICs) for Next-Generation Information Technologies. *PRX Quantum*, 2(1):017002, 2021. doi:10.1103/PRXQuantum.2.017002.

[12] D. D. Awschalom, R. Hanson, J. Wrachtrup, and B. B. Zhou. Quantum technologies with optically interfaced solid-state spins. *Nat. Photon.*, 12(9):516–527, 2018. doi:10.1038/s41566-018-0232-2.

[13] D. D. Awschalom, H. Bernien, R. Brown, A. Clerk, E. Chitambar, A. Dibos, J. Dionne, M. Eriksson, B. Fefferman, G. D. Fuchs, J. Gambetta, E. Goldschmidt, S. Guha, F. J. Heremans, K. D. Irwin, A. B. Jayich, L. Jiang, J. Karsch, M. Kasevich, S. Kolkowitz, P. G. Kwiat, T. Ladd, J. Lowell, D. Maslov, N. Mason, A. Y. Matsuura, R. McDermott, R. van Meter, A. Miller, J. Orcutt, M. Saffman, M. Schleier-Smith, M. K. Singh, P. Smith, M. Suchara, F. Toudeh-Fallah, M. Turlington, B. Woods, and T. Zhong. A Roadmap for Quantum Interconnects, 2022.

[14] G. Balasubramanian, I. Y. Chan, R. Kolesov, M. Al-Hmoud, J. Tisler, C. Shin, C. Kim, A. Wojcik, P. R. Hemmer, A. Krueger, T. Hanke, A. Leitenstorfer, R. Bratschitsch, F. Jelezko, and J. Wrachtrup. Nanoscale imaging magnetometry with diamond spins under ambient conditions. *Nature*, 455(7213):648–651, 2008. doi:10.1038/nature07278.

[15] G. Balasubramanian, P. Neumann, D. Twitchen, M. Markham, R. Kolesov, N. Mizuochi, J. Isoya, J. Achard, J. Beck, J. Tissler, V. Jacques, P. R. Hemmer, F. Jelezko, and J. Wrachtrup. Ultralong spin coherence time in isotopically engineered diamond. *Nat. Mater.*, 8(5):383–387, 2009. doi:10.1038/nmat2420.

[16] P. Balasubramanian, C. Osterkamp, O. Brinza, M. Rollo, I. Robert-Philip, P. Goldner, V. Jacques, F. Jelezko, J. Achard, and A. Tallaire. Enhancement of the creation yield of NV ensembles in a chemically vapour deposited diamond. *Carbon*, 194:282–289, 2022. doi:10.1016/j.carbon.2022.04.005.

[17] N. Bar-Gill, L. M. Pham, C. Belthangady, D. Le Sage, P. Cappellaro, J. R. Maze, M. D. Lukin, A. Yacoby, and R. Walsworth. Suppression of spin-bath dynamics for improved coherence of multi-spin-qubit systems. *Nat. Commun.*, 3(1):858, 2012. doi:10.1038/ncomms1856.

[18] N. Bar-Gill, L. M. Pham, A. Jarmola, D. Budker, and R. L. Walsworth. Solid-state electronic spin coherence time approaching one second. *Nat. Commun.*, 4(1):1743, 2013. doi:10.1038/ncomms2771.

[19] R. C. Barklie and J. Guven. 13C hyperfine structure and relaxation times of the P1 centre in diamond. *J. Phys. C: Solid State Phys.*, 14(25):3621, 1981. doi:10.1088/0022-3719/14/25/009.

[20] J. F. Barry, J. M. Schloss, E. Bauch, M. J. Turner, C. A. Hart, L. M. Pham, and R. L. Walsworth. Sensitivity optimization for NV-diamond magnetometry. *Rev. Mod. Phys.*, 92(1):015004, 2020. doi:10.1103/RevModPhys.92.015004.

[21] L. C. Bassett, F. J. Heremans, C. G. Yale, B. B. Buckley, and D. D. Awschalom. Electrical tuning of single nitrogen-vacancy center optical transitions enhanced by photoinduced fields. *Phys. Rev. Lett.*, 107(26):266403, 2011. doi:10.1103/PhysRevLett.107.266403.

[22] A. Batalov, C. Zierl, T. Gaebel, P. Neumann, I. Y. Chan, G. Balasubramanian, P. R. Hemmer, F. Jelezko, and J. Wrachtrup. Temporal coherence of photons emitted by single nitrogen-vacancy defect centers in diamond using optical rabi-oscillations. *Phys. Rev. Lett.*, 100(7):077401, 2008. doi:10.1103/PhysRevLett.100.077401.

[23] E. Bauch, S. Singh, J. Lee, C. A. Hart, J. M. Schloss, M. J. Turner, J. F. Barry, L. M. Pham, N. Bar-Gill, S. F. Yelin, and R. L. Walsworth. Decoherence of ensembles of nitrogen-vacancy centers in diamond. *Phys. Rev. B*, 102(13):134210, 2020. doi:10.1103/PhysRevB.102.134210.

[24] S. L. Bayliss, P. Deb, D. W. Laorenza, M. Onizhuk, G. Galli, D. E. Freedman, and D. D. Awschalom. Enhancing Spin Coherence in Optically Addressable Molecular Qubits through Host-Matrix Control. *Phys. Rev. X*, 12(3):031028, 2022. doi:10.1103/PhysRevX.12.031028.

[25] I. Bayn, E. H. Chen, M. E. Trusheim, L. Li, T. Schröder, O. Gaathon, M. Lu, A. Stein, M. Liu, K. Kisslinger, H. Clevenson, and D. Englund. Generation of Ensembles of Individually Resolvable Nitrogen Vacancies Using Nanometer-Scale Apertures in Ultrahigh-Aspect Ratio Planar Implantation Masks. *Nano Lett.*, 15(3):1751–1758, 2015. doi:10.1021/nl504441m.

[26] M. K. Bhaskar, R. Riedinger, B. Machielse, D. S. Levonian, C. T. Nguyen, E. N. Knall, H. Park, D. Englund, M. Lončar, D. D. Sukachev, and M. D. Lukin. Experimental demonstration of memory-enhanced quantum communication. *Nature*, 580(7801):60–64, 2020. doi:10.1038/s41586-020-2103-5.

[27] F. Bloch. Über die Quantenmechanik der Elektronen in Kristallgittern. *Z. Phys.*, 52 (7):555–600, 1929. doi:10.1007/BF01339455.

[28] D. Bluvstein, Z. Zhang, and A. C. Bleszynski Jayich. Identifying and Mitigating Charge Instabilities in Shallow Diamond Nitrogen-Vacancy Centers. *Phys. Rev. Lett.*, 122(7): 076101, 2019. doi:10.1103/PhysRevLett.122.076101.

[29] D. Bluvstein, Z. Zhang, C. A. McLellan, N. R. Williams, and A. C. Bleszynski Jayich. Extending the Quantum Coherence of a Near-Surface Qubit by Coherently Driving the Paramagnetic Surface Environment. *Phys. Rev. Lett.*, 123(14):146804, 2019. doi:10.1103/PhysRevLett.123.146804.

[30] M. Bockstedte, F. Schütz, T. Garratt, V. Ivády, and A. Gali. Ab initio description of highly correlated states in defects for realizing quantum bits. *npj Quantum Mater.*, 3 (1):31, 2018. doi:10.1038/s41535-018-0103-6.

[31] H. J. Bower and M. C. R. Symons. Electron spin resonance spectra associated with nitrogen in diamonds. *Nature*, 210(5040):1037–1038, 1966. doi:10.1038/2101037a0.

[32] C. Bradac, W. Gao, J. Forneris, M. E. Trusheim, and I. Aharonovich. Quantum nanophotonics with group IV defects in diamond. *Nat. Commun.*, 10(1):5625, 2019. doi:10.1038/s41467-019-13332-w.

[33] C. E. Bradley, J. Randall, M. H. Abobeih, R. C. Berrevoets, M. J. Degen, M. A. Bakker, M. Markham, D. J. Twitchen, and T. H. Taminiau. A Ten-Qubit Solid-State Spin Register with Quantum Memory up to One Minute. *Phys. Rev. X*, 9(3):031045, 2019. doi:10.1103/PhysRevX.9.031045.

[34] K. Bray, B. Regan, A. Trycz, R. Previdi, G. Seniutinas, K. Ganesan, M. Kianinia, S. Kim, and I. Aharonovich. Single Crystal Diamond Membranes and Photonic Resonators Containing Germanium Vacancy Color Centers. *ACS Photonics*, 5(12):4817–4822, 2018. doi:10.1021/acsphotonics.8b00930.

[35] S. J. Breuer and P. R. Briddon. Energy barrier to reorientation of the substitutional nitrogen in diamond. *Phys. Rev. B*, 53(12):7819–7822, 1996. doi:10.1103/PhysRevB.53.7819.

[36] D. A. Broadway, N. Dontschuk, A. Tsai, S. E. Lillie, C. T.-K. Lew, J. C. McCallum, B. C. Johnson, M. W. Doherty, A. Stacey, L. C. L. Hollenberg, and J.-P. Tetienne. Spatial mapping of band bending in semiconductor devices using in situ quantum sensors. *Nat. Electron.*, 1(9):502–507, 2018. doi:10.1038/s41928-018-0130-0.

[37] R. Brouri, A. Beveratos, J.-P. Poizat, and P. Grangier. Photon antibunching in the fluorescence of individual color centers in diamond. *Opt. Lett.*, 25(17):1294 – 1296, 2000. doi:10.1364/OL.25.001294.

[38] M. J. Burek, N. P. de Leon, B. J. Shields, B. J. M. Hausmann, Y. Chu, Q. Quan, A. S. Zibrov, H. Park, M. D. Lukin, and M. Lončar. Free-Standing Mechanical and Photonic Nanostructures in Single-Crystal Diamond. *Nano Lett.*, 12(12):6084–6089, 2012. doi:10.1021/nl302541e.

[39] W. K. Burton, N. Cabrera, F. C. Frank, and N. F. Mott. The growth of crystals and the equilibrium structure of their surfaces. *Philosophical Transactions of the Royal Society of London. Series A, Mathematical and Physical Sciences*, 243(866):299–358, 1951. doi:10.1098/rsta.1951.0006.

[40] A. Butcher, X. Guo, R. Shreiner, N. Delegan, K. Hao, P. J. Duda III, D. D. Awschalom, F. J. Heremans, and A. A. High. High-Q Nanophotonic Resonators on Diamond Membranes using Templated Atomic Layer Deposition of TiO_2. *Nano Lett.*, 20(6): 4603–4609, 2020. doi:10.1021/acs.nanolett.0c01467.

[41] J. Bylander, S. Gustavsson, F. Yan, F. Yoshihara, K. Harrabi, G. Fitch, D. G. Cory, Y. Nakamura, J. S. Tsai, and W. D. Oliver. Noise spectroscopy through dynamical decoupling with a superconducting flux qubit. *Nat. Phys.*, 7(7):565–570, 2011. doi:10.1038/nphys1994.

[42] B. Campbell and A. Mainwood. Radiation Damage of Diamond by Electron and Gamma Irradiation. *phys. status solidi (a)*, 181(1):99–107, 2000. doi:10.1002/1521-396X(200009)181:1<99::AID-PSSA99>3.0.CO;2-5.

[43] D. R. Candido and M. E. Flatté. Interplay between charge and spin noise in the near-surface theory of decoherence and relaxation of C_{3v} symmetry qutrit spin-1 centers. *arXiv*, page 2303.13370, 2023. doi:10.48550/arXiv.2303.13370.

[44] D. R. Candido, G. D. Fuchs, E. Johnston-Halperin, and M. E. Flatté. Predicted strong coupling of solid-state spins via a single magnon mode. *Mater. Quantum Technol.*, 1 (1):011001, 2021. doi:10.1088/2633-4356/ab9a55.

[45] F. Casola, T. van der Sar, and A. Yacoby. Probing condensed matter physics with magnetometry based on nitrogen-vacancy centres in diamond. *Nat. Rev. Mater.*, 3(1): 17088, 2018. doi:10.1038/natrevmats.2017.88.

[46] S. Chakravarthi, C. Moore, A. Opsvig, C. Pederson, E. Hunt, A. Ivanov, I. Christen, S. Dunham, and K.-M. C. Fu. Window into NV center kinetics via repeated annealing and spatial tracking of thousands of individual NV centers. *Phys. Rev. Mater.*, 4(2): 023402, 2020. doi:10.1103/PhysRevMaterials.4.023402.

[47] S. Chatterjee, P. E. Dolgirev, I. Esterlis, A. A. Zibrov, M. D. Lukin, N. Y. Yao, and E. Demler. Single-spin qubit magnetic spectroscopy of two-dimensional superconductivity. *Phys. Rev. Res.*, 4(1):L012001, 2022. doi:10.1103/PhysRevResearch.4.L012001.

[48] D. J. Cherniak, E. B. Watson, V. Meunier, and N. Kharche. Diffusion of helium, hydrogen and deuterium in diamond: Experiment, theory and geochemical applications. *Geochim. Cosmochim. Acta*, 232:206–224, 2018. doi:10.1016/j.gca.2018.04.029.

[49] J. Choi, H. Zhou, H. S. Knowles, R. Landig, S. Choi, and M. D. Lukin. Robust Dynamic Hamiltonian Engineering of Many-Body Spin Systems. *Phys. Rev. X*, 10(3): 031002, 2020. doi:10.1103/PhysRevX.10.031002.

[50] P. Chrostoski, P. Kehayias, and D. H. Santamore. Surface roughness noise analysis and comprehensive noise effects on depth-dependent coherence time of NV centers in diamond. *Phys. Rev. B*, 106(23):235311, 2022. doi:10.1103/PhysRevB.106.235311.

[51] A. A. Clerk. *Quantum Dissipation and Quantum Measurement [lecture notes]*. Pritzker School of Molecular Engineering, University of Chicago, 2020.

[52] A. A. Clerk, M. H. Devoret, S. M. Girvin, F. Marquardt, and R. J. Schoelkopf. Introduction to quantum noise, measurement, and amplification. *Rev. Mod. Phys.*, 82(2): 1155–1208, 2010. doi:10.1103/RevModPhys.82.1155.

[53] A. T. Collins and I. Kiflawi. The annealing of radiation damage in type Ia diamond. *J. Phys. Condens. Matter*, 21(36):364209, 2009. doi:10.1088/0953-8984/21/36/364209.

[54] R. J. Cook and D. H. Whiffen. Electron nuclear double resonance study of a nitrogen centre in diamond. *Proc. Math. Phys. Eng. Sci.*, 295(1441):99–106, 1966. doi:10.1098/rspa.1966.0228.

[55] A. Cooper, W. K. C. Sun, J.-C. Jaskula, and P. Cappellaro. Identification and Control of Electron-Nuclear Spin Defects in Diamond. *Phys. Rev. Lett.*, 124(8):083602, 2020. doi:10.1103/PhysRevLett.124.083602.

[56] A. Cox, M. E. Newton, and J. M. Baker. 13C, 14N and 15N ENDOR measurements on the single substitutional nitrogen centre (P1) in diamond. *J. Phys.: Condens. Matter*, 6:551–563, 1994. doi:10.1088/0953-8984/6/2/025.

[57] G. Davies. Dynamic Jahn-Teller distortions at trigonal optical centres in diamond. *J Phys. C Solid State Phys.*, 12(13):2551–2566, 1979. doi:10.1088/0022-3719/12/13/019.

[58] G. Davies and M. F. Hamer. Optical studies of the 1.945 eV vibronic band in diamond. *Proc. Math. Phys. Eng. Sci.*, 348(1653):285–298, 1976. doi:10.1098/rspa.1976.0039.

[59] G. Davies, S. C. Lawson, A. T. Collins, A. Mainwood, and S. J. Sharp. Vacancy-related centers in diamond. *Phys. Rev. B*, 46(20):13157–13170, 1992. doi:10.1103/PhysRevB.46.13157.

[60] E. J. Davis, B. Ye, F. Machado, S. A. Meynell, W. Wu, T. Mittiga, W. Schenken, M. Joos, B. Kobrin, Y. Lyu, Z. Wang, D. Bluvstein, S. Choi, C. Zu, A. C. Bleszynski Jayich, and N. Y. Yao. Probing many-body dynamics in a two-dimensional dipolar spin ensemble. *Nat. Phys.*, 2023. doi:10.1038/s41567-023-01944-5.

[61] G. de Lange, Z. H. Wang, D. Ristè, V. V. Dobrovitski, and R. Hanson. Universal Dynamical Decoupling of a Single Solid-State Spin from a Spin Bath. *Science*, 330 (6000):60–63, 2010. doi:10.1126/science.1192739.

[62] N. P. de Leon, K. M. Itoh, D. Kim, K. K. Mehta, T. E. Northup, H. Paik, B. S. Palmer, N. Samarth, S. Sangtawesin, and D. W. Steuerman. Materials challenges and opportunities for quantum computing hardware. *Science*, 372(6539):eabb2823, 2021. doi:10.1126/science.abb2823.

[63] R. de Sousa. Electron Spin as a Spectrometer of Nuclear-Spin Noise and Other Fluctuations. In M. Fanciulli, editor, *Electron Spin Resonance and Related Phenomena in Low-Dimensional Structures*. Springer Berlin, Heidelberg, 2009. ISBN 978-3-540-79364-9. doi:10.1007/978-3-540-79365-6.

[64] S. Debnath, N. M. Linke, C. Figgatt, K. A. Landsman, K. Wright, and C. Monroe. Demonstration of a small programmable quantum computer with atomic qubits. *Nature*, 536(7614):63–66, 2016. doi:10.1038/nature18648.

[65] C. L. Degen, F. Reinhard, and P. Cappellaro. Quantum sensing. *Rev. Mod. Phys.*, 89 (3):035002, 2017. doi:10.1103/RevModPhys.89.035002.

[66] M. J. Degen, S. J. H. Loenen, H. P. Bartling, C. E. Bradley, A. L. Meinsma, M. Markham, D. J. Twitchen, and T. H. Taminiau. Entanglement of dark electron-nuclear spin defects in diamond. *Nat. Commun.*, 12(1):3470, 2021. doi:10.1038/s41467-021-23454-9.

[67] S. Dhomkar, H. Jayakumar, P. R. Zangara, and C. A. Meriles. Charge Dynamics in near-Surface, Variable-Density Ensembles of Nitrogen-Vacancy Centers in Diamond. *Nano Lett.*, 18(6):4046–4052, 2018. doi:10.1021/acs.nanolett.8b01739.

[68] M. W. Doherty, N. B. Manson, P. Delaney, and L. C. L. Hollenberg. The negatively charged nitrogen-vacancy centre in diamond: the electronic solution. *New J. Phys.*, 13 (2):025019, 2011. doi:10.1088/1367-2630/13/2/025019.

[69] M. W. Doherty, N. B. Manson, P. Delaney, F. Jelezko, J. Wrachtrup, and L. C. L. Hollenberg. The nitrogen-vacancy colour centre in diamond. *Phys. Rep.*, 528(1):1–45, 2013. doi:10.1016/j.physrep.2013.02.001.

[70] F. Dolde, I. Jakobi, B. Naydenov, N. Zhao, S. Pezzagna, C. Trautmann, J. Meijer, P. Neumann, F. Jelezko, and J. Wrachtrup. Room-temperature entanglement between single defect spins in diamond. *Nat. Phys.*, 9(3):139–143, 2013. doi:10.1038/nphys2545.

[71] P. E. Dolgirev, S. Chatterjee, I. Esterlis, A. A. Zibrov, M. D. Lukin, N. Y. Yao, and E. Demler. Characterizing two-dimensional superconductivity via nanoscale noise magnetometry with single-spin qubits. *Phys. Rev. B*, 105(2):024507, 2022. doi:10.1103/PhysRevB.105.024507.

[72] B. L. Dwyer, L. V. H. Rodgers, E. K. Urbach, D. Bluvstein, S. Sangtawesin, H. Zhou, Y. Nassab, M. Fitzpatrick, Z. Yuan, K. De Greve, E. L. Peterson, H. Knowles, T. Sumarac, J.-P. Chou, A. Gali, V. V. Dobrovitski, M. D. Lukin, and N. P. de Leon. Probing Spin Dynamics on Diamond Surfaces Using a Single Quantum Sensor. *PRX Quantum*, 3(4):040328, 2022. doi:10.1103/PRXQuantum.3.040328.

[73] H. B. Dyer, F. A. Raal, L. Du Preez, and J. H. N. Loubser. Optical absorption features associated with paramagnetic nitrogen in diamond. *Philos. Mag. (Abingdon)*, 11(112): 763–774, 1965. doi:10.1080/14786436508230081.

[74] A. M. Edmonds, U. F. S. D'Haenens-Johansson, R. J. Cruddace, M. E. Newton, K.-M. C. Fu, C. Santori, R. G. Beausoleil, D. J. Twitchen, and M. L. Markham. Production of oriented nitrogen-vacancy color centers in synthetic diamond. *Phys. Rev. B*, 86(3): 035201, 2012. doi:10.1103/PhysRevB.86.035201.

[75] T. R. Eichhorn, C. A. McLellan, and A. C. Bleszynski Jayich. Optimizing the formation of depth-confined nitrogen vacancy center spin ensembles in diamond for quantum sensing. *Phys. Rev. Mater.*, 3(11):113802, 2019. doi:10.1103/PhysRevMaterials.3.113802.

[76] A. Einstein. Über einen die Erzeugung und Verwandlung des Lichtes betreffenden heuristischen Gesichtspunkt. *Ann. Phys.*, 322(6):132–148, 1905. doi:10.1002/andp.19053220607.

[77] M. Fanciulli, S. Jin, and T. Moustakas. Nitrogen in diamond thin films. *Physica B Condens. Matter*, 229(1):27–36, 1996. doi:10.1016/S0921-4526(96)00506-6.

[78] D. Farfurnik, N. Alfasi, S. Masis, Y. Kauffmann, E. Farchi, Y. Romach, Y. Hovav, E. Buks, and N. Bar-Gill. Enhanced concentrations of nitrogen-vacancy centers in diamond through TEM irradiation. *Appl. Phys. Lett.*, 111(12):123101, 2017. doi:10.1063/1.4993257.

[79] R. Farrer. On the substitutional nitrogen donor in diamond. *Solid State Commun.*, 7 (9):685–688, 1969. doi:10.1016/0038-1098(69)90593-6.

[80] F. Fávaro de Oliveira, D. Antonov, Y. Wang, P. Neumann, S. A. Momenzadeh, T. Häußermann, A. Pasquarelli, A. Denisenko, and J. Wrachtrup. Tailoring spin defects in diamond by lattice charging. *Nat. Commun.*, 8(1):15409, 2017. doi:10.1038/ncomms15409.

[81] C. Findler, J. Lang, C. Osterkamp, M. Nesládek, and F. Jelezko. Indirect overgrowth as a synthesis route for superior diamond nano sensors. *Sci. Rep.*, 10(1):22404, 2020. doi:10.1038/s41598-020-79943-2.

[82] G. D. Fuchs, V. V. Dobrovitski, R. Hanson, A. Batra, C. D. Weis, T. Schenkel, and D. D. Awschalom. Excited-state spectroscopy using single spin manipulation in diamond. *Phys. Rev. Lett.*, 101(11):117601, 2008. doi:10.1103/PhysRevLett.101.117601.

[83] P. Fuchs, T. Jung, M. Kieschnick, J. Meijer, and C. Becher. A cavity-based optical antenna for color centers in diamond. *APL Photonics*, 6(8):086102, 2021. doi:10.1063/5.0057161.

[84] M. Fukami, D. R. Candido, D. D. Awschalom, and M. E. Flatté. Opportunities for Long-Range Magnon-Mediated Entanglement of Spin Qubits via On- and Off-Resonant Coupling. *PRX Quantum*, 2(4):040314, 2021. doi:10.1103/PRXQuantum.2.040314.

[85] T. Fukui, Y. Doi, T. Miyazaki, Y. Miyamoto, H. Kato, T. Matsumoto, T. Makino, S. Yamasaki, R. Morimoto, N. Tokuda, M. Hatano, Y. Sakagawa, H. Morishita, T. Tashima, S. Miwa, Y. Suzuki, and N. Mizuochi. Perfect selective alignment of nitrogen-vacancy centers in diamond. *Appl. Phys. Express*, 7(5):055201, 2014. doi:10.7567/APEX.7.055201.

[86] O. Gaathon, J. S. Hodges, E. H. Chen, L. Li, S. Bakhru, H. Bakhru, D. Englund, and R. M. Osgood. Planar fabrication of arrays of ion-exfoliated single-crystal-diamond membranes with nitrogen-vacancy color centers. *Opt. Mater.*, 35(3):361–365, 2013. doi:10.1016/j.optmat.2012.09.020.

[87] T. Gaebel, M. Domhan, I. Popa, C. Wittmann, P. Neumann, F. Jelezko, J. R. Rabeau, N. Stavrias, A. D. Greentree, S. Prawer, J. Meijer, J. Twamley, P. R. Hemmer, and J. Wrachtrup. Room-temperature coherent coupling of single spins in diamond. *Nat. Phys.*, 2(6):408–413, 2006. doi:10.1038/nphys318.

[88] Á. Gali. *Ab initio* theory of the nitrogen-vacancy center in diamond. *Nanophotonics*, 8(11):1907–1943, 2019. doi:10.1515/nanoph-2019-0154.

[89] B.-C. Gallheber, M. Fischer, M. Mayr, J. Straub, and M. Schreck. Growth, stress, and defects of heteroepitaxial diamond on Ir/YSZ/Si(111). *J. Appl. Phys.*, 123(22):225302, 2018. doi:10.1063/1.5025709.

[90] V. Giovannetti, S. Lloyd, and L. Maccone. Quantum-Enhanced Measurements: Beating the Standard Quantum Limit. *Science*, 306(5700):1330, 2004. doi:10.1126/science.1104149.

[91] R. M. Goldblatt, A. M. Martin, and A. A. Wood. Tunable gyromagnetic augmentation of nuclear spins in diamond. *Phys. Rev. B*, 105(2):L020405, 2022. doi:10.1103/PhysRevB.105.L020405.

[92] J. P. Goss, R. Jones, M. I. Heggie, C. P. Ewels, P. R. Briddon, and S. Öberg. Theory of hydrogen in diamond. *Phys. Rev. B*, 65(11):115207, 2002. doi:10.1103/PhysRevB.65.115207.

[93] D. M. Greenberger, M. A. Horne, and A. Zeilinger. Going Beyond Bell's Theorem. In M. Kafatos, editor, *Bell's Theorem, Quantum Theory and Conceptions of the Universe*, pages 69–72. Springer Netherlands, Dordrecht, 1989. ISBN 978-94-017-0849-4.

[94] D. Griffiths. *Introduction to Quantum Mechanics.* Pearson Prentice Hall, Hoboken, 2nd edition, 2004. ISBN 0-13-111892-7.

[95] P. Grivickas, P. Ščajev, N. Kazuchits, S. Lastovskii, L. F. Voss, A. M. Conway, A. Mazanik, O. Korolik, V. Bikbajevas, and V. Grivickas. Carrier recombination and diffusion in high-purity diamond after electron irradiation and annealing. *Appl. Phys. Lett.*, 117(24):242103, 2020. doi:10.1063/5.0028363.

[96] A. Gruber, A. Dräbenstedt, C. Tietz, L. Fleury, J. Wrachtrup, and C. V. Borczyskowski. Scanning Confocal Optical Microscopy and Magnetic Resonance on Single Defect Centers. *Science*, 276(5321):2012, 1997. doi:10.1126/science.276.5321.2012.

[97] X. Guo, N. Delegan, J. C. Karsch, Z. Li, T. Liu, R. Shreiner, A. Butcher, D. D. Awschalom, F. J. Heremans, and A. A. High. Tunable and Transferable Diamond Membranes for Integrated Quantum Technologies. *Nano Lett.*, 21(24):10392–10399, 2021. doi:10.1021/acs.nanolett.1c03703.

[98] E. L. Hahn. Spin Echoes. *Phys. Rev.*, 80(4):580–594, 1950. doi:10.1103/PhysRev.80.580.

[99] R. Hanson, F. M. Mendoza, R. J. Epstein, and D. D. Awschalom. Polarization and Readout of Coupled Single Spins in Diamond. *Phys. Rev. Lett.*, 97(8):087601, 2006. doi:10.1103/PhysRevLett.97.087601.

[100] J. Harrison, M. J. Sellars, and N. B. Manson. Optical spin polarisation of the N-V centre in diamond. *J. Lumin.*, 107(1):245–248, 2004. doi:10.1016/j.jlumin.2003.12.020.

[101] M. V. Hauf, B. Grotz, B. Naydenov, M. Dankerl, S. Pezzagna, J. Meijer, F. Jelezko, J. Wrachtrup, M. Stutzmann, F. Reinhard, and J. A. Garrido. Chemical control of the charge state of nitrogen-vacancy centers in diamond. *Phys. Rev. B*, 83(8):081304, 2011. doi:10.1103/PhysRevB.83.081304.

[102] K. Hayashi, Y. Matsuzaki, T. Ashida, S. Onoda, H. Abe, T. Ohshima, M. Hatano, T. Taniguchi, H. Morishita, M. Fujiwara, and N. Mizuochi. Experimental and theoretical analysis of noise strength and environmental correlation time for ensembles of nitrogen-vacancy centers in diamond. *J Phys. Soc. Japan*, 89(5):054708, 2020. doi:10.7566/JPSJ.89.054708.

[103] B. Hensen, H. Bernien, A. E. Dréau, A. Reiserer, N. Kalb, M. S. Blok, J. Ruitenberg, R. F. L. Vermeulen, R. N. Schouten, C. Abellán, W. Amaya, V. Pruneri, M. W. Mitchell, M. Markham, D. J. Twitchen, D. Elkouss, S. Wehner, T. H. Taminiau, and R. Hanson. Loophole-free Bell inequality violation using electron spins separated by 1.3 kilometres. *Nature*, 526(7575):682–686, 2015. doi:10.1038/nature15759.

[104] E. D. Herbschleb, H. Kato, Y. Maruyama, T. Danjo, T. Makino, S. Yamasaki, I. Ohki, K. Hayashi, H. Morishita, M. Fujiwara, and N. Mizuochi. Ultra-long coherence times amongst room-temperature solid-state spins. *Nat. Commun.*, 10(1):3766, 2019. doi:10.1038/s41467-019-11776-8.

[105] F. J. Heremans, G. D. Fuchs, C. F. Wang, R. Hanson, and D. D. Awschalom. Generation and transport of photoexcited electrons in single-crystal diamond. *Appl. Phys. Lett.*, 94(15):152102, 2009. doi:10.1063/1.3120225.

[106] F. J. Heremans, C. G. Yale, and D. D. Awschalom. Control of Spin Defects in Wide-Bandgap Semiconductors for Quantum Technologies. *Proc. IEEE*, 104(10):2009–2023, 2016. doi:10.1109/JPROC.2016.2561274.

[107] S. L. N. Hermans, M. Pompili, H. K. C. Beukers, S. Baier, J. Borregaard, and R. Hanson. Qubit teleportation between non-neighbouring nodes in a quantum network. *Nature*, 605(7911):663–668, 2022. doi:10.1038/s41586-022-04697-y.

[108] R. Høy Jensen, E. Janitz, Y. Fontana, Y. He, O. Gobron, I. P. Radko, M. Bhaskar, R. Evans, C. D. Rodríguez Rosenblueth, L. Childress, A. Huck, and U. L. Andersen. Cavity-Enhanced Photon Emission from a Single Germanium-Vacancy Center in a Diamond Membrane. *Phys. Rev. Appl.*, 13(6):64016, 2020. doi:10.1103/PhysRevApplied.13.064016.

[109] P. Hu and S. R. Hartmann. Theory of spectral diffusion decay using an uncorrelated-sudden-jump model. *Phys. Rev. B*, 9(1):1–13, 1974. doi:10.1103/PhysRevB.9.1.

[110] L. B. Hughes, Z. Zhang, C. Jin, S. A. Meynell, B. Ye, W. Wu, Z. Wang, E. J. Davis, T. E. Mates, N. Y. Yao, K. Mukherjee, and A. C. Bleszynski Jayich. Two-dimensional spin systems in PECVD-grown diamond with tunable density and long coherence for enhanced quantum sensing and simulation. *APL Mater.*, 11(2):021101, 2023. doi:10.1063/5.0133501.

[111] D. C. Hunt, D. J. Twitchen, M. E. Newton, J. M. Baker, T. R. Anthony, W. F. Banholzer, and S. S. Vagarali. Identification of the neutral carbon $\langle 100 \rangle$-split interstitial in diamond. *Phys. Rev. B*, 61(6):3863–3876, 2000. doi:10.1103/PhysRevB.61.3863.

[112] T.-Y. Hwang, J. Lee, S.-W. Jeon, Y.-S. Kim, Y.-W. Cho, H.-T. Lim, S. Moon, S.-W. Han, Y.-H. Choa, and H. Jung. Sub-10 nm Precision Engineering of Solid-State Defects via Nanoscale Aperture Array Mask. *Nano Lett.*, 22(4):1672–1679, 2022. doi:10.1021/acs.nanolett.1c04699.

[113] J. Isberg, A. Tajani, and D. J. Twitchen. Photoionization measurement of deep defects in single-crystalline CVD diamond using the transient-current technique. *Phys. Rev. B*, 73(24):245207, 2006. doi:10.1103/PhysRevB.73.245207.

[114] H. Ishiwata, M. Nakajima, K. Tahara, H. Ozawa, T. Iwasaki, and M. Hatano. Perfectly aligned shallow ensemble nitrogen-vacancy centers in (111) diamond. *Appl. Phys. Lett.*, 111(4):043103, 2017. doi:10.1063/1.4993160.

[115] N. T. Islam, C. Ci, W. Lim, C. Cahall, J. Kim, and D. J. Gauthier. Provably secure and high-rate quantum key distribution with time-bin qudits. *Sci. Adv.*, 3(11):e1701491, 2017. doi:10.1126/sciadv.1701491.

[116] J. Isoya, H. Kanda, Y. Uchida, S. C. Lawson, S. Yamasaki, H. Itoh, and Y. Morita. EPR identification of the negatively charged vacancy in diamond. *Phys. Rev. B*, 45 (3):1436–1439, 1992. doi:10.1103/PhysRevB.45.1436.

[117] V. Jacques, P. Neumann, J. Beck, M. Markham, D. Twitchen, J. Meijer, F. Kaiser, G. Balasubramanian, F. Jelezko, and J. Wrachtrup. Dynamic polarization of single nuclear spins by optical pumping of nitrogen-vacancy color centers in diamond at room temperature. *Phys. Rev. Lett.*, 102(5):7–10, 2009. doi:10.1103/PhysRevLett.102.057403.

[118] I. Jakobi, S. A. Momenzadeh, F. Fávaro de Oliveira, J. Michl, F. Ziem, M. Schreck, P. Neumann, A. Denisenko, and J. Wrachtrup. Efficient creation of dipolar coupled nitrogen-vacancy spin qubits in diamond. *J. Phys. Conf. Ser.*, 752(1):012001, 2016. doi:10.1088/1742-6596/752/1/012001.

[119] E. Janitz, K. Herb, L. A. Völker, W. S. Huxter, C. L. Degen, and J. M. Abendroth. Diamond surface engineering for molecular sensing with nitrogen—vacancy centers. *J. Mater. Chem. C*, 10(37):13533–13569, 2022. doi:10.1039/D2TC01258H.

[120] F. Jelezko and J. Wrachtrup. Quantum Information Processing with Defects. In T. Beth and G. Leuchs, editors, *Quantum Information Processing*, pages 150–161. WILEY-VCH Verlag GmbH & Co. KGaA, 2005. ISBN 978-3-527-60600-9. doi:10.1002/3527606009.ch12.

[121] F. Jelezko, T. Gaebel, I. Popa, A. Gruber, and J. Wrachtrup. Observation of Coherent Oscillations in a Single Electron Spin. *Phys. Rev. Lett.*, 92(7):076401, 2004. doi:10.1103/PhysRevLett.92.076401.

[122] P. C. Jerger, Y.-X. Wang, M. Onizhuk, B. S. Soloway, M. T. Solomon, C. Egerstrom, F. J. Heremans, G. Galli, A. A. Clerk, and D. D. Awschalom. Detecting spin bath polarization with quantum quench phase shifts of single spins in diamond. *arXiv*, page 2303.02233, 2023. doi:10.48550/arXiv.2303.02233.

[123] E. Joos, H. Dieter Zeh, C. Kiefer, D. Giulini, J. Kupsch, and I.-O. Stamatescu. *Decoherence and the Appearance of a Classical World in Quantum Theory*. Springer Berlin, Heidelberg, 2003. ISBN 978-3-642-05576-8. doi:10.1007/978-3-662-05328-7.

[124] M. Joos, D. Bluvstein, Y. Lyu, D. Weld, and A. B. Jayich. Protecting qubit coherence by spectrally engineered driving of the spin environment. *npj Quantum Inf.*, 8(1):47, 2022. doi:10.1038/s41534-022-00560-0.

[125] P. Jurcevic and L. C. G. Govia. Effective qubit dephasing induced by spectator-qubit relaxation. *Quantum Sci. Technol.*, 7(4):045033, 2022. doi:10.1088/2058-9565/ac8cad.

[126] W. Kaiser and W. L. Bond. Nitrogen, A Major Impurity in Common Type I Diamond. *Phys. Rev.*, 115(4):857–863, 1959. doi:10.1103/PhysRev.115.857.

[127] N. Kalb, A. A. Reiserer, P. C. Humphreys, J. J. W. Bakermans, S. J. Kamerling, N. H. Nickerson, S. C. Benjamin, D. J. Twitchen, M. Markham, and R. Hanson. Entanglement distillation between solid-state quantum network nodes. *Science*, 356 (6341):928–932, 2017. doi:10.1126/science.aan0070.

[128] S. Kanai, F. J. Heremans, H. Seo, G. Wolfowicz, C. P. Anderson, S. E. Sullivan, M. Onizhuk, G. Galli, D. D. Awschalom, and H. Ohno. Generalized scaling of spin qubit coherence in over 12,000 host materials. *Proc. Natl. Acad. Sci. U.S.A.*, 119(15): e2121808119, 2022. doi:10.1073/pnas.2121808119.

[129] A. Kandala, A. Mezzacapo, K. Temme, M. Takita, M. Brink, J. M. Chow, and J. M. Gambetta. Hardware-efficient variational quantum eigensolver for small molecules and quantum magnets. *Nature*, 549(7671):242–246, 2017. doi:10.1038/nature23879.

[130] E. Kapit. The upside of noise: engineered dissipation as a resource in superconducting circuits. *Quantum Sci. Technol.*, 2(3):033002, 2017. doi:10.1088/2058-9565/aa7e5d.

[131] S. Kawai, H. Yamano, T. Sonoda, K. Kato, J. J. Buendia, T. Kageura, R. Fukuda, T. Okada, T. Tanii, T. Higuchi, M. Haruyama, K. Yamada, S. Onoda, T. Ohshima, W. Kada, O. Hanaizumi, A. Stacey, T. Teraji, S. Kono, J. Isoya, and H. Kawarada. Nitrogen-Terminated Diamond Surface for Nanoscale NMR by Shallow Nitrogen-Vacancy Centers. *J. Phys. Chem. C*, 123(6):3594–3604, 2019. doi:10.1021/acs.jpcc.8b11274.

[132] R. Kawase, H. Kawashima, H. Kato, N. Tokuda, S. Yamasaki, M. Ogura, T. Makino, and N. Mizuochi. n-type diamond synthesized with tert-butylphosphine for long spin coherence times of perfectly aligned NV centers. *J. Appl. Phys.*, 132(17):174504, 2022. doi:10.1063/5.0101215.

[133] T. A. Kennedy, J. S. Colton, J. E. Butler, R. C. Linares, and P. J. Doering. Long coherence times at 300 K for nitrogen-vacancy center spins in diamond grown by chemical vapor deposition. *Appl. Phys. Lett.*, 83(20):4190–4192, 2003. doi:10.1063/1.1626791.

[134] L. Kevan and L. D. Kispert. *Electron Spin Double Resonance Spectroscopy.* Wiley, 1976. ISBN 978-0-608-10854-4.

[135] R. U. A. Khan, B. L. Cann, P. M. Martineau, J. Samartseva, J. J. P. Freeth, S. J. Sibley, C. B. Hartland, M. E. Newton, H. K. Dhillon, and D. J. Twitchen. Colour-causing defects and their related optoelectronic transitions in single crystal CVD diamond. *J. Phys. Condens. Matter*, 25(27):275801, 2013. doi:10.1088/0953-8984/25/27/275801.

[136] M. Kim, H. J. Mamin, M. H. Sherwood, K. Ohno, D. D. Awschalom, and D. Rugar. Decoherence of Near-Surface Nitrogen-Vacancy Centers Due to Electric Field Noise. *Phys. Rev. Lett.*, 115(8):087602, 2015. doi:10.1103/PhysRevLett.115.087602.

[137] C. Kittel. *Introduction to Solid State Physics.* John Wiley & Sons, Hoboken, 8th edition, 2004. ISBN 0-471-41526-X.

[138] J. R. Klauder and P. W. Anderson. Spectral Diffusion Decay in Spin Resonance Experiments. *Phys. Rev.*, 125(3):912–932, 1962. doi:10.1103/PhysRev.125.912.

[139] H. S. Knowles, D. M. Kara, and M. Atatüre. Demonstration of a Coherent Electronic Spin Cluster in Diamond. *Phys. Rev. Lett.*, 117(10):100802, 2016. doi:10.1103/PhysRevLett.117.100802.

[140] B. Kraus, H. P. Büchler, S. Diehl, A. Kantian, A. Micheli, and P. Zoller. Preparation of entangled states by quantum Markov processes. *Phys. Rev. A*, 78(4):042307, 2008. doi:10.1103/PhysRevA.78.042307.

[141] Y. Kuratomi, N. Okazaki, T. Ishihara, T. Arai, and S. Kira. Variability of Breath-by-Breath Tidal Volume and its Characteristics in Normal and Diseased Subjects. *Jpn. J. Med.*, 24(2):141–149, 1985. doi:10.2169/internalmedicine1962.24.141.

[142] S. Lawson, G. Davies, A. T. Collins, and A. Mainwood. Migration energy of the neutral vacancy in diamond. *J. Phys. Condens. Matter*, 4(9):L125, 1992. doi:10.1088/0953-8984/4/9/001.

[143] S. C. Lawson, D. Fisher, D. C. Hunt, and M. E. Newton. On the existence of positively charged single-substitutional nitrogen in diamond. *J. Phys. Condens. Matter*, 10(27): 6171, 1998. doi:10.1088/0953-8984/10/27/016.

[144] D. C. Lay. *Linear Algebra and Its Applications*. Addison-Wesley Longman, 3rd edition, 2002. ISBN 0-201-70970-8.

[145] D. Le Sage, K. Arai, D. R. Glenn, S. J. DeVience, L. M. Pham, L. Rahn-Lee, M. D. Lukin, A. Yacoby, A. Komeili, and R. L. Walsworth. Optical magnetic imaging of living cells. *Nature*, 496(7446):486–489, 2013. doi:10.1038/nature12072.

[146] J. Lee, M. Tatsuta, A. Xu, E. Bauch, M. J. H. Ku, and R. L. Walsworth. Dressed-state control of effective dipolar interaction between strongly-coupled solid-state spins. *arXiv*, page 2203.07610, 2022. doi:10.48550/arXiv.2203.07610.

[147] J. C. Lee, A. P. Magyar, D. O. Bracher, I. Aharonovich, and E. L. Hu. Fabrication of thin diamond membranes for photonic applications. *Diam. Relat. Mater.*, 33:45–48, 2013. doi:10.1016/j.diamond.2012.12.008.

[148] M. Lesik, N. Raatz, A. Tallaire, P. Spinicelli, R. John, J. Achard, A. Gicquel, V. Jacques, J.-F. Roch, J. Meijer, and S. Pezzagna. Production of bulk NV centre arrays by shallow implantation and diamond CVD overgrowth. *phys. status solidi (a)*, 213(10):2594–2600, 2016. doi:10.1002/pssa.201600219.

[149] M. H. Levitt. *Spin Dynamics: Basics of Nuclear Magnetic Resonance*. John Wiley & Sons, West Sussex, 2nd edition, 2008. ISBN 0-470-51117-6.

[150] G. Lindblad. On the generators of quantum dynamical semigroups. *Commun. Math. Phys.*, 48(2):119–130, 1976. doi:10.1007/BF01608499.

[151] G.-Q. Liu, X. Feng, N. Wang, Q. Li, and R.-B. Liu. Coherent quantum control of nitrogen-vacancy center spins near 1000 kelvin. *Nat. Commun.*, 10(1):1344, 2019. doi:10.1038/s41467-019-09327-2.

[152] Y. Liu, S. Shankar, N. Ofek, M. Hatridge, A. Narla, K. M. Sliwa, L. Frunzio, R. J. Schoelkopf, and M. H. Devoret. Comparing and combining measurement-based and driven-dissipative entanglement stabilization. *Phys. Rev. X*, 6(1):011022, 2016. doi:10.1103/PhysRevX.6.011022.

[153] J. H. N. Loubser and W. P. van Ryneveld. The dynamic Jahn - Teller and other effects in the high-temperature electron spin resonance spectrum of nitrogen in diamond. *Br. J. Appl. Phys.*, 18(7):1029, 1967. doi:10.1088/0508-3443/18/7/127.

[154] J. H. N. Loubser and J. A. van Wyk. Optical spin-polarisation in a triplet state in irradiated and annealed type Ib diamonds. *Diamond Res.*, pages 11 – 14, 1977. URL `https://www.osti.gov/etdeweb/biblio/5220761`.

[155] J. H. N. Loubser and J. A. van Wyk. Electron spin resonance in the study of diamond. *Rep. Prog. Phys.*, 41(8):1201–1248, 1978. doi:10.1088/0034-4885/41/8/002.

[156] A. Lozovoi, D. Daw, H. Jayakumar, and C. A. Meriles. Dark defect charge dynamics in bulk chemical-vapor-deposition-grown diamonds probed via nitrogen vacancy centers. *Phys. Rev. Mater.*, 4(5):053602, 2020. doi:10.1103/PhysRevMaterials.4.053602.

[157] T. Lühmann, R. John, R. Wunderlich, J. Meijer, and S. Pezzagna. Coulomb-driven single defect engineering for scalable qubits and spin sensors in diamond. *Nat. Commun.*, 10(1):4956, 2019. doi:10.1038/s41467-019-12556-0.

[158] F. Machado, E. A. Demler, N. Y. Yao, and S. Chatterjee. Quantum noise spectroscopy of dynamical critical phenomena. *arXiv*, page 2211.02663, 2022. doi:10.48550/arXiv.2211.02663.

[159] E. R. MacQuarrie, T. A. Gosavi, N. R. Jungwirth, S. A. Bhave, and G. D. Fuchs. Mechanical Spin Control of Nitrogen-Vacancy Centers in Diamond. *Phys. Rev. Lett.*, 111(22):227602, 2013. doi:10.1103/PhysRevLett.111.227602.

[160] B. J. Maertz, A. P. Wijnheijmer, G. D. Fuchs, M. E. Nowakowski, and D. D. Awschalom. Vector magnetic field microscopy using nitrogen vacancy centers in diamond. *Appl. Phys. Lett.*, 96(9):092504, 2010. doi:10.1063/1.3337096.

[161] A. Magnus. *The secrets of Albertus Magnus: of the vertues of hearbs, stones, and certain beasts*. London, 1650. URL `http://resource.nlm.nih.gov/2301096R`.

[162] A. P. Magyar, J. C. Lee, A. M. Limarga, I. Aharonovich, F. Rol, D. R. Clarke, M. Huang, and E. L. Hu. Fabrication of thin, luminescent, single-crystal diamond membranes. *Appl. Phys. Lett.*, 99(8):81913, 2011. doi:10.1063/1.3628463.

[163] P. Maletinsky, S. Hong, M. S. Grinolds, B. Hausmann, M. D. Lukin, R. L. Walsworth, M. Lončar, and A. Yacoby. A robust scanning diamond sensor for nanoscale imaging with single nitrogen-vacancy centres. *Nat. Nanotechnol.*, 7(5):320–324, 2012. doi:10.1038/nnano.2012.50.

[164] H. J. Mamin, M. Kim, M. H. Sherwood, C. T. Rettner, K. Ohno, D. D. Awschalom, and D. Rugar. Nanoscale Nuclear Magnetic Resonance with a Nitrogen-Vacancy Spin Sensor. *Science*, 339(6119):557–560, 2013. doi:10.1126/science.1231540.

[165] N. B. Manson, J. P. Harrison, and M. J. Sellars. Nitrogen-vacancy center in diamond: Model of the electronic structure and associated dynamics. *Phys. Rev. B*, 74(10): 104303, 2006. doi:10.1103/PhysRevB.74.104303.

[166] N. B. Manson, M. Hedges, M. S. J. Barson, R. Ahlefeldt, M. W. Doherty, H. Abe, T. Ohshima, and M. J. Sellars. NV^{-}–N^{+} pair centre in 1b diamond. *New J. Phys.*, 20(11):113037, 2018. doi:10.1088/1367-2630/aaec58.

[167] F. Marquardt and A. Püttmann. Introduction to dissipation and decoherence in quantum systems. *arXiv*, page 0809.4403, 2008. doi:10.48550/arXiv.0809.4403.

[168] J. P. D. Martin, N. B. Manson, D. C. Doetschman, M. J. Sellars, R. Neuhaus, and E. Wilson. Spectral hole burning and Raman heterodyne signals associated with an avoided crossing in the NV centre in diamond. *J. Lumin.*, 86(3):355–362, 2000. doi:10.1016/S0022-2313(00)00179-4.

[169] J. R. Maze, P. L. Stanwix, J. S. Hodges, S. Hong, J. M. Taylor, P. Cappellaro, L. Jiang, M. V. Gurudev Dutt, E. Togan, A. S. Zibrov, A. Yacoby, R. L. Walsworth, and M. D. Lukin. Nanoscale magnetic sensing with an individual electronic spin in diamond. *Nature*, 455(7213):644–647, 2008. doi:10.1038/nature07279.

[170] B. McCullian, H. Cheung, H. Chen, and G. Fuchs. Quantifying the Spectral Diffusion of N-V Centers by Symmetry. *Phys. Rev. Appl.*, 18(6):064011, 2022. doi:10.1103/PhysRevApplied.18.064011.

[171] A. McDonald and A. A. Clerk. Exact Solutions of Interacting Dissipative Systems via Weak Symmetries. *Phys. Rev. Lett.*, 128(3):033602, 2022. doi:10.1103/PhysRevLett.128.033602.

[172] C. A. McLellan, B. A. Myers, S. Kraemer, K. Ohno, D. D. Awschalom, and A. C. Bleszynski Jayich. Patterned Formation of Highly Coherent Nitrogen-Vacancy Centers Using a Focused Electron Irradiation Technique. *Nano Lett.*, 16(4):2450–2454, 2016. doi:10.1021/acs.nanolett.5b05304.

[173] J. Meijer, B. Burchard, M. Domhan, C. Wittmann, T. Gaebel, I. Popa, F. Jelezko, and J. Wrachtrup. Generation of single color centers by focused nitrogen implantation. *Appl. Phys. Lett.*, 87(26):261909, 2005. doi:10.1063/1.2103389.

[174] S. A. Meynell, C. A. McLellan, L. B. Hughes, W. Wang, T. E. Mates, K. Mukherjee, and A. C. Bleszynski Jayich. Engineering quantum-coherent defects: The role of substrate miscut in chemical vapor deposition diamond growth. *Appl. Phys. Lett.*, 117 (19):194001, 2020. doi:10.1063/5.0029715.

[175] J. Michl, T. Teraji, S. Zaiser, I. Jakobi, G. Waldherr, F. Dolde, P. Neumann, M. W. Doherty, N. B. Manson, J. Isoya, and J. Wrachtrup. Perfect alignment and preferential orientation of nitrogen-vacancy centers during chemical vapor deposition diamond growth on (111) surfaces. *Appl. Phys. Lett.*, 104(10):102407, 2014. doi:10.1063/1.4868128.

[176] W. B. Mims. Phase Memory in Electron Spin Echoes, Lattice Relaxation Effects in $\mathrm{CaWO_4}$: Er, Ce, Mn. *Phys. Rev.*, 168(2):370–389, 1968. doi:10.1103/PhysRev.168.370.

[177] W. B. Mims, K. Nassau, and J. D. McGee. Spectral Diffusion in Electron Resonance Lines. *Phys. Rev.*, 123(6):2059–2069, 1961. doi:10.1103/PhysRev.123.2059.

[178] T. Mittiga, S. Hsieh, C. Zu, B. Kobrin, F. Machado, P. Bhattacharyya, N. Z. Rui, A. Jarmola, S. Choi, D. Budker, and N. Y. Yao. Imaging the Local Charge Environment of Nitrogen-Vacancy Centers in Diamond. *Phys. Rev. Lett.*, 121(24):246402, 2018. doi:10.1103/PhysRevLett.121.246402.

[179] T. Miyazaki, Y. Miyamoto, T. Makino, H. Kato, S. Yamasaki, T. Fukui, Y. Doi, N. Tokuda, M. Hatano, and N. Mizuochi. Atomistic mechanism of perfect alignment of nitrogen-vacancy centers in diamond. *Appl. Phys. Lett.*, 105(26):261601, 2014. doi:10.1063/1.4904988.

[180] N. Mizuochi, P. Neumann, F. Rempp, J. Beck, V. Jacques, P. Siyushev, K. Nakamura, D. J. Twitchen, H. Watanabe, S. Yamasaki, F. Jelezko, and J. Wrachtrup. Coherence of single spins coupled to a nuclear spin bath of varying density. *Phys. Rev. B*, 80(4): 041201(R), 2009. doi:10.1103/PhysRevB.80.041201.

[181] B. A. Myers, A. Das, M. C. Dartiailh, K. Ohno, D. D. Awschalom, and A. C. Bleszynski Jayich. Probing Surface Noise with Depth-Calibrated Spins in Diamond. *Phys. Rev. Lett.*, 113(2):027602, 2014. doi:10.1103/PhysRevLett.113.027602.

[182] B. A. Myers, A. Ariyaratne, and A. C. Bleszynski Jayich. Double-Quantum Spin-Relaxation Limits to Coherence of Near-Surface Nitrogen-Vacancy Centers. *Phys. Rev. Lett.*, 118(19):197201, 2017. doi:10.1103/PhysRevLett.118.197201.

[183] B. Naydenov, F. Reinhard, A. Lämmle, V. Richter, R. Kalish, U. F. S. D'Haenens-Johansson, M. Newton, F. Jelezko, and J. Wrachtrup. Increasing the coherence time of single electron spins in diamond by high temperature annealing. *Appl. Phys. Lett.*, 97(24):242511, 2010. doi:10.1063/1.3527975.

[184] J. N. Neethirajan, T. Hache, D. Paone, D. Pinto, A. Denisenko, R. Stöhr, P. Udvarhelyi, A. Pershin, A. Gali, J. Wrachtrup, K. Kern, and A. Singha. Controlled Surface Modification to Revive Shallow NV^{--} Centers. *Nano Lett.*, 23(7):2563–2569, 2023. doi:10.1021/acs.nanolett.2c04733.

[185] P. Neumann, R. Kolesov, V. Jacques, J. Beck, J. Tisler, A. Batalov, L. Rogers, N. B. Manson, G. Balasubramanian, F. Jelezko, and J. Wrachtrup. Excited-state spectroscopy of single NV defects in diamond using optically detected magnetic resonance. *New J. Phys.*, 11(1):013017, 2009. doi:10.1088/1367-2630/11/1/013017.

[186] P. Neumann, R. Kolesov, B. Naydenov, J. Beck, F. Rempp, M. Steiner, V. Jacques, G. Balasubramanian, M. L. Markham, D. J. Twitchen, S. Pezzagna, J. Meijer, J. Twamley, F. Jelezko, and J. Wrachtrup. Quantum register based on coupled electron spins in a room-temperature solid. *Nat. Phys.*, 6(4):249–253, 2010. doi:10.1038/nphys1536.

[187] C. T. Nguyen, D. D. Sukachev, M. K. Bhaskar, B. Machielse, D. S. Levonian, E. N. Knall, P. Stroganov, C. Chia, M. J. Burek, R. Riedinger, H. Park, M. Lončar, and M. D. Lukin. An integrated nanophotonic quantum register based on silicon-vacancy spins in diamond. *Phys. Rev. B*, 100(16):165428, 2019. doi:10.1103/PhysRevB.100.165428.

[188] C. T. Nguyen, D. D. Sukachev, M. K. Bhaskar, B. Machielse, D. S. Levonian, E. N. Knall, P. Stroganov, R. Riedinger, H. Park, M. Lončar, and M. D. Lukin. Quantum Network Nodes Based on Diamond Qubits with an Efficient Nanophotonic Interface. *Phys. Rev. Lett.*, 123(18):183602, 2019. doi:10.1103/PhysRevLett.123.183602.

[189] M. A. Nielsen and I. L. Chuang. *Quantum Computation and Quantum Information.* Cambridge U.P., Cambridge, 10th anniversary edition, 2011.

[190] A. P. Nizovtsev, S. Y. Kilin, F. Jelezko, I. Popa, A. Gruber, C. Tietz, and J. Wrachtrup. Spin-selective low temperature spectroscopy on single molecules with a triplet-triplet optical transition: Application to the NV defect center in diamond. *Opt. Spectrosc.*, 94(6):848 – 858, 2003. doi:10.1134/1.1586735.

[191] K. Ohno. *Nanometer-scale engineering of shallow spins in diamond.* PhD Thesis, University of California, Santa Barbara, 2014.

[192] K. Ohno, F. J. Heremans, L. C. Bassett, B. A. Myers, D. M. Toyli, A. C. Bleszynski Jayich, C. J. Palmstrøm, and D. D. Awschalom. Engineering shallow spins in diamond with nitrogen delta-doping. *Appl. Phys. Lett.*, 101(8):082413, 2012. doi:10.1063/1.4748280.

[193] K. Ohno, F. Joseph Heremans, C. F. de las Casas, B. A. Myers, B. J. Alemán, A. C. Bleszynski Jayich, and D. D. Awschalom. Three-dimensional localization of spins in diamond using 12C implantation. *Appl. Phys. Lett.*, 105(5):052406, 2014. doi:10.1063/1.4890613.

[194] H. Okushi, H. Watanabe, S. Ri, S. Yamanaka, and D. Takeuchi. Device-grade homoepitaxial diamond film growth. *J. Cryst. Growth*, 237-239:1269–1276, 2002. doi:10.1016/S0022-0248(01)02144-3.

[195] M. Onizhuk and G. Galli. Substrate-controlled dynamics of spin qubits in low dimensional van der Waals materials. *Appl. Phys. Lett.*, 118(15):154003, 2021. doi:10.1063/5.0048399.

[196] M. Onizhuk and G. Galli. PyCCE: A Python Package for Cluster Correlation Expansion Simulations of Spin Qubit Dynamics. *Adv. Theory Simul.*, 4(11):2100254, 2021. doi:10.1002/adts.202100254.

[197] M. Onizhuk, K. C. Miao, J. P. Blanton, H. Ma, C. P. Anderson, A. Bourassa, D. D. Awschalom, and G. Galli. Probing the Coherence of Solid-State Qubits at Avoided Crossings. *PRX Quantum*, 2(1):010311, 2021. doi:10.1103/PRXQuantum.2.010311.

[198] C. Osterkamp, M. Mangold, J. Lang, P. Balasubramanian, T. Teraji, B. Naydenov, and F. Jelezko. Engineering preferentially-aligned nitrogen-vacancy centre ensembles in CVD grown diamond. *Sci. Rep.*, 9(1):5786, 2019. doi:10.1038/s41598-019-42314-7.

[199] H. Ozawa, K. Tahara, H. Ishiwata, M. Hatano, and T. Iwasaki. Formation of perfectly aligned nitrogen-vacancy-center ensembles in chemical-vapor-deposition-grown diamond (111). *Appl. Phys. Express*, 10(4):045501, 2017. doi:10.7567/APEX.10.045501.

[200] E. Paladino, Y. Galperin, G. Falci, and B. L. Altshuler. $1/f$ noise: Implications for solid-state quantum information. *Rev. Mod. Phys.*, 86(2):361–418, 2014. doi:10.1103/RevModPhys.86.361.

[201] H. Park, J. Lee, S. Han, S. Oh, and H. Seo. Decoherence of nitrogen-vacancy spin ensembles in a nitrogen electron-nuclear spin bath in diamond. *npj Quantum Inf.*, 8 (1):95, 2022. doi:10.1038/s41534-022-00605-4.

[202] C. Peaker, M. Atumi, J. Goss, P. Briddon, A. Horsfall, M. Rayson, and R. Jones. Assignment of 13C hyperfine interactions in the P1-center in diamond. *Diam. Relat. Mater.*, 70:118–123, 2016. doi:10.1016/j.diamond.2016.10.013.

[203] C. V. Peaker, J. P. Goss, P. R. Briddon, A. B. Horsfall, and M. J. Rayson. The vacancy–hydrogen defect in diamond: A computational study. *phys. status solidi (a)*, 212(11):2431–2436, 2015. doi:10.1002/pssa.201532215.

[204] M. Pfender, N. Aslam, H. Sumiya, S. Onoda, P. Neumann, J. Isoya, C. A. Meriles, and J. Wrachtrup. Nonvolatile nuclear spin memory enables sensor-unlimited nanoscale spectroscopy of small spin clusters. *Nat. Commun.*, 8(1):834, 2017. doi:10.1038/s41467-017-00964-z.

[205] L. M. Pham, N. Bar-Gill, D. Le Sage, C. Belthangady, A. Stacey, M. Markham, D. J. Twitchen, M. D. Lukin, and R. L. Walsworth. Enhanced metrology using preferential orientation of nitrogen-vacancy centers in diamond. *Phys. Rev. B*, 86(12):121202, 2012. doi:10.1103/PhysRevB.86.121202.

[206] L. M. Pham, S. J. DeVience, F. Casola, I. Lovchinsky, A. O. Sushkov, E. Bersin, J. Lee, E. Urbach, P. Cappellaro, H. Park, A. Yacoby, M. Lukin, and R. L. Walsworth. NMR technique for determining the depth of shallow nitrogen-vacancy centers in diamond. *Phys. Rev. B*, 93(4):045425, 2016. doi:10.1103/PhysRevB.93.045425.

[207] H. Pinto, R. Jones, D. W. Palmer, J. P. Goss, P. R. Briddon, and S. Öberg. On the diffusion of NV defects in diamond. *phys. status solidi (a) appl. mater. sci.*, 209(9): 1765–1768, 2012. doi:10.1002/pssa.201200050.

[208] A. H. Piracha, P. Rath, K. Ganesan, S. Kühn, W. H. P. Pernice, and S. Prawer. Scalable Fabrication of Integrated Nanophotonic Circuits on Arrays of Thin Single Crystal Diamond Membrane Windows. *Nano Lett.*, 16(5):3341–3347, 2016. doi:10.1021/acs.nanolett.6b00974.

[209] M. Pompili, S. L. N. Hermans, S. Baier, H. K. C. Beukers, P. C. Humphreys, R. N. Schouten, R. F. L. Vermeulen, M. J. Tiggelman, L. dos Santos Martins, B. Dirkse, S. Wehner, and R. Hanson. Realization of a multinode quantum network of remote solid-state qubits. *Science*, 372(6539):259–264, 2021. doi:10.1126/science.abg1919.

[210] M. Prelas, G. Popovici, and L. K. Bigelow, editors. *Handbook of Industrial Diamonds and Diamond Films*. Marcel Dekker, New York, 1st edition, 1997. ISBN 0-8247-9994-1.

[211] J. R. Rabeau, P. Reichart, G. Tamanyan, D. N. Jamieson, S. Prawer, F. Jelezko, T. Gaebel, I. Popa, M. Domhan, and J. Wrachtrup. Implantation of labelled single nitrogen vacancy centers in diamond using N15. *Appl. Phys. Lett.*, 88(2):023113, 2006. doi:10.1063/1.2158700.

[212] N. F. Ramsey. A Molecular Beam Resonance Method with Separated Oscillating Fields. *Phys. Rev.*, 78(6):695–699, 1950. doi:10.1103/PhysRev.78.695.

[213] D. A. Redman, S. Brown, R. H. Sands, and S. C. Rand. Spin dynamics and electronic states of N-V centers in diamond by EPR and four-wave-mixing spectroscopy. *Phys. Rev. Lett.*, 67(24):3420–3423, 1991. doi:10.1103/PhysRevLett.67.3420.

[214] E. C. Reynhardt, G. L. High, and J. A. van Wyk. Temperature dependence of spin-spin and spin-lattice relaxation times of paramagnetic nitrogen defects in diamond. *J. Chem. Phys.*, 109(19):8471–8477, 1998. doi:10.1063/1.477511.

[215] K. Rezai, S. Choi, M. D. Lukin, and A. O. Sushkov. Probing dynamics of a two-dimensional dipolar spin ensemble using single qubit sensor. *arXiv*, page 2207.10688, 2022. doi:10.48550/arXiv.2207.10688.

[216] R. Robertson, J. J. Fox, and A. E. Martin. Two types of diamond. *Philos. Trans. Royal Soc. A*, 232(707-720):463–535, 1933. doi:10.1098/rsta.1934.0013.

[217] Y. Romach, C. Müller, T. Unden, L. J. Rogers, T. Isoda, K. M. Itoh, M. Markham, A. Stacey, J. Meijer, S. Pezzagna, B. Naydenov, L. P. McGuinness, N. Bar-Gill, and F. Jelezko. Spectroscopy of surface-induced noise using shallow spins in diamond. *Phys. Rev. Lett.*, 114(1):017601, 2015. doi:10.1103/PhysRevLett.114.017601.

[218] L. Rondin, G. Dantelle, A. Slablab, F. Grosshans, F. Treussart, P. Bergonzo, S. Perruchas, T. Gacoin, M. Chaigneau, H.-C. Chang, V. Jacques, and J.-F. Roch. Surface-induced charge state conversion of nitrogen-vacancy defects in nanodiamonds. *Phys. Rev. B*, 82(11):115449, 2010. doi:10.1103/PhysRevB.82.115449.

[219] L. Rondin, J. P. Tetienne, P. Spinicelli, C. Dal Savio, K. Karrai, G. Dantelle, A. Thiaville, S. Rohart, J. F. Roch, and V. Jacques. Nanoscale magnetic field mapping with a single spin scanning probe magnetometer. *Appl. Phys. Lett.*, 100(15):153118, 2012. doi:10.1063/1.3703128.

[220] L. Rondin, J.-P. Tetienne, T. Hingant, J.-F. Roch, P. Maletinsky, and V. Jacques. Magnetometry with nitrogen-vacancy defects in diamond. *Rep. Prog. Phys.*, 77(5): 056503, 2014. doi:10.1088/0034-4885/77/5/056503.

[221] J. Rosa, M. Vaněček, M. Nesládek, and L. M. Stals. Photoionization cross-section of dominant defects in CVD diamond. *Diam. Relat. Mater.*, 8(2):721–724, 1999. doi:10.1016/S0925-9635(98)00354-9.

[222] E. L. Rosenfeld, L. M. Pham, M. D. Lukin, and R. L. Walsworth. Sensing Coherent Dynamics of Electronic Spin Clusters in Solids. *Phys. Rev. Lett.*, 120(24):243604, 2018. doi:10.1103/PhysRevLett.120.243604.

[223] T. Rosskopf, A. Dussaux, K. Ohashi, M. Loretz, R. Schirhagl, H. Watanabe, S. Shikata, K. M. Itoh, and C. L. Degen. Investigation of Surface Magnetic Noise by Shallow Spins in Diamond. *Phys. Rev. Lett.*, 112(14):147602, 2014. doi:10.1103/PhysRevLett.112.147602.

[224] T. Rosskopf, J. Zopes, J. M. Boss, and C. L. Degen. A quantum spectrum analyzer enhanced by a nuclear spin memory. *npj Quantum Inf.*, 3(1):1–7, 2017. doi:10.1038/s41534-017-0030-6.

[225] M. Ruf, M. IJspeert, S. van Dam, N. de Jong, H. van den Berg, G. Evers, and R. Hanson. Optically Coherent Nitrogen-Vacancy Centers in Micrometer-Thin Etched Diamond Membranes. *Nano Lett.*, 19(6):3987–3992, 2019. doi:10.1021/acs.nanolett.9b01316.

[226] A. E. Rugar, C. Dory, S. Sun, and J. Vučković. Characterization of optical and spin properties of single tin-vacancy centers in diamond nanopillars. *Phys. Rev. B*, 99(20): 205417, 2019. doi:10.1103/PhysRevB.99.205417.

[227] R. G. Ryan, A. Stacey, K. M. O'Donnell, T. Ohshima, B. C. Johnson, L. C. L. Hollenberg, P. Mulvaney, and D. A. Simpson. Impact of Surface Functionalization on the Quantum Coherence of Nitrogen-Vacancy Centers in Nanodiamonds. *ACS Appl. Mater. Interfaces*, 10(15):13143–13149, 2018. doi:10.1021/acsami.7b19238.

[228] C. Saguy, C. Cytermann, B. Fizgeer, V. Richter, Y. Avigal, N. Moriya, R. Kalish, B. Mathieu, and A. Deneuville. Diffusion of hydrogen in undoped, p-type and n-type doped diamonds. *Diam. Relat. Mater.*, 12(3):623–631, 2003. doi:10.1016/S0925-9635(02)00403-X.

[229] S. Sangtawesin, T. O. Brundage, Z. J. Atkins, and J. R. Petta. Highly tunable formation of nitrogen-vacancy centers via ion implantation. *Appl. Phys. Lett.*, 105(6): 063107, 2014. doi:10.1063/1.4892971.

[230] S. Sangtawesin, B. L. Dwyer, S. Srinivasan, J. J. Allred, L. V. H. Rodgers, K. De Greve, A. Stacey, N. Dontschuk, K. M. O'Donnell, D. Hu, D. A. Evans, C. Jaye, D. A. Fischer, M. L. Markham, D. J. Twitchen, H. Park, M. D. Lukin, and N. P. de Leon. Origins of

Diamond Surface Noise Probed by Correlating Single-Spin Measurements with Surface Spectroscopy. *Phys. Rev. X*, 9(3):031052, 2019. doi:10.1103/PhysRevX.9.031052.

[231] S. Schindler and R. Mirman. The decomposition of the tensor product of representations of the symmetric group. *J. Math. Phys.*, 18(8):1678–1696, 1977. doi:10.1063/1.523469.

[232] L. Schlipf, T. Oeckinghaus, K. Xu, D. B. R. Dasari, A. Zappe, F. Fávaro de Oliveira, B. Kern, M. Azarkh, M. Drescher, M. Ternes, K. Kern, J. Wrachtrup, and A. Finkler. A molecular quantum spin network controlled by a single qubit. *Sci. Adv.*, 3(8):e1701116, 2017. doi:10.1126/sciadv.1701116.

[233] M. Schlosshauer. *Decoherence and the Quantum-To-Classical Transition.* Springer Berlin, Heidelberg, 2007. ISBN 978-3-540-35773-5. doi:10.1007/978-3-540-35775-9.

[234] M. Schlosshauer. Quantum decoherence. *Phys. Rep.*, 831:1–57, 2019. doi:10.1016/j.physrep.2019.10.001.

[235] M. Schreck, S. Gsell, R. Brescia, and M. Fischer. Ion bombardment induced buried lateral growth: the key mechanism for the synthesis of single crystal diamond wafers. *Sci. Rep.*, 7(1):44462, 2017. doi:10.1038/srep44462.

[236] E. Schrödinger. An Undulatory Theory of the Mechanics of Atoms and Molecules. *Phys. Rev.*, 28(6):1049–1070, 1926. doi:10.1103/PhysRev.28.1049.

[237] R. Shankar. *Principles of Quantum Mechanics.* Plenum Press, New York, 2nd edition, 1994.

[238] C. Shinei, Y. Masuyama, M. Miyakawa, H. Abe, S. Ishii, S. Saiki, S. Onoda, T. Taniguchi, T. Ohshima, and T. Teraji. Nitrogen related paramagnetic defects: Decoherence source of ensemble of NV^- center. *J. Appl. Phys.*, 132(21):214402, 2022. doi:10.1063/5.0103332.

[239] L. H. Shul'man, I. M. Zaritskiĭ, and G. A. Padzyarei. Reorientation of the Jahn-Teller distortion in nitrogen impurity centers in diamond. *Sov. phys., Solid state*, 8:1842, 1967.

[240] E. Sideras-Haddad, S. H. Connell, J. P. F. Sellschop, I. Z. Machi, D. Rebuli, R. D. Maclear, and B. P. Doyle. Hydrogen and oxygen chemistry and dynamics in diamond studied by nuclear microscopic techniques. *Nucl. Instrum. Methods Phys. Res. B*, 181 (1):419–425, 2001. doi:10.1016/S0168-583X(01)00595-X.

[241] Y. K. Siew, G. Sarkar, X. Hu, J. Hui, A. See, and C. T. Chua. Thermal Curing of Hydrogen Silsesquioxane. *J. Electrochem. Soc.*, 147(1):335, 2000. doi:10.1149/1.1393196.

[242] R. N. Simons. *Coplanar Waveguide Circuits, Components, and Systems.* John Wiley & Sons, 2001. ISBN 978-0-471-16121-9.

[243] P. Siyushev, M. H. Metsch, A. Ijaz, J. M. Binder, M. K. Bhaskar, D. D. Sukachev, A. Sipahigil, R. E. Evans, C. T. Nguyen, M. D. Lukin, P. R. Hemmer, Y. N. Palyanov, I. N. Kupriyanov, Y. M. Borzdov, L. J. Rogers, and F. Jelezko. Optical and microwave control of germanium-vacancy center spins in diamond. *Phys. Rev. B*, 96(8):81201, 2017. doi:10.1103/PhysRevB.96.081201.

[244] C. P. Slichter. *Principles of Magnetic Resonance*. Springer Berlin, Heidelberg, 3rd edition, 1990. ISBN 978-3-642-08069-2. doi:10.1007/978-3-662-09441-9.

[245] W. V. Smith, P. P. Sorokin, I. L. Gelles, and G. J. Lasher. Electron-Spin Resonance of Nitrogen Donors in Diamond. *Phys. Rev.*, 115(6):1546–1552, 1959. doi:10.1103/PhysRev.115.1546.

[246] P. Spinicelli, A. Dréau, L. Rondin, F. Silva, J. Achard, S. Xavier, S. Bansropun, T. Debuisschert, S. Pezzagna, J. Meijer, V. Jacques, and J. F. Roch. Engineered arrays of nitrogen-vacancy color centers in diamond based on implantation of CN$^-$ Molecules through nanoapertures. *New J. Phys.*, 13(2):025014, 2011. doi:10.1088/1367-2630/13/2/025014.

[247] A. Stacey, T. J. Karle, L. P. McGuinness, B. C. Gibson, K. Ganesan, S. Tomljenovic-Hanic, A. D. Greentree, A. Hoffman, R. G. Beausoleil, and S. Prawer. Depletion of nitrogen-vacancy color centers in diamond via hydrogen passivation. *Appl. Phys. Lett.*, 100(7):071902, 2012. doi:10.1063/1.3684612.

[248] D. H. Staelin, A. W. Morgenthaler, and J. A. Kong. *Electromagnetic waves*. Pearson, London, 1st edition, 1993. ISBN 0-13-225871-4.

[249] P. L. Stanwix, L. M. Pham, J. R. Maze, D. Le Sage, T. K. Yeung, P. Cappellaro, P. R. Hemmer, A. Yacoby, M. D. Lukin, and R. L. Walsworth. Coherence of nitrogen-vacancy electronic spin ensembles in diamond. *Phys. Rev. B*, 82(20):201201, 2010. doi:10.1103/PhysRevB.82.201201.

[250] T. Staudacher, F. Ziem, L. Häussler, R. Stöhr, S. Steinert, F. Reinhard, J. Scharpf, A. Denisenko, and J. Wrachtrup. Enhancing the spin properties of shallow implanted nitrogen vacancy centers in diamond by epitaxial overgrowth. *Appl. Phys. Lett.*, 101 (21):212401, 2012. doi:10.1063/1.4767144.

[251] T. Staudacher, F. Shi, S. Pezzagna, J. Meijer, J. Du, C. A. Meriles, F. Reinhard, and J. Wrachtrup. Nuclear magnetic resonance spectroscopy on a (5-nanometer)^3 sample volume. *Science*, 339(6119):561–563, 2013. doi:10.1126/science.1231675.

[252] D. D. Sukachev, A. Sipahigil, C. T. Nguyen, M. K. Bhaskar, R. E. Evans, F. Jelezko, and M. D. Lukin. Silicon-Vacancy Spin Qubit in Diamond: A Quantum Memory Exceeding 10 ms with Single-Shot State Readout. *Phys. Rev. Lett.*, 119(6):223602, 2017. doi:10.1103/PhysRevLett.119.223602.

[253] A. O. Sushkov, I. Lovchinsky, N. Chisholm, R. L. Walsworth, H. Park, and M. D. Lukin. Magnetic Resonance Detection of Individual Proton Spins Using Quantum Reporters. *Phys. Rev. Lett.*, 113(19):197601, 2014. doi:10.1103/PhysRevLett.113.197601.

[254] D. Suter and G. A. Álvarez. Colloquium: Protecting quantum information against environmental noise. *Rev. Mod. Phys.*, 88(4):041001, 2016. doi:10.1103/RevModPhys.88.041001.

[255] K. Tahara, H. Ozawa, T. Iwasaki, N. Mizuochi, and M. Hatano. Quantifying selective alignment of ensemble nitrogen-vacancy centers in (111) diamond. *Appl. Phys. Lett.*, 107(19):193110, 2015. doi:10.1063/1.4935709.

[256] S. Takahashi, R. Hanson, J. van Tol, M. S. Sherwin, and D. D. Awschalom. Quenching Spin Decoherence in Diamond through Spin Bath Polarization. *Phys. Rev. Lett.*, 101 (4):047601, 2008. doi:10.1103/PhysRevLett.101.047601.

[257] A. Tallaire, A. T. Collins, D. Charles, J. Achard, R. Sussmann, A. Gicquel, M. E. Newton, A. M. Edmonds, and R. J. Cruddace. Characterisation of high-quality thick single-crystal diamond grown by CVD with a low nitrogen addition. *Diam. Relat. Mater.*, 15(10):1700–1707, 2006. doi:10.1016/j.diamond.2006.02.005.

[258] A. Tallaire, M. Kasu, K. Ueda, and T. Makimoto. Origin of growth defects in CVD diamond epitaxial films. *Diam. Relat. Mater.*, 17(1):60–65, 2008. doi:10.1016/j.diamond.2007.10.003.

[259] J. M. Taylor, P. Cappellaro, L. Childress, L. Jiang, D. Budker, P. R. Hemmer, A. Yacoby, R. Walsworth, and M. D. Lukin. High-sensitivity diamond magnetometer with nanoscale resolution. *Nat. Phys.*, 4(10):810–816, 2008. doi:10.1038/nphys1075.

[260] C. J. Terblanche and E. C. Reynhardt. Room-temperature field dependence of the electron spin–lattice relaxation times of paramagnetic P1 and P2 centers in diamond. *Chem. Phys. Lett.*, 322(3):273–279, 2000. doi:10.1016/S0009-2614(00)00411-5.

[261] N. Tokuda. Homoepitaxial Diamond Growth by Plasma-Enhanced Chemical Vapor Deposition. In N. Yang, editor, *Novel Aspects of Diamond: From Growth to Applications*, pages 1–29. Springer International Publishing, Cham, 2019. ISBN 978-3-030-12469-4. doi:10.1007/978-3-030-12469-4_1.

[262] D. M. Toyli, C. D. Weis, G. D. Fuchs, T. Schenkel, and D. D. Awschalom. Chip-scale nanofabrication of single spins and spin arrays in diamond. *Nano Lett.*, 10(8): 3168–3172, 2010. doi:10.1021/nl102066q.

[263] D. M. Toyli, D. J. Christle, A. Alkauskas, B. B. Buckley, C. G. Van de Walle, and D. D. Awschalom. Measurement and Control of Single Nitrogen-Vacancy Center Spins above 600 K. *Phys. Rev. X*, 2(3):031001, 2012. doi:10.1103/PhysRevX.2.031001.

[264] F. Treussart, V. Jacques, E. Wu, T. Gacoin, P. Grangier, and J. F. Roch. Photoluminescence of single colour defects in 50 nm diamond nanocrystals. *Phys. B: Condens. Matter*, 376-377:926–929, 2006. doi:10.1016/j.physb.2005.12.232.

[265] D. J. Twitchen, D. Hunt, V. Smart, M. E. Newton, and J. M. Baker. Correlation between ND1 optical absorption and the concentration of negative vacancies determined by electron paramagnetic resonance (EPR). *Diam. Relat. Mater.*, 8(8):1572–1575, 1999. doi:10.1016/S0925-9635(99)00038-2.

[266] A. M. Tyryshkin, S. Tojo, J. J. L. Morton, H. Riemann, N. V. Abrosimov, P. Becker, H. J. Pohl, T. Schenkel, M. L. W. Thewalt, K. M. Itoh, and S. A. Lyon. Electron spin coherence exceeding seconds in high-purity silicon. *Nature Materials*, 11(2):143–147, 2012. doi:10.1038/nmat3182.

[267] R. Ulbricht, S. T. van der Post, J. P. Goss, P. R. Briddon, R. Jones, R. U. A. Khan, and M. Bonn. Single substitutional nitrogen defects revealed as electron acceptor states in diamond using ultrafast spectroscopy. *Phys. Rev. B*, 84(16):165202, 2011. doi:10.1103/PhysRevB.84.165202.

[268] T. K. Unden, D. Louzon, M. Zwolak, W. H. Zurek, and F. Jelezko. Revealing the Emergence of Classicality Using Nitrogen-Vacancy Centers. *Phys. Rev. Lett.*, 123(14): 140402, 2019. doi:10.1103/PhysRevLett.123.140402.

[269] A. Valentin, O. Brinza, S. Farhat, J. Achard, and F. Bénédic. 3D kinetic Monte-Carlo simulations of diamond growth on (1 0 0) surfaces. *Diam. Relat. Mater.*, 123:108865, 2022. doi:10.1016/j.diamond.2022.108865.

[270] A. van der Ziel. On the noise spectra of semi-conductor noise and of flicker effect. *Physica*, 16(4):359–372, 1950. doi:10.1016/0031-8914(50)90078-4.

[271] E. van Oort, N. B. Manson, and M. Glasbeek. Optically detected spin coherence of the diamond N-V centre in its triplet ground state. *J. Phys. C: Solid State Phys.*, 21 (23):4385, 1988. doi:10.1088/0022-3719/21/23/020.

[272] L. Viola and S. Lloyd. Dynamical suppression of decoherence in two-state quantum systems. *Phys. Rev. A*, 58(4):2733–2744, 1998. doi:10.1103/PhysRevA.58.2733.

[273] L. Viola, E. Knill, and S. Lloyd. Dynamical Decoupling of Open Quantum Systems. *Phys. Rev. Lett.*, 82(12):2417–2421, 1999. doi:10.1103/PhysRevLett.82.2417.

[274] N. H. Wan, T.-J. Lu, K. C. Chen, M. P. Walsh, M. E. Trusheim, L. De Santis, E. A. Bersin, I. B. Harris, S. L. Mouradian, I. R. Christen, E. S. Bielejec, and D. Englund. Large-scale integration of artificial atoms in hybrid photonic circuits. *Nature*, 583 (7815):226–231, 2020. doi:10.1038/s41586-020-2441-3.

[275] G. Wang, C. Li, H. Tang, B. Li, F. Madonini, F. F. Alsallom, W. K. C. Sun, P. Peng, F. Villa, J. Li, and P. Cappellaro. Manipulating solid-state spin concentration through charge transport. *arXiv*, page 2302.12742, 2023. doi:10.48550/arXiv.2302.12742.

[276] Y. D. Wang and A. A. Clerk. Reservoir-engineered entanglement in optomechanical systems. *Phys. Rev. Lett.*, 110(25):253601, 2013. doi:10.1103/PhysRevLett.110.253601.

[277] H. Weyl. *Theory of Groups and Quantum Mechanics.* Princeton U.P., Princeton, 1931.

[278] S. J. Whiteley, G. Wolfowicz, C. P. Anderson, A. Bourassa, H. Ma, M. Ye, G. Koolstra, K. J. Satzinger, M. V. Holt, F. J. Heremans, A. N. Cleland, D. I. Schuster, G. Galli, and D. D. Awschalom. Spin–phonon interactions in silicon carbide addressed by Gaussian acoustics. *Nat. Phys.*, 15(5):490–495, 2019. doi:10.1038/s41567-019-0420-0.

[279] G. Wolfowicz, F. J. Heremans, C. P. Anderson, S. Kanai, H. Seo, A. Gali, G. Galli, and D. D. Awschalom. Quantum guidelines for solid-state spin defects. *Nat. Rev. Mater.*, 6(10):906–925, 2021. doi:10.1038/s41578-021-00306-y.

[280] X. Xiao and N. Zhao. Proposal for observing dynamic Jahn–Teller effect by single solid-state defects. *New J. Phys.*, 18(10):103022, 2016. doi:10.1088/1367-2630/18/10/103022.

[281] M. Xie, X. Yu, L. V. H. Rodgers, D. Xu, I. Chi-Dur, A. Toros, N. Quack, N. P. de Leon, and P. C. Maurer. Biocompatible surface functionalization architecture for a diamond quantum sensor. *Proc. Natl. Acad. Sci. U.S.A.*, 119(8):e2114186119, 2022. doi:10.1073/pnas.2114186119/.

[282] T. Xie, Z. Zhao, X. Kong, W. Ma, M. Wang, X. Ye, P. Yu, Z. Yang, S. Xu, P. Wang, Y. Wang, F. Shi, and J. Du. Beating the standard quantum limit under ambient conditions with solid-state spins. *Sci. Adv.*, 7(32):abg9204, 2021. doi:10.1126/sciadv.abg9204.

[283] T. Yamamoto, T. Umeda, K. Watanabe, S. Onoda, M. L. Markham, D. J. Twitchen, B. Naydenov, L. P. McGuinness, T. Teraji, S. Koizumi, F. Dolde, H. Fedder, J. Honert, J. Wrachtrup, T. Ohshima, F. Jelezko, and J. Isoya. Extending spin coherence times of diamond qubits by high-temperature annealing. *Phys. Rev. B*, 88(7):075206, 2013. doi:10.1103/PhysRevB.88.075206.

[284] H. Yamano, S. Kawai, K. Kato, T. Kageura, M. Inaba, T. Okada, I. Higashimata, M. Haruyama, T. Tanii, K. Yamada, S. Onoda, W. Kada, O. Hanaizumi, T. Teraji, J. Isoya, and H. Kawarada. Charge state stabilization of shallow nitrogen vacancy centers in diamond by oxygen surface modification. *Jpn. J. Appl. Phys.*, 56(4S):04CK08, 2017. doi:10.7567/JJAP.56.04CK08.

[285] F. Yan, S. Gustavsson, J. Bylander, X. Jin, F. Yoshihara, D. G. Cory, Y. Nakamura, T. P. Orlando, and W. D. Oliver. Rotating-frame relaxation as a noise spectrum analyser of a superconducting qubit undergoing driven evolution. *Nature Communications*, 4(1):2337, 2013. doi:10.1038/ncomms3337.

[286] Y. Yanay and A. A. Clerk. Reservoir engineering with localized dissipation: Dynamics and prethermalization. *Phys. Rev. Res.*, 2(2):023177, 2020. doi:10.1103/PhysRevResearch.2.023177.

[287] W. Yang and R.-B. Liu. Quantum many-body theory of qubit decoherence in a finite-size spin bath. *Phys. Rev. B*, 78(8):085315, 2008. doi:10.1103/PhysRevB.78.085315.

[288] W. Yang and R.-B. Liu. Quantum many-body theory of qubit decoherence in a finite-size spin bath. II. Ensemble dynamics. *Phys. Rev. B*, 79(11):115320, 2009. doi:10.1103/PhysRevB.79.115320.

[289] N. Y. Yao, L. Jiang, A. V. Gorshkov, Z.-X. Gong, A. Zhai, L.-M. Duan, and M. D. Lukin. Robust Quantum State Transfer in Random Unpolarized Spin Chains. *Phys. Rev. Lett.*, 106(4):040505, 2011. doi:10.1103/PhysRevLett.106.040505.

[290] A. M. Zaitsev. *Optical Properties of Diamond: A Data Handbook*. Springer-Verlag Berlin, Heidelberg, 2013. ISBN 978-3-642-08585-7.

[291] I. M. Zaritskiĭ, V. Y. Bratus', V. S. Vikhin, A. S. Vishnevskii, A. A. Konchits, and V. M. Ustintsev. Spin-lattice relaxation of a Jahn-Teller nitrogen center in diamond. *Sov. Phys., Solid State*, 18:3226–3230, 1976.

[292] P. Zeeman. XXXII. On the influence of magnetism on the nature of the light emitted by a substance. *Lond. Edinb. Dublin philos. mag. j. sci.*, 43(262):226–239, 1897. doi:10.1080/14786449708620985.

[293] K. Zhang, S. Ghosh, S. Saxena, and M. V. Gurudev Dutt. Nanoscale spin detection of copper ions using double electron-electron resonance at room temperature. *Phys. Rev. B*, 104(22):224412, 2021. doi:10.1103/PhysRevB.104.224412.

[294] T. Zhang, G. Pramanik, K. Zhang, M. Gulka, L. Wang, J. Jing, F. Xu, Z. Li, Q. Wei, P. Cigler, and Z. Chu. Toward Quantitative Bio-sensing with Nitrogen–Vacancy Center in Diamond. *ACS Sens.*, 6(6):2077–2107, 2021. doi:10.1021/acssensors.1c00415.

[295] W.-l. Zhang, L.-r. Lou, W. Zhu, and G.-z. Wang. Enhancing fluorescence of shallow nitrogen-vacancy centers in diamond by surface coating with titanium oxide layers. *Chinese J. Chem. Phys.*, 32(5):521–524, 2019. doi:10.1063/1674-0068/cjcp1904069.

[296] Z. Zhang, M. Joos, D. Bluvstein, Y. Lyu, and A. C. Bleszynski Jayich. Reporter-spin-assisted T1 relaxometry. *arXiv*, page 2208.11470, 2022. doi:10.48550/arXiv.2208.11470.

[297] N. Zhao, S. W. Ho, and R. B. Liu. Decoherence and dynamical decoupling control of nitrogen vacancy center electron spins in nuclear spin baths. *Phys. Rev. B*, 85(11):115303, 2012. doi:10.1103/PhysRevB.85.115303.

[298] Z. Zhao, X. Ye, S. Xu, P. Yu, Z. Yang, X. Kong, Y. Wang, T. Xie, F. Shi, and J. Du. Sub-nanotesla Sensitivity at the Nanoscale with a Single Spin. *arXiv*, page 2205.04415, 2022. doi:10.48550/arXiv.2205.04415.

[299] T.-X. Zheng, A. Li, J. Rosen, S. Zhou, M. Koppenhöfer, Z. Ma, F. T. Chong, A. A. Clerk, L. Jiang, and P. C. Maurer. Preparation of Metrological States in Dipolar-Interacting Spin Systems. *npj Quantum Inf.*, 8:150, 2022. doi:10.1038/s41534-022-00667-4.

[300] J. F. Ziegler, M. D. Ziegler, and J. P. Biersack. SRIM – The stopping and range of ions in matter (2010). *Nucl. Instrum. Methods Phys. Res. B*, 268(11):1818–1823, 2010. doi:10.1016/j.nimb.2010.02.091.

[301] P. J. Zomer, M. H. D. Guimarães, J. C. Brant, N. Tombros, and B. J. van Wees. Fast pick up technique for high quality heterostructures of bilayer graphene and hexagonal boron nitride. *Appl. Phys. Lett.*, 105(1):13101, 2014. doi:10.1063/1.4886096.

[302] C. Zu, F. Machado, B. Ye, S. Choi, B. Kobrin, T. Mittiga, S. Hsieh, P. Bhattacharyya, M. Markham, D. Twitchen, A. Jarmola, D. Budker, C. R. Laumann, J. E. Moore, and N. Y. Yao. Emergent hydrodynamics in a strongly interacting dipolar spin ensemble. *Nature*, 597(7874):45–50, 2021. doi:10.1038/s41586-021-03763-1.

[303] W. H. Zurek. Pointer basis of quantum apparatus: Into what mixture does the wave packet collapse? *Phys. Rev. D*, 24(6):1516–1525, 1981. doi:10.1103/PhysRevD.24.1516.

[304] W. H. Zurek. Environment-induced superselection rules. *Phys. Rev. D*, 26(8):1862–1880, 1982. doi:10.1103/PhysRevD.26.1862.